

Lessons from the Yellowstone  
wolf experiment p. 1302

Local tools against threats  
to world heritage p. 1317

Watching protein synthesis  
in living cells pp. 1316 & 1367

# Science



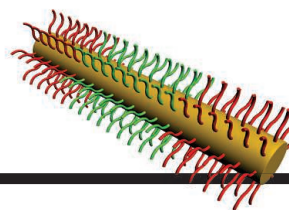
\$10  
20 MARCH 2015  
[sciencemag.org](http://sciencemag.org)

AAAS

## *Swiftly structured*

Accelerated 3D printing  
crafts objects from  
a liquid pool p. 1349

# CONTENTS



## 1310 & 1329

From cylinders to 3D  
superstructures

20 MARCH 2015 • VOLUME 347 • ISSUE 6228



## NEWS

### IN BRIEF

**1294** Roundup of the week's news

### IN DEPTH

#### **1296 MERS SURGES AGAIN, BUT PANDEMIC JITTERS EASE**

The camel virus appears to be less lethal and more prevalent in humans than assumed *By K. Kupferschmidt*

#### **1297 NEW SATELLITE RADAR COULD FIND 100,000 UNDERWATER MOUNTAINS**

Better seamount maps could improve tsunami predictions and models of carbon mixing in the deep ocean *By E. Hand*

#### **1298 ORIGIN-OF-LIFE PUZZLE CRACKED**

Study explains how three essential classes of molecules could have formed simultaneously *By R. F. Service*

#### **1299 WOES FOR 'EXERCISE HORMONE'**

Challenged antibody assays raise new questions about hoped-for obesity drug target *By K. Servick*

#### **1300 BIOLOGISTS DEVISE INVASION PLAN FOR MUTATIONS**

"Gene drive" technique could fight insect-borne disease, but some call for safeguards *By J. Bohannon*

► REPORT BY V. M. GANTZ AND E. BIER

10.1126/science.aaa5945

#### **1301 EMBRYO ENGINEERING ALARM**

Researchers call for restraint in genome editing *By G. Vogel*

► PERSPECTIVE BY D. BALTIMORE ET AL.

10.1126/science.aab1028

### FEATURE

#### **1302 LESSONS FROM THE WILD LAB**

Yellowstone Park is a real-world laboratory of predator-prey relations *By V. Morell*

## INSIGHTS

### PERSPECTIVES

#### **1308 ALL THAT GLITTERS NEED NOT BE GOLD**

Refractory plasmonic ceramics provide durable nanophotonic solutions *By A. Boltasseva and V. M. Shalae*

#### **1310 BUILDING SUPERMICELLES FROM SIMPLE POLYMERS**

Precise control of the polymer building blocks enables synthesis of a range of micrometer-scale structures *By I.-H. Lee et al.*

► REPORT P. 1329



#### **1312 METABOLIC CONTROL OF EPILEPSY**

Seizures may be controlled by targeting inexcitable elements of the nervous system *By H. E. Scharfman*

► REPORT P. 1362

#### **1313 TAMING CH<sub>5</sub><sup>+</sup>, THE "ENFANT TERRIBLE" OF CHEMICAL STRUCTURES**

Ion-counting spectroscopy reveals the low-energy states of a molecule with highly dynamic bonds *By T. Oka*

► REPORT P. 1346

#### **1314 WHAT IS THE QUESTION?**

Mistaking the type of question being considered is the most common error in data analysis *By J. T. Leek and R. D. Peng*

#### **1316 A TRICK'N WAY TO SEE THE PIONEER ROUND OF TRANSLATION**

Watching where and when individual messenger RNAs direct protein synthesis in live cells *By M. W. Popp and L. E. Maquat*

► REPORT P. 1367

#### **1317 CREATING A SAFE OPERATING SPACE FOR ICONIC ECOSYSTEMS**

Manage local stressors to promote resilience to global change *By M. Scheffer et al.*

#### **1319 HOLDING YOUR BREATH FOR LONGEVITY**

A nutrient-sensing protein is important for the health of hematopoietic stem cells during aging

*By A. Ocampo and J. C. I. Belmonte*

► REPORT P. 1374

### BOOKS ET AL.

#### **1321 HUXLEY'S CHURCH AND MAXWELL'S DEMON**

*By M. Stanley, reviewed by C. Smith*

#### **1322 NOTE-BY-NOTE COOKING**

*By H. This,*

#### **THE IN VITRO MEAT COOKBOOK**

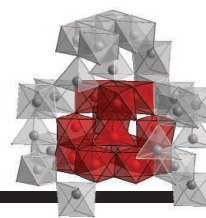
*By K. van Mensvoort and H.-J. Grievink, reviewed by J. Ubbink*

Science Staff .....	1292
New Products .....	1378
Science Careers .....	1379



# CONTENTS

20 MARCH 2015 • VOLUME 347 • ISSUE 6228



1359

Capturing an elusive ion cluster



## LETTERS

### 1323 DRONES: BALANCING RISK AND POTENTIAL

By T. S. Gregory et al.

### 1323 CYBER-ATTACK RISK LOW FOR MEDICAL DEVICES

By Z. T. H. Tse et al.

### 1324 REGULATORY HURDLES FOR AGRICULTURE GMOs

By P. Hackett and D. Carroll

## RESEARCH

## IN BRIEF

1325 From *Science* and other journals

## REVIEW

### 1328 MATERIALS SCIENCE

Materials that couple sensing, actuation, computation, and communication

M. A. McEvoy and N. Correll

REVIEW SUMMARY; FOR FULL TEXT:

[dx.doi.org/10.1126/science.1261689](http://dx.doi.org/10.1126/science.1261689)

► PODCAST

## REPORTS

### 1329 MICELLE ASSEMBLY

Multidimensional hierarchical self-assembly of amphiphilic cylindrical block comicelles

H. Qiu et al.

► PERSPECTIVE P. 1310

### 1333 SOLAR PHYSICS

The crucial role of surface magnetic fields for the solar dynamo

R. Cameron and M. Schüssler

### 1335 SUPERCONDUCTIVITY

Broken translational and rotational symmetry via charge stripe order in underdoped  $\text{YBa}_2\text{Cu}_3\text{O}_{6+y}$

R. Comin et al.

### 1339 HEAVY FERMIONS

Chirality density wave of the “hidden order” phase in  $\text{URu}_2\text{Si}_2$

H.-H. Kung et al.

### 1342 APPLIED OPTICS

Multiwavelength achromatic metasurfaces by dispersive phase compensation

F. Aieta et al.

### 1346 VIBRATIONAL DYNAMICS

Experimental ground-state combination differences of  $\text{CH}_5^+$

O. Asvany et al.

► PERSPECTIVE P. 1313

### 1349 ADDITIVE MANUFACTURING

Continuous liquid interface production of 3D objects

J. R. Tumbleston et al.

### PALEOANTHROPOLOGY

#### 1352 Early *Homo* at 2.8 Ma from

Ledi-Geraru, Afar, Ethiopia

B. Villmoare et al.

1355 Late Pliocene fossiliferous sedimentary record and the environmental context of early *Homo* from Afar, Ethiopia

E. N. DiMaggio et al.

### 1359 CRYSTAL GROWTH

Aqueous formation and manipulation of the iron-oxo Keggin ion

O. Sadeghi et al.

### 1362 EPILEPSY TREATMENT

Targeting LDH enzymes with a stiripentol analog to treat epilepsy

N. Sada et al.

► PERSPECTIVE P. 1312

### 1367 TRANSLATION

An RNA biosensor for imaging the first round of translation from single cells to living animals

J. M. Halstead et al.

► PERSPECTIVE P. 1316

### 1371 RNA BIOCHEMISTRY

Determination of in vivo target search kinetics of regulatory noncoding RNA

J. Fei et al.

### 1374 STEM CELL AGING

A mitochondrial UPR-mediated metabolic checkpoint regulates hematopoietic stem cell aging

M. Mohrin et al.

► PERSPECTIVE P. 1319

## DEPARTMENTS

### 1293 EDITORIAL

Ignorance is not an option

By Marcia McNutt

### 1386 WORKING LIFE

A grad school survival guide

By Andrew Gaudet

## ON THE COVER



Continuous liquid interface production (CLIP) uses a tunable photochemical process to rapidly transform 3D models into physical objects (such as

this 9.2-cm-high Eiffel Tower). By balancing exposure of dissolved reagents to UV light, which triggers photopolymerization, and oxygen, which inhibits the reaction, Tumbleston *et al.* use CLIP to grow objects from a pool of resin at speeds 25 to 100 times faster than traditional layer-by-layer 3D printing. See page 1349. Photo: Deanne Fitzmaurice

SCIENCE (ISSN 0036-8075) is published weekly on Friday, except the last week in December, by the American Association for the Advancement of Science, 1200 New York Avenue, NW, Washington, DC 20005. Periodicals mail postage (publication No. 484460) paid at Washington, DC, and additional mailing offices. Copyright © 2015 by the American Association for the Advancement of Science. The title SCIENCE is a registered trademark of the AAAS. Domestic individual membership and subscription (51 issues): \$153 (\$74 allocated to subscription). Foreign postage extra: Mexico, Caribbean (surface mail) \$55; other countries (air assist delivery) \$85. First class, airmail, student, and emeritus rates on request. Canadian rates with GST available upon request. GST #R1254 88122. Publications Mail Agreement Number 1069624. Printed in the U.S.A. Change of address: Allow 4 weeks, giving old and new addresses and 8-digit account number. Postmaster: Send change of address to AAAS, P.O. Box 96178, Washington, DC 20090-6178. Single-copy sales: \$10.00 current issue, \$15.00 back issue prepaid includes surface postage; bulk rates on request. Authorization to photocopy material for internal or personal use under circumstances not falling within the fair use provisions of the Copyright Act is granted by AAAS to libraries and other users registered with the Copyright Clearance Center (CCC) Transactional Reporting Service, provided that \$30.00 per article is paid directly to CCC, 222 Rosewood Drive, Danvers, MA 01923. The identification code for Science is 0036-8075. Science is indexed in the Reader's Guide to Periodical Literature and in several specialized indexes.

# Ignorance is not an option

Suppose future governments of the world discover that a single nation is taking the unprecedented action of spraying sulfur dioxide into the stratosphere to cool Earth's surface temperature by a few degrees celsius? The move is intended to increase the fraction of solar energy that is reflected from Earth back into space—a measure known as modifying Earth's albedo. The nation was prompted by a failed harvest the previous year, the result of greenhouse gas buildup in the atmosphere that boosted average summer temperatures above 32°C. National leaders turn to the science community for answers: What does this action mean for any individual country? Will it make the drought in São Paulo better or worse? If the wheat yield falls in northern Russia, could it be due to the albedo modification? Can science apportion damage caused by such an intervention? Should the United Nations block such action?

For the moment, this scenario remains hypothetical. However, the impacts of climate change are indeed real. Before long, they may well provoke citizens to demand that their leaders take more drastic actions for the sake of the economy and public health, and to avoid civil unrest and international conflict. If world leaders are to respond effectively, they must be equipped with an understanding of the risks in all dimensions, including environmental, political, social, and economic, that an albedo modification action might present.

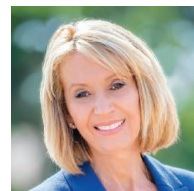
As demonstrated by the effects of large volcanic eruptions that inject particles into the stratosphere, albedo modification is the only option on the table that is known to cool Earth's surface quickly. Given that greenhouse gas emissions continue to rise globally, the risks of not knowing more about the effects, hazards, and intended and unintended consequences of this procedure are starting to outweigh the risks of conducting research to learn more about it. For this reason, a recent U.S. National Research Council (NRC) report,\* written by a committee that I chaired, says that more research is needed on albedo

modification so that the scientific community can answer questions such as those posed in the scenario above. The committee also advocates the need for improved capacity to detect and measure changes in radiative forcing (the difference between solar energy absorbed by Earth and radiated back to space) that are associated with changes in albedo, and the resulting effects on climate. In particular, the committee prioritizes research directed at poorly constrained climate parameters, such as Earth's radiation balance, as well as studies that address the human dimensions of albedo modification, such as the ethical, economic, and legal aspects. Some very small-scale field research might be justified, but only under governance that involves civil society in decisions on what should be allowed in order to advance understanding while reducing risk.

A few scientists and members of the general community have responded to the report's recommendations with the concern that it is dangerous to discuss albedo modification openly and to propose research. The committee considered very carefully the “double moral

hazard” that conducting research could lead society to regard albedo modification as an easy “backup plan” to needed mitigation and adaptation measures, whereas forgoing research could lead to irresponsible deployment of albedo modification without appropriate information on its likely consequences. Both communities expressed fear that research will lead to inevitable deployment. The committee hopes that the NRC report will stir widespread concern about the prospect of albedo modification as a response to climate change. While very strongly recommending against deployment of this measure at climate-altering scales at this time, the report's first recommendation is to implement climate change mitigation and adaptation strategies: the lowest-risk options. Although we hope that a scenario like the one above will not present itself, society is no longer at the point where ignorance about albedo modification is acceptable.

— Marcia McNutt



Marcia McNutt  
Editor-in-Chief  
Science Journals

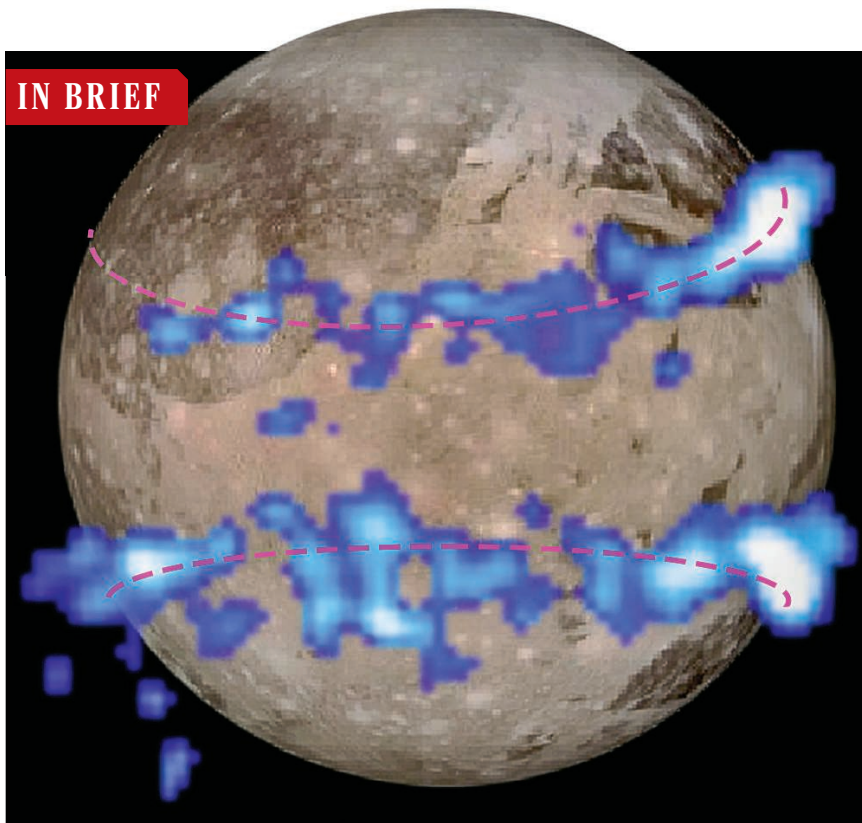


*“leaders...must be equipped with an understanding of the risks... that an albedo modification action might present.”*

\*National Research Council, *Climate Intervention: Reflecting Sunlight to Cool Earth* (National Academies Press, Washington, DC, 2015); [www.nap.edu/catalog/18988/climate-intervention-reflecting-sunlight-to-cool-earth](http://www.nap.edu/catalog/18988/climate-intervention-reflecting-sunlight-to-cool-earth).



## IN BRIEF



## Ganymede's hidden ocean

**T**he solar system's largest moon, in orbit around Jupiter, harbors an underground ocean containing more water than all the oceans on Earth. Ganymede's smooth icy surface—evidence of past resurfacing by the ocean—had already hinted that an ocean lay beneath. But new observations of the 5300-kilometer-wide moon by the Hubble Space Telescope, published online last week in the *Journal of Geophysical Research: Space Physics*, remove any remaining doubt. Ganymede's magnetic field produces two auroral belts (detectable in the ultraviolet, shown); these belts rock back and forth due to interactions with Jupiter's own magnetic field. But a third magnetic field, emanating from the electrically conductive, salty ocean and induced by Jupiter's field, counterbalances the rocking of the auroral belts. The Hubble study suggests that the ocean is no more than 330 kilometers below the surface. Ganymede is the fourth moon with a subsurface ocean, joining Jupiter's Europa and Saturn's Titan and Enceladus; Ceres, the largest object in the asteroid belt, may also have one. Such oceans are considered good places to look for life.

## AROUND THE WORLD

### Rewarding staff scientists

**BETHESDA, MARYLAND** | The U.S. National Cancer Institute (NCI) plans to test an idea aimed at bringing stability to biomedical research labs: an award to support scientists who want to spend their careers doing research but don't want to be the harried principal investigator who runs the lab and chases research grants. Last week, the agency rolled out the details for the "research specialist award" at an NCI advisory board meeting. The 5-year, renewable award, which could cover up to 100% of salary, would be aimed at scientists with a master's, Ph.D., M.D., or other advanced degree holding positions such as lab research scientist or core facility manager. NCI plans to earmark \$5 million for 50 or 60 awards over 18 months and will issue a request for applications later this year. <http://scim.ag/NCIstaffaward>

### 23andMe tackles drug discovery

**MOUNTAIN VIEW, CALIFORNIA** | Armed with the DNA of its 850,000 customers, direct-to-consumer genetic testing company 23andMe is shifting gears and plans to develop drugs itself. The firm announced last week that it will create a therapeutics group to mine its genomes—amassed from the sale of \$99 saliva test kits—for new drug leads. The company has made several deals recently to sell portions of that database to pharmaceutical companies, including Pfizer and Genentech. Now, it will bring on Richard Scheller, former head of research and development at Genentech, to head its in-house discovery efforts. "I wanted to see if we could really take advantage of the full potential of the human genome," Scheller told *Forbes*, "and thought that this is the best place to do that."

### Hunting genes in East London

**LONDON** | Researchers plan to recruit 100,000 Pakistanis and Bangladeshis in East London and search their DNA for genes that, when missing, protect against disease. The East London Genes & Health study will focus on two groups who suffer

high rates of poor health, yet are left out of large genetics studies. Because of marriage between close relatives, they are also more likely to include “knockouts,” individuals who lack a functional copy of a gene. If such a person is unusually healthy, a drug that targets the same gene in other people might prevent or treat illness. Study leaders at Queen Mary University of London will spend 4 years recruiting volunteers age 16 and older, healthy or ill, and will link their DNA data and health records. Funding of £4 million comes from the Wellcome Trust and the U.K. Medical Research Council. <http://scim.ag/EastLondhealth>

## Cholesterol drugs may help heart

SAN DIEGO, CALIFORNIA | Two

experimental cholesterol-lowering drugs may protect against heart attacks. The drugs, evolocumab and alirocumab, block a protein called PCSK9 that has drawn interest because people with mutations that disable its gene have extremely low low-density lipoprotein cholesterol levels. Now, studies presented at the American College of Cardiology conference this week and published in *The New England Journal of Medicine* show the drugs' efficacy against heart disease. In the alirocumab trial, 27 of 1550 people on the drug (1.7%) had a cardiovascular event, compared with 26 of 788 people (3.3%) on placebo. The gap was similar for evolocumab: 29 of 2976 (0.95%) people in two trials had heart trouble within a year on the drug, compared with 31 of 1489 (2.18%) of those not taking it. Doctors caution that more information is needed, especially on the long-term safety of both therapies.

## Scientists oppose air gun ban

ROME | The heads of many of Italy's research institutes are opposing a new bill that would, if made law, punish users of seismic air guns with jail sentences of between 1 and 3 years. Air guns are used in underwater seismic surveys around the world, but some evidence suggests the blasts of sound they emit can injure or kill whales, dolphins, and other sea



## An index of nonnative sea life

A catalog of more than a thousand alien species found in Earth's oceans launched this week. The World Register of Introduced Marine Species describes an initial 1457 species within the comprehensive World Register of Marine Species (launched in 2007) that have been spread by humans beyond their historic ranges. To create the list, a team of researchers sponsored by the Flanders Marine Institute in Ostend, Belgium, and the International Union for Conservation of Nature's Invasive Species Specialist Group spent 2 years compiling databases of invasive species and consulting nearly 2500 scientific papers. Entries note whether the alien species are causing economic losses or—like this red lionfish, a venomous native of the Indian and Pacific oceans now found in the Caribbean Sea—ecological trouble.

life. The Italian institute heads last week signed a letter arguing that the proposed ban is based on bad science and would harm research, particularly studies aimed at better understanding earthquakes and volcanoes. They suggested that the bill's real aim is to oppose hydrocarbon exploration. The research heads acknowledged that air guns can harm animals but argue for the use of measures to limit the harmful effects, such as carrying out surveys when ocean mammals are absent or present in limited numbers.

## Detente on NSF peer review?

WASHINGTON, D.C. | Congressional support for peer review at the National Science Foundation (NSF) used to be a given. But for the past 2 years, Representative Lamar Smith (R-TX), chair of the science committee in the U.S. House of Representatives, has complained that NSF's grantsmaking system has greenlighted research that is frivolous or unimportant. So it was noteworthy last week when Smith declared that his inquiry into dozens of NSF awards has found “nothing to suggest it is not the best available means for making very difficult, complex decisions.” Smith isn't throwing in the towel; committee staffers visited NSF last Friday to pore over a dozen

grants, some dating from 2008. But Smith's backhanded compliment, combined with new NSF policies aimed at doing a better job of explaining the value of its research to society, could be good news for NSF's beleaguered merit review process. <http://scim.ag/NSFpeerturn>

## NEWSMAKERS

### New director for DOE lab

Steven Ashby, a computational mathematician, will become director of Pacific Northwest National Laboratory (PNNL) in Richland, Washington, the Department of Energy's (DOE's) lead laboratory for chemistry, environmental science, and data analytics. Ashby, 55, has served as PNNL's deputy director for science and technology since 2008 and will succeed Michael Kluse, who is retiring. “He's a great choice,” says Mark Peters, associate lab director for energy and global security at Argonne National Laboratory in Lemont, Illinois. “When it comes to thinking about what the system can do to support science and national security, he's one of the people [DOE leaders] call.” PNNL has a staff of 4283 and a \$1.0 billion annual budget. Ashby takes the helm on 1 April. <http://scim.ag/AshbyPNNL>





IN DEPTH

Dromedary camels are an important reservoir of the MERS virus.

## INFECTIOUS DISEASES

# MERS surges again, but pandemic jitters ease

The camel virus appears to be less lethal and more prevalent in humans than assumed

By Kai Kupferschmidt

As winter fades to spring in the Arabian Peninsula, the deadly Middle East respiratory syndrome (MERS), discovered in 2012, is on the rise again. The region reported eight cases in December, 33 in January, and 68 in February, the vast majority of them in Saudi Arabia. March looks set to bring even more cases: When *Science* went to press, 30 infections had been reported.

But worries that the MERS virus could cause a runaway human outbreak, as its distant cousin SARS did in 2003, have begun to subside. Scientists now know that MERS has been around for decades, is probably not nearly as lethal as they thought, and is unlikely to evolve into a pandemic, says Christian Drosten, a virologist at the University of Bonn in Germany. "With everything we have learned in the last 3 years, I now think it is much less likely that this will become a global problem."

Still, many things about the virus remain unknown, including how common human infections are and how exactly it spreads. That worries virologist Albert Osterhaus of Erasmus MC in Rotterdam, the Netherlands. "This is really something that is knocking on the door," he says, "and the question is, do we take it seriously?"

Most scientists believe dromedary camels are the main reservoir for the virus. Camels show few symptoms when infected, but antibodies found in old blood samples show that the virus

has been widespread in the animals for at least the past 20 years. Puzzlingly, most of the more than 1000 known patients so far have become infected not from camels but in a hospital, from other MERS patients; in the spring of 2014, hospital infections led to a huge spike in cases (see graphic). Basic infection control measures could put an end to this, according to the World Health Organization (WHO). Even many of those who became infected outside a hospital report no exposure to camels, however.

Some clues to the mystery come from a massive, as-yet-unpublished study led by former Saudi Deputy Minister of Health Ziad Memish and Drosten. The researchers looked for antibodies against the MERS virus—a telltale sign of a past infection—in

more than 10,000 blood samples taken in 2012 and 2013 from a representative sample of the Saudi population. They found antibodies in 15 people, most of them from rural provinces. (In slaughterhouse workers, who kill camels and handle meat, they found antibodies in five of 140 samples, a rate 23 times as high.)

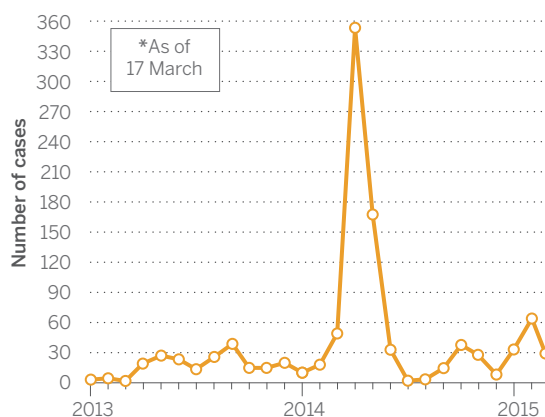
Extrapolating those numbers—"a bit dangerous," Drosten admits—suggests that more than 40,000 people in Saudi Arabia had a recent MERS infection. Clearly, the vast majority of infections goes undetected, which suggests that patients who report no exposure to camels probably caught the virus from others with a mild infection, Drosten argues. The data also suggest that the case fatality rate is much lower than current estimates of about 40%. "Something in the single digits is much more likely," Drosten says.

The question is whether its occasional forays into the human population will give the virus a chance to adapt and become better at human-to-human transmission, which could start a real epidemic. "We have pretty good evidence that if the virus stays the way it is, that each little entry into the human population quickly extinguishes," says Stanley Perlman, a researcher studying MERS at the University of Iowa in Iowa City. "But we cannot be sure that it won't mutate."

Vincent Munster, a virologist at the National Institute of Allergy and Infectious Diseases in Hamilton, Montana, thinks the genetics of MERS make that unlikely. Unlike other RNA viruses,

## Tip of the iceberg

Reported MERS cases, shown by month, may only be a fraction of the total.



which generally mutate quickly, MERS and other coronaviruses have enzymes to correct mistakes when their RNA is copied. From a public health point of view, MERS is still a niche virus, Munster says. “But then we would have said the same thing about Ebola 2 years ago,” he adds.

MERS does seem to be perfectly adapted to camels. In a study published last year, Munster and colleagues infected three male camels with MERS virus isolated from a human patient. In humans, the pathogen infects the lower respiratory tract, making it hard to transmit from person to person. In the camels, however, the virus infected the upper respiratory tract and was excreted in high concentrations in nasal secretions, ideal for infecting people and other camels.

The seasonal pattern in human cases probably results from camel breeding cycles in the Middle East. Most camels are born in winter; they stay with their mother for a year before they are separated and gathered into herds of young camels. There, the virus seems to spread quickly from animal to animal, an annual viral explosion that puts people at risk of infection, too.

That’s why vaccinating young camels may be the easiest way to protect humans, Perlman says. A group led by Gerd Sutter of Ludwig Maximilian University in Munich, Germany, has developed a vaccine based on a pox virus called modified vaccinia Ankara (MVA). Safely testing the vaccine in MERS-free camels was a huge challenge, but a team at Erasmus MC bought eight such camels on the Canary Islands and shipped them to a biosafety level 3 facility in Barcelona. Late last year, four of the animals were vaccinated with the MVA strain; then all eight were inoculated with the MERS virus. The scientists are sorting through the data now and hope to publish results soon. Meanwhile, scientists at the U.S. National Institutes of Health and Colorado State University have vaccinated three camels and three alpacas with a vaccine made of the MERS spike protein and an adjuvant.

The vaccines are unlikely to prevent infection completely, because camels with antibodies still seem to harbor the virus. Osterhaus hopes that vaccination will reduce the amount of virus the animals secrete, which would lower the risk to humans. But the market for a vaccine is uncertain. Camel owners and traders are unlikely to be interested because the virus does not seem to harm their animals, says Elmoubasher Farag, who studies MERS at Qatar’s health ministry in Doha: “Frankly speaking, I know my people will not accept a camel vaccine.” ■

## OCEANOGRAPHY

# New satellite radar could find 100,000 underwater mountains

Better seamount maps could improve tsunami predictions and models of carbon mixing in the deep ocean

By Eric Hand

**T**he submarine never saw it coming. In 2005, the nuclear-powered *USS San Francisco* crashed into an undersea extinct volcano, known as a seamount, in the western Pacific Ocean, killing one crew member and crippling the vessel. Although the sub

have to rely on an indirect method: using orbiting radar satellites to trace subtle bumps and depressions in the water surface, which mirror the shape of the sea floor. Even the most advanced map, published in *Science* last October (*Science*, 3 October 2014, p. 65), has trouble identifying and locating seamounts less than 2 kilometers tall. But now, a new study

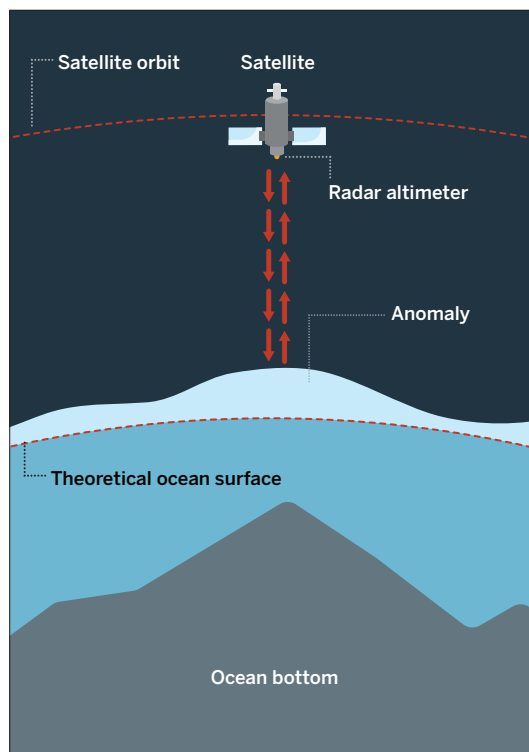
demonstrates how a French radar instrument on an Indian satellite could greatly enhance seamount maps, putting submariners on safer courses while helping with climate science, fisheries science, and tsunami forecasts.

The French radar instrument, called AltiKa, could boost the number of known seamounts from 10,000 to 100,000, says Walter Smith, a marine geophysicist at the National Oceanic and Atmospheric Administration in College Park, Maryland. “We’re going to find more of them with AltiKa than we’ve found before,” he says. “How many there are that are waiting to be discovered is an open question.”

AltiKa, on the Indian SARAL satellite that launched in 2013, is a radar altimeter that measures the height of the ocean surface. The instrument primarily serves climate researchers, who want to track sea-level rise. But like other satellite radar altimeters, it can also detect the subtle bulge of water that gathers over a seamount, because of the slightly enhanced gravity at that spot. By subtracting the effects of tides and weather on the shape of the water surface, scientists can nail down

## Bulge marks the spot

Extra gravity due to the mass of a seamount creates a bulge of water that can be measured from space.



returned to dock in Guam and a larger disaster was averted, the accident underscores one of marine geologists’ biggest complaints: Earth’s oceans are still mostly aqua incognita.

With only about 10% of the sea floor mapped with high-resolution sonar from ships, scientists assembling global maps

the gravity signal, and hence a seamount’s height and shape. Unlike most other satellite radars, which rely on the Ku radar band, AltiKa scans the sea with a Ka-band radar, which emits shorter wavelengths—yielding a smaller footprint and a faster sampling rate. At three spots in the Pacific Ocean, Smith showed, AltiKa can spot sea-



mounts as small as 1 kilometer tall.

Smith's results were published online on 12 March in *Marine Geodesy* in advance of a special issue on the AltiKa instrument. Paul Wessel, a marine geophysicist at the University of Hawaii, Manoa, says the study is a good proof of principle showing how AltiKa can enable marine geologists to see more clearly. "It pushes the envelope a bit further," he says.

The scientific payoff extends beyond submarine navigation. For example, tsunami waves are sensitive to the roughness on the ocean floor; seamounts slow a passing tsunami, bending and deflecting its energy. A better map would improve tsunami predictions. Also sensitive to seafloor roughness are the internal waves in oceans that bring up deep, cold, nutrient-rich waters to the surface and carry dissolved atmospheric carbon dioxide to ocean depths. "Knowing the seafloor bathymetry better would definitely improve the mixing models that we use," says Steven Jayne, a physical oceanographer at Woods Hole Oceanographic Institution in Massachusetts.

Seamounts are also important for ecology, because they provide a rich habitat for many species, sustained by the nutrient-rich deep waters that well up near seamounts. One drawback to a more refined map, says Peter Auster, an ecologist at the Mystic Aquarium in Connecticut, is that it could aid certain destructive commercial fishing operations, which have been known to target seamounts and quickly strip them of fish. On the flip side, Auster says, a more complete map could help ecologists piece together evolutionary patterns of biogeography: how related species leaped from one underwater island to another.

For now, AltiKa traces out the same narrow tracks across the ocean, orbit upon orbit, rather than varying its course to achieve global mapping coverage. Smith hopes that as SARAL approaches the end of its mission lifetime in a few years, project managers will allow the satellite to drift into a mapping orbit. He notes that that same decision was eventually made for the satellites Jason and CryoSat-2—and the resulting gravity data helped create the map published in *Science* last year. "Until they do that," Wessel says, "you're only going to get good data on small strips."

AltiKa's principal investigator, Jacques Verron, of the Laboratory of Geophysical and Industrial Flows in Grenoble, France, says India and France have not seriously discussed changing the satellite's orbit to make the global gravity map, but he plans to raise the issue at future meetings with India's space agency. ■

## BIOCHEMISTRY

# Origin-of-life puzzle cracked

## Study explains how three essential classes of molecules could have formed simultaneously

By Robert F. Service

**T**he origin of life is a set of paradoxes. To get it started, there must have been a genetic molecule—something like DNA or RNA—capable of passing along blueprints for making proteins, the workhorse molecules of life. But modern cells cannot copy DNA and RNA without the help of proteins themselves. Worse, none of these molecules can do their jobs without fatty lipids, which provide the cell membranes needed to contain them. In yet another chicken-and-egg complication, protein-based enzymes (encoded by genetic molecules) are needed to synthesize lipids.

Now, researchers say they see a way out. A pair of simple compounds, which would have been abundant on early Earth, can give rise to a network of simple reactions able to produce all three classes of biomolecules—nucleic acids, amino acids, and lipids. The new work, published online this week in *Nature Chemistry*, does not prove that this is how life started, but it may help explain a key mystery. "This is a very important paper," says Jack Szostak, a molecular biologist and origin-of-life researcher at Massachusetts General Hospital in Boston. "It proposes [how] almost all of the essential building blocks for life could be assembled in one geological setting."

Scientists have long touted their own favorite scenarios for which set of biomolecules formed first. "RNA World" proponents suggest RNA may have been the pioneer; not only does it carry genetic information, but it can also serve as a proteinlike chemical catalyst. Metabolism-first proponents argue that simple metal catalysts, found in minerals, may have created a soup of organic building blocks that could have given rise to the other biomolecules.

The RNA World hypothesis got a big boost in 2009. Chemists led by John Sutherland at the University of Cambridge in the United Kingdom reported that two relatively simple precursor compounds, acetylene and

formaldehyde, could undergo a sequence of reactions to produce two of RNA's four nucleotide building blocks, showing a plausible route by which RNA could have formed on its own in the primordial soup. Critics, though, pointed out that acetylene and formaldehyde are still somewhat complex molecules themselves. That raised the question of where they came from.

So Sutherland and his colleagues set out to see if they could find a route to RNA from even simpler starting materials. They succeeded. Sutherland's team now reports that it created nucleic acid precursors starting with just hydrogen cyanide (HCN), hydrogen sulfide (H<sub>2</sub>S), and ultraviolet (UV) light. What is more, Sutherland says, the same conditions also create the starting materials for amino acids and lipids.

His team argues that early Earth was a favorable setting for those reactions. HCN is abundant in comets, which pelted the newborn planet. Impacts would also have

produced enough energy to synthesize HCN from hydrogen, carbon, and nitrogen. Likewise, Sutherland says, H<sub>2</sub>S was thought to have been common on early Earth, as was the UV radiation that could drive the

reactions and metal-containing minerals that could have catalyzed them.

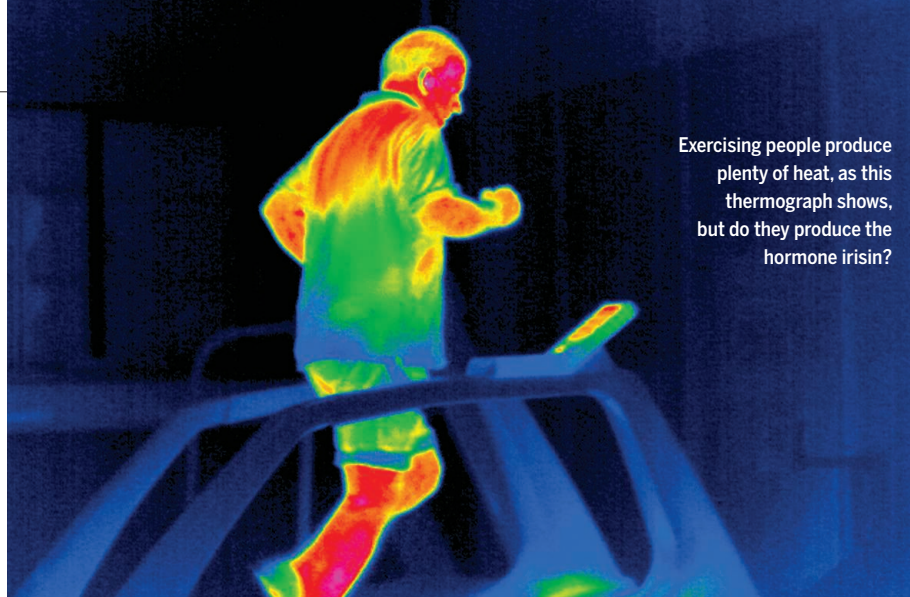
Sutherland cautions that the reactions for the three sets of building blocks are different enough from one another—requiring different metal catalysts, for example—that they likely would not have all occurred in the same location. Instead, slight variations in chemistry and energy could have favored the creation of one set of building blocks or another in different places on land. "Rain-water would then wash these compounds into a common pool," says Dave Deamer, an origin-of-life researcher at the University of California, Santa Cruz.

Could life have kindled in that common pool? That detail is almost certainly lost to history. But the idea and the "plausible chemistry" behind it are worth careful thought, Deamer says. Szostak agrees. "I am sure that it will be debated for some time to come." ■

---

**"Almost all of the essential building blocks for life could be assembled in one geological setting."**

**Jack Szostak**, Massachusetts General Hospital



Exercising people produce plenty of heat, as this thermograph shows, but do they produce the hormone irisin?

## BIOMEDICINE

# Woes for 'exercise hormone'

Challenged antibody assays raise new questions about hoped-for obesity drug target

By Kelly Servick

**B**ack in 2012, it seemed like a critical find for obesity researchers: a molecule that regulates how the body stores and uses fat. The hormone, dubbed irisin after a Greek goddess, appeared to amp up energy expenditure in mice after exercise, opening up potential treatments for diabetes and obesity. But inconsistent follow-up studies caused some scientists to doubt that it plays any role in human metabolism. Now, a study questioning the reliability of the antibody-based test kits often used to detect irisin has raised further doubts about the hormone—and the use of such tests in general.

In the original irisin study, published in *Nature*, cell biologist Bruce Spiegelman of Harvard Medical School in Boston and colleagues described how a protein called FNDC5 produced in muscles after exercise seemed to promote healthy metabolism in mice. They showed that an FNDC5 fragment, irisin, was secreted into the bloodstream and prompted energy-storing white fat cells to behave more like energy-burning brown fat cells. They also detected irisin in serum from human blood, and levels seemed to increase after weeks of endurance training.

Spiegelman and Harvard licensed the discovery to Ember Therapeutics, a company he had co-founded in 2011. And other labs tried to expand on the idea that irisin is a key regulator of metabolism and a potential drug target for metabolic disease. While

some studies that measured the hormone's levels in human blood saw surges in irisin after exercise, others found no effect.

Harold Erickson, a biochemist at Duke University in Durham, North Carolina, came across the 2012 paper while reading outside his field to design a lecture for medical students on connective tissue, cartilage, and bone. As he studied it more closely, he became concerned about its validity. For one, the antibody Spiegelman's team had used to react with irisin in a blood sample recognized a portion of the FNDC5 protein that is not part of irisin, according to a catalog from the company that made the antibody. Erickson published the observation in 2013. Spiegelman countered that there was an error in the company's description.

Other groups raised separate concerns. In 2013, a team led by diabetes researcher Jürgen Eckel at the University of Düsseldorf in Germany found that the human gene that codes for FNDC5 has an unusual DNA starting sequence that causes it to produce the protein at much lower levels than does the gene found in most other animals. The group concluded that the effects of irisin observed in mice are unlikely to hold for humans.

The field was soon polarized. "It seems there's been ... two very entrenched camps," says Francesco Celi, an endocrinologist at Virginia Commonwealth University in Richmond who has studied irisin as part of research on energy expenditure after exposure to cold.

And more groups entered the fray, as companies put out standard enzyme-linked

immunosorbent assays (ELISAs)—a simple way to test for irisin in serum. The tests depend on irisin-binding antibodies isolated from animals injected with the hormone. Erickson wondered if these antibodies were reacting to multiple proteins in human blood, detecting irisin where there was none. "The people who bought these assays never seemed to question whether the ELISA was totally specific for irisin," he says.

Now, Erickson and colleagues have found that the antibodies in four commercial ELISA kits react to proteins that are too large to be irisin. Their study, published last week in *Scientific Reports*, also failed to find any irisin in the blood of several animal species, including horses that had just done strenuous exercise.

The new paper "fundamentally changes the debate" about irisin, says James Timmons, a systems biologist at King's College London who has also refuted the link between FNDC5 and exercise in humans. There is "no reliable positive data on [irisin] in humans," he argues, and previous papers based on ELISA tests should be retracted.

One irisin ELISA-maker contacted by *Science* points out that even the size of the circulating irisin molecule is still the subject of debate, which leads to inconsistencies in how labs measure the hormone. "We are waiting for further studies that clarify and solve this issue," says Olivier Donzé, chief scientific officer at Adipogen in San Diego, California, which supplied one of the kits tested in Erickson's study.

Spiegelman stresses that not all the previous studies of irisin in humans have relied on ELISA kits. Last year, for example, Celi reported modest levels of the hormone in people's blood, and increases after exercise, using a more complex technique called mass spectrometry, which identifies molecules in a sample by ionizing them and weighing their components.

To some, the new concerns about irisin tests point out a broader issue. "Every new substance, particularly if it's interesting, generates a rush to develop assays," Celi says. "Most of these first assays are not that reliable." Indeed, antibodies with poor specificity are "the elephant in the room for much of medical science," Timmons says.

The first-generation irisin tests may have been particularly problematic, Celi adds, because the hormone belongs to a very common family of proteins called fibronectins, to which antibodies could also react. Based on his results, Celi believes irisin is important, and wants to do more studies on its activity. Others have given up, however. Ember Therapeutics says it's no longer pursuing the hormone. ■



## BIOTECHNOLOGY

# Biologists devise invasion plan for mutations

“Gene drive” technique could fight insect-borne disease, but some call for safeguards

By John Bohannon

On 28 December 2014, Valentino Gantz and Ethan Bier checked on the fruit flies that had just hatched in their lab at the University of California (UC), San Diego. By the classic rules of Mendelian genetics, only one out of four of the newborn flies should have shown the effects of the mutation their mothers carried, an X-linked recessive trait that causes a loss of pigmentation similar to albinism. Instead, nothing but pale yellow flies kept emerging. “We were stunned,” says Bier, who is Gantz’s Ph.D. adviser. “It was like the sun rose in the west rather than the east.” They hammered out a paper and submitted it to *Science* 3 days later.

In the study, published online this week (<http://scim.ag/VMGantz>), Gantz and Bier report that the introduced mutation disabled both normal copies of a pigmentation gene on the fruit fly chromosomes, transmitting itself to the next generation with 97% efficiency—a near-complete invasion of the genome. The secret of its success: an increasingly popular gene-editing toolkit called CRISPR (*Science*, 23 August 2013, p. 833), which Gantz and Bier adapted to give the mutation an overwhelming advantage. The technique is the latest—and some say, most impressive—example of gene drive: biasing inheritance to spread a gene rapidly through a population, or even an entire species. At this level of efficiency, a single mosquito equipped with a parasite-blocking gene could in theory spread malaria resistance through an entire breeding population in a single season (see diagram).

The paper comes amid intense soul-searching among gene drive researchers, with calls for public dialogue and self-policing for the technology (*Science*, 8 August 2014, p. 626). George Church, a geneticist at Harvard Medical School in Boston who is a leader in the field, believes the new study should not have been published, because it does not include measures to restrain the spread of unintended mutations. “It is a step too far,” he says.

Creating a gene drive system wasn’t Gantz’s original goal, Bier says. “We were just trying to solve a practical problem.” Gantz studies the development of fruit fly wing veins, for which he must create flies

with multiple mutations. That’s typically painstaking work, requiring large numbers of flies over many generations to create a single multimutant. Last summer, Gantz made a tweak to the CRISPR system, in which an engineered bacterial protein, Cas9, uses a string of RNA to find and delete, replace, or otherwise edit a target DNA sequence. By equipping the CRISPR gene cassette with DNA sequences flanking the targeted gene, Gantz hoped to create a mutation that would “auto-catalyze.” Once incorporated on one chromosome, it would produce new copies of the CRISPR complex that would target and edit the gene everywhere it appeared.

Bier realized that Gantz’s self-replicating gene cassette could cause gene drive. After

discussions with UC San Diego, the university gave the experiment the green light if certain biosafety measures were taken: The flies are kept in three layers of tubes and boxes, and the lab is locked behind five doors with fingerprint security.

Gantz and Bier knew they had achieved the first goal, making double mutants in one step, on 18 December last year, when yellow female flies developed from embryos injected with a CRISPR cassette targeting the X chromosome pigmentation gene. But they wanted to know whether the engineered gene could make it through the germ cells and invade the next generation. The yellow flies they saw on 28 December confirmed that it did, and with 97% efficiency.

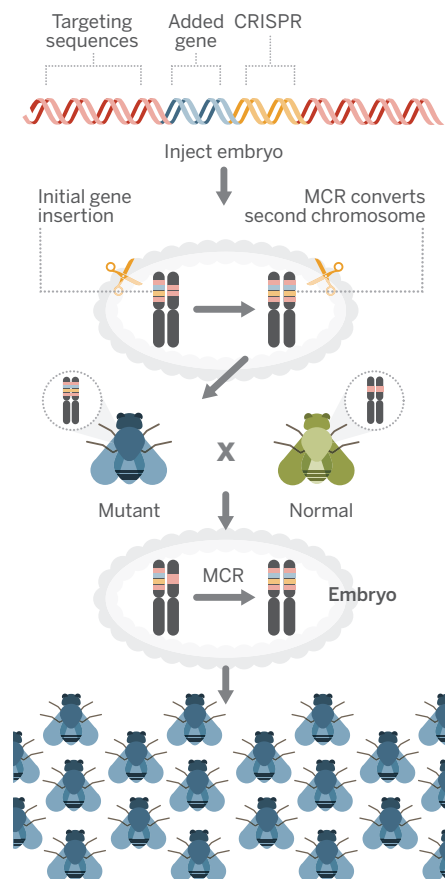
The technique is “fantastic,” says geneticist Anthony James of UC Irvine, whose lab made the first transgenic mosquitoes nearly 2 decades ago with a far more laborious technique. Bier and James are already collaborating to create a mosquito equipped with genes designed to block the transmission of malaria and dengue fever—and to quickly spread through a population. “We’re hoping for results by the end of the year,” James says.

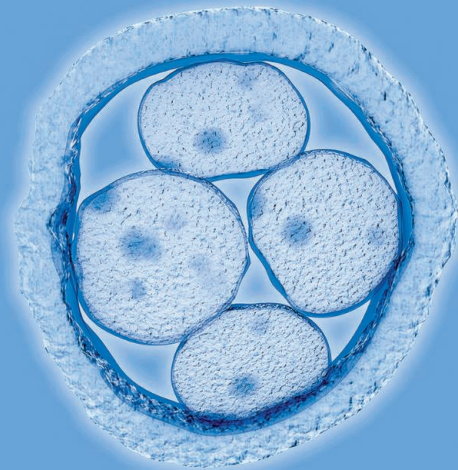
It’s not the only horse in the gene drive race. Church’s group also has a CRISPR approach that works at near-perfect efficiency in yeast. It includes built-in precautions designed to prevent the system from running amok. For example, Church avoids incorporating Cas9’s gene and the targeting RNA sequence into a single cassette, so that unintended genes can’t become accidentally incorporated and spread. Because Gantz and Bier’s method does not have such safeguards, “it encourages a standard of behavior that is much lower than what we’re recommending,” Church says. “What will spread is not literally their mutant flies, but their protocol.”

Bier rejects the criticism. “The safeguards that [Church] is using in yeast just can’t work in flies,” he notes. “I bristle when people say that we haven’t thought carefully about this,” adds James, who last year co-authored a World Health Organization report on precautions for use of transgenic mosquitos. “And how could we not publish this work? Nothing is served by hiding things. The whole point is to show that it is possible and have a public discussion.” ■

## Driven to excess

A method dubbed mutagenic chain reaction (MCR) may be able to drive an added gene, such as one for disease resistance, through an insect population.





An early human embryo, the focus of controversy.

## BIOETHICS

# Embryo engineering alarm

Researchers call for restraint in genome editing

By **Gretchen Vogel**

**A**silomar. The word conjures up not only stunning California coastline but also vexing questions posed by new, potentially world-changing technologies. In 1975, the Asilomar conference center hosted a meeting where molecular biologists, physicians, and lawyers crafted guidelines for research that altered the DNA of living organisms. Now, scientists are calling for another Asilomar—this time to discuss the possibility of genetically engineered human beings.

In 1975, the notion of someday using recombinant DNA to design human babies was too remote to seriously consider, says David Baltimore, a molecular biologist and president emeritus of the California Institute of Technology in Pasadena, who helped organize the first Asilomar meeting. What's changed now is the explosion of powerful new genome-editing technologies such as CRISPR-Cas9, zinc fingers, and TALENs. They have made it easy for anyone with basic molecular biology training to insert, remove, and edit genes in cells—including sperm, eggs, and embryos—potentially curing genetic diseases or adding desirable traits. “The time has come where you can’t brush that possibility aside,” Baltimore says.

Rumors are rife, presumably from anonymous peer reviewers, that scientists in China have already used CRISPR on human embryos and have submitted papers on their results. They have apparently not tried to establish any pregnancies, but the rumors alarm researchers who fear that such papers, published before broad discussions of the risks and benefits of genome editing, could

trigger a public backlash that would block legitimate uses of the technology.

“If there were a rogue laboratory in the world somewhere that could get access to embryos, in principle it would be possible,” says Jennifer Doudna, a molecular biologist at the University of California, Berkeley, who helped develop CRISPR. Even before rumors surfaced, she organized a January meeting with scientists, ethicists, and law experts to discuss what steps the scientific community could take to ensure the technology would be used safely and ethically.

In two commentaries, one published online this week in *Science* (<http://scim.ag/DBaltimore>) and one in *Nature* last week, two groups of scientists take a stab at recommendations. In *Nature*, one of the researchers who helped develop zinc-finger nucleases, Edward Lanphier, and four colleagues call for a moratorium on any experiments that involve editing genes in human embryos or cells that could give rise to sperm or eggs. “Should a truly compelling case ever arise for the therapeutic benefit of germline modification, we encourage an open discussion around the appropriate course of action,” they write.

In the *Science* commentary, which grew out of the January meeting, Doudna, Baltimore, and 16 colleagues stop short of a blanket moratorium. They call on scientists to “strongly discourage ... attempts at germline genome modification for clinical application

in humans,” but leave open the possibility of research with human cells as long as they are not used to establish a pregnancy.

Most of the signatories of the *Science* commentary think such experiments could answer legitimate scientific questions, Doudna says. Editing genes in germ cells could help researchers understand certain kinds of infertility, for example, and altering the genes in one-celled embryos could shed light on the earliest stages of human development.

But scientists don’t yet understand all the possible side effects of tinkering with germ cells or embryos. Monkeys have been born from CRISPR-edited embryos, but at least half of the 10 pregnancies in the monkey experiments ended in miscarriage. In the monkeys that were born, not all cells carried the desired changes, so attempts to eliminate a disease gene might not work. The editing can also damage off-target sites in the genome.

Those uncertainties, together with existing regulations, are sufficient to prevent responsible scientists from attempting any genetically altered babies, says George Church, a molecular geneticist at Harvard Medical School in Boston. Although he signed the *Science* commentary, he says the discussion “strikes me as a bit exaggerated.” He maintains that a de facto moratorium is in place for all technologies until they’re proven safe. “The challenge is to show that the benefits are greater than the risks.”

Doudna and others are not so sure current regulations suffice. Although many European countries ban germline genetic engineering in humans, the United States and China do not have such laws. Research with private funds is subject to little oversight in the

United States, although any attempts to establish a pregnancy would need approval from the U.S. Food and Drug Administration. In China, any clinical use is prohibited by the Ministry of Health guidelines, but not by law.

Whether or not another Asilomar meeting is called, the topic has caught the attention of

several science policy groups, including the Nuffield Council on Bioethics, the Hinxton Group, and the National Academy of Sciences. Church hopes such discussions will tackle a question that he says both commentaries avoid: “What is the scenario that we’re actually worried about? That it won’t work well enough? Or that it will work too well?” ■

*With reporting by Jocelyn Kaiser, Dennis Normile, and Christina Larson.*

## Past pauses

Biologists have called for research moratoriums before.

**1975**

Recombinant DNA studies

**1997**

Human reproductive cloning

**2012**

Influenza gain-of-function studies



FEATURES

# LESSONS FROM THE WILD LAB

Yellowstone Park is a real-world  
laboratory of predator-prey relations

By **Virginia Morell**,  
*in Yellowstone National Park, Wyoming*

**J**ust before dawn on an icy January morning, Doug Smith skied off a main trail and headed toward a branch of Blacktail Deer Creek, pushing into thickets of willow, aspen, and wild rose. I followed, picking my way through the bare branches. They arched above our heads, and we didn't see the female moose until she burst from cover on the far side of the stream. She trotted smartly up a hill, then looked back to study us.

"That's a first," said Smith, a park wildlife biologist and the leader of its wolf, elk, and beaver projects. "I've never seen moose here. It used to be all elk." He stopped to show me where a nibbling moose, perhaps the cow we'd startled, had trimmed a few willows. "That kind of browsing is actually good for the willows; it stimulates new growth," he said. "Elk, though, eat willows almost to the ground."

He recalled riding along this same stretch of creek in the summer of 1995, when hundreds of elk browsed the banks. Their droppings littered the ground and the willows were mere stubs. "It's so different now."

Willows, aspen, cottonwood, and alders are beginning to flourish again along streams in Yellowstone's northern range, an area known for its elk herd. Biologists debate just why this shift has occurred. But many agree that a key factor is an animal we didn't see that morning, but whose presence we felt: the gray wolf.

Twenty years ago this month, not far from Blacktail Deer Creek, Smith and other park biologists set radio collars on six wolves, opened the door of their pen, and watched them bound away. Today, 95 Rocky Mountain gray wolves (*Canis lupus*) in 11 packs live in Yellowstone, hunting primarily elk, deer, and bison. The political controversy over the return of a feared predator continues, as does pressure to hunt them outside the park, but among ecologists there's little dissent: "Putting the wolves back was a bold and remarkable move," says Adrian Manning, an ecologist at the Australian National University in Canberra. "Nothing on this scale had been done before in restoration ecology."

The wolves' return set in motion a natural—and therefore uncontrolled—experiment that is still unfolding. "We were witnessing something that no one had seen before," Smith said. "Bringing the wolves back gave us an unprecedented opportunity to see how apex predators affect an ecosystem." With the reintroduction, Yellowstone be-

Yellowstone's elk, like this cow and calf near Old Faithful, face a changing ecosystem that includes wolves and cougars.



came only one of two places “in the lower 48 where you find the entire assemblage of large carnivores and ungulates that were present at the end of the Pleistocene,” says Scott Creel, an ecologist at Montana State University (MSU), Bozeman, who has studied carnivores in the park and in Africa.

It’s almost impossible to overestimate the park’s influence on conservation decisions around the world, Manning adds. “We know

every last wolf to managing the bison like livestock, each intervention has had long-lasting consequences that scientists are still trying to understand and correct.

In recent years, biologists have gathered data on all of these perturbations and found clever ways to establish some controls and test hypotheses. Many think that the wolves triggered a cascade of changes in species from elk to coyotes to willows to bison to

an intact ecosystem is so much easier than trying to restore it once the pieces have been lost.”

**MOST PEOPLE THINK OF YELLOWSTONE** in its early days as a pristine wilderness barely touched by people. Nothing could be further from the truth. Archaeologists know that human hunters were in the park at least 11,000 years ago: Part of a Clovis projectile point made from Yellowstone obsidian was uncovered close to the park’s north entrance in 1959, and an intact 10,000-year-old atlatl (spear-thrower) was discovered near the park 5 years ago.

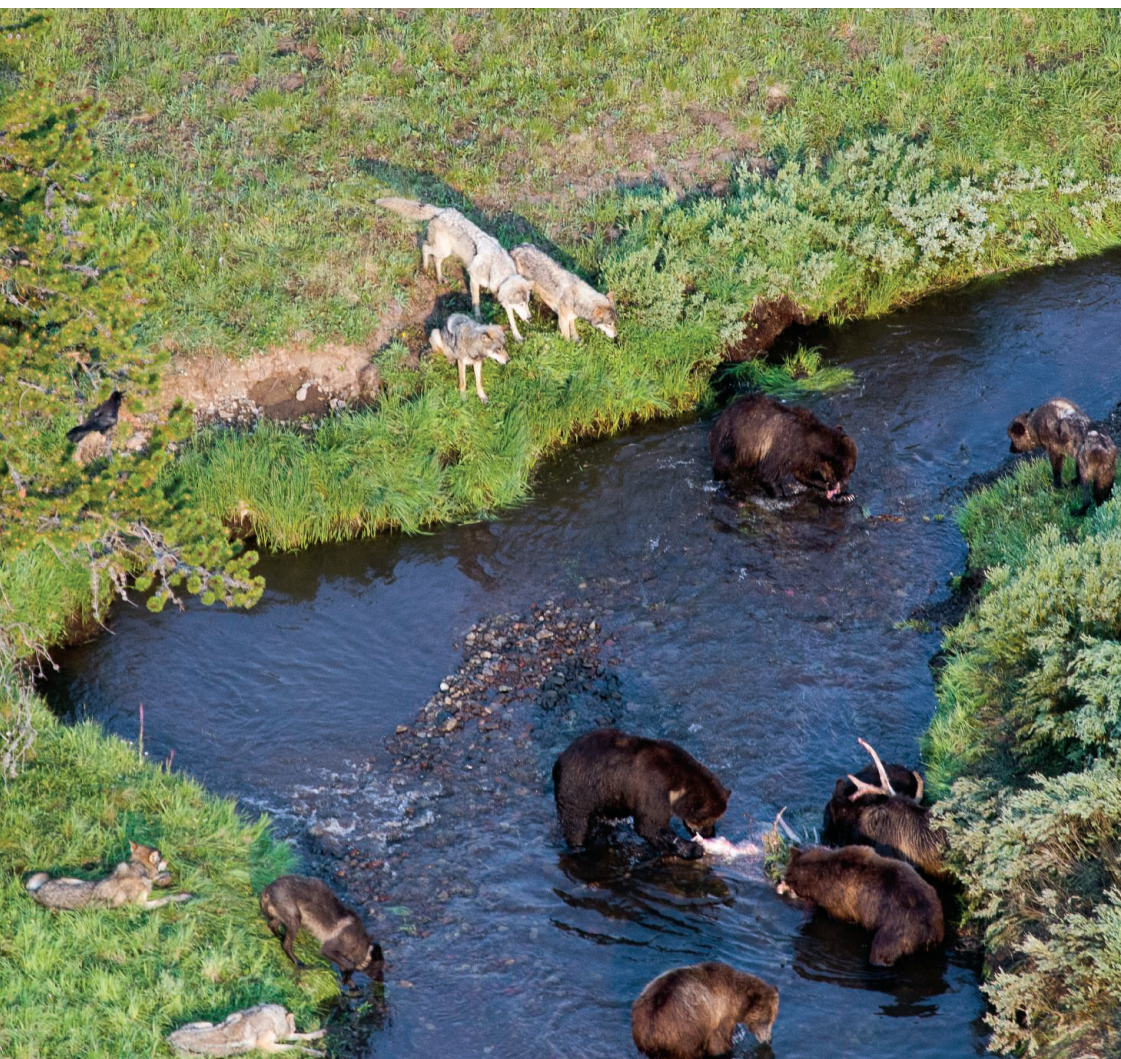
By the time the first European-American trapper arrived in the early 1800s, at least a dozen groups of Native Americans were hunting the region’s abundant wildlife. Herds of elk, pronghorn, bison, and mule deer roamed the northern range; cougars and bighorn sheep patrolled the rocky, mountainous interior; moose wandered the marshy meadows to the south; and grizzly bears ranged wherever they chose. The predator community of grizzly and black bears, wolves, coyotes, cougars, lynxes, bobcats, foxes, wolverines, and other, smaller species was intact, and it included humans.

Word soon spread about the area’s beauty, wildlife, and hydrothermal wonders. In 1872, Congress set aside 8297 square kilometers for Yellowstone National Park, the first such park in the world—“the best idea America ever had,” as writer Wallace Stegner once said.

The congressional act stated that “wanton destruction of the fish and game” should be prevented. But the young park’s authorities had no means of

enforcing these words. Many naturalists of the time loathed big predators because they killed “noble” game animals such as elk, and officials encouraged the killing of carnivores. Meanwhile, hunters shot so many thousands of ungulates as well as predators that one historian described the slaughter as an “ecological holocaust.”

In less than a decade, wolves, cougars, and many smaller predators were largely gone from Yellowstone—a drastic culling whose consequences are still playing out. Grizzly bears (*Ursus arctos horribilis*) escaped this



One of Yellowstone’s 11 wolf packs waits while grizzlies feed on the remains of an elk likely brought down by the wolves.

the ecological theory and how the bits and pieces are supposed to work. But to see it happening as you can in Yellowstone is really quite remarkable.”

Yet the wolves are only one of many such natural experiments playing out in Yellowstone, and some scientists are cautious about attributing all the park’s recent changes solely to these carnivores. Since its founding in 1872, Yellowstone has been treated as something of a living laboratory, subject to shifting biases and ideas about how best to manage it. From shooting ev-

beavers. But other predators, including cougars and grizzly bears, may also be reshaping the ecosystem. Other scientists argue that climate change—drought, in particular—has been an equal or even greater partner in the transformation. And ecologists disagree over just how restored Yellowstone actually is.

Yet all concur that the restoration has taught important lessons, perhaps the most important being “there’s no quick fix once an apex predator is gone,” as Tom Hobbs, an ecologist at Colorado State University (CSU), Fort Collins, puts it. “Maintaining





**On the hunt.** An adult male wolf (above, left) leads the hunt on an older cow elk in Yellowstone. Such kills have curbed the elk population and prevented the ungulates from overbrowsing, allowing shrubs and trees to regrow. As a defense against wolves, elk now roam Yellowstone (above, right) in smaller bands.



fate because park visitors enjoyed seeing them. (In the 1930s, one hotel built an outdoor arena with bleachers so 1500 people could view the 50 or more bears snuffling among the garbage every night.)

In 1886, the U.S. Army was summoned to protect the park from poachers, and the soldiers also rid it of the last of the wolves and cougars. “Killing all these predators was the first natural experiment in the park,” says William Ripple, an ecologist at Oregon State University (OSU), Corvallis. “The idea was to make Yellowstone a paradise for the elk.”

As a result, for many decades, elk (*Cervus canadensis nelsoni*), vegetarian eating machines that both browse on shrubs and graze on grass, have been the “drivers of Yellowstone’s ecosystem,” Smith says. By the early 1930s, when every large predator except coyotes and bears was gone, the elk population stood at about 10,000 in the northern range. It was the largest elk herd in North America and another tourist attraction.

The abundant elk began cropping the park’s vegetation, particularly the tasty woody plants along streams, causing severe erosion and leading to worries that they and

other herbivores would starve. From the 1930s to the 1960s, park officials did everything they could to shrink the herd. Rangers and hunters shot and relocated elk by the tens of thousands. Some years they succeeded in reducing the numbers, but without continual culling, the animals bounced right back. “They just shot and shot elk; they shot left and right, and they pulled the carcasses out with Sno-Cats,” Ripple says. “And still the vegetation could not come back.”

This experiment ended in 1968, because Americans felt that shooting elk clashed with the growing idea of national parks as sanctuaries for wildlife. For the next 27 years, until 1995, the elk were left alone, neither fed by humans during the harshest winters as they once were, nor shot in the park. “Another experiment,” Ripple says.

In the absence of predators, the elk rebounded, soaring to at least 19,000 in the northern range by 1994. The elk were running the park, but from an ecologist’s viewpoint, they were running it right into the ground.

To reduce the numbers, Montana allowed elk that migrated outside the park to be

hunted, first bull elk in fall and then also female elk, including pregnant ones, in winter. “Locals called it the ‘meat locker hunt,’” Smith said, “because the success rate was so high.” In 1995, the human hunt was upped so that hunters took about 9% of the elk population each year. That same year, the wolves were brought back. Yellowstone’s ecosystem shifted yet again.

For starters, elk numbers plunged. By 2008, the northern range herd was down to just over 6000 animals—a drop of almost 70% from its peak. The combination of more wolves and fewer elk touched off a cascade of favorable effects, Smith and his colleagues say. Willows grew taller and stream banks greened, creating thickets where songbirds once again sang and nested. Bison and deer increased, filling niches reopened by the decline of elk. Today, in terms of biological richness, “Yellowstone is as good as it’s ever been,” says Smith, who details the changes in the most recent issue of the *Annual Review of Ecology, Evolution, and Systematics*. “Better even than it was in 1872.”

Graphs of the numbers of wolf and elk in

PHOTOS: (LEFT TO RIGHT) DANIEL STAHLER/NPS; © DON JOHNSTON/ALL CANADA PHOTOS/CORBIS





Yellowstone's northern range now display a classic predator-prey correlation, similar to the iconic curve seen on Isle Royale in Michigan, where wolf and moose numbers cycled in tandem over decades, Smith says. As the wolves thinned the elk herds, their own numbers have suffered. In Yellowstone's northern range, wolf and elk populations are both down 60% from their peaks. "The decline in the elk has led to a decline in the wolves," explains MSU's Creel. "They're pretty tightly coupled."

Creel argues that wolf kills aren't the only factor driving the elk decline. "The other half is behavioral," he says. His research indicates that elk pregnancy rates have dropped by 20% to 40% across the park since the wolves were reintroduced. That's exactly the opposite of what you'd expect, as pregnancy rates typically go up when the overall population numbers fall, he explained in *PLOS ONE* last July. Yellowstone's elk may have changed when and where they feed to avoid the wolves. "They have to spend more time digging in the winter to begin to feed," he says, "and the quality of the food they are eating is lower. And that's all day every day."

The rise in predators has affected the elk's movements on the landscape, Smith agrees.

At the Mammoth Hot Springs Terraces, a hydrothermal feature that in winter resembles an icy, tiered cake, about 20 elk, a mix of cows and calves, grazed on patches of brown grasses poking through a snowy crust when I visited in January. "We used to see groups of hundreds of elk here," Smith said. "Now, it's rare to see more than 15 to 20 together. We think that's because of the wolves; [smaller herds] may make the elk harder to find and hunt." (The wolves, though, are wise to their prey's tactics and have even slain the Mammoth elk on the steps of the nearby buildings.)

Creel's ideas are hotly debated. Some argue that the wolves were initially too scarce to have greatly influenced elk feeding patterns. Others say that indirect measures of elk pregnancy rates (as determined by a pregnancy-associated protein) do not reveal a decline. They also cite unpublished data that elk on the northern range, facing the park's densest wolf population, have a high pregnancy rate. Several scientists think the wolves have had only a minor effect on the elk and other species, arguing that drought and warmer winters have played more crucial roles.

Ecologist John Vucetich from Michigan Technological University in Houghton

blames the meat locker hunt, which felled females in their prime, for the elk's dramatic decline between 1995 and 2005. "It's exactly what you'd predict," he says. Smith, too, thinks wolves are not the whole story. "We have to look at the full suite of predators—the cougars and grizzly bears, and smaller predators," he says. "And the human hunters."

**WHILE ALL EYES** were on the wolves, another predator stealthily reclaimed Yellowstone: cougars. No one knows when the first cats crept back. But in 1972, officials spotted a mother and two cubs. In 1995, the year the wolves were reintroduced, researchers estimated that 15 to 20 cougars were already making their home in Yellowstone.

"It's been a natural experiment," says park biologist, Dan Stahler, who oversees the park's cougar study, using two words I became accustomed to hearing. "No one paid very much attention to cougars at first," he says, "partly because they brought themselves back and partly because they're very quiet and secretive. They kill a lot of deer and elk, but we don't see them doing the killing. We don't hear them howling."

His team now tracks the cats from January to March, collecting scat and fur for



## Highs and lows

Since Yellowstone's founding, animals have been removed, added, culled, or allowed to flourish.

**1872**

Founding of Yellowstone National Park

**1886**

Soldiers brought in to stop poaching

**1902**

21 bison in park's northern range (NR)

**1907**

Soldiers directed to kill predators; bears spared

**1914**

Elk numbers hit 35,000

**1926**

Last wolves and cougars in park eliminated

**1936**

Predator killing ends; coyotes protected

**1944**

Aldo Leopold recommends restoring wolves

**1960**

Program to reduce elk through hunting, shooting, relocating

**1968**

End of elk reduction program; about 3172 elk in NR

**1972**

Cougar spotted in park

**1976**

Winter "meat locker hunt" begins

**Late 1980s**

Lake trout introduced to Yellowstone Lake; cutthroat (shown) decline

**Late 1988**

Moose populations are slow to recover from major fire

**1994**

Elk population 19,000 in NR

**1995**

Wolves reintroduced

**2010**

NR elk population 4635  
Meat locker hunt ends

**2013**

95 wolves in park, 34 in NR

**2014**

4900 bison in park  
3.6 million human visitors



genetic analysis and documenting kill sites. They have also set up camera and video traps at dens, trails, and kills, enabling them to witness behaviors rarely seen before. "Everyone talks about cougars being solitary animals," Stahler said. "But the videos are revealing that they're more social than we'd realized," for instance leaving scent markings to communicate with one another.

Preliminary data show that at least 22 cougars have colonized the northern range, the same area that wolves and elk prefer. Stahler suspects that the cats' population may be close to that of the wolves' in this area, about 35—and they may kill more elk than wolves do. Each adult cougar in the northern range killed about 52 elk each year, studies have shown. A wolf takes about 22 elk per year. The cats kill more because they stash their prey and then typically lose much of the carcass to other predators, often a wolf.

Around 2013, cougars turned to eating more mule deer than elk. "We weren't tracking them, so we can't say when or why they made this switch, or if it will last," Stahler said. "The lower numbers of elk may have made room for more mule deer." That kind of change, a sign of growing biodiversity, is exactly what ecologists had predicted that carnivores—whether feline or canine—would bring to Yellowstone.

Although good for the park, such diversity adds extra complexity to all of those natural experiments. Many biologists say that another, often underestimated predator also affects elk and therefore the rest of the ecosystem: the grizzly bear. Some 150 inhabit the park, and they target newborn elk. Although the bears' numbers haven't grown appreciably since the wolves came back, their appetite for tiny elk has ballooned, thanks to another case of human meddling—this one involving fish.

In the late 1980s and early 1990s, non-native lake trout were moved into Yellowstone Lake, explains Todd Koel, a conservation biologist at the park who specializes in fisheries. No one knows who did the deed, but the results proved catastrophic for the native cutthroat trout, whose numbers plummeted. That in turn hurt the grizzlies, which once gorged on spawning cutthroat in streams every spring, as scientists explained in a 2013 study in the *Journal of Wildlife Management*. "The fish were one of the bears' major sources of energy after hibernating," says David Mattson, an ecologist and grizzly bear expert at Yale University.

But lake trout don't spawn in streams, and they live at depths beyond the reach of the bears. Without cutthroat trout, the bears turned increasingly to another meaty

PHOTOS: (TOP TO BOTTOM) © BETTMANN/CORBIS; © 167/BARRETT HEDGES/OCEAN/CORBIS; © JAY FLEMING/CORBIS; © TOM MURPHY/NATIONAL GEOGRAPHIC CREATIVE/CORBIS; © MARA K TASHJIAN/GETTY IMAGES



item that showed up each spring: newborn elk. “Every elk population within grizzly bear areas has declined,” Mattson said. This web of trout-bear-elk offers another, often forgotten lesson, these ecologists say: Terrestrial and aquatic ecosystems aren’t separate spheres, but are tightly linked.

**WHATEVER DROVE THE ELK’S DECLINE,** it has turned out to be good news for many other species, including bison, which compete with elk for food and habitat. Today, bison number more than 3500 on the northern range, up from about 250 in 1966 (and only 21 in 1902). “Elk were the drivers of Yellowstone’s ecosystem for the last 100 years,” Smith says, “but now their star is dimming. Bison are on the rise”—setting the stage for yet another natural experiment.

This one, however, is complicated because bison are heavily managed. Those that wander too far beyond park boundaries are rounded up like livestock, corralled, and culled, because they carry brucellosis, a disease easily transmitted to cattle. With so many bison confined to the northern range, the 1-ton-truck-sized animals are cropping woody plants that had been recovering from the elk, says Ripple, who reported on this with OSU’s Robert Beschta last year in *Ecohydrology*. So far, the bison have proven to be too dangerous a prey for wolves to make any dent in the numbers of this big ungulate.

Beavers, too, are prospering. Once common in the northern range (25 colonies were counted in the 1920s), they almost vanished in the 1950s after the abundant elk consumed the willows and aspen, which beavers need for food and building dams. After the wolves came back, Ripple and Beschta documented the regrowth of woody plants along several northern range drainages. A year after the wolf restoration, there was one beaver colony in this area; now there are 12.

But beaver habitat has not recovered as fast as researchers expected. In some areas, the willows remain stunted even when not heavily browsed. “They are not restored,” says CSU’s Hobbs. To find out why, he and CSU ecologist David Cooper are conducting the only controlled, gold-standard experiment in Yellowstone. The park generally does not allow the ecosystem to be physically altered, but it made an exception af-

ter the National Research Council urged a study of beavers and willows.

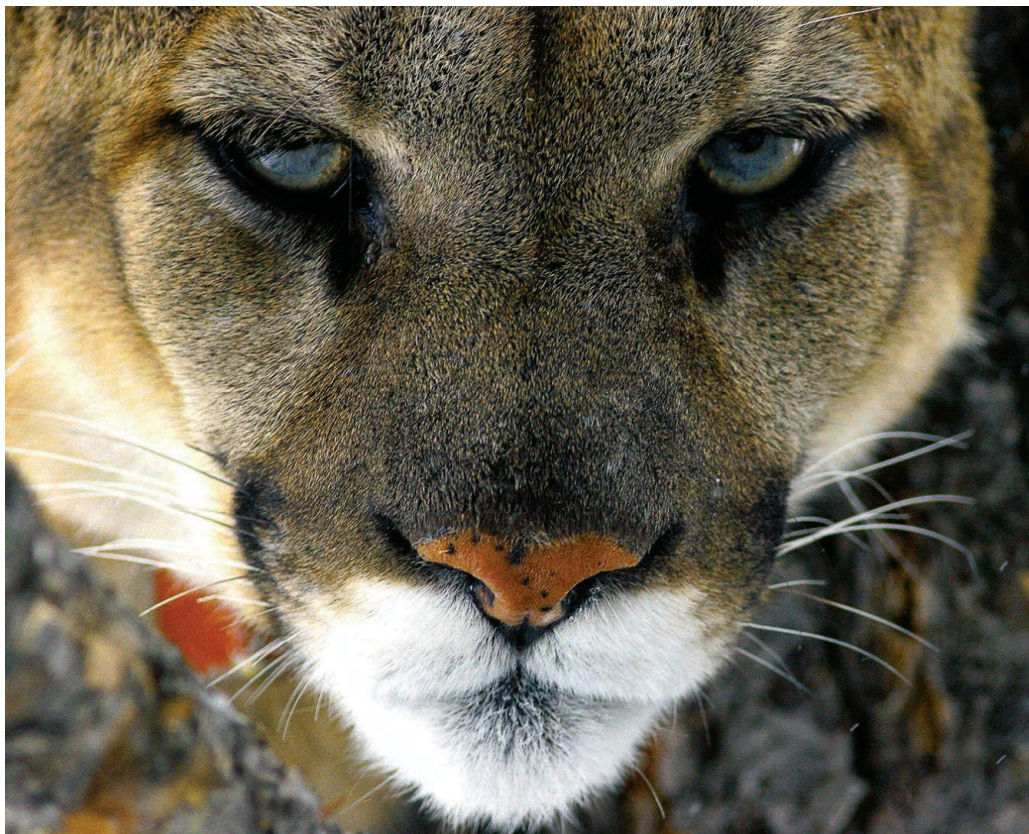
In 2001, Hobbs and Cooper built dams on four streams to imitate those of beavers, creating pools. They fenced both dammed and undammed areas to exclude browsing animals, mimicking the effects of wolves. After a decade, as they reported with Kristin Marshall in the *Journal of Ecology* last year, only willows in plots that were both dammed and fenced were fully restored.

Willows need more than wolves, the team concluded. They need beavers to raise the groundwater table, so their roots have

reversal of the effects of over-browsing,” Hobbs says. “That’s why our experiment is continuing.”

These new data have scientists backing away from the idea that the reintroduction of the wolves has fully restored Yellowstone’s ecosystem. Instead, they believe that the park—or some parts of it—remains in a state of recovery, struggling with the legacy of the predator removal decades ago.

To Hobbs, one key lesson is just how long a landscape can be scarred. “Those profound effects are difficult to reverse. In some parts of Yellowstone, it’s doubtful



Once exterminated, cougars are back in Yellowstone, although heavily hunted outside the park.

a steady supply of water, and to create the mud flats where their seeds can sprout. The Catch-22 is that the beavers can’t return until the willows do. Although the rodents have recolonized larger rivers, such as the Lamar, they’ve been slow to return to many smaller streams. Hobbs thinks that’s because while the wolves were gone, the elk induced a change of state, turning some riparian areas into grasslands inhospitable to willows.

It’s not clear when—or if—that will change. Although beavers have been spotted along some of the willow-stunted streams, they have yet to build durable dams. “It may be that the elk population is only now reaching a level that’s low enough for a

you’ll ever get back to the original state, which is why maintaining an intact ecosystem is so important.”

Other scientists, such as Ripple and Beschta, are more hopeful. “It’s only been 2 decades” since the wolf reintroduction, Ripple says, “and look at all that’s happened and all we’ve learned.”

Manning agrees. “People will look back in 200 years and see the return of the wolves [to Yellowstone] as a profound moment in restoration ecology,” he says. “Yellowstone set a benchmark for the rest of the world.” And in conservation and restoration biology, fields that are all too often burdened with setbacks and losses, those inspirational effects may be the most important of all. ■





## PERSPECTIVES

### MATERIALS SCIENCE

# All that glitters need not be gold

Refractory plasmonic  
ceramics provide durable  
nanophotonic solutions

By Alexandra Boltasseva<sup>1,2</sup> and  
Vladimir M. Shalaev<sup>1,2</sup>

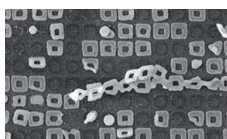
**R**ecent years have seen dramatic growth in the field of nanoscale optics. The advantages of nanophotonics—wide bandwidth, no cross-talk, high speed, and compactness—are key factors enabling optical technologies that have an impact on many areas of society, including information and communications, imaging and sensing, health care, energy, manufacturing, and national security. Gold nanostructures have long been seen as building blocks for subwavelength optical and hybrid electronic-photonic systems providing functional solutions for the above-mentioned applications (1). By making use of the resonant properties of metal nanostructures, particularly the subwavelength coupled oscillations known as surface plasmons, the fields of plasmonics and optical metamaterials have brought forth numerous nanoscale device concepts (1, 2).

Nanophotonics technologies offering extreme durability would be of great use in defense and intelligence, information technology, and the aerospace, energy, chemical, and oil and gas industries. However, most of the optical systems commercially available or in development today fall short of meeting the challenges that such applications would require, particularly where wide temperature ranges, high pressure,



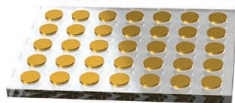
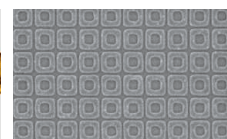
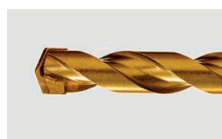
PHOTO: © DANIEL ALEXANDER/DESIGN PICS/CORBIS

## Optoelectronics in harsh environments



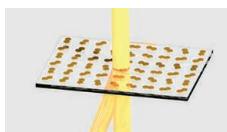
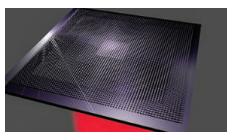
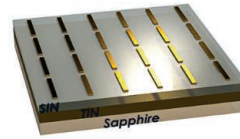
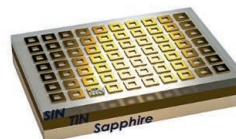
### Materials

Gold: Soft, low melting point  
TiN: Robust, durable, stable, refractory



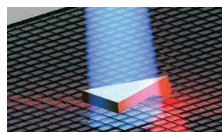
### Design concepts

Nanoantennas, nanoparticles,  
metasurfaces: Plasmonic nanoscale  
building blocks



### Extreme-durability photonics

High-T sensors and flat optics;  
thermophotovoltaics:  
heat-assisted data recording; thermal therapy



**Golden titanium nitride.** TiN, used nowadays to coat domes of Russian churches, is also seen as a replacement for gold in device concepts that make use of nanoscale plasmonic resonances enabling unparalleled optical functionalities. Because of their softness and low melting point, noble metals are not suitable for applications in extreme operational conditions such as high temperature and harsh chemicals. Plasmonic ceramic materials such as TiN serve as refractory (high temperature–stable) building blocks that could enable ultradurable photonic technologies for use in information technology, oil and gas production, and other industrial processes. **(Top)** Au (left) and TiN (right) nanostructures after exposure to heat; melting point of TiN is 2930°C. **(Middle)** Schematics of a TiN-based plasmonic nanoparticle array and colloidal plasmonic particles (left) and light absorber designs (right). **(Bottom)** Plasmonic device applications.

harsh chemical environments, and strong vibrations are present. Despite many device demonstrations for on-chip optics, data recording, sensing, imaging, and solar energy harvesting, the proposed gold-based devices fail to meet the application-specific requirements that real devices face in extreme operational conditions. Because of the softness of noble metals and their low melting points, conventional plasmonic structures cannot provide chemically, mechanically, and thermally stable solutions for the realization of rugged optical equipment.

The discovery of plasmonic ceramic materials as alternative “metals” marks the beginning of a technology-driven era for the fields of plasmonics and nanophotonics (3, 4). Transition metal nitrides such as titanium nitride (TiN) and zirconium nitride (ZrN) have recently been proposed as refractory—that is, capable of sustaining high-temperature plasmonic materials (4) that exhibit good optical properties while also offering biocompatibility, compatibility with CMOS (complementary metal-oxide semiconductor) devices, chemical stability, corrosion resistance, and mechanical strength and durability (see the figure). The attractiveness of TiN for practical devices

is illustrated by its extensive use in semiconductor manufacturing, microelectronics, and biotechnology.

Plasmonic ceramics can provide a unique platform for an emerging energy conversion concept, namely solar thermophotovoltaics (STPV), which promises efficiencies up to 85% (5). The high operational temperatures (well above 800°C) and the low melting points of noble metals have hindered progress in the STPV field. By contrast, TiN absorbers have been shown to provide high optical absorption (about 95%) over a broad range while enduring strong light illumination (6). TiN also holds great promise to enable efficient, TPV-based waste heat recovery. Heat energy harvesting could have a transformative effect on many industries, including metal casting, aerospace, and gas and oil, by providing fossil fuel-based power generation, fuel-fired cells, and portable power generators. TiN's properties are also well suited for solar thermoelectric generators (7), plasmon-mediated photocatalysis (8), and plasmon-assisted chemical vapor deposition (9).

Another heat-generating application of plasmonic nanoparticles is in health care. Because metallic nanoparticles can concentrate light and efficiently heat a confined nanoscale volume around the plasmonic structure (10), they can be used in thermal therapy, in which nanoparticles delivered to a tumor region can be heated via laser il-

lumination and induce the death of cancerous cells. Gold nanoparticles are now being investigated for uses in cancer therapy as drug carriers, photothermal agents, contrast agents, and radiosensitizers. However, gold nanoparticles resonate at specific light wavelengths that lie outside the biological transparency window, thus requiring larger dimensions and complex geometries such as nanoshells (10); in turn, larger sizes affect nanoparticles' pharmacokinetics, biodistribution, and in vivo toxicity. TiN nanofabricated particles have been shown to exhibit plasmonic resonance in the biological transparency window and higher heating efficiencies than gold (6). Moreover, TiN obviates the need for complex geometries and provides a simple, small-size particle solution that is critical in optimizing cellular uptake and clearance from the body. Because TiN is a contamination-safe material already widely used in surgical tools, implants, and food-contact applications, TiN particles could become a solution for tumor-selective photothermal therapy and medical imaging.

Refractory plasmonic materials are also candidates for applications that make use of nanometer-scale field enhancement and local heating. An example of such application is an emerging, higher-density data recording approach, namely heat-assisted magnetic recording (HAMR) (11). In contrast to noble metals that are prone to deformations such as melting and creep, any degradation

<sup>1</sup>School of Electrical & Computer Engineering, Birck Nanotechnology Center, Purdue University, West Lafayette, IN 47907, USA. <sup>2</sup>Nano-Meta Technologies Inc., 1281 Win Hentschel Boulevard, West Lafayette, IN 47906, USA. E-mail: aeb@purdue.edu



of refractory plasmonic materials can be avoided with the proper material integration (6). TiN antennae have recently been shown to satisfy the stringent requirements for an optically efficient, durable HAMR near-field transducer, thereby paving the way to the next-generation data recording systems (6).

The durability and refractory properties of TiN and ZrN could also make them the material building blocks for high-temperature, harsh-environment optical sensors and flat photonic components such as ultrathin lenses, as well as for spatial light modulators using the concepts of the emerging field of metasurfaces (12). Refractory flat optical components would last longer in harsh environments, provide more reliable data, and offer ultracompactness combined with a planar fabrication process. In the oil and gas industry, for example, ultracompact, extremely durable plasmonic sensors could replace electrical sensors and enable new measurement concepts for pressure, flow, drill bit temperature, and breakage detection.

The stability of TiN, along with its high conductivity and corrosion resistance, makes it an ideal material for nanofabrication. TiN can be used for making durable imprint stamps with unparalleled hardness and resistance to wet chemistry processes. When combined with emerging plasmonic nanolithography schemes, TiN films can be used to create multiple-use master molds and fabrication concepts for large-scale patterning at resolutions below 10 nm.

Having an excellent combination of performance properties, durability and contamination safety, plasmonic ceramics hold promise for enabling highly robust, ultracompact, CMOS-compatible optical devices capable of addressing numerous application-specific challenges and operating in harsh environments containing high temperatures, shock, and contaminants. ■

#### REFERENCES AND NOTES

1. H. A. Atwater, *Sci. Am.* **296**, 56 (April 2007).
2. N. I. Zheludev, Y. S. Kivshar, *Nat. Mater.* **11**, 917 (2012).
3. A. Boltasseva, H. A. Atwater, *Science* **331**, 290 (2011).
4. U. Guler *et al.*, *Science* **344**, 263 (2014).
5. S. Fan, *Nat. Nanotechnol.* **9**, 92 (2014).
6. U. Guler, V. M. Shalae, A. Boltasseva, *Mater. Today* **10.1016/j.mattod.2014.10.039** (2014).
7. D. Kraemer *et al.*, *Nat. Mater.* **10**, 532 (2011).
8. C. Clavero, *Nat. Photonics* **8**, 95 (2014).
9. D. A. Boyd, L. Greengard, M. Brongersma, M. Y. El-Naggar, D. G. Goodwin, *Nano Lett.* **6**, 2592 (2006).
10. L. R. Hirsch *et al.*, *Proc. Natl. Acad. Sci. U.S.A.* **100**, 13549 (2003).
11. W. Challener *et al.*, *Nat. Photonics* **3**, 220 (2009).
12. N. Yu *et al.*, *Science* **334**, 333 (2011).

#### ACKNOWLEDGMENTS

We thank A. Kildishev, U. Guler, and R. T. Bonnecaze for fruitful discussions. Support from AFOSR MURI grant 123885-5079396, ARO grant W911 NF-13-1-0226, and NSF grant DMR-1120923.

10.1126/science.aaa8282

#### MATERIALS SCIENCE

## Building supermicelles from simple polymers

Precise control of the polymer building blocks enables synthesis of a range of micrometer-scale structures

By In-Hwan Lee, Suyong Shin,  
Tae-Lim Choi

**T**oy blocks such as Lego allow complex structures to be built from the simple blocks. Similarly, synthetic chemists are attempting to make large and complex molecules from simple reagents (1). On page 1329 of this issue, Qiu *et al.* (2) report an elegant strategy for making well-defined micrometer-scale superstructures by using a series of polymerization techniques and selective self-assembly processes.

A classic strategy for making large molecules is polymerization, which yields macromolecules as large as 10 nm. However, as the sizes increase, it becomes much harder to control their shapes and molecular weights. Also, conventional polymerizations produce macromolecules with a range of molecular weights. Living polymerization overcomes some of these problems, producing macromolecules with controlled molecular weight and narrow dispersity (3). This approach has allowed the synthesis of block copolymers that consist of at least two distinct polymer segments connected together.

To obtain even larger molecules (with diameters of several hundred nanometers), chemists have developed supramolecules, which consist of molecules connected by noncovalent interactions. For example, amphiphilic block copolymers produced by living polymerization can self-assemble into various micelles (4), such as spheres, cylinders, vesicles (5), toroidal rings (6), caterpillars (7–9), and stars (10), when placed in a selective solvent in which one segment is soluble and the other is not. Again, controlling the sizes and shapes of the micelles is extremely challenging. Recently, Manners, Winnik, and co-workers reported crystallization-driven self-assembly (CDSA), a living supramolecular micellization strategy that yields polymeric nanostructures with very narrow dispersity (11–13).

Qiu *et al.* now build on this strategy to create much larger, but well-defined, micrometer-scale supermicelles from amphiphilic cylindrical triblock comicelles (which consist of three connected micelle segments). The lengths and widths of each segment

are precisely controlled through the living CDSA method. The first step for the supermicellization is to prepare narrow-disperse block copolymers (see the figure, panels A and B) by living anionic polymerization. These polymers, which contain crystalline poly(ferrocenyldimethylsilane) (PFS), self-assemble in selective solvents to yield short seeds after sonication. From these exposed crystalline PFS seeds, cylindrical micelles can grow epitaxially upon adding unimeric block copolymers, because these unimers selectively crystallize on the seeds. This self-assembly process is exactly the same as a living polymerization, allowing the length and width of each segment to be controlled.

In the second step, the authors prepare amphiphilic triblock comicelles. Because both ends of cylindrical micelles are growing

---

**“Controlling the complexity of large molecules is one of the central themes in synthetic chemistry.”**

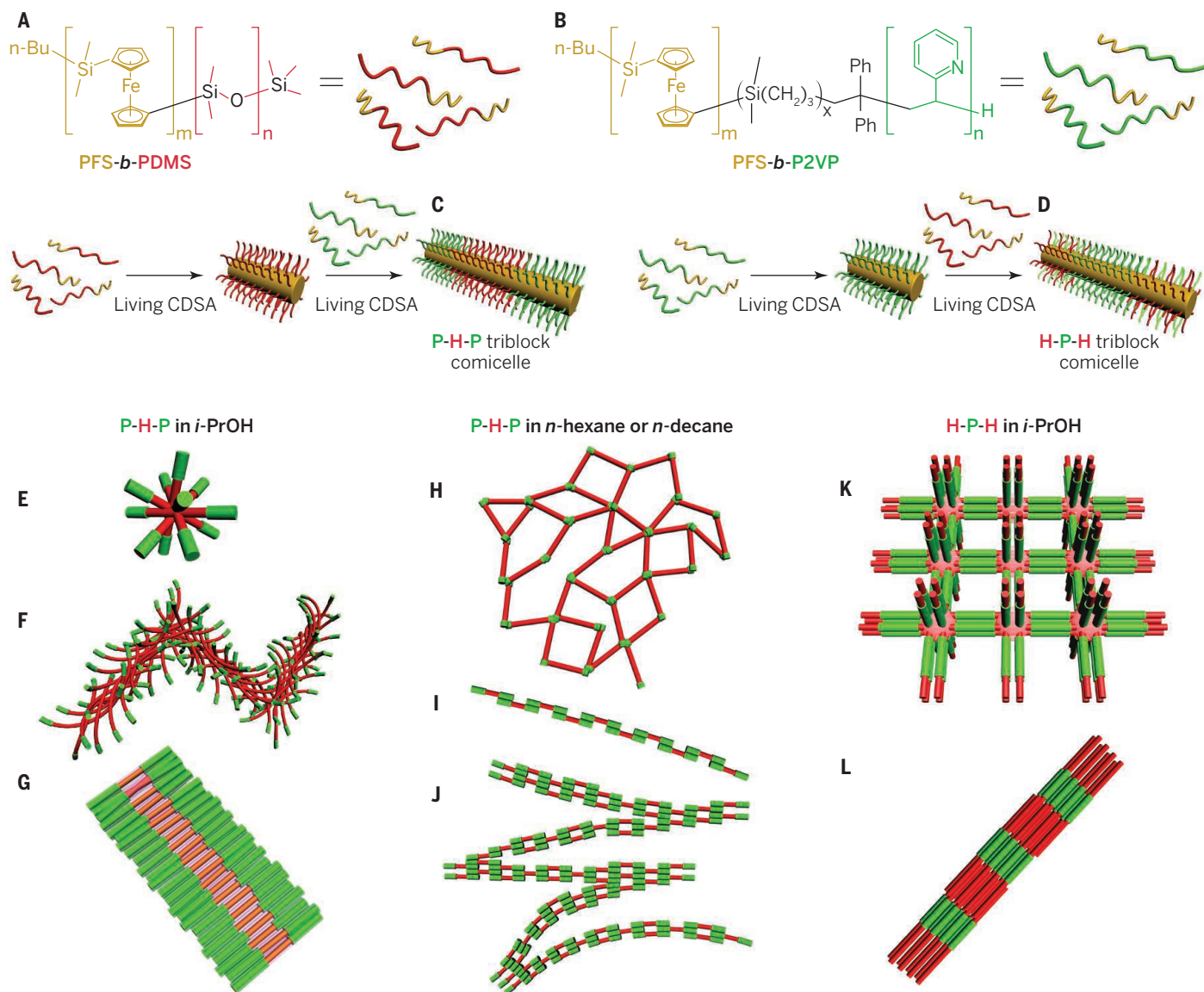
---

in the living polymerization manner, addition of different unimers with a block of PFS produces triblock comicelles with precisely controlled lengths and widths (see the figure, panels C and D).

Finally, Qiu *et al.* induce supermicellization in selective solvents. For instance, the terminal P segments of P-H-P triblock comicelles are soluble in polar isopropanol, and these comicelles therefore undergo supermicellization in *i*-PrOH to shield the insoluble H segment. Previously, comicelles with thick P segments yielded only simple supermicelles such as spheres (see the figure, panel E) and tilted-elongated micelles (panel F) (14). However, switching to thinner P segments leads to micrometer-scale train-track-like or cylindrical brushlike supermicelles, because side-by-side stacking of the H block is now favored (see the figure, panel G).

---

Department of Chemistry, Seoul National University, Seoul, 151-747, South Korea. E-mail: tlc@snu.ac.kr



**Supermicelle assembly.** Qiu *et al.* show that triblock comicelles can be created through living CDSA (**A** and **B**). After forming P-H-P and H-P-H triblock comicelles (**C** and **D**), various micrometer-scale superstructures self-assemble in different solvents (**E** to **L**).

Changing the solvent to nonpolar *n*-hexane results in the formation of totally different supermicelles. Now, *n*-hexane becomes the selective solvent for the H segments, and the terminal P segments become sticky ends to promote the supermicellization. As a result, loops are formed (see the figure, panel I). Adding *n*-decane leads to supermicelles resembling frameworks (panel H) or chain networks (panel J).

What happens when H-P-H triblock comicelles (with inverse polarity to the P-H-P ones) undergo supermicellization? Those comicelles containing short H-terminal segments produce three-dimensional superlattices (see the figure, panel K), whereas those with longer H segments form one-dimensional superlattices (panel L). Because these superstructures are larger than a micrometer, they can be visualized not only by

transmission electron microscope in the dry state but also by confocal laser scanning microscopy in solution.

Controlling the complexity of large molecules is one of the central themes in synthetic chemistry. In this regard, the diversity and beauty of the micrometer-scale well-defined superstructures reported by Qiu *et al.* is remarkable. The precise shape control is only possible because the length and the width of each comicelle are precisely controlled by both living covalent and supramolecular polymerizations, which then lead to a series of selective self-assembly processes. Future studies should aim to control the sizes of the supermicelles, add useful functions, or speed up the synthesis processes by employing direct in situ self-assembly methods (8, 10, 15).

The supermicelles reported by Qiu *et al.* bear some analogy to biological machines

such as the ribosome. Synthetic chemists are by no means approaching the complexity and elegance of these biological systems, but with this report, at least, we are one step closer. ■

#### REFERENCES

1. K. C. Nicolaou *et al.*, *J. Am. Chem. Soc.* **136**, 16444 (2014).
2. H. Qiu *et al.*, *Science* **347**, 1329 (2015).
3. O. W. Webster, *Science* **251**, 887 (1991).
4. T. Aida, E. W. Meijer, S. I. Stupp, *Science* **335**, 813 (2012).
5. D. E. Discher, A. Eisenberg, *Science* **297**, 967 (2002).
6. D. J. Pochan *et al.*, *Science* **306**, 94 (2004).
7. H. Cui *et al.*, *Science* **317**, 647 (2007).
8. K.-Y. Yoon *et al.*, *J. Am. Chem. Soc.* **134**, 14291 (2012).
9. A. H. Gröschel *et al.*, *Nature* **503**, 247 (2013).
10. I.-H. Lee *et al.*, *J. Am. Chem. Soc.* **135**, 17695 (2013).
11. X. Wang *et al.*, *Science* **317**, 644 (2007).
12. J. B. Gilroy *et al.*, *Nat. Chem.* **2**, 566 (2010).
13. P. A. Rupar *et al.*, *Science* **337**, 559 (2012).
14. H. Qiu *et al.*, *Angew. Chem. Int. Ed.* **51**, 11882 (2012).
15. N. J. Warren, S. P. Armes, *J. Am. Chem. Soc.* **136**, 10174 (2014).

10.1126/science.aaa8681



## NEUROSCIENCE

# Metabolic control of epilepsy

Seizures may be controlled by targeting inexcitable elements of the nervous system

By Helen E. Scharfman

It has been assumed that anticonvulsants or antiepileptic drugs, now called antiseizure drugs (ASDs), act on the underpinnings of nerve cell firing: ion channels that generate action potentials, or neurotransmitter receptors that control synaptic transmission. The breakthroughs heralded by the first generation of ASDs, such as the GABA<sub>A</sub> ( $\gamma$ -aminobutyric acid type A) receptor modulator phenobarbital and the sodium channel antagonist phenytoin, are a major reason for this view. The emergence of second- and third-generation ASDs that also inhibit ion channels provided additional support. However, as epilepsy research has matured, our understanding of ASDs has also. The report by Sada *et al.* (1) on page 1362 of this issue exemplifies this trend. The study raises a surprising question: Should the focal point of ASD development actually be neurons?

Epileptic seizures result from excessive and abnormal neuron activity in the brain. Suggesting that neuronal firing is tangential to epilepsy therefore may seem radical—and illogical—given that seizures are mediated by neurons. But there is now considerable evidence that inexcitable elements of the central nervous system, such

## “Should the focal point of ASD development actually be neurons?”

as astrocytes, the vasculature, and the immune system, play a far greater role than first thought (2–5). The observations of Sada *et al.* point to epilepsy as a disease of energy metabolism rather than neuronal discharge, a strong shift in the neurocentric view of epilepsy.

A so-called ketogenic diet consists mostly of fat, with minimal carbohydrates. Thus, ketones become a major source of energy. The use of this regimen for epilepsy arose after parents found it effective in their children when ASDs were not. Other dietary manipulations, such as caloric restriction, have not played a major role in epilepsy treatment (6). That simply changing diet could quickly and dramatically reduce seizures sparked a wave of new research and a greater understanding of how glucose metabolism, dependent on relationships between astrocytes and neurons, modulates seizures (7). Indeed, epilepsy might be considered a type of diabetes, as has been suggested for Alzheimer's disease, sometimes named “type 3” diabetes (8). In epilepsy,

lowering circulating glucose concentrations could be therapeutic (9).

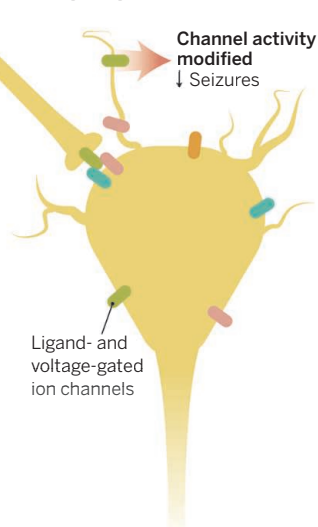
Sada *et al.* report that inhibition of lactate dehydrogenase (LDH), an enzyme critical in the metabolic cross-talk between astrocytes and neurons, blocked neuron excitation (that typify seizures) in vitro, and also prevented seizures in an animal model of epilepsy. Although LDH may dehydrogenate several substrates, the one highlighted by the authors, and probably most important in the context of seizures, is lactate. Generation of lactate in astrocytes, followed by its transport to neurons [the lactate “shuttle” (9)], allows lactate to become an energy substrate for neurons when energy demand is high, such as when seizures occur.

A compelling aspect of these data is the comprehensive use of recordings of electrical activity when LDH is experimentally manipulated in single cells, pairs of neurons and astrocytes, as well as in a mouse model of epilepsy. The efficacy in vivo is important because treatments that inhibit neuron hyperactivation in vitro or block seizures in normal animals do not always have efficacy in “ASD resistant” epilepsy, where complex changes occur in neuronal gene expression, neuronal circuitry, astrocytes, blood vessels, and inflammation.

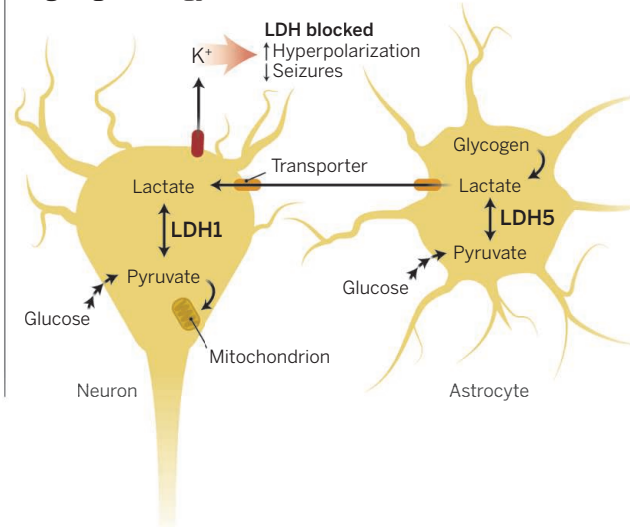
Sada *et al.* also show that one of the currently available ASDs, stiripentol, exerts its effect—at least in part—by inhibiting LDH. This finding raises the possibility that other ASDs may alter energy metabolism in the brain (see the figure). This idea is attractive because many ASDs have mechanisms of action that are not well explained, or have modest effects on most ligand- or voltage-gated ion channels. The authors also make the case that K<sub>ATP</sub> channels in neurons are likely to mediate the effects of LDH inhibition, consistent with the emergence of these ion channels as the ultimate target of a ketogenic diet (10). By activating K<sub>ATP</sub> channels, neurons hyperpolarize, making it less likely that action potentials will be generated.

The findings of Sada *et al.* are not without some caveats, however. For example, the actions of LDH on metabolism, even in a normal nerve cell, are likely to be complex, and the metabolism in the epileptic brain even more so. One reason is that astrocytes typically become “reactive” in epilepsy, in response to tissue injury or for other reasons. Yet all astrocytes may not change, leading to heterogeneous alterations in energy metabolism that vary depending on brain area, type of epilepsy, and other factors.

### Drug target: Neurons



### Drug target: Energy metabolism



**Not so neurocentric.** The classic view explains antiseizure drug action as directly blocking ion channels in neurons. An alternative view is that drugs that block energy metabolism in both neurons and astrocytes can treat epilepsy.

Nathan Kline Institute for Psychiatric Research and New York University Langone Medical Center, Orangeburg, NY 10962, USA. E-mail: helen.scharfman@nyumc.org

Indeed, there is some disagreement about the efficacy of a ketogenic diet in previous studies, and heterogeneity may be one reason. Sada *et al.* address this issue by showing that LDH inhibition hyperpolarizes diverse types of principal cells (neurons that extend axons to the next brain area in a functional pathway to mediate seizures), including those in the substantia nigra and in the hippocampus. Thus, LDH inhibition is effective across different brain areas. Interestingly, blocking LDH failed to affect GABAergic neurons, showing remarkable specificity for principal cells that generate seizures and not the interneurons that inhibit the principal cells.

Reducing pyruvate in cultured neurons results in dehydrogenation of lactate, which was protective against hyperactivity. However, increasing the exogenous pyruvate concentration was beneficial in previous experiments using different endpoints (11, 12). This discrepancy suggests that LDH inhibition will potentially be important in many contexts, but it is likely that the effect of blocking this enzyme will depend on how it is altered and where (e.g., neurons versus astrocytes). Fortuitously, it is possible to manipulate neurons selectively because LDH1 (one of the five forms of LDH) is primarily neuronal (9).

In the short time that epileptic rodents were treated with stiripentol in the Sada *et al.* study, there was remarkable efficacy of LDH inhibition. Would it have continued? Metabolism is remarkably resilient, and compensatory changes are common. Would there be side effects, given the widespread and complex nature of metabolism? Sada *et al.* offer much food for thought as well as fuel for the fire between those who focus on the neurons to control epilepsy, and those who champion the astrocytes. ■

#### REFERENCES

1. N. Sada, S. Lee, T. Katsu, T. Otsuki, T. Inoue, *Science* **347**, 1362 (2015).
2. U. Heinemann, D. Kaufer, A. Friedman, *Glia* **60**, 1251 (2012).
3. D. A. Coulter, T. Eid, *Glia* **60**, 1215 (2012).
4. A. Vezzani, J. French, T. Bartfai, T. Z. Baram, *Nat. Rev. Neurol.* **7**, 31 (2011).
5. R. M. Kaminski, M. A. Rogawski, H. Klitgaard, *Neurotherapeutics* **11**, 385 (2014).
6. C. E. Stafstrom, J. Rho, *Epilepsy and the Ketogenic Diet* (Springer Science+Business, New York, 2004).
7. C. E. Stafstrom, A. Roopra, T. P. Sutula, *Epilepsia* **49** (suppl. 8), 97 (2008).
8. S. M. de la Monte, M. Tong, N. Lester-Coll, M. Plater Jr., J. R. Wands, *J. Alzheimers Dis.* **10**, 89 (2006).
9. L. Pellerin, P. J. Magistretti, *J. Cereb. Blood Flow Metab.* **32**, 1152 (2012).
10. A. Lutas, G. Yellen, *Trends Neurosci.* **36**, 32 (2013).
11. S. Desagher, J. Glowinski, J. Prémont, *J. Neurosci.* **17**, 9060 (1997).
12. E. Isopi *et al.*, *Neurobiol. Dis.* 10.1016/j.nbd.2014.11.013 (2014).

10.1126/science.aaa9607

#### VIBRATIONAL DYNAMICS

## Taming $\text{CH}_5^+$ , the “enfant terrible” of chemical structures

Ion-counting spectroscopy reveals the low-energy states of a molecule with highly dynamic bonds

By Takeshi Oka

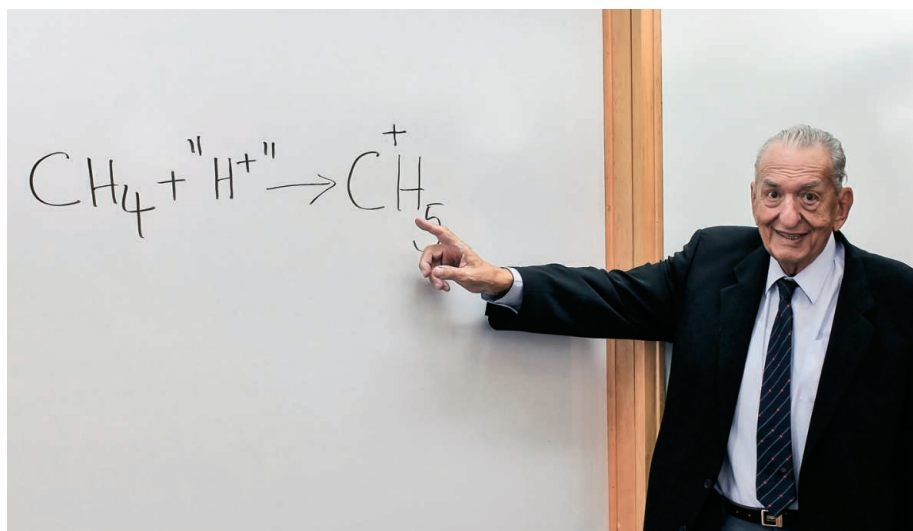
**P**rotonated methane,  $\text{CH}_5^+$ , is a quantum dynamical system that challenges our understanding of chemical bonding and structure. The bonding does not lead to a trigonal bipyramid. Instead, the five protons swarm around the central carbon, and this gives rise to an incredibly complex vibration-rotation-tunneling infrared spectrum (1), making it an “enfant terrible” for spectroscopists. Ab initio theory has found that “there is essentially no barrier to hydrogen scrambling” (2) and “the very concept of molecular structure becomes problematic for this molecule” (3). For its parent molecule,  $\text{CH}_4$ , each rotational level corresponds to one quantum state, but for  $\text{CH}_5^+$  it corresponds to  $2 \times 5! = 240$  states. However, on page 1346 of this issue, Asvany *et al.* (4) report combination differences (Co-Diffs) of the low-energy levels of  $\text{CH}_5^+$ , a first step at “taming” its spectrum.

For me, these results are exciting because I have been on the trail of this carbocation for decades. After I reported the infrared spectrum of  $\text{H}_3^+$  in 1980 (5), I received a let-

“...the very concept of molecular structure becomes problematic for this molecule...”

ter from George Olah, in which he asked, “I wonder whether a similar technique would enable to observe the infrared spectrum of  $\text{CH}_5^+$ . It is of great interest to organic chemists...” I did not know Olah or  $\text{CH}_5^+$ , the pivotal reaction intermediate in Olah’s superacid chemistry that would lead to his 1994 Nobel Prize (see the figure) (6). I was simply delighted that my work of astrophysical interest was also important for organic chemists.

The “similar technique” became a general method with the invention by Saykally of velocity modulation detection (7), which allowed the study of protonated ions, such as  $\text{NH}_4^+$  and  $\text{H}_3\text{O}^+$  (8). However, for plasmas containing  $\text{CH}_4$ , we obtained extremely complicated spectra with over 10,000 lines.



**Superacids and interstellar chemistry.** The discovery of the infrared spectrum of  $\text{H}_3^+$ , a strong proton donor (acid) central in interstellar chemistry, prompted the query from George Olah to search for  $\text{CH}_5^+$ . This molecule is pivotal in the superacid chemistry pioneered by Olah. The molecular bonding is fluxional and its spectrum is extremely complicated, but the high-resolution ion-counting spectroscopy at 4 K and 10 K observed by Asvany *et al.* identify crucial CoDiffs of low-energy states.



Many of these lines were found to be of other carbocations, such as  $\text{CH}_3^+$ ,  $\text{C}_2\text{H}_3^+$ ,  $\text{C}_2\text{H}_2^+$ , and  $\text{CH}_2^+$  [for a review, see (8)]. Each time I proudly reported these discoveries, Olah responded, “impressive, but what about  $\text{CH}_5^+$ ?” After “weeding out” those thousands of understood spectral lines, the remaining messy spectrum was undecipherable, and the 900 lines of  $\text{CH}_5^+$  were reported without assignment (1). Even purely empirical attempts at finding some regularity of the spectrum were not successful.

Asvany *et al.* have been able to determine the energy separation between several pairs of lowest levels using the action spectroscopy invented by Schlemmer and Gerlich (9). The proton affinity of  $\text{CH}_4$  (5.72 eV) is slightly greater than that of  $\text{CO}_2$  (5.68 eV) so the reaction  $\text{CH}_5^+ + \text{CO}_2 \rightarrow \text{CH}_4 + \text{CO}_2\text{H}^+$  is endothermic. Addition of a resonant 3.3- $\mu\text{m}$  (0.37 eV) laser photon makes this reaction exothermic. Thus, they can do spectroscopy by counting  $\text{CO}_2\text{H}^+$  ions rather than photons. This paradigm shift from photon- to

**“As in Olah’s chemistry on Earth,  $\text{CH}_5^+$  is pivotal for producing hydrocarbons in space... I anticipate that this enfant terrible will be caught in interstellar space far ahead of its theoretical understanding..”**

ion-counting spectroscopy has increased the sensitivity—instead of needing  $10^{13}$  ions,  $10^3$   $\text{CH}_5^+$  suffice. Also, trapped ions can be cooled to cryogenic temperature, which leads to a 100 times increase in accuracy.

The 2897 lines observed by Asvany *et al.* at 10 K demonstrate the complexity of the  $\text{CH}_5^+$  spectrum. In contrast,  $\text{CH}_4$  at 10 K has only four rotational levels with quantum number  $J < 3$  populated and only 10 transitions can be observed. The 300 times increase in spectral density from  $\text{CH}_4$  to  $\text{CH}_5^+$  is caused by proton scrambling and inversion motion. Rotational assignments could be made that differ from those they reported, but these are minor details—the CoDiff values are correct and the key to advancing our understanding.

In spite of the complexity, each quantum level can be specified by using the total proton spin quantum number and the parity

(10). The scrambling of the five protons with spin 1/2 produces a total nuclear spin angular momentum  $I$  according to the formula

$$[D_{1/2}]^5 = D_{5/2} + 4D_{3/2} + 5D_{1/2}$$

This formula means that each of the levels of  $\text{CH}_5^+$  have  $I = 5/2$  ( $A_1$ ),  $3/2$  ( $G_1$ ), or  $1/2$  ( $H_1$ ), and the number of levels are in the ratio of 1:4:5 and the CoDiffs 1:16:25. Each level also has a definite parity of + or – and their numbers are equal. The CoDiffs reported by Asvany *et al.* are for levels with  $I = 3/2$  and  $1/2$  and the same parity. The next step will be to find CoDiffs with different parity, which the authors note could be tackled by applying their method for far-infrared spectroscopy.

The results by Asvany *et al.* put the experiment far ahead of the theory. To date, Wang and Carrington’s computation (11), based on the potential energy surface (PES) of Jin *et al.* (12), seems to be the only frontal attack to this problem, but it does not include rotation. A brute-force variational calculation of the five protons with an accurate PES may be the way to solve this problem. Such treatment has been successful for  $\text{H}_3^+$ , but the formalism and computation will be much more demanding for a five-proton system.

As in Olah’s chemistry on Earth,  $\text{CH}_5^+$  is pivotal for producing hydrocarbons in space. The lines list by Asvany *et al.* suffices for detecting interstellar  $\text{CH}_5^+$ , but we badly need strongest lines for  $I = 5/2$  ( $A_1$ ). The classical  $\text{CH}_3^+$  ion is yet to be detected, so detection of the nonclassical  $\text{CH}_5^+$  will be difficult but worth a try. Once the far-infrared transitions are observed, including  $I = 5/2$  levels, more sensitive observational techniques can be used. I anticipate that this enfant terrible will be caught in interstellar space far ahead of its theoretical understanding, which will take at least a few more decades. ■

#### REFERENCES

1. E. T. White, J. Tang, T. Oka, *Science* **284**, 135 (1999).
2. P. R. Schreiner, S.-J. Kim, H. F. Schaefer, III, P. von Ragué Schleyer, *J. Chem. Phys.* **99**, 3716 (1993).
3. H. Müller, W. Kutzelnigg, J. Noga, W. Klopper, *J. Chem. Phys.* **106**, 1863 (1997).
4. O. Asvany, K. M. T. Yamada, S. Brünken, A. Potapov, S. Schlemmer, *Science* **347**, 1346 (2015).
5. T. Oka, *Phys. Rev. Lett.* **45**, 531 (1980).
6. G. A. Olah, *Angew. Chem. Int. Ed. Engl.* **34**, 1393 (1995).
7. C. S. Gudeman, M. H. Begemann, J. Pfaff, R. J. Saykally, *Phys. Rev. Lett.* **50**, 727 (1983).
8. T. Oka, *J. Phys. Chem. A* **117**, 9308 (2013).
9. S. Schlemmer, T. Kuhn, E. Lescop, D. Gerlich, *Int. J. Mass Spectrom.* **185–187**, 589 (1999).
10. P. R. Bunker, B. Ostojic, S. Yurchenko, *J. Mol. Struct.* **695–696**, 253 (2004).
11. X.-G. Wang, T. Carrington Jr., *J. Chem. Phys.* **129**, 234102 (2008).
12. Z. Jin, B. J. Braams, J. M. Bowman, *J. Phys. Chem. A* **110**, 1569 (2006).

#### STATISTICS

## What is the question?

Mistaking the type of question being considered is the most common error in data analysis

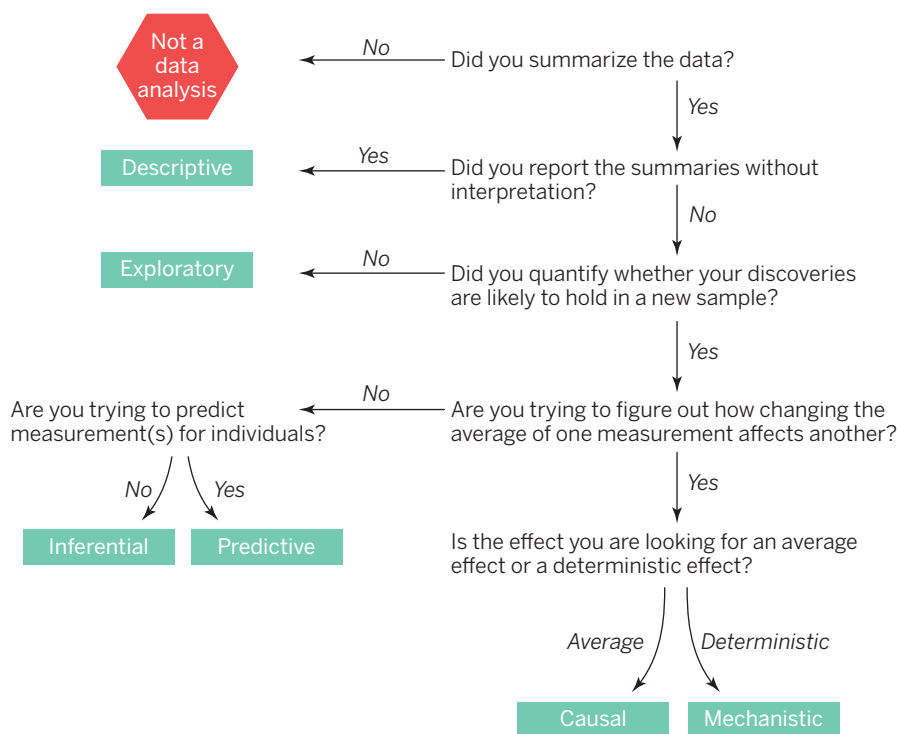
By Jeffery T. Leek and Roger D. Peng

Over the past 2 years, increased focus on statistical analysis brought on by the era of big data has pushed the issue of reproducibility out of the pages of academic journals and into the popular consciousness (1). Just weeks ago, a paper about the relationship between tissue-specific cancer incidence and stem cell divisions (2) was widely misreported because of misunderstandings about the primary statistical argument in the paper (3). Public pressure has contributed to the massive recent adoption of reproducible research tools, with corresponding improvements in reproducibility. But an analysis can be fully reproducible and still be wrong. Even the most spectacularly irreproducible analyses—like those underlying the ongoing lawsuits (4) over failed genomic signatures for chemotherapy assignment (5)—are ultimately reproducible (6). Once an analysis is reproducible, the key question we want to answer is, “Is this data analysis correct?” We have found that the most frequent failure in data analysis is mistaking the type of question being considered.

Any specific data analysis can be broadly classified into one of six types (see the figure). The least challenging of these is a descriptive data analysis, which seeks to summarize the measurements in a single data set without further interpretation. An example is the United States Census, which aims to describe how many people live in different parts of the United States, leaving the interpretation and use of these counts to Congress and the public.

An exploratory data analysis builds on a descriptive analysis by searching for discoveries, trends, correlations, or relationships between the measurements to generate ideas or hypotheses. The four-star planetary system Tatooine was discovered

Data analysis flowchart



when amateur astronomers explored public astronomical data from the Kepler telescope (7). An exploratory analysis like this seeks to make discoveries, but can rarely confirm those discoveries. Follow-up studies and additional data were needed to confirm the existence of Tatooine (8).

An inferential data analysis quantifies whether an observed pattern will likely hold beyond the data set in hand. This is the most common statistical analysis in the formal scientific literature. An example is a study of whether air pollution correlates with life expectancy at the state level in the United States (9). In nonrandomized experiments, it is usually only possible to determine the existence of a relationship between two measurements, but not the underlying mechanism or the reason for it.

Going beyond an inferential data analysis, which quantifies the relationships at population scale, a predictive data analysis uses

a subset of measurements (the features) to predict another measurement (the outcome) on a single person or unit. Web sites like FiveThirtyEight.com use polling data to predict how people will vote in an election. Predictive data analyses only show that you can predict one measurement from another; they do not necessarily explain why that choice of prediction works.

A causal data analysis seeks to find out what happens to one measurement on average if you make another measurement change. Such an analysis identifies both the magnitude and direction of relationships between variables on average. For example, decades of data show a clear causal relationship between smoking and cancer (10). If you smoke, it is certain that your risk of cancer will increase. The causal effect is real, but it affects your average risk.

Finally, a mechanistic data analysis seeks to show that changing one measurement

always and exclusively leads to a specific, deterministic behavior in another. For example, data analysis has shown how wing design changes air flow over a wing, leading to decreased drag. Outside of engineering, mechanistic data analysis is extremely challenging and rarely achievable.

Mistakes in the type of data analysis and therefore the conclusions that can be drawn from data are made regularly. In the last 6 months, we have seen inferential analyses of the relationship between cellphones and brain cancer interpreted as causal (11) or the exploratory analysis of Google search terms related to flu outbreaks interpreted as a predictive analysis (12). The mistake is so common that it has been codified in standard phrases (see the table).

Determining which question is being asked can be even more complicated when multiple analyses are performed in the same study or on the same data set. A key danger is causal creep—for example, when a randomized trial is used to infer causation for a primary analysis and data from secondary analyses are given the same weight. To accurately represent a data analysis, each step in the analysis should be labeled according to its original intent.

Confusion between data analytic question types is central to the ongoing replication crisis, misconstrued press releases describing scientific results, and the controversial claim that most published research findings are false (13, 14). The solution is to ensure that data analytic education is a key component of research training. The most important step in that direction is to know the question. ■

REFERENCES

1. "How science goes wrong," *The Economist*, 19 October 2013; see [www.economist.com/news/leaders/21588069-scientific-research-has-changed-world-now-it-needs-change-itself-how-science-goes-wrong](http://www.economist.com/news/leaders/21588069-scientific-research-has-changed-world-now-it-needs-change-itself-how-science-goes-wrong).
2. C. Tomasetti, B. Vogelstein, *Science* **347**, 78 (2015).
3. See [www.bbc.com/news/magazine-30786970](http://www.bbc.com/news/magazine-30786970).
4. Duke's Legal Stance: We Did No Harm, *The Cancer Letter Publications* (2015); see [www.cancerletter.com/articles/20150123\\_2](http://www.cancerletter.com/articles/20150123_2).
5. A. Potti et al., *Nat. Med.* **12**, 1294 (2006).
6. K. A. Baggerly, K. R. Coombes, *Ann. Appl. Stat.* **3**, 1309 (2009).
7. "Planet with four stars discovered by citizen astronomers," *Wired UK* (2012); see [www.wired.co.uk/news/archive/2012-10/15/four-starred-planet](http://www.wired.co.uk/news/archive/2012-10/15/four-starred-planet).
8. M. E. Schwamb et al.; <http://arxiv.org/abs/1210.3612> (2013).
9. A. W. Correia et al., *Epidemiology* **24**, 23 (2013).
10. O. A. Panagiotou et al., *Cancer Res.* **74**, 2157 (2014).
11. E. Oster, Cellphones Do Not Give You Brain Cancer, *FiveThirtyEight* (2015); see <http://fivethirtyeight.com/features/cellphones-do-not-give-you-brain-cancer/>.
12. D. M. Lazer, R. Kennedy, G. King, A. Vespignani, The Parable of Google Flu: Traps in Big Data Analysis (2014); see <http://dash.harvard.edu/handle/1/12016836>.
13. L. R. Jager, J. T. Leek, *Biostatistics* **15**, 1 (2014).
14. A. Gelman, K. O'Rourke, *Biostatistics* **15**, 18 (2014).

Published online 26 February 2015;  
10.1126/science.aaa6146

Common mistakes

REAL QUESTION TYPE	PERCEIVED QUESTION TYPE	PHRASE DESCRIBING ERROR
Inferential	Causal	"Correlation does not imply causation"
Exploratory	Inferential	"Data dredging"
Exploratory	Predictive	"Overfitting"
Descriptive	Inferential	"n of 1 analysis"



## RNA

# A TRICK'n way to see the pioneer round of translation

Watching where and when individual messenger RNAs direct protein synthesis in live cells

By Maximilian W. Popp<sup>1,2</sup> and  
Lynne E. Maquat<sup>1,2</sup>

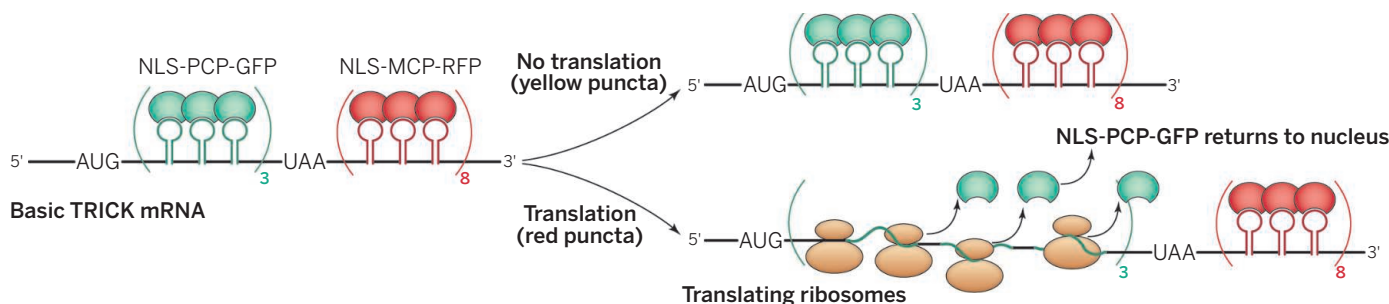
**B**ecause proteins are largely the ultimate effectors of genotype, controlling the process of protein synthesis in space and time can play a critical role in cell metabolism. The subcellular localization of messenger RNAs (mRNAs) and their ensuing translation into proteins are known to be exploited to regulate processes such as development, cell

teins, forming messenger ribonucleoprotein (mRNP) complexes. Like a bulldozer, the large and highly processive ribosome can strip off mRNA-bound proteins, a fact that Halstead *et al.* exploit in their technique, termed “translating RNA imaging by coat protein knock-off” or “TRICK.” The authors label reporter mRNAs through the targeted binding of two engineered fluorescent proteins. Two orthogonal stem-loop structures that can be translated are grafted into the reporter mRNA. One is the MS2 bacteriophage

tures during nuclear mRNA biosynthesis (see the figure).

Using imaging and computer software, the authors are able to rapidly capture images of single mRNP particles as they are synthesized and transported in living cells. Color combinations indicate translational status: All reporter mRNAs were labeled with NLS-MCP-RFP in the 3' UTR. Although prior to translation, mRNAs are also bound by NLS-PCP-GFP in the coding region, this is no longer the case after the first round of translation. Indeed, at steady state, ~94% of all cytoplasmic reporter mRNAs were translated at least once and thus labeled with only NLS-MCP-RFP.

To demonstrate the utility of their technology, the authors examined the various claims that translation occurs in the nucleus, which was first reported in the 1950s (3) and periodically revived since (4, 5), although today largely discounted (6). Halstead *et al.* observed with single-molecule resolution that ~91% of reporter mRNAs were doubly



**A neat translation TRICK.** The TRICK methodology for monitoring translational status of individual mRNAs in live cells. AUG, translation initiation codon; UAA, translation termination codon.

motility, and neurotransmission. However, a dearth of tools for observing where and when mRNA translation occurs with single-molecule resolution in live cells has limited analysis to primarily ensemble, often static, biochemical measurements. On page 1367 of this issue, Halstead *et al.* (1) have filled this need by developing a method for visualizing mRNA translation in both live cells and whole animals.

The ribosome is a large macromolecular machine that moves along the mRNA, reading the genetic information encoded in the RNA template and catalyzing amide bond formation to generate polypeptides. In cells, the template mRNAs do not exist as naked polymers but rather are decorated with pro-

coat protein-binding site (MBS), and the other is the phage PP7 coat protein-binding site (PBS). These mRNAs are coexpressed with a nuclear localization signal (NLS)-tagged red fluorescent protein (RFP) fused to the MS2 coat protein (MCP) (collectively NLS-MCP-RFP) that binds only to the MBS, and an NLS-tagged green fluorescent protein (GFP) similarly fused to the PP7 coat protein (PCP) (collectively NLS-PCP-GFP) that binds to the PBS (2).

Placement within the mRNA reporter is key: Six PBS hairpins are inserted in the mRNA coding region, and 24 MBS hairpins are located after the UGA stop codon in the 3'-untranslated region (3' UTR). Thus, during translation, any NLS-PCP-GFP proteins bound to the PBS will be displaced by the ribosome, while any NLS-MCP-RFP proteins remain bound to the 3' UTR, untouched by the ribosome. Tagging the fluorescent proteins with an NLS ensures that proteins removed during translation in the cytoplasm are returned to the nucleus and cannot rebound to cytoplasmic mRNA, creating a depot of fluorescent proteins that can immediately find their cognate RNA struc-

labeled (untranslated) in the nucleus in live U-2 OS human osteosarcoma cells. The authors further substantiated this conclusion with the finding that cycloheximide treatment, which would freeze polyribosomes along the mRNA so as to occlude rebinding of NLS-PCP-GFP to the coding region, did not yield singly labeled nuclear species.

Halstead *et al.* next focused on stressful conditions, such as nutrient deprivation or oxidative stress, and how they decrease global translation and concomitantly induce formation of stress granules and processing bodies (P-bodies), which are non-membrane-delimited cytoplasmic organelles that contain distinct mRNP constituents (7). Transcripts with a 5'-terminal oligopyrimidine (5' TOP) motif are sequestered within RNA granules during stress (8), a process that the authors monitored using a TRICK reporter bearing the 5' TOP motif. In response to oxidative stress in HeLa human adenocarcinoma cells, the pool of 5' TOP TRICK reporter mRNAs partitioned into two translationally repressed cytoplasmic pools: One resided within granules, and the other was not sequestered. The TRICK method made it possible to follow

<sup>1</sup>Department of Biochemistry and Biophysics, School of Medicine and Dentistry, University of Rochester, Rochester, NY, USA, <sup>2</sup>Center for RNA Biology, University of Rochester, Rochester, NY, USA. E-mail: lynne\_maquat@urmc.rochester.edu

both pools independently during stress recovery to show that those mRNAs in granules remained translationally repressed, whereas the nonsequestered pool went on to initiate translation.

Halstead *et al.* also demonstrated that the method is applicable to whole-animal studies by constructing transgenic flies (*Drosophila*) bearing the requisite fluorescent protein fusions, as well as an *oskar* mRNA-based TRICK reporter. The maternally produced *oskar* mRNA is transported from nurse cells in which it is made into the oocyte, where it localizes to the posterior pole at later stages and is necessary for germ cell formation (9). Halstead *et al.* were able to confirm that *oskar* mRNA is translationally repressed until it localizes to the posterior pole.

By design, the TRICK method assays the first round of translation. The basis of the method, i.e., the ability of the ribosome to strip off proteins from newly synthesized mRNAs, is also used by cells as a means of quality control via nonsense-mediated mRNA decay (NMD). During pre-mRNA splicing, the exon-junction complex (EJC) is deposited upstream of exon-exon junctions (10). Generally, mRNAs containing premature termination codons (PTCs) are recognized as abnormal because during the first, or pioneer round of translation (11, 12), translating ribosomes do not strip off EJCs after the PTC (13). Aside from clear utility as a sensor for the NMD-critical pioneer round of translation, the TRICK method will doubtless find useful applications in other areas in which translational repression and/or bursts of localized translation control important processes such as long-term potentiation in neurons during learning (14) and disruption of RNA granule formation during viral infection (15). ■

#### REFERENCES AND NOTES

1. J. M. Halstead *et al.*, *Science* **347**, 1367 (2015).
2. A. R. Buxbaum *et al.*, *Nat. Rev. Mol. Cell Biol.* **16**, 95 (2015).
3. V. G. Allfrey, *Proc. Natl. Acad. Sci. U.S.A.* **40**, 881 (1954).
4. S. Apcher *et al.*, *Proc. Natl. Acad. Sci. U.S.A.* **110**, 17951 (2013).
5. A. David *et al.*, *J. Cell Biol.* **197**, 45 (2012).
6. J. E. Dahlberg, E. Lund, E. B. Goodwin, *RNA* **9**, 1 (2003).
7. V. Balagopal, R. Parker, *Curr. Opin. Cell Biol.* **21**, 403 (2009).
8. C. K. Damgaard, J. Lykke-Andersen, *Genes Dev.* **25**, 2057 (2011).
9. A. Ephrussi, R. Lehmann, *Nature* **358**, 387 (1992).
10. F. Lejeune, Y. Ishigaki, X. Li, L. E. Maquat, *EMBO J.* **21**, 3536 (2002).
11. Y. Ishigaki *et al.*, *Cell* **106**, 607 (2001).
12. L. E. Maquat, W. Y. Tarn, O. Isken, *Cell* **142**, 368 (2010).
13. M. W. Popp, L. E. Maquat, *Annu. Rev. Genet.* **47**, 139 (2013).
14. K. C. Martin *et al.*, *Curr. Opin. Neurobiol.* **10**, 587 (2000).
15. R. E. Lloyd *Wiley Interdiscip. Rev. RNA* **4**, 317 (2013).

#### ACKNOWLEDGMENTS

Research on NMD in the Maquat lab is supported by NIH grant R01 GM59614 (L.E.M.). M.W.P. is a Howard Hughes Medical Institute Fellow of the Damon Runyon Cancer Research Foundation (DRG-2119-12).

#### CLIMATE AND CONSERVATION

## Creating a safe operating space for iconic ecosystems

Manage local stressors to promote resilience to global change

By M. Scheffer<sup>1\*</sup>, S. Barrett<sup>2</sup>, S. R. Carpenter<sup>3</sup>, C. Folke<sup>4</sup>, A. J. Green<sup>5</sup>, M. Holmgren<sup>6</sup>, T. P. Hughes<sup>7</sup>, S. Kosten<sup>8</sup>, I. A. van de Leemput<sup>1</sup>, D. C. Nepstad<sup>9</sup>, E. H. van Nes<sup>1</sup>, E. T. H. M. Peeters<sup>1</sup>, B. Walker<sup>10</sup>

**A**lthough some ecosystem responses to climate change are gradual, many ecosystems react in highly nonlinear ways. They show little response until a threshold or tipping point is reached where even a small perturbation may trigger collapse into a state from which recovery is difficult (1). Increasing evidence shows that the critical climate level for such collapse may be altered by conditions that can be managed locally. These synergies between local stressors and climate change provide potential opportunities for proactive management. Although their clarity and scale make such local

**POLICY** approaches more conducive to action than global greenhouse gas management, crises in iconic UNESCO World Heritage sites illustrate that such stewardship is at risk of failing.

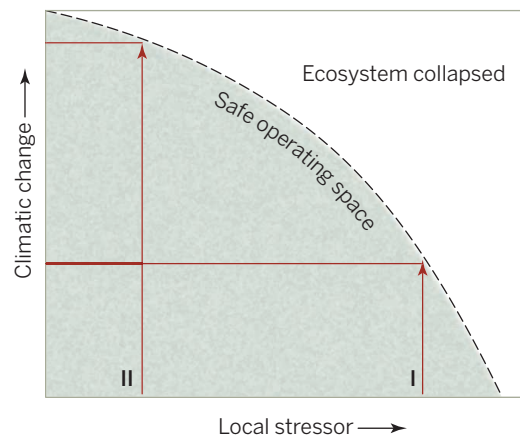
The term “safe operating space” frames the problem of managing our planet in terms of staying within acceptable levels or “boundaries” for global stressors (2). Uncertainty is accounted for by aiming to keep well on the safe side of such boundaries. The safe levels of different stressors at global scales are mostly considered independently. However, in ecosystems a safe level for one stressor is often strongly dependent on the level of other stressors. This implies that if such synergies are understood, local stressors may be effectively managed to enhance tolerance to global climate change (see first figure).

**LOCAL AND FEASIBLE.** The feasibility of managing the climate sensitivity of ecosystems is becoming increasingly evident. Obviously, local interventions are no panacea for the threats of climatic change. For example, melting of arctic sea ice with its far-reaching ecological consequences cannot be arrested by local management. However, ways of

building climate resilience are emerging for a variety of ecosystems, ranging from control of local sources of ocean acidification (3) to management of grazing pressure on dry ecosystems (4). We focus here on lakes, coral reefs, and tropical forests.

In lakes, warming and nutrient loading have similar effects on the likelihood that the ecosystem will tip into encroachment by floating plants or into dominance by toxic cyanobacteria (5). Experiments and field studies on different scales revealed intricate mechanisms that drive the synergy between effects of warming and nutrient load—e.g., boosted nutrient cycling—and shifts in the competitive advantage that favor small, rapidly reproducing fish species, cyanobacteria, and floating plants (5, 6). Although the synergy of climate and nutrient stressors implies double jeopardy to many wetlands, the good news is that reducing the nutrient load can compensate for the effects of warming. For example, data from lakes across continents and climate zones suggest that a reduction in nutrient concentrations by one-third can compensate for the effect of a 1°C increase in water temperature when it comes to the risk of cyanobacterial dominance (6).

In coral reefs, resilience depends strongly on locally manageable stressors such as fish-

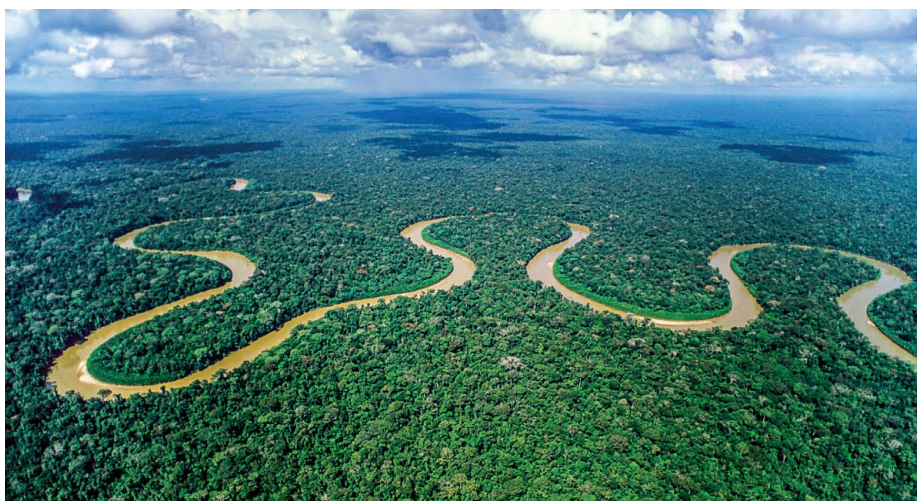


**Schematic representation of safe operating space.** In ecosystems at risk of collapse, safe boundaries for local stressors, such as harvest rates or pollution, often change with climate change. A local stressor that is currently at a safe level (I) needs to be adjusted to a lower value to keep the system within the safe operating space in a future climate (II).



ing pressure and water quality. For example, the takeover of most Caribbean reefs by seaweeds was triggered by sea-urchin mortality but was facilitated in many locations by high nutrient loading and overharvesting of fish functional groups that controlled the seaweeds (7). On the Great Barrier Reef, coral

recovery rates after the 1998 bleaching event were markedly suppressed by experimental exclusion of herbivorous fishes (8). Local conservation efforts can help in maintaining and enhancing resilience and in limiting longer-term damage from bleaching and other climate-related effects.



Examples of iconic ecosystems where climate change may trigger transitions to a different state. From top to bottom: the Doñana wetlands, the Amazon rainforest, and the Great Barrier Reef.

In tropical forests, resilience is under pressure from climate change as well as local stressors such as deforestation, logging, and fire (9). Forests become stressed by increases in temperature (10) and by greater rainfall variability (4). One important near-term risk from drought is a self-reinforcing shift to a contrasting fire-maintained state. Recent experiments confirm cascading effects of a decline in canopy cover, which favor invasion by flammable grasses (11). The removal of trees makes the forest more fire-prone, increasing the risk of further transition to open woodland in dry years (9, 11). In addition, there is a substantial positive feedback effect of forest cover on regional precipitation, implying that loss of forest contributes to overall reduction in rainfall (9). Thus, maintaining a critical mass of forested areas and preventing opening of the closed canopy structure are powerful tools to enhance the safe operating space of tropical forests in the face of rising drought risks.

**WORLD HERITAGE AT RISK.** Despite the solid scientific basis for managing climate resilience in such ecosystems, failure to do so is putting globally important ecosystems at risk. We highlight crises faced by three iconic World Heritage Areas (see second figure).

The Doñana wetlands in southern Spain provide the most important wintering site for waterfowl in Europe. They contain the largest temporary pond complex in Europe, with a diversity of amphibians and invertebrates. Despite the site's protected status, the marshes are threatened by eutrophication due to pollution and reduced flow of incoming streams, promoting toxic cyanobacterial blooms, and dominance by invasive floating plants that create anoxic conditions in the water. In addition, groundwater extraction for strawberry culture and beach tourism also has major effects (12). Little has been done to control these local stressors, leaving Doñana unnecessarily vulnerable to climate change. UNESCO has just rated this World Heritage Site as under "very high threat."

<sup>1</sup>Department of Aquatic Ecology and Water Quality Management, Wageningen University, NL-6700 AA Wageningen, Netherlands. <sup>2</sup>School of International and Public Affairs, Columbia University, New York, NY 10027, USA. <sup>3</sup>Center for Limnology, University of Wisconsin, Madison, WI 53706, USA. <sup>4</sup>Beijing Institute of Ecological Economics, Royal Swedish Academy of Sciences, and the Stockholm Resilience Center, Stockholm University, SE104 05 Stockholm, Sweden. <sup>5</sup>Estación Biológica de Doñana, EBD-CSIC, 41092 Sevilla, Spain. <sup>6</sup>Resource Ecology Group, Wageningen University, NL-6700 AA Wageningen, Netherlands. <sup>7</sup>Australian Research Council Centre of Excellence for Coral Reef Studies, James Cook University, Townsville, QLD 4811, Australia. <sup>8</sup>Aquatic Ecology and Environmental Biology, Radboud University Nijmegen, Institute of Water and Wetland Research, 6525 AJ Nijmegen, Netherlands. <sup>9</sup>Earth Innovation Institute, San Francisco, CA 94110, USA. <sup>10</sup>CSIRO Land and Water, Canberra, ACT 2601, Australia. <sup>11</sup>E-mail: marten.scheffer@wur.nl



The Great Barrier Reef is the largest coral system in the world. In response to multiple threats, fishing has been prohibited since 2004 over 33% of the Great Barrier Reef Marine Park, and efforts have begun to reduce runoff of nutrients, pesticides, herbicides, and sediments from land. However, these interventions may be too little, too late. Approximately half of the coral cover has been lost in recent decades (13), and the outlook is “poor, and declining,” with climate change, coastal development, and dredging as major future threats (14). The World Heritage Committee has warned that in the absence of a solid long-term plan, it would consider listing the reef as “in danger” in 2015 (15).

The Amazon rainforest is one of the world’s great biological treasures and a vital component of Earth’s climate system. Yet this ecosystem is under increasing pressure from climate change as well as local stressors such as logging and forest fire (9). Brazil has shown leadership by slowing down Amazon deforestation by 70% (16) and by creating the largest protected area (PA) network in the world. Yet these successes are now being partially undermined by major infrastructure and natural resource extraction projects and by shifts in legislation (17).

**FRAMING FOR ACTION.** The evidence we have for enhancing climate resilience of ecosystems places direct responsibility on governments to ensure implementation. However, investment will only happen if costs of refraining from activities that undermine resilience are distributed in ways that lead to effective action. Realizing such incentive schedules may be challenging. However, there are three specific reasons that building a safe operating space for ecosystems by controlling local stressors is more conducive to immediate action than global control of greenhouse gases.

*From global to local commons.* Potential incentives for local protection are much stronger than those to supply the global public good of abating greenhouse gas emissions (18), for the same reason that countries tend to favor adaptation over mitigation. Mitigation requires global collective action and is vulnerable to free riding, whereas adaptation can be done unilaterally, with benefits accruing almost exclusively to the country doing the adaptation. However, iconic ecosystems also provide a global public good. This is why they are on the World Heritage list in the first place. In some cases, the local interventions can result in substantial global mitigation. For instance, slowing down Amazon deforestation made Brazil a global leader in climate change mitigation (16).

*From high to low uncertainty.* Perceived uncertainty has often paralyzed policy (19), and experimental evidence suggests that uncertainty about climate change tipping points undermines efforts to avoid crossing a dangerous threshold (20). There is less uncertainty on the ecosystem level than on the global level when it comes to effects of management options.

*From negative to positive framing.* Gloom-and-doom perceptions may backfire to block action. Terms such as “extreme events” and “catastrophic transitions” may express the urgency of the matter. However, social experiments reveal that accounts of disastrous future effects of climate change can invoke cognitive dissonance that causes many people to disbelieve climate change altogether. This response disappears if a feasible approach to take action and abate the problems is presented simultaneously (21). A positive, action-oriented framing of a safe operating space for the world’s iconic ecosystems may help stimulate societal consensus that climate change is real and should be addressed. ■

#### REFERENCES AND NOTES

1. M. Scheffer, S. Carpenter, J. A. Foley, C. Folke, B. Walker, *Nature* **413**, 591 (2001).
2. J. Rockström *et al.*, *Ecol. Soc.* **14**, 32 (2009).
3. R. P. Kelly *et al.*, *Science* **332**, 1036 (2011).
4. M. Holmgren, M. Hirota, E. H. Van Nes, M. Scheffer, *Nat. Clim. Change* **3**, 755 (2013).
5. B. Moss *et al.*, *Inland Waters* **1**, 101 (2011).
6. S. Kosten *et al.*, *Glob. Change Biol.* **18**, 118 (2012).
7. T. P. Hughes *et al.*, *Science* **301**, 929 (2003).
8. T. P. Hughes *et al.*, *Curr. Biol.* **17**, 360 (2007).
9. Y. Malhi *et al.*, *Science* **319**, 169 (2008).
10. K. J. Feeley, S. Joseph Wright, M. N. Nur Supardi, A. R. Kassim, S. J. Davies, *Ecol. Lett.* **10**, 461 (2007).
11. P. M. Brando *et al.*, *Proc. Natl. Acad. Sci. U.S.A.* **111**, 6347 (2014).
12. C. Guardiola-Albert, C. R. Jackson, *Wetlands* **31**, 907 (2011).
13. D. R. Bellwood, T. P. Hughes, C. Folke, M. Nyström, *Nature* **429**, 827 (2004).
14. *A Great Barrier Reef Marine Park, Great Barrier Reef Outlook Report 2014: In Brief* (Great Barrier Reef Marine Park Authority, Townsville, Queensland, 2014).
15. D. Normile, L. Dayton, *Science* **346**, 683 (2014).
16. D. Nepstad *et al.*, *Science* **344**, 1118 (2014).
17. J. Ferreira *et al.*, *Science* **346**, 706 (2014).
18. E. Ostrom, J. Burger, C. B. Field, R. B. Norgaard, D. Policansky, *Science* **284**, 278 (1999).
19. N. Oreskes, E. M. Conway, *Merchants of Doubt: How a Handful of Scientists Obscured the Truth on Issues from Tobacco Smoke to Global Warming* (Bloomsbury Press, New York, 2010).
20. S. Barrett, A. Dannenberg, *Nat. Clim. Change* **4**, 36 (2014).
21. M. Feinberg, R. Willer, *Psychol. Sci.* **22**, 34 (2011).

#### ACKNOWLEDGMENTS

M.S. is supported by a European Research Council advanced grant and Spinoza award. C.F. is supported by the Stellenbosch Institute for Advanced Study. S.R.C.’s research is supported by NSF. A.J.G. was supported by a WIMEK research fellowship and S.K. by Nederlandse Organisatie voor Wetenschappelijk Onderzoek (NWO) Veni grant 86312012. M.S., C.F., and S.R.C. are also at the South American Institute for Resilience and Sustainability Studies. This work was carried out under the program of the Netherlands Earth System Science Centre (NESSC).

10.1126/science.aaa3769

## STEM CELLS

# Holding your breath for longevity

A nutrient-sensing protein is important for the health of hematopoietic stem cells during aging

By Alejandro Ocampo and Juan Carlos Izpisua Belmonte

**A**ging is a complex process. Progressive molecular changes lead to a decline in the ability of living beings to maintain homeostasis and overcome cellular stress, protein damage, and disease (1). At the organismal level, stem cells play a fundamental role in maintaining tissue integrity, and their functional and proliferative exhaustion is a major cause of aging (2). Hematopoietic stem cells, which reside in the bone marrow and give rise to all blood cell types, are a favored model for studying stem cell aging.

*“...decline of stem cell function with age due to intrinsic factors...and extrinsic factors...could potentially be reverted...”*

However, the exact molecular mechanisms underlying their aging remain unknown. Sirtuins, a family of nutrient-sensing proteins (SIRT1 to SIRT7) that regulate gene expression and protein function in mammalian cells, orchestrate multiple pathways that are associated with age-related processes and longevity. On page 1374 of this issue, Mohrin *et al.* (3) connect SIRT7 to a metabolic checkpoint that controls aging in hematopoietic stem cells.

SIRT7 is a nicotinamide adenine dinucleotide (NAD)-dependent deacetylase that senses the nutrient status of a cell and adjusts cell function accordingly. Thus, under nutrient deprivation, SIRT7 alters transcription to reduce cell metabolism and decrease cell growth, thereby promoting cell survival. By analyzing all proteins that



# Faith in science

The complex relationship between science and religion in Victorian Britain

By Crosbie Smith

**B**ut I should be very sorry if an interpretation founded on a most conjectural scientific hypothesis were to get fastened to the text in Genesis," wrote the devout Christian physicist James Clerk Maxwell to a friend in 1876. "The rate of change of scientific hypothesis is naturally much more rapid than that of Biblical interpretations, so that if an interpretation is founded on such a hypothesis, it may help to keep the hypothesis above ground long after it ought to be buried and forgotten." Maxwell's words were characteristically subtle. His first sentence suggests that his major concern was in protecting the integrity of Biblical scriptures, implying that serious damage could occur should these texts be linked to speculative scientific hypotheses that subsequently proved untenable. His second sentence, however, strongly suggests that any such bonding of conjectural scientific hypothesis to scriptural text would actually damage the progress of science.

In *Huxley's Church and Maxwell's Demon*, Matthew Stanley explores the historical and conceptual nuances of the complex relationship of science and religion in the late Victorian period. Stanley uses the contrasting values of the "genuinely religious" Maxwell and his contemporary—Thomas Henry Huxley, the agnostic biologist who was known as "Darwin's bulldog" for his advocacy of Darwin's theory of evolution—to illustrate the transition from theistic to naturalistic science.

Readers, however, may question the extent to which the rather unassuming and ever-subtle Maxwell can be portrayed as a representative member of the theistic camp. Indeed, the book's very title reflects this inherent problem: Huxley's "church" facetiously refers to the naturalistic canons

widely enunciated in direct opposition to orthodox Christianity, but Maxwell's "demon" refers to the physicist's largely private struggle to elucidate the concept of irreversibility that stood at the core of the new second law of thermodynamics.

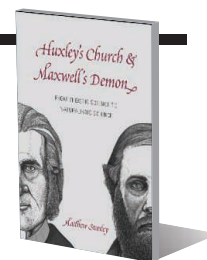
With a long line of mainstream scientific practitioners, including Isaac Newton and Robert Boyle, theistic science, in recent decades, has been much investigated by historians. Natural philosophers regarded the laws of nature as divinely established for the orderly governance of the world, sustained as uniform and unchangeable, except by God's will. Rightly undertaken in a spirit of humility, scientific investigation was believed to reveal these laws to humankind, along with the manifold benefits that such knowledge of the natural order could provide. Thus, the uniformity of nature, resting upon faith in a divine being who never acted arbitrarily, made possible the advance of human science. Stanley argues that traditional theistic science is radically different from the present-day theory of "Intelligent Design," which, he emphasizes, lies outside mainstream science and refuses to acknowledge methodological principles such as the uniformity of nature and the provisional character of scientific knowledge.

Challenging the values of theistic science, Thomas Huxley represented a new and ambitious generation of scientists who interpreted uniformity as naturalistic rather than theistic. According to Stanley, Huxley believed that "one could only assume uniformity if there was no active deity able to disrupt natural processes." Huxley had rich cultural resources on which to draw to challenge the established views. For example, Charles Lyell's *Principles of Geology* offered a compelling model that explained Earth's history using only observable agents such as water and heat (1).

Stanley's book draws upon a wealth of recent scholarship on Victorian science and religion. It is also extremely well grounded in a variety of primary texts, including private correspondence, public lectures, and

**Huxley's Church and Maxwell's Demon: From Theistic Science to Naturalistic Science**

Matthew Stanley  
University of Chicago Press, 2014. 372 pp.



published scientific papers. Its primary goal—to demonstrate how the scientific enterprise gradually shifted from a theistic to a naturalistic approach—is impressively pursued. However, the book is not without flaws. For example, to identify Maxwell as an aristocrat, as Stanley does early in the book, is somewhat misleading. With no hereditary

title, the "thick-accented Scot" scarcely fits the image of a fully fledged member of the British aristocracy. Stanley also tends to characterize Maxwell as "a fairly conservative evangelical" without placing him in opposition to what the British historian Boyd Hilton calls the "extreme evangelicals," most of whom rejected uniformity in favor of arbitrary divine action and retribution (2). Finally, more attention might have been given to the difference between formal and informal communications about theistic science. Although informed by religious beliefs, natural philosophers tended to exclude religious and political claims from their published work, while often speaking freely on such matters in public lectures, sermons, and, of course, private letters.

Nevertheless, Stanley has produced a book that will challenge the general reader, stimulate academic discussion, and contribute much to understanding the subtleties and diversities of past and present scientific practice and religious debate.

## REFERENCES

1. C. Lyell, *The Principles of Geology: Being an Attempt to Explain the Former Changes of the Earth's Surface, by Reference to Causes now in Operation* (3 volumes) (John Murray, London, 1830–1833).
2. B. Hilton, *The Age of Atonement: The Influence of Evangelicalism on Social and Economic Thought, 1785–1865* (Oxford Univ. Press, Oxford, 1992).

The reviewer is at the University of Kent, Canterbury CT2 7NZ, UK. E-mail: c.smith@kent.ac.uk



The world's first lab-grown burger debuted in 2013 with a hefty €250,000 price tag.

## GASTRONOMY

# Food futurism

Today's technologies, tomorrow's dinner table

By Job Ubbink

In the surge of recent books dealing with our food, our diet, and the way we cook, two stand out for highlighting radical, modernist avenues toward the future of food. *The In Vitro Meat Cookbook* and *Note-by-Note Cooking* are each based on simple and straightforward ideas. The first focuses on cooking with meat grown in tissue culture, whereas the latter book deals with food prepared from pure ingredients, such as hydrocolloids, emulsifiers, and flavor compounds (the resulting tastes and flavors are referred to as “notes”). In content and presentation, the two books are very different; however, the central idea of each is developed in the context of established and experimental scientific and technological approaches. Both, in addition, discuss aspects related to culinary creation, our emotional and cultural interaction with food, and food sustainability.

*The In Vitro Meat Cookbook* is an artfully designed book, the backbone of which consists of 45 illustrated recipes using meat that might one day be grown in a bioreactor. The recipes are interspersed with chapters on meat production and consumption, animal welfare, and technological issues.

Many of the dishes presented in *The In Vitro Meat Cookbook* are enticing, at least for the meat lover, although it is rather optimistically argued that if animals were removed from the equation, even vegetarians could now indulge in meat dishes. Would you not like to sink your teeth into a good portion of

in vitro kebab or have a bite of “roast raptor”? Or what about trying the slippery, wriggling “throat tickler”? This synthetic sea anemone, like many of the meats featured in the book, is unfortunately relegated to the distant future. Not all in vitro meats are that remote, however, as the authors acknowledge with a recipe for the first in vitro hamburger, created in 2013 by a team of researchers at Maastricht University.

An important element of the book is the essay “Growing the Future of Meat,” which tones down the generally upbeat message by raising some key issues. One problem of in vitro meat is that, in addition to animal stem cells, fetal bovine serum is needed to efficiently culture animal cells. This should not be an issue, as it is likely that with advances in biotechnology, this serum can be replaced with a synthetic medium. More serious are the risks of large-scale culturing of animal tissue. Who would like to be responsible for the first outbreak of food poisoning due to infection of a meat cultivator, for example? The authors also raise the point that the negative consequences of novel technologies are usually underestimated and often cannot be foreseen and encourage us to adopt a broad approach toward the future of our food, encompassing established as well as novel technologies.

*Note-by-Note Cooking* is a personal and occasionally idiosyncratic manifesto on the creation of dishes from pure ingredients and includes a discussion of food properties such as consistency, taste, smell, and color from a physical-chemical perspective. The central premise of the book is highly relevant for our food future, both in industrial food manufacturing and in innovative restaurant cooking. In each of these venues, there is a trend toward the use of essentially pure ingredients, albeit almost always in combination with traditional ingredients. *Note-by-Note Cooking* extrapolates on this trend and provides it with a foundation on which to build. Ideally, this will help to bring the use of these “pure” ingredients from the industrial imitation of traditional foods to overt roles

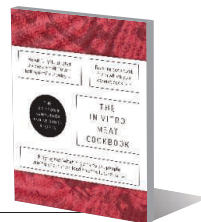
## Note-by-Note Cooking The Future of Food

Hervé This  
Columbia University Press,  
2014. 286 pp.



## The In Vitro Meat Cookbook The Lab Grown Hamburger and 45 Other Recipes

Koert van Mensvoort and  
Hendrik-Jan Grievink  
BIS, 2014. 192 pp.



in the creation of truly innovative foods.

*Note-by-Note Cooking* is marred by a significant number of sloppy formulations and inadequate explanations. Meats, vegetables, and fruits are not gels but tissues, for example. Implicitly using but not explaining Avogadro's number and discussing the physical and chemical properties of food constituents such as proteins and carbohydrates without invoking the concept of hydrogen bonding are also unsatisfactory. The lack of scientific rigor is a missed opportunity, as carefully formulated descriptions of the fundamental concepts are essential for a true interaction between scientists and chefs. Moreover, “note-by-note” recipes only figure in a brief appendix and are not truly integrated into the book's narrative.

Aspects of food sustainability are discussed in both books—but unconvincingly because quantitative analyses are lacking. In *The In Vitro Meat Cookbook*, the authors loosely claim that their approach promotes sustainability of meat production because the energy input of in vitro meat is lower than that of beef but still higher than chicken, while greenhouse gas emissions are reduced. In *Note-by-Note Cooking*, the effect of cooking with pure compounds on food sustainability is postulated but not substantiated. Given the need to first isolate individual compounds from complex ingredient sources and then reconstitute them in new combinations, this approach does not appear to be very sustainable, as it implies an entropic penalty of truly colossal dimensions.

Both books capture the essence of important technological developments currently pervading the food field, albeit in a hyperbolic way resembling the futuristic art of the early 20th century. Although it is unlikely that the ingredients, dishes, and cooking styles as presented in *The In Vitro Meat Cookbook* and in *Note-by-Note Cooking* will come to our kitchens exactly as described, one can be sure that important aspects will affect our daily food sooner rather than later.

The reviewer is at Food Concept & Physical Design, “The Mill,” CH-4112 Flüh, Switzerland. E-mail: job.ubbink@themill.ch



## LETTERS

Edited by Jennifer Sills

## Drones: Balancing risk and potential

WE AGREE WITH D. Shultz ("Game of drones," News, special section on the End of Privacy, 30 January, p. 497) that "[t]he opportunities—and potential violations of privacy—seem endless" from the technology of unmanned aircraft systems (UAS). Although implementation of privacy laws and Federal Aviation Administration (FAA) flight restrictions regarding UAS may seemingly protect the public (1), they may also disrupt industrial UAS applications. All new technologies carry risks; the key is how we can better manage risks and establish best practices for operating within each industry.

Power distribution companies have been developing UAS to inspect power lines and power plant facilities commonly located in public regions, reducing the need to place their employees in high-risk situations (2). The use of drones greatly reduces the personal risk associated with power line inspections, allowing regular inspections to be performed more efficiently while reducing the number of major power shortages associated with normal wear and tear in power utilities. Unregulated privacy laws will stifle these applications, potentially halting related technological advances (3).

Many other approaches to increase privacy protection are possible. DJI Innovations Inc., a leader in commercial drones, is implementing an "Opt-Out" program that covers airports and government-regulated sensitive areas (4). Drone Deploy, a third-party organization, is developing an international database for the public to register their home/property

as a no-fly zone. Upon the next drone firmware and software update, the drone will be prevented from flying over areas listed in the database (5).

**T. Stan Gregory,<sup>1\*</sup> Zion Tsz Ho Tse,<sup>1\*†</sup> Dexter Lewis<sup>2</sup>**

<sup>1</sup>College of Engineering, University of Georgia, Athens, GA 30602, USA. <sup>2</sup>Southern Company Services, Inc., Birmingham, AL 35291, USA.

\*The authors contributed equally to this work.

†Corresponding author. E-mail: ziontse@uga.edu

### REFERENCES

1. G. S. McNeal, "What you need to know about the Federal Government's drone privacy rules," *Forbes* (2015); [www.forbes.com/sites/gregorymcneal/2015/02/15/the-drones-are-coming-heres-what-president-obama-thinks-about-privacy](http://www.forbes.com/sites/gregorymcneal/2015/02/15/the-drones-are-coming-heres-what-president-obama-thinks-about-privacy).
2. J. I. Larrauri, G. Sorrosal, M. González, "Automatic system for overhead power line inspection using an Unmanned Aerial Vehicle—RELIFO project," in *2013 International Conference on Unmanned Aircraft Systems (ICUAS)* (IEEE, Atlanta, GA, 2013), pp. 244–252.
3. B. Wolfgang, "FAA's failure to regulate U.S. drone boom creates climate of confusion," *Washington Times* (2015); [www.washingtontimes.com/news/2015/jan/6/faa-failure-to-regulate-us-drone-boom-creates-clim/?page=all](http://www.washingtontimes.com/news/2015/jan/6/faa-failure-to-regulate-us-drone-boom-creates-clim/?page=all).
4. DJI Innovations, No Fly Zones ([www.dji.com/fly-safe/category-mc](http://www.dji.com/fly-safe/category-mc)).
5. J. Barrie, "You can now ban drones from flying over your home and looking into your window," *Business Insider* (2015); [www.businessinsider.com/noflyzone-prevents-drones-from-flying-over-individual-property-2015-2](http://www.businessinsider.com/noflyzone-prevents-drones-from-flying-over-individual-property-2015-2).

## Cyber-attack risk low for medical devices

WE CONCUR WITH D. Clery ("Could your pacemaker be hackable?," News, special section on The End of Privacy, 30 January, p. 499) that the U.S. Food and Drug Administration (FDA) has focused on reliability, safety, and efficacy for specific medical devices, with no targeted focus on protecting against malicious cyber attacks. Although cybersecurity is a legitimate concern, sensationalized fictional entertainment like the television series "Homeland" may exaggerate the real risks.

Health care practitioners, industry,

and insurance payers follow regulations from the FDA, Department of Health and Human Services, Centers for Medicare and Medicaid Services, and the Code of Federal Regulations (CFR). Cybersecurity, as part of the FDA's mandate for risk profile assessment (1, 2), should receive attention from device manufacturers, given that vulnerabilities could potentially lead to downstream issues with CFR or FDA guidelines (3).

Despite reports about their potential cybersecurity vulnerability (4), medical devices are rarely accessible for hackers to attack. Also, patients and doctors can always disable and overwrite the remote control option. Medical devices requiring occasional Internet access are rarely life-supporting equipment. Patient data is encrypted and transferred through a secured network with redundant securities and risk mitigation strategies (5).

Cybersecurity is a theoretical issue in interventional devices such as surgical robotics. The robotic da Vinci surgical systems are integrated into U.S. medical practice but are rarely connected to unsecured networks. Nevertheless, vulnerabilities may exist despite FDA clearance, as the "FDA allows devices to be marketed when the probable benefits to patients outweigh the probable risks" (1). The FDA assesses the incremental risk-benefit ratio and decides whether a new device is cleared, using the current technology as the standard. Risk profiling and failure modes are identified and defined by the FDA routinely, and tangible cybersecurity risks should perhaps be factored into that assessment, even if the risk is small.

**Zion Tsz Ho Tse,<sup>1\*†</sup> Sheng Xu,<sup>2†</sup> Isaac Chun-Hai Fung,<sup>3</sup> Bradford J. Wood<sup>2</sup>**

<sup>1</sup>College of Engineering, The University of Georgia, Athens, GA 30602, USA. <sup>2</sup>Center for Interventional Oncology, National Institutes of Health, Bethesda, MD 20892, USA. <sup>3</sup>Department of Epidemiology, Jiann-Ping Hsu College of Public Health, Georgia Southern University, Statesboro, GA 30460, USA.

\*Corresponding author. E-mail: ziontse@uga.edu

†These authors contributed equally to this work.

### REFERENCES AND NOTES

1. FDA, Medical Devices, Cybersecurity ([www.fda.gov/MedicalDevices/ProductsandMedicalProcedures/ConnectedHealth/ucm373213.htm](http://www.fda.gov/MedicalDevices/ProductsandMedicalProcedures/ConnectedHealth/ucm373213.htm)).
2. FDA, "Content of premarket submissions for management of cybersecurity in medical devices," *Federal Register, The Daily Journal of the United States Government* (2014); [www.federalregister.gov/articles/2014/10/02/2014-23457/content-of-premarket-submissions-for-management-of-cybersecurity-in-medical-devices-guidance-for](http://www.federalregister.gov/articles/2014/10/02/2014-23457/content-of-premarket-submissions-for-management-of-cybersecurity-in-medical-devices-guidance-for).
3. J. Hsu, "Feds probe cybersecurity dangers in medical devices," *IEEE Spectrum* (2014); <http://spectrum.ieee.org/tech-talk/biomedical/devices/feds-probe-cybersecurity-dangers-in-medical-devices>.
4. Industrial Control Systems Cyber Emergency Response Team, "Medical devices hard-coded passwords" (2013); <https://ics-cert.us-cert.gov/alerts/ICS-ALERT-13-164-01>.
5. U.S. Department of Health and Human Services, Health Insurance Portability and Accountability Act (HIPAA).



PHOTO: © MIKE SEGAR/REUTERS/CORBIS

Administrative Simplification Statute and Rules (2015); [www.hhs.gov/ocr/privacy/hipaa/administrative/index.html](http://www.hhs.gov/ocr/privacy/hipaa/administrative/index.html).  
6. Disclaimer/Acknowledgments: The views and opinions of authors expressed herein do not necessarily state or reflect those of the U.S. Government nor does it constitute policy, endorsement, or recommendation by the U.S. Government or National Institutes of Health (NIH). Reference U.S. Code of Federal Regulations or U.S. Food and Drug Administration for further information.

# Regulatory hurdles for agriculture GMOs

WE HAVE BEEN engaged for decades in genetic engineering and genome editing of organisms of agricultural importance. However, research on food organisms is suffering because of a failure of regulatory agencies. Since the first introduction of genetically modified germplines of animals in 1981 (1–3), and plants 2 years later (4), U.S. regulators have failed to approve a single genetically modified animal of agricultural importance (5), and most new crop varieties do not make it through governmental review (6). This reluctance to approve new products is not based on scientifically sound analysis. Rather, it is largely due to pandering by officials to various

pressure groups and politicians.  
New genetic technologies have revolutionized our ability to make precise changes in genomes that will enable the survival, increased yields, and improved nutritional value of plants and animals raised in diverse microenvironments that currently exist and are changing in response to climatic changes. These alterations can be constructed and evaluated at a genome level for about \$200,000 and field tested for under \$10 million each (7). Based on the only genetically modified animal that has gone through full regulatory review, the costs can be more than \$60 million (8) and include years of legal wrangling. These are expenses that only a few large corporations can afford, and then only for products with enormous sales potential. As a result, many of the most effective products that agricultural research can develop never make it to the consumer.  
Another, pernicious result of the regulatory bottleneck is on young investigators who realize this problem and train in other areas. Regulators and political officials must recognize that genetically modified products are safe, well characterized, and capable of addressing substantial national and international needs (9, 10). Taxpayers

have already paid for the research and should enjoy the benefits. It is a sad but inescapable reality that the government is running a bait-and-switch program, which citizens do not deserve.

**Perry Hackett<sup>1\*</sup> and Dana Carroll<sup>2</sup>**

<sup>1</sup>Department of Genetics, Cell Biology, and Development, Center for Genome Engineering, University of Minnesota, Minneapolis, MN 55455, USA.  
<sup>2</sup>Department of Biochemistry, School of Medicine, University of Utah, Salt Lake City, UT 84112, USA.

\*Corresponding author. E-mail: [hacke004@umn.edu](mailto:hacke004@umn.edu)

## REFERENCES AND NOTES

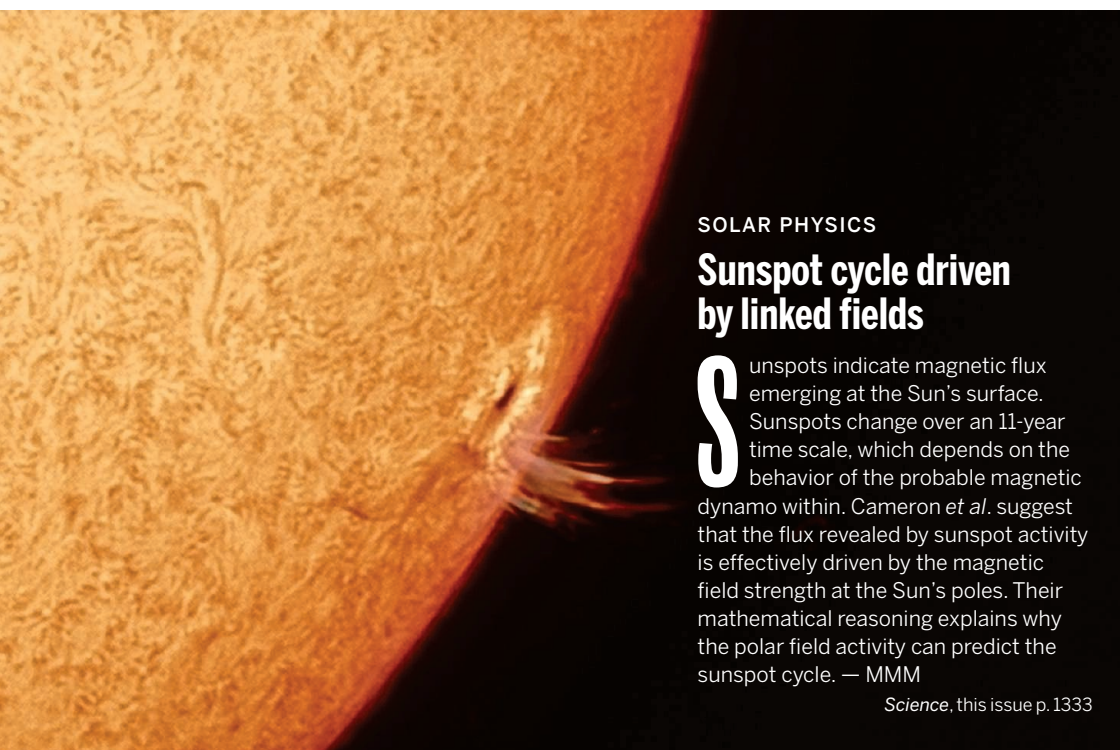
1. J. W. Gordon, F. H. Ruddle, *Science* **214**, 1244 (1981).
2. F. Costantini, E. Lacy, *Nature* **294**, 92 (1981).
3. R. Brinster *et al.*, *Cell* **27**, 223 (1981).
4. R. T. Fraley *et al.*, *Proc. Natl. Acad. Sci. U.S.A.* **80**, 4803 (1983).
5. A few genetically modified animals have been approved for purposes other than agriculture. For example, genetically modified goats, approved in 2009 ([www.gpo.gov/fdsys/pkg/FR-2009-02-11/html/E9-2881.htm](http://www.gpo.gov/fdsys/pkg/FR-2009-02-11/html/E9-2881.htm)), produce anti-thrombin in their milk, which is isolated and used as a medicine to treat humans. GLOFISH, which exhibit strong expression of enhanced fluorescent protein genes, are tropical aquarium fish that are not used for food purposes and do not pose any threat to the food supply ([www.fda.gov/AnimalVeterinary/DevelopmentApprovalProcess/GeneticEngineering/GeneticallyEngineeredAnimals/ucm161437.htm](http://www.fda.gov/AnimalVeterinary/DevelopmentApprovalProcess/GeneticEngineering/GeneticallyEngineeredAnimals/ucm161437.htm)).
6. J. K. Miller, K. J. Bradford, *Nat. Biotechnol.* **28**, 1012 (2010).
7. W. Tan *et al.*, *Proc. Natl. Acad. Sci. U.S.A.* **110**, 16526 (2013).
8. H. Ledford, *Nature* **497**, 17 (2013).
9. L. DeFrancesco, *Nat. Biotech.* **31**, 794 (2013).
10. A. L. Van Eenennaam, A. E. Young, *J. Anim. Sci.* **92**, 4255 (2014).





## IN SCIENCE JOURNALS

Edited by Stella Hurtley



### SOLAR PHYSICS

## Sunspot cycle driven by linked fields

**S**unspots indicate magnetic flux emerging at the Sun's surface. Sunspots change over an 11-year time scale, which depends on the behavior of the probable magnetic dynamo within. Cameron *et al.* suggest that the flux revealed by sunspot activity is effectively driven by the magnetic field strength at the Sun's poles. Their mathematical reasoning explains why the polar field activity can predict the sunspot cycle. — MMM

*Science*, this issue p. 1333

A sunspot emerges at the solar surface

### MICELLE ASSEMBLY

## Cylindrical polymer micelles pack in 3D

When you control chemistry, solvents, temperature, and concentration, surfactants and block copolymers will readily assemble into micelles, rods, and other structures. Qiu *et al.* take this to new lengths through precise selection of longer polymer blocks that self-assemble through a crystallization process (see the Perspective by Lee *et al.*). They chose polymer blocks that were either hydrophobic or polar and used miscible solvents that were each ideal for only one of the blocks. Their triblock micelles generated a wide variety of stable three-dimensional

superstructures through side-by-side stacking and end-to-end intermicellar association. — MSL

*Science*, this issue p. 1329;

see also p. 1310

### STEM CELL AGING

## Keeping stem cells in tip top condition

Stem cells are important in the maintenance and growth of tissues. For the health of the organism as a whole, it is important that only healthy stem cells be used. Mohrin *et al.* elucidated a regulatory branch of the mitochondrial unfolded protein response that is coupled to cellular energy metabolism and proliferation in stem cells

(see the Perspective by Ocampo and Belmonte). Mitochondrial protein folding stress triggered a metabolic checkpoint that regulates the cell cycle. Deregulation of this pathway interfered with stem cell quiescence and compromised regenerative function. — SMH

*Science*, this issue p. 1374;

see also p. 1319

### EPILEPSY TREATMENT

## Targeting metabolism to tackle seizures

About 1% of us suffer from epilepsy. Unfortunately, presently available drugs do not work for a third of epileptic patients. Sada *et al.* wanted to

develop compounds to treat drug-resistant epilepsy (see the Perspective by Scharfman). They focused on a metabolic pathway in the brain, the astrocyte-neuron lactate shuttle. They found that lactate dehydrogenase, a key molecule in nerve cell metabolism, controls brain excitability. Searching for a substance that selectively targets this molecule, they found a potential anti-epileptic drug that strongly suppressed drug-resistant epilepsy in an animal model. — PRS

*Science*, this issue p. 1362;

see also p. 1312

### CRYSTAL GROWTH

## From iron clusters to iron mineral

Growing a mineral out of solution, either in the lab or in nature, requires the assembly of atoms or clusters of ions. The structure of some common iron oxides hints that tiny iron-oxygen clusters may serve as mineral building blocks, but isolating these often unstable clusters is challenging. Sadeghi *et al.* not only isolated but were able to control the growth and dissolution of an iron-oxygen cluster that is a likely precursor to the most common iron oxide mineral, ferrihydrite. — NW

*Science*, this issue p. 1359

### CONSERVATION ECOLOGY

## Habitat fragmentation reduces biodiversity

The destruction of natural habits and encroachment by human activities lead to a loss of biodiversity and fragmented



Ongoing deforestation in the Brazilian rainforest

ecosystems. However, ecologists have long argued about the contribution of fragmentation to the loss of biodiversity. Haddad *et al.* synthesized a diverse set of studies of the impacts of habitat fragmentation that together covered multiple biomes over five continents and nearly four decades. Habitat fragmentation did indeed lower biodiversity of diverse species by around 50% within a few decades. Furthermore, 70% of the world's forested areas are close enough to human activity for biodiversity to be threatened by fragmentation. — BJP

*Sci. Adv.* 10.1126/sciadv.1500052 (2015).

## PALEOANTHROPOLOGY

### Finding *Homo* nearly 3 million years ago

The fossil record of humans is notoriously patchy and incomplete. Even so, skeletal remains and artifacts unearthed in Africa in recent decades have done much to illuminate human evolution. But what is the origin of the genus *Homo*? Villmoare *et al.* found a fossil mandible and teeth from the Afar region in Ethiopia. The find extends the record of recognizable *Homo* by at least half a million years, to almost 2.8 million years ago. The morphological traits of the fossil align more closely with *Homo* than with any other hominid genus. DiMaggio *et al.* confirm the ancient date of the site and suggest that these early humans lived in a setting that was more open and arid than previously thought. — AMS

*Science*, this issue p. 1352, p. 1355

## IMMUNOLOGY

### Limiting allergic responses with B cells

Although most immunological B cells promote immune responses, some B cells secrete the anti-inflammatory cytokine interleukin-10 (IL-10) and have immunosuppressive properties. Kim *et al.* found that these B cells inhibited the activation of mast cells, immune cells that are critical regulators of allergic reactions. Mice lacking these special B cells had more severe symptoms of anaphylaxis. Mast cell inhibition required physical contact with the B cells, which stimulated the B cells to produce more IL-10. Thus, IL-10-producing B cells might provide a therapeutic target for treating allergic diseases. — JFF

*Sci. Signal.* **8**, ra28 (2015).

## APPLIED OPTICS

### Color correcting planar optics

The functionality of many bulk optical elements can now be replaced by specially designed structures fabricated in thin films. This planar optics approach, however, has generally been applicable to only a narrow band of wavelengths. Aieta *et al.* show that chromatic dispersion, or color dependence, can be compensated for by the judicious design of the surface. The results demonstrate a general approach for the fabrication of broadband and lightweight optical elements that can be engineered into planar thin films. — ISO

*Science*, this issue p. 1342

## IN OTHER JOURNALS

Edited by **Kristen Mueller**  
and **Jesse Smith**

## ELECTROCHEMISTRY

### Silver's salty twist on water splitting

When plants split water during photosynthesis, they expel oxygen as a by-product. Ironically, it's this oxygen-generating step that's also proving the most difficult to optimize in artificial photosynthetic schemes, where the practical goal is simply to release the oxygen while accumulating hydrogen for fuel. Du *et al.* explore an alternative scheme, whereby the electrons to make the hydrogen come from chloride ions—already abundant in seawater—instead of other water molecules. Specifically, they show that dissolved silver ions act as efficient electrocatalysts for chloride oxidation, provided that the chloride is present at a high enough concentration to form (AgCl<sub>2</sub>)<sup>-</sup> and (AgCl<sub>3</sub>)<sup>2-</sup> ions, both of which are more soluble and more reactive than AgCl. — JSY

*J. Am. Chem. Soc.* 10.1021/jacs.5b00037 (2015).

## PALEOECOLOGY

### Plant community structure through time

A wide variety of biotic and abiotic factors controls the abundance and biomass of plant species in ecological communities over time. Although challenging to tease apart, doing so may help scientists to better understand the effects of climate change on various ecosystems. Jeffers *et al.* combined analysis of fossil pollen records, isotopic analysis, paleotemperature reconstruction, and population modeling to study the factors that influenced the structure of tree communities in Scotland 12,700 to 5200 years ago. For most of the species in the community, interactions between plants controlled their abundance, more than soil nitrogen availability or growing-season temperature. — AMS

*J. Ecol.* **103**, 459 (2015).

## NOSOCOMIAL INFECTION

### No clear bacterial culprit for NEC

Of all the obstacles faced by premature infants, necrotizing enterocolitis (NEC) is a particularly scary one. The disease kills developing intestinal tissues and sometimes the infants themselves. Scientists still don't know what causes NEC, but because the disease responds to antibiotics, they suspect that a contagious bacterium may be to blame. Raveh-Sadka *et al.* used a metagenomics approach to identify the microbes present in premature hospitalized infants during a NEC outbreak. They found that these babies shared very few bacterial strains, suggesting that no single bacterium caused the outbreak. Although this indicates that hospitals have good barriers in place to stop the spread of dangerous bacteria in these fragile infants, the cause of NEC remains a mystery. — KLM

*eLife* **4**, e05477 (2015).



PHOTO: © PHOTOSHOT HOLDINGS LTD / ALAMY



## AGING

### DNA mutations do not age yeast

The molecular basis of aging—just what it is that wears out and causes the functional decline of an aged cell or organism—remains unclear. In hope of better understanding this, Kaya *et al.* monitored individual yeast cells and sequenced their DNA to test whether accumulated DNA mutations are a cause of replicative aging in yeast. The number of daughter cells produced before a mother yeast cell dies defines the replicative life span of the mother cell. But the cells accumulated only 0.4 mutations over the life span of an average cell. Thus, at least in yeast, DNA mutations do not seem to cause aging. — LBR

*Aging Cell* 10.1111/ace.12290 (2015).

## CLIMATE CHANGE

### An underground route to the atmosphere

As climate changes and temperatures rise, so do concerns that methane emissions from



Arctic lakes, like this one in eastern Greenland, could emit more methane due to climate warming

the Arctic may increase, because methane is a powerful greenhouse gas. Arctic lakes are known to be an important source of methane, but the origins of their emissions are not well understood. Paytan *et al.* investigated Toolik Lake, Alaska, in order to determine what fraction of the methane it emits is from microbial activity within the lake versus how much is transported into the lake by groundwater. They find that groundwater supplies a major fraction of the lake's methane, which implies that if

Arctic warming causes this type of groundwater flow to increase, then the methane flux from lakes to the atmosphere could grow as well. — HJS

*Proc. Natl. Acad. Sci. U.S.A.* 10.1073/pnas.1417392112 (2015)

## NONCODING RNA

### Circular RNA transcriptional circuits

Scientists first observed circular RNAs, a type of noncoding RNA, in mammalian cells over 30 years

ago but are only now beginning to elucidate their functions. Circular RNAs generally contain either exclusively gene exon or gene intron sequences. Li *et al.* now describe an unusual class of circular RNAs in human cells that contain both exon and intron sequences. These RNAs localized to the nucleus, where they bound to protein components of the transcription machinery and RNA components of the splicing machinery. By binding to the promoters of their own genes, they fine-tuned transcriptional activation of these genes. — GR

*Nat. Struct. Mol. Biol.* 10.1038/nsmb.2959 (2015).

## INFECTIOUS DISEASE

### A virulence factor comes under scrutiny

The human pathogen *Streptococcus pyogenes* produces streptolysin S (SLS), a virulence factor that helps the pathogen to invade host cells and to evade recognition by the host immune system. Maxson *et al.* show that the HIV protease inhibitor nelfinavir blocks a key step during SLS biosynthesis. The authors synthesize and test nelfinavir analogs to study the role of the SagE protein in the SLS biosynthesis pathway. Use of these analogs to inhibit SLS production will help to elucidate how SLS contributes to *S. pyogenes* virulence and may even lead to novel treatment strategies. — JFU

*ACS Chem. Biol.* 10.1021/cb500843r (2015)



Pre-term infants are especially susceptible to necrotizing enterocolitis

## ALSO IN SCIENCE JOURNALS

Edited by Stella Hurtley

## MATERIALS SCIENCE

## Adding autonomy to materials science

Shape-memory alloys can alter their shape in response to a change in temperature. This can be thought of as a simple autonomous response, albeit one that is fully programmed at the time of fabrication. It is now possible to build materials or combinations of materials that can sense and respond to their local environment, in ways that might also include simple computations and communication. McEvoy and Correll review recent developments in the creation of autonomous materials. They look at how individual abilities are added to a material and the current limitations in the further development of "robotic materials." — MSL

*Science*, this issue p. 1328

## TRANSLATION

## Measuring translation in space and time

The ribosome translates the information contained within messenger RNAs (mRNAs) into proteins. When and where ribosomes encounter mRNAs can regulate gene expression. Halstead *et al.* developed an RNA biosensor that allows single molecules of mRNAs that have never been translated to be distinguished from ones that have undergone translation by the ribosome in living cells (see the Perspective by Popp and Maquat). The authors demonstrated the utility of their

technique by examining the spatial and temporal regulation of translation in single cells and in *Drosophila* oocytes during development. — BAP

*Science*, this issue p. 1367;  
see also p. 1316

## ADDITIVE MANUFACTURING

## Fast, continuous, 3D printing

Although three-dimensional (3D) printing is now possible using relatively small and low-cost machines, it is still a fairly slow process. This is because 3D printers require a series of steps to cure, replenish, and reposition themselves for each additive cycle. Tumbleston *et al.* devised a process to effectively grow solid structures out of a liquid bath. The key to the process is the creation of an oxygen-containing "dead zone" between the solid part and the liquid precursor where solidification cannot occur. The precursor liquid is then renewed by the upward movement of the growing solid part. This approach made structures tens of centimeters in size that could contain features with a resolution below 100  $\mu\text{m}$ . — MSL

*Science*, this issue p. 1349

## RNA BIOCHEMISTRY

## RNA kinetics may define regulatory hierarchy

The double-helical structure of DNA suggests immediately how nucleic acid polymers can recognize and bind to homologous sequences. Target recognition

by RNA is vital in many biological processes. Fei *et al.* used super-resolution microscopy of tagged RNAs and computer modeling to understand how RNA-RNA base-pairing reactions occur in vivo. They studied a small RNA (sRNA) that targets a messenger RNA (mRNA) for degradation in bacteria. They observed a slow rate of association as the sRNA searched for its mRNA target, but thereafter a fast rate of dissociation. This explains the need for high concentrations of sRNA to cause mRNA degradation. The sRNA found different target mRNAs at different rates, allowing the generation of a regulatory hierarchy. — GR

*Science*, this issue p. 1371

## REGENERATIVE MEDICINE

## Healing heart borrows from development

With a limited ability to repair itself after injury, the mature heart may need to look to development for some lessons. By reactivating pathways that are present during mammalian development, it may be possible to encourage cardiac regeneration. In mice, Tian *et al.* found that the microRNA cluster mir302-367 stimulates cardiomyocyte proliferation during early heart development by inhibiting the Hippo signaling pathway. Transient treatment with mimics of mir302-367 promoted cardiac regeneration in mice after myocardial infarction, suggesting that such small RNAs can be harnessed therapeutically to repair the adult heart. — MLF

*Sci. Transl. Med.* **7**, 279ra38 (2015).

## HEAVY FERMIONS

## Uncovering the symmetry of a hidden order

Cooling matter generally makes it more ordered and may induce dramatic transitions: Think of water becoming ice. With increased order comes loss of symmetry; water in its liquid form will look the same however you rotate it, whereas ice will not. Kung *et al.* studied the symmetry properties of a mysteriously ordered phase of the material  $\text{URu}_2\text{Si}_2$  that appears at 17.5 K. They shone laser light on the crystal and studied the shifts in the frequency of the light. The electron orbitals of the uranium had a handedness to them that alternated between the atomic layers. — JS

*Science*, this issue p. 1339

## STATISTICS

## Are you asking the right questions of your data?

Data analyses are central to scientific inquiry. But not all data analyses are the same, and confusing one kind of analysis with another can lead to wrong interpretations. In a Perspective, Leek and Peng argue that data analyses can be grouped into six types, ranging from comparatively simple descriptive analyses to much more challenging predictive, causal, and mechanistic analyses. In studies that involve multiple analyses of different types, it is crucial to be aware of the analysis type at each step. — JFU

*Science*, this issue p. 1314



## SUPERCONDUCTIVITY

### Picking out the elusive stripes

Copper-oxide superconductors have periodic modulations of charge density. Typically, the modulation is not the same for the whole crystal, but breaks up into small nanosized domains. Bulk experiments show that the density is modulated along both axes in the copper-oxide plane, but it is not clear whether this is true only on the scale of the whole crystal or also locally, for each domain. Comin *et al.* analyzed the charge order in the

compound  $\text{YBa}_2\text{Cu}_3\text{O}_{6+y}$ , using resonant x-ray scattering, and found that it was consistent with a local unidirectional, so-called stripy, ordering. — JS

*Science*, this issue p. 1335

## VIBRATIONAL DYNAMICS

### Getting a handle on the $\text{CH}_5^+$ spectrum

Protonated methane,  $\text{CH}_5^+$ , fascinates chemists because it seems to break the rules. There's no obvious place for the fifth hydrogen to bind, and so what happens is that all five

hydrogens shuffle about like participants in an endless round of a musical chairs game. And yet the molecule has a vibrational spectrum that suggests some semblance of tighter ordering. Asvany *et al.* have now measured high-resolution vibrational spectra at two low temperatures (10 and 4 K). (See the Perspective by Oka). Their accompanying analysis makes headway on assigning the peaks and enhancing understanding of the molecule's dynamic structure. — JSY

*Science*, this issue p. 1346;  
see also p. 1313

## REVIEW SUMMARY

## MATERIALS SCIENCE

# Materials that couple sensing, actuation, computation, and communication

M. A. McEvoy and N. Correll\*

**BACKGROUND:** The tight integration of sensing, actuation, and computation that biological systems exhibit to achieve shape and appearance changes (like the cuttlefish and birds in flight), adaptive load support (like the banyan tree), or tactile sensing at very high dynamic range (such as the human skin) has long served as inspiration for engineered systems. Artificial materials with such capabilities could enable airplane wings and vehicles with the ability to adapt their aerodynamic profile or camouflage in the environment, bridges and other civil structures that could detect and repair damages, or robotic skin and prosthetics with the ability to sense touch and subtle textures. The vision for such materials has been articulated repeatedly in science and fiction (“programmable matter”) and periodically has undergone a renaissance with the advent of new enabling technology such as fast digital electronics in the 1970s and microelectromechanical systems in the 1990s.

**ADVANCES:** Recent advances in manufacturing, combined with the miniaturization of electronics that has culminated in providing the power of a desktop computer of

the 1990s on the head of a pin, is enabling a new class of “robotic” materials that transcend classical composite materials in functionality. Whereas state-of-the-art composites are increasingly integrating sensors and actuators at high densities, the availability of cheap and small microprocessors will allow these materials to function autonomously. Yet, this vision requires the tight integration of material science, computer science, and other related disciplines to make fundamental advances in distributed algorithms and manufacturing processes. Advances are currently being made in individual disciplines rather than system integration, which has become increasingly possible in recent years. For example, the composite materials community has made tremendous advances in composites that integrate sensing for non-destructive evaluation, and actuation (for example, for shape-changing airfoils), as well as their manufacturing. At the same time, computer science has created an entire field concerned with distributed algorithms to collect, process, and act upon vast collections of information in the field of sensor networks. Similarly, manufacturing has been revolu-

tionized by advances in three-dimensional (3D) printing, as well as entirely new methods for creating complex structures from unfolding or stretching of patterned 2D composites. Finally, robotics and controls have made advances in controlling robots with

## ON OUR WEB SITE

Read the full article at <http://dx.doi.org/10.1126/science.1261689>

multiple actuators, continuum dynamics, and large numbers of distributed sensors. Only a few systems have taken advantage of these advances, however, to create materials that tightly integrate sensing, actuation, computation, and communication in a way that allows them to be mass-produced cheaply and easily.

**OUTLOOK:** Robotic materials can enable smart composites that autonomously change their shape, stiffness, or physical appearance in a fully programmable way, extending the functionality of classical “smart materials.” If mass-produced economically and available as a commodity, robotic materials have the potential to add unprecedented functionality to everyday objects and surfaces, enabling a vast array of applications ranging from more efficient aircraft and vehicles, to sensorial robotics and prosthetics, to everyday objects like clothing and furniture. Realizing this vision requires not only a new level of interdisciplinary collaboration between the engineering disciplines and the sciences, but also a new model of interdisciplinary education that captures both the disciplinary breadth of robotic materials and the depth of individual disciplines. ■

The list of author affiliations is available in the full article online.

\*Corresponding author. E-mail: [ncorrell@colorado.edu](mailto:ncorrell@colorado.edu)  
Cite this article as M. A. McEvoy and N. Correll, *Science* 347, 1261689 (2015). DOI: 10.1126/science.1261689



(Top) Biological systems that tightly integrate sensing, actuation, computation, and communication and (bottom) the engineering applications that could be enabled by materials that take advantage of similar principles. (From left) The cuttlefish (camouflage), an eagle's wings (shape change), the banyan tree (adaptive load support), and human skin (tactile sensing).



## REVIEW

## MATERIALS SCIENCE

# Materials that couple sensing, actuation, computation, and communication

M. A. McEvoy and N. Correll\*

Tightly integrating sensing, actuation, and computation into composites could enable a new generation of truly smart material systems that can change their appearance and shape autonomously. Applications for such materials include airfoils that change their aerodynamic profile, vehicles with camouflage abilities, bridges that detect and repair damage, or robotic skins and prosthetics with a realistic sense of touch. Although integrating sensors and actuators into composites is becoming increasingly common, the opportunities afforded by embedded computation have only been marginally explored. Here, the key challenge is the gap between the continuous physics of materials and the discrete mathematics of computation. Bridging this gap requires a fundamental understanding of the constituents of such robotic materials and the distributed algorithms and controls that make these structures smart.

Advancements in material science, manufacturing processes, and the continual miniaturization of electronic components have enabled a class of multifunctional materials that tightly integrate sensing, actuation, communication, and computation. We refer to such materials as “robotic materials,” analogous to the field of robotics, which combines mechanisms with sensing and control. Unlike conventional stimuli-response materials that change

one or two physical properties in response to an external stimulus, robotic materials make the relationship between signals measured from embedded sensors and the material properties activated by embedded actuators fully programmable. Such materials are inspired by the multifunctionality of biological systems and have a wide range of applications, examples of both of which are shown in Fig. 1.

For example, inspired by the impressive abilities of the cuttlefish or chameleon (*1*) to change their appearance in response to the environment, various artificial mechanisms, ranging from op-

tical metamaterials (*2, 3*) to smart composites (*4*), have been proposed. Although these mechanisms have the potential to induce appearance change, few works have attempted the system-level integration of sensing, pattern recognition, and distributed control into a composite material that can actually respond to the environment in the way that animals do.

Morphing aerodynamic surfaces could improve efficiency during different flight regimes, reduce noise, and save fuel. Early designs used mechanical actuators in series that would distort the shape of the wing (*5–8*). However, these concepts do not scale: Every additional actuator increases the required load-carrying capacity of all actuators in the chain. This leads to increased weight, which again requires stronger (and heavier) actuators. Robotic materials might alleviate this problem through a tighter integration of sensing, actuation, and control—for example, by combining variable stiffness with bending actuation.

Materials that self-diagnose and self-repair are ubiquitous in biological systems, some of which can adapt to changing structural loads such as human bones or trees that can grow additional roots to accommodate changing load requirements. In an engineering context, nondestructive evaluation (NDE) devices embedded into wings, bridges, and other safety critical systems should make it possible to detect potential problems before they appear while reducing costs for inspection and maintenance (*9*). Combined with actuators, materials could self-repair by releasing chemical agents in the material (*10*), or locally change their stiffness to redistribute loads.

Artificial skins promise to equip prosthetic and robotic hands with tactile sensing that comes close to that of human performance. Existing systems do not yet provide the resolution, bandwidth, and dynamic range of the human skin (*11*). Here, integrating computation into the skin



**Fig. 1. Biological systems that tightly integrate sensing, actuation, and controls and the engineering applications that could benefit from a similar approach.** (Top) Biological systems exhibiting multifunctionality such as the cuttlefish (camouflage), an eagle's wings (shape change), the banyan tree (adaptive load bearing), and human skin (tactile sensing). (Bottom) Engineering applications that could take advantage of similar principles, motivating novel

materials that tightly integrate sensing, actuation, computation, and communication. Credits: cuttlefish: N. Hobgood/WikiMedia Commons; bald eagle Alaska: C. Chapman/WikiMedia Commons; banyan tree: W. Knight/WikiMedia Commons; human skin: A. McEvoy; men in camouflage hunting gear: H. Ryan/U.S. Fish and Wildlife Service; 21st century aerospace vehicle: NASA; Sydney Harbour Bridge: I. Brown/WikiMedia Commons; cyberhand: Prensilia S.R.L./ Prensilia.com

can alleviate the bandwidth requirements of high-resolution, high-dynamic range sensing by preprocessing and help to discern task-relevant information from background noise.

Creating robotic materials that address the above applications with seamlessly integrated, mass-produced products will require advances in material science and manufacturing. However, macroscopic robotic materials with useful functionality can already be realized with existing materials and processes. Examples shown in Fig. 2 include an amorphous façade that recognizes a user's input gestures and responds with changes in its opacity and color (12), a dress that can localize sound sources and indicate their direction using vibro-tactile feedback (13), a shape-changing variable stiffness beam (14), and a robotic skin that senses touch and texture (15).

High-value applications such as airfoils, prosthetics, and camouflage might be among the first to find favorable trade-offs between added functionality and increased cost, weight, and inferior structural properties of embedding sensing, actuation, and computation. In the long run, solving system integration and manufacturing challenges that are common to robotic materials, and therefore reducing the cost to make them, might enable a new class of smart everyday materials: dinner tables that selectively keep dishes hot or cold by locally sensing the presence of objects and their initial temperature and then controlling appropriate actuators; insoles that measure pressure and locally change their cushioning to adapt to fatigue of their wearer; or print magazines that use semiconducting ink to implement computation, capacitive sensing, and light emission to print video games or movie previews on their back.

## Background

An early vision of smart materials with embedded, networked computation are networks of microelectromechanical systems (MEMS) (16). MEMS allowed for the manufacturing of microscale structures with the same processes that are used for making conventional analog and digital semiconductor circuits, permitting their tight integration. An example of a mainstream MEMS device is an accelerometer that consists of a cantilevered beam with a small mass and circuitry to measure its displacement during acceleration, and can easily be mass-produced. Whereas (16) emphasizes the use of MEMS for creating high-density sensing arrays and proposes the concept of “smart dust,” tiny MEMS sensing devices that could be deployed in large numbers and carried away by the wind, this vision is extended by (17) to millimeter-scale units that can locomote by themselves, allowing the resulting structures to reconfigure and form “programmable matter.”

In addition to the material science challenges, such a vision poses a series of deep challenges in networking and computation, which has inspired two active fields, namely, sensor networks and amorphous computing. Amorphous computing (18) has laid the foundation for computation in large-scale distributed systems

in which individual computing elements can be unreliable and do not need to be manufactured in a precise geometrical arrangement. Hardware demonstrations that came out of this movement include “paintable computing” (19), a distributed system of locally communicating nodes that used gradient information to display lines and simple characters; pattern formation in bacterial colonies that are receptive to chemical gradients and can be designed to act as simple high-, low- and band-pass filters (20); and a modular robotic (21) system that can adapt its shape to the environment via local sensing (22). At the same time, the sensor network community has begun to explore the foundations of networking and routing in these systems (23), although focusing almost exclusively on geospatial sensing applications rather than integrating sensor networks into materials.

The vision of materials that can change their physical properties has also been explored in the context of designing new interactions between computers and people. “Tangible bits” (24) or “radical atoms” (25) promote the idea of presenting information in physical form, not limited

to pixels. This concept has found physical implementation in “pushpin computing” (26), which seeks to engineer additional layers of information in everyday objects such as push pins and floor tiles, and a series of works that involve interaction with materials that change their physical properties such as stiffness (27), physical extension (28), or weight (29). As such, these works explore a series of applications as well as their enabling principles, but leave their implementation in systems or products to science and engineering.

Distributed MEMS, the related concepts it helped spawn, and modular robotics emphasize the system-level integration of sensing, actuation, computation, and communication, but fall short in addressing the structural properties of the resulting systems. The structural properties of a composite are an integral part of “multifunctional materials,” a field that traditionally aims to optimize design by addressing both structural (e.g., strength and stiffness) and nonstructural (e.g., sensing and actuation, self-healing, energy harvesting) requirements of a system (30), but largely ignores the opportunities

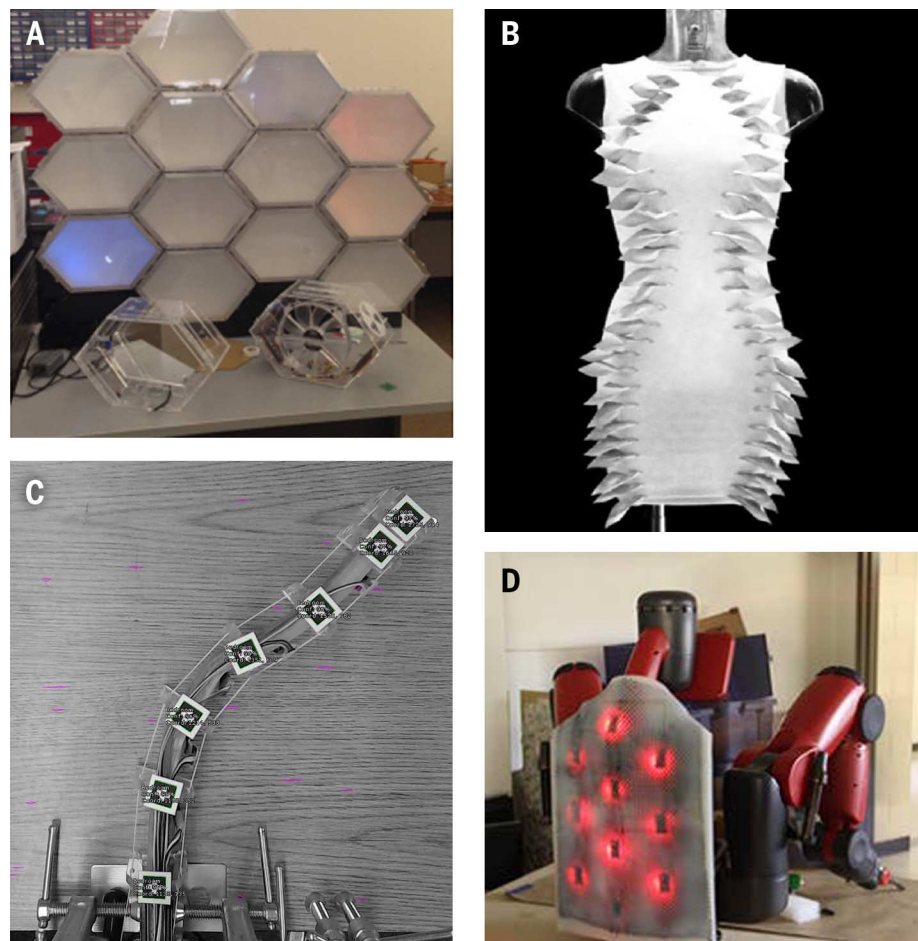


**Fig. 2. Examples of robotic materials that combine sensing, actuation, computation, and communication.** (A) An amorphous façade that recognizes gestures and changes its opacity and color (12); (B) a dress that can localize sound sources and indicate their direction through vibro-tactile feedback (13); (C) a shape-changing variable stiffness beam (14); and (D) a robotic skin that senses touch and texture (15).



of integrated computation that have been articulated by (16, 18, 31). Multifunctionality at the nano- and microscale has also been studied in physics in the context of metamaterials. Metamaterials are “macroscopic composites having a man-made, three-dimensional, periodic cellular architecture designed to produce an optimized combination, not available in nature, of two or more responses to specific excitation” (32). Metamaterials classically exploit the frequency properties of structures to deflect optical waves in nonnatural ways, but the above definition allows a broader interpretation, both in terms of the constituents of individual cells and their scale, making it applicable to some of the computational systems discussed here.

The physical properties of the material itself affect not just sensing and actuation, but also computation. Indeed, material dynamics allow one to shift classes of computation such as feedback control (e.g., by exploiting thermal or chemical deformation to regulate a process), rectification [e.g., to compensate for motion parallax in an insect’s eye (33)], or transformation of a signal into the frequency domain (e.g., in the cochlea in the inner ear), by simply tuning the geometry and material properties of a structure. This effect is known as “morphological computation” (34) and has become an important aspect of the design of robotic systems.

### Constituent parts of robotic materials

Robotic materials consists of sensors, actuators, computing, and communication elements. While these terms are very broad, this section focuses

on elements that have been developed, or are suitable for, integration into composites, and have the potential to enable robotic materials with novel, unprecedented functionality.

### Sensing

Classical stimuli-response materials “sense” their environment in that they change some of their properties in response to one or more external stimuli, including acoustic, electromagnetic, optical, thermal, and mechanical. Robotic materials integrate dedicated sensors that, in combination with appropriate signal processing, let the composite identify and respond to environmental patterns of arbitrary complexity, limited only by available sensors and computation. An example of complex signal processing that can be accomplished in a robotic material is to sense and localize textures that touch an artificial skin (15) (Fig. 2D). This artificial skin is made by distributing nodes throughout a silicon-based material. Each node is equipped with a microphone and can analyze the high-frequency sound signal generated by a texture rubbing the skin. Local communication between nodes allows the position of the touch to be triangulated. Once triangulated, the node closest to the source analyzes the material and classifies it. With this approach, the nodes sample and process high-bandwidth information locally and then route high-level information back to a central computer only when important events occur. This example, using embedded MEMS microphones, lends itself to many related material-centric applications such as sound localization (13, 35),

vibration analysis (36, 37), or—when combined with piezo actuators—structural health monitoring (9, 38–40).

Similarly, accelerometers can detect impacts (9) or determine orientation of a robotic material with respect to gravity. Capacitive touch sensors (11) can be embedded into the surface of a robotic material as input devices. Optical sensors such as color sensors, infrared sensors, or photoresistors can measure ambient light levels for camouflage applications. Thermistors would allow robotic materials to measure temperature of either the environment or the material itself at high resolution (41, 42). Mechanical sensors that measure applied force (43, 44), strain (45, 46), or deflection (47) can monitor the flow over an aerodynamic surface and monitor its shape change as it morphs into an optimal shape.

Most of the sensors discussed above have been developed for, or are at least suitable for, operation while embedded in a material. Deploying such sensors in large numbers and at high densities requires, however, solving problems in system integration, which can partly be alleviated by colocating those sensors with computing elements to preprocess and network information, as discussed below.

### Actuation

In a robotic material, actuation refers to changing the material properties of the underlying base material. Some possible actuations are expanding, contracting, changing stiffness, changing surface texture, or changing color (Fig. 3), while possible actuators include heat, electricity, light, magnetism, or the release of chemicals.

Variable stiffness actuators have received attention as the basis for morphing airfoils and active vibration control, resulting in a large number of actuators that are potentially suitable for use in robotic materials. One common approach to variable stiffness is sandwiching a thermoplastic between two metal plates (48, 49) and then exploiting the thermoplastic’s change in stiffness with increasing temperature. When the thermoplastic is at a low temperature, the metal plates are tightly coupled together, acting as a single stiff composite. At higher temperatures, the thermoplastic has much less resistance to shear and the plates act as if they were uncoupled from each other, creating a composite with a much lower stiffness. A similar approach is shown in (50, 51), which segments the rigid layers and uses a shape memory polymer (52) as the sandwich layer. Instead of melting, friction between plates can also be altered pneumatically. In (27), a number of sheets are inserted into a vacuum bag, which remains extremely flexible until a vacuum is applied and the deformed shape is locked in place. Similarly, particle jamming (53) is a technique where a granular material is encased in a very flexible material. When pressed against an object, the granular material conforms to the object’s shape. Evacuating the case causes the material to contract and harden, pinching the object.

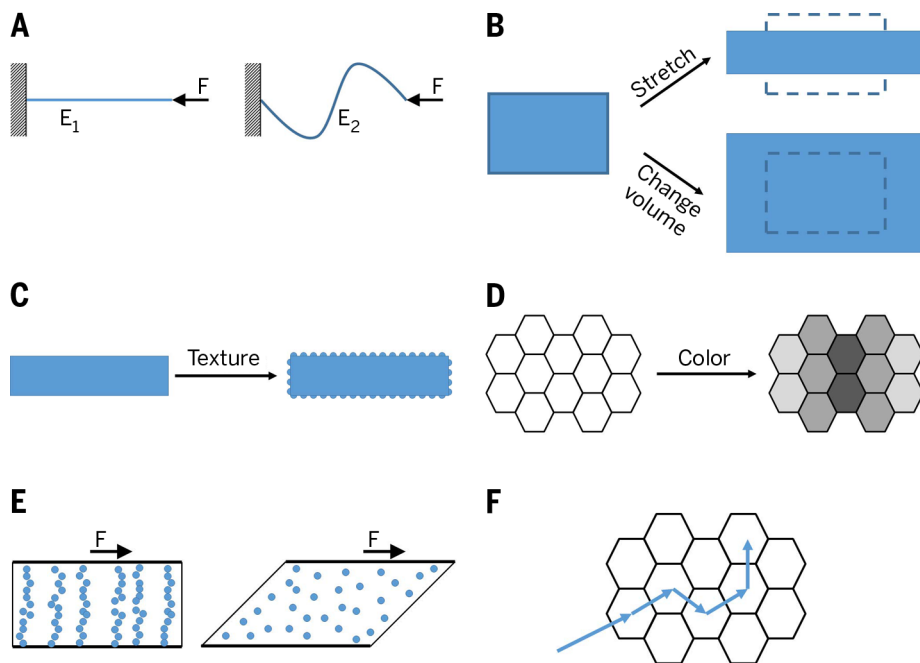


**Fig. 3. The in situ actuators of a robotic material work to change the material properties of the base material.** Changes in (A) stiffness and (B) volume could enable shape-changing robotic materials. Robotic skins could utilize changes in (C) appearance and (D) surface texture. Self-healing and self-regenerating robotic materials could use venous systems enabled by (E) variable viscosity fluids or (F) the rerouting of the healing compounds through the material.

Simply changing the stiffness of a material, however, will not result in a shape-changing material; actuation forces must be applied to the material to initiate the change. Recent advances in the development of artificial muscles might make their large-scale integration into robotic materials feasible. An artificial muscle made from fishing line or conductive sewing thread is described in (54). The artificial muscles are created by twisting the threads until they start to coil up on themselves. The stroke and actuation force can be tuned by changing the weight used when coiling the thread, using multiple coils, or by coiling around a mandrel. Shape memory alloys have been used in many artificial muscle applications (55). Typically nickel-titanium or copper-aluminum-nickel alloys, shape memory alloys can change from a deformed shape back to their parent shape when heated above their transition temperature. Shape memory alloy actuated joints were used in a fabricated bat wing (56) and in origami-inspired robots (57), demonstrating how artificial muscles could be embedded into a robotic material. McKibben actuators are pneumatic artificial muscles that are light weight, flexible, and can achieve large displacements (58–60). McKibben actuators place an inflatable bladder inside of a woven mesh. When the bladder is inflated, the diameter of the woven mesh expands while the length contracts. Efforts to miniaturize these devices are reviewed in (60), while (59) presents a McKibben actuator that makes use of shape memory polymer to maintain the actuator's displacement without continuous control, demonstrating how a robotic material could use both variable stiffness materials and artificial muscles to achieve shape change.

Pneumatic and hydraulic systems that create volumetric changes have been extensively used in soft robots and could be implemented in a robotic material to create distributed volumetric changes for shape-changing and morphing applications. Chambers embedded into a soft elastomer can be filled with fluid or air, causing the elastomer to expand and change its shape. This effect has been used for locomotion in (61–64) where soft robots are able to crawl, roll, swim, and bend into an arbitrary two-dimensional (2D) configuration, respectively. A challenge of pneumatic and hydraulic robotic materials is not only pressure distribution, but also the requirement for possibly large numbers of miniature valves. A miniature electrorheological fluid based valve (65) or a miniature latchable microvalve based on low-melting point metals (66) could be embedded into such robotic materials and enable the control of fluidic channels in a self-healing composite (10) or the control of embedded fluidic channels for camouflage and display in soft robots (4). Here, the soft robots are designed with microfluidic networks that can be filled with colored, temperature-controlled fluid to change their appearance in both the visible and infrared spectrum.

Volumetric change can also be influenced by the construction of the base material itself. In

a cellular material, changing the geometry allows designs with different Poisson ratios (67). This also allows large changes in a material's area or volume; for example, (68) describes geometries that are allowed to buckle in local regions, drastically reducing their surface area. Similar to sensors for robotic materials, the actuators discussed here lend themselves to implementation in large numbers and parallel operation. Furthermore, computation might overcome integration challenges by reducing communication requirements due to local control.

### Local computation

Although it might be possible to route actuation signals and sensing information in and out of the material to where this information is processed centrally, this approach becomes increasingly difficult with both the required bandwidth and the number of sensors and actuators to be embedded. A system such as the sensing skin (15) illustrates this difficulty with respect to sensing, a shape-changing material such as (14) with respect to actuation, and the smart façade with respect to a combination of both. Routing vibration signals sampled at 1 kHz becomes increasingly difficult when the number of sensors increases. Instead, when computing information locally, only selected information needs to be transferred outside of the material. In the shape-changing material (14) that controls local stiffness by melting, temperature readings are only used locally for feedback control and are not needed outside of the material. Therefore, the desired stiffness profile needs only to be sent once and can then be controlled locally. Finally, a façade whose transparency and color can be adjusted by a user does not need to disseminate sensed gestures through the system, but only the resulting actuation command that the user intends.

Algorithms that run on a robotic material must have the following properties: (i) They must scale as the material grows in size; (ii) they must be able to run with the limited computation and memory resources provided in each node; and (iii) they have to be robust with respect to the failure of individual nodes. A necessary condition for scalability is to limit information exchange to local communication, and algorithms that run in constant time, independent of the size of the network, are known as local algorithms. An overview of such algorithms is presented in (69, 70) in the context of wireless sensor networks. These local algorithms are used to determine conflict-free sets of activities, such as simultaneous data transmissions, by using matching, independent sets, and coloring algorithms, which are important primitives in higher-level distributed algorithms. One major limitation of the algorithms discussed in (69) is that they assume synchronous communication, which creates additional overhead; see, e.g., (71).

From a computational perspective, robotic materials can be viewed as an amorphous (18) or spatial computer (72), which attempt to for-

mulate a distributed computation model for systems that are limited to local communication and limited computational resources at each node. A key challenge in amorphous computing is how to design local interactions so that a desired global behavior can emerge. One approach to address this problem is using programming languages that provide abstractions that allow one to describe desired global behaviors and then automatically compile the corresponding local rules. What programming paradigm (i.e., procedural or functional) is most conducive to programming large numbers of distributed computing elements remains an open question, and (72) provides a comprehensive survey of the field.

Designing distributed algorithms and solving the global-to-local challenge are hard problems. Their solution is not on the critical path for large-scale deployment of computing infrastructure into robotic materials, which might benefit from enhanced signal processing, local control, and networking, all of which are established fields.

### Local communication

Robotic materials require embedded communication not only to transport sensing and control information, but also for more complex spatial dynamics to emerge. The key challenge for transporting data is that point-to-point connections from sensing locations to a central processing unit quickly become infeasible owing to the large number of cable crossings, the effect of embedded wiring on the material's structural properties, or radio-frequency challenges. The local computation in robotic materials offers not only local preprocessing of sensing information, but also the routing of information through a computer network; i.e., a shared communication channel that is arbitrated by all participants of the network, a problem that has been widely studied in sensor networks (73, 74).

Local computation becomes particularly interesting when individual processing nodes can access information from neighboring nodes via local communication. Some example robotic materials that take extensive advantage of this feature are distributed gesture recognition in an amorphous façade (12), where local communication is used to pass tactile sensing events along the physical path where they occur; texture identification in a robotic skin (15), where local communication allows triplets of nodes to triangulate the location of a vibration event by comparing local measurements; and distributed sensor-based control of a rolling robot (62), where local communication is used to infer the overall orientation of the material with respect to the ground.

The speed of communication through a robotic material has a notable effect on the performance of the robotic material. For example, a robotic skin that touches a hot surface needs to process and route that event quickly through the material, and might forgo the processing and forwarding of high-bandwidth texture information. In addition to actual bandwidth,



communication speed is also highly dependent on the network topology (75) and node density (76), which leads to important design considerations in robotic materials, as density and topology affect not only the computational properties of the system, but also its structural properties. Finally, tighter integration of future robotic materials, consisting of possibly millions of tiny computing elements, might require a departure from traditional networking and routing algorithms, necessitating solutions that trade-off performance with memory (77) or computational (78, 79) requirements.

There are only a few works that address hardware implementations of wired communication infrastructure embedded into materials. Various robotic skins use hierarchical standard industry bus-systems, which, however, scale poorly both with respect to bandwidth as well as to the total number of nodes that the system can support (11). A distributed optical sensor network built into multifunctional materials that allows the distribution of both power and information for structural health monitoring applications is described in (80). Here, the use of optical wave guides that can transport both power and information has the potential to minimize impact on structural properties, but is limited in the power density that it can achieve. In practice, combinations of peer-to-peer wired communication and long-range, high-bandwidth backbones using wired buses or wireless links might allow a robotic material to maintain both scalability and overall throughput.

### System integration and manufacturing

Being able to integrate sensing, actuation, computation, communication, and power infrastructure into composites at high densities in a scalable fashion is a key challenge in making robotic materials viable. This challenge is illustrated in Fig. 4A, which shows a block of the amorphous façade and the robotic skin before embedding in rubber, providing a glance at the different manufacturing and integration steps these systems require. Yet, turning the amorphous façade prototype (12) shown in Figs. 2 and 4 into a composite material that looks like glass to the naked eye, but can change its opacity and integrates high-resolution sensing to interact with its user, could be accomplished by layering existing technology such as liquid crystal sheets, organic light-emitting diodes, and silicon-based analog electronics. Similarly, a single element of a texture-sensitive skin (15)—computation, analog electronics, and MEMS microphone—is small enough to fabricate in dense arrays on a soft, stretchable substrate that would seamlessly integrate with robotic systems. A key challenge here is that the scales of the individual computational nodes and that of the resulting robotic material vary by multiple orders of magnitude. Current manufacturing techniques for nano- and microscale manufacturing do not scale well to create systems at the meter scale, and vice versa.

If the required sensing and actuation can be reduced to a single integrated system, CMOS and MEMS processing techniques can be used to cre-

ate highly stretchable sensor and actuator networks such as those of (81, 82). Such a system is illustrated in Fig. 4B, which shows a network of temperature sensors that can be embedded into a fiber composite. In (81), piezo sensor and actuator arrays that can be used as sensors for structural health monitoring were screen printed and then deposited onto a polyimide layer. In both systems, the interconnects are made in a spiral spring-like shape so that they can stretch to cover an area that is orders of magnitude larger. These approaches are currently limited by the number of interconnect wires that can be run in parallel while preserving the high degree of flexibility and also by the feasibility of creating complex circuits that require a variety of base materials.

Instead of silicon-based computation, robotic materials could also perform computation using polymer electronics (83). Although a series of computational devices have been demonstrated with ink-jet printing (84), this technology has reached only a few mainstream applications because of the large size, low speed, and poor yield of the resulting circuits. While these challenges limit the use of polymer electronics in conventional computing applications that require millions of transistors to function in concert, they do not apply to a distributed computing system in which each computational element performs a limited number of functions.

The integration of rigid components into a soft flexible substrate is also an active area of

study. Silicon-based materials, as well as other elastomers, do not bond well with many materials. Embedding of components into such materials requires perforation of the material (62) or attaching the rigid components to an embedded mesh (15). Alternatively, rigid components can be integrated into soft substrates by embedding them into substrates with gradually decreasing stiffness (85). A promising approach to integrate electronic components into solid materials of arbitrary shapes comes from the local functionalization of a base polymer so that a copper solution adheres to the surface (86). The resulting structural part with embedded copper traces can then be populated in a modified printed circuit board assembly machine.

Electromechanical components, printed circuit boards, and interconnects can also be integrated by shape deposition manufacturing (87). In this process, placeholders for parts or interconnects are subtracted from the base material. Once the components have been placed, they can be embedded into the structure by adding another precision machined layer. Another approach to create structural parts with embedded interconnects is 3D printing with conductive carbon-infused ABS (acrylonitrile butadiene styrene) or PLA (polylactic acid) filaments (88). However, this approach is currently limited by the high electrical resistance of the filaments. Finally, multifunctional materials can be manufactured by layering composites from which

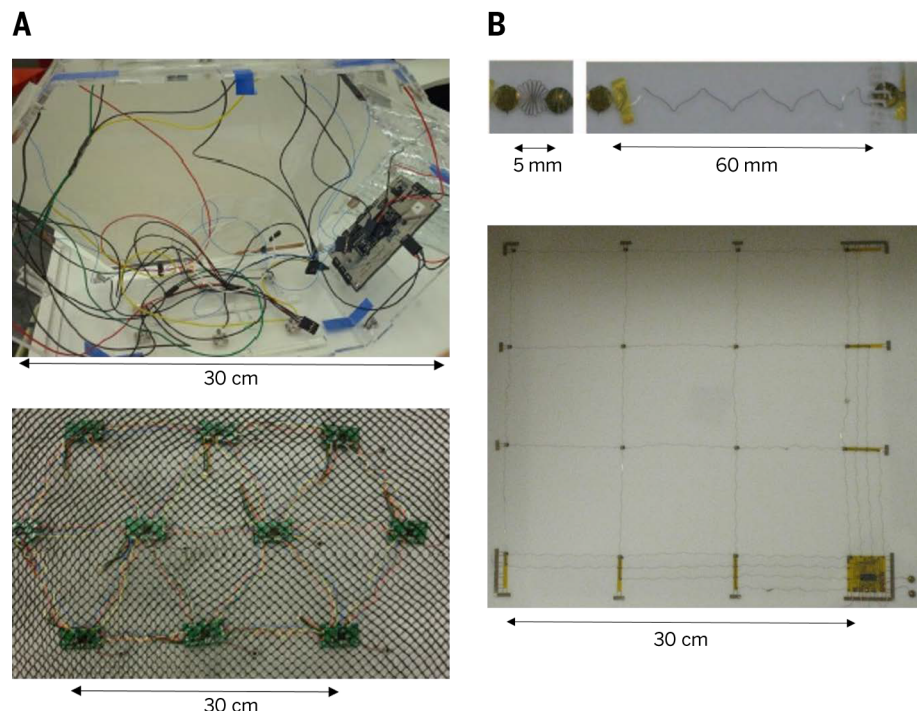


**Fig. 4. Macroscale and microscale manufacturing techniques for robotic materials.** (A) The inside of the amorphous façade (12) (top) and the texture-sensitive skin (15) (bottom), both consisting of discrete printed circuit boards, wiring, and structural materials. (B) A network of temperature sensors for embedding into a composite from (82). The micromanufactured structure is produced by semiconductor manufacturing techniques and is then stretched by an order of magnitude.

unnneeded pieces are removed by laser cutting, before another layer is added. Together with folding, this approach allows articulated, miniature 3D objects to be mass-produced (89).

Because power and interconnections between nodes must already be embedded into a robotic material, actuators that require only electric current promise to be the easiest type of actuator to embed. Hydraulic and pneumatic actuators, along with electro- and magnetorheological fluids and low-melting point alloys, are much more challenging to embed owing to the fluidic channels that must also be incorporated into the material, usually requiring the combination of molding and embedding of parts such as valves (62).

Despite the large selection of available sensors and actuators, the lack of automated manufacturing techniques that can bridge the micro and macro scales is a key challenge to achieving robotic materials that are economically viable. Solving these problems might require advances not only in processing techniques, but also in automation and robotics in order to better integrate the existing techniques described above.

### Control of robotic materials

Robotic materials require control at two different levels: (i) local control of each actuator, either in open or closed loop using feedback from an appropriate sensor and/or state information from neighboring controllers; and (ii) global control that implements a desired spatiotemporal pattern across the material, either in a distributed or centralized manner. For example, to achieve shape change in (42), the material embeds a thermistor, power electronics, and a small microcontroller colocated with each heating element to implement feedback control of a precise temperature across a bar to vary its stiffness by melting. In (14), a global controller then solves the inverse kinematics of a beam with many such variable stiffness elements in series to achieve a desired shape, and disseminates appropriate stiffness values into the robotic material where they are controlled by local feedback. An example of local control that requires neighborhood information is the rolling belt from (62), where a state transition from deflated to inflated to induce rolling motion is a function not only of the local sensor, but also of those to the left and to the right of each controller.

These type of controllers pose two fundamental challenges: (i) Designing controllers requires a fundamental understanding of the material dynamics, e.g., how they heat, deform, or change appearance as a function of energy provided and time; and (ii) understanding how large numbers of distributed controllers interact. Both of these problems are further complicated by the fact that the dynamics of the underlying physics are continuous, whereas the computational aspects of the system are discrete. This is illustrated in Fig. 5.

There are two approaches to making these systems analytically tractable: discretizing the material by describing it as a lumped element

model or maintaining its continuous properties by modeling it as a distributed parameter system. Lumped element models of mechanical systems can be solved relatively easily—e.g., by using variational integrators (90, 91)—whereas distributed parameter systems require solving partial differential equations (PDEs). Assuming that the distribution of the computing elements is quasi-continuous—consistent with the amorphous computing paradigm (18)—allows part of this burden to be moved into the material itself and permits the individual computing elements to each solve parts of the relevant PDEs (92).

Despite the large body of work on the control of large-scale distributed systems, many of which are relevant to the control of robotic materials (93, 94), only a few of these approaches have been explored experimentally owing to the absence of systems that provide access to thousands of sensors and actuators. In addition to providing the ability to implement distributed control inside the material, robotic materials also offer the possibility of predicting their own dynamics, which is an important capability in a distributed model-predictive control framework (95).

### Education

Understanding robotic materials requires an interdisciplinary systems perspective, which is currently not provided by materials science, computer science or robotics curricula alone. While the lack of a common language is a recurrent challenge in interdisciplinary fields, the discrete nature of computation and continuous nature of material physics share almost no common concepts and do not provide a smooth transition such as exists between biology and chemistry, material science and physics, or even biology and physics. A possible way to introduce system-based thinking that spans both the computational and physical is by hands-on, introductory engineering courses (96). By providing students with the basic skills of rapid prototyping, embedding computation (e.g., via the Arduino platform), and materials knowledge, and tasking them to design a robotic material that combines sensing, actuation, and computation, the students can be led to think about

how material properties affect computation and vice versa. For example, when designing a cell phone cover that changes its color using thermochromic polymers and embedded thermistors and heating, students can choose to either deepen their understanding of the feedback control aspects of the system or the relationships between energy, volume, and heat of the material. Graduate classes on robotic materials could follow a similar format, bringing together students with expert knowledge in the various subdisciplines.

### Conclusion

Robotic materials are a new class of multifunctional materials that are enabled by recent advances in material science, electronics, distributed computation, and manufacturing. Although composites now include the ability to sense damage or self-repair, for example, none of the state-of-the-art composites fully integrate sensing, actuation, computation, and communication.

Of the applications highlighted, many would substantially benefit from integrated distributed computation. In general, decentralized computation is critical when either the required sensing bandwidth is high or when the material requires high-speed feedback control. In both cases, routing of information to a central processing system quickly becomes infeasible. These problems are common to seemingly unrelated applications such as camouflage or morphing airplane wings, which are currently being investigated by disjoint communities.

Although a number of manufacturing processes for robotic materials exist, ranging from deposition to folding, robotic materials will require vertical integration of a number of these processes. Additional challenges include programming techniques that synthesize low-level code from a high-level, emergent behavior provided by the designer, and creating interfaces between disciplines that allow experts from currently disjoint disciplines to address common system challenges. If these challenges can be overcome, robotic materials will lead to robotic systems with unprecedented sensitivity and adaptivity that address applications from shape-changing airplane wings to sensitive prosthetic devices.

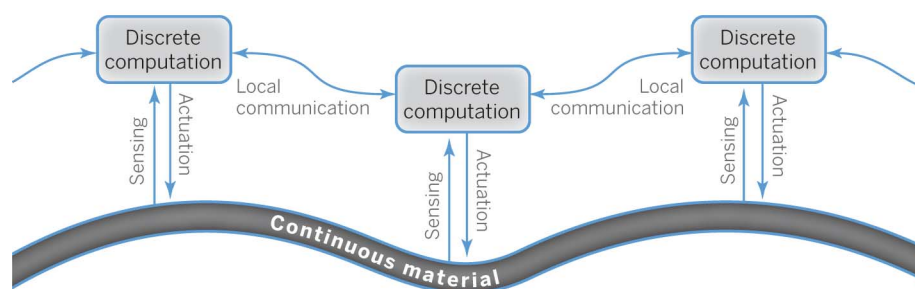


**Fig. 5. Relationship between cyber and physical components of a robotic material.** Continuous material properties can be sensed, processed in a computing element, and actuated upon. Whereas sensors, actuators, and computing elements are at discrete locations and can communicate locally, the material itself provides continuous coupling between sensors and actuators at different locations.



## REFERENCES AND NOTES

- M. Stevens, S. Merilaita, Animal camouflage: Current issues and new perspectives. *Philos. Trans. R. Soc. Lond. B Biol. Sci.* **364**, 423–427 (2009). doi: [10.1098/rstb.2008.0217](#); pmid: [18990674](#)
- V. M. Shalaeval et al., Negative index of refraction in optical metamaterials. *Opt. Lett.* **30**, 3356–3358 (2005). doi: [10.1364/OL.30.003356](#); pmid: [16389830](#)
- U. Leonhardt, Metamaterials: Towards invisibility in the visible. *Nat. Mater.* **8**, 537–538 (2009). doi: [10.1038/nmat2472](#); pmid: [19543308](#)
- S. A. Morin et al., Camouflage and display for soft machines. *Science* **337**, 828–832 (2012). doi: [10.1126/science.1222149](#); pmid: [22904008](#)
- C. Thill, J. Etches, I. Bond, K. Potter, P. Weaver, Morphing skins. *Aeronaut. J.* **112**, 117 (2008).
- S. Barbarino, O. Bilgen, R. M. Ajaj, M. I. Friswell, D. J. Inman, A review of morphing aircraft. *J. Intell. Mater. Syst. Struct.* **22**, 823–877 (2011). doi: [10.1177/1045389X11414084](#)
- S. Vasista, L. Tong, K. Wong, Realization of morphing wings: A multidisciplinary challenge. *J. Aircr.* **49**, 11–28 (2012). doi: [10.2514/1.C031060](#)
- T. A. Weisshaar, Morphing aircraft systems: Historical perspectives and future challenges. *J. Aircr.* **50**, 337–353 (2013). doi: [10.2514/1.C031456](#)
- D. Adams, *Health Monitoring of Structural Materials and Components: Methods with Applications* (Wiley, 2007).
- B. Blaiszik et al., Self-healing polymers and composites. *Annu. Rev. Mater. Res.* **40**, 179–211 (2010). doi: [10.1146/annurev-matsci-070909-104532](#)
- R. S. Dahiya, G. Metta, M. Valle, G. Sandini, Tactile sensing—from humans to humanoids. *IEEE Trans. Robotics* **26**, 1 (2010). doi: [10.1109/TRO.2009.2033627](#)
- N. Farrow, N. Sivagnanasadan, N. Correll, Gesture based distributed user interaction system for a reconfigurable self-organizing smart wall. *Proceedings of the 8th International Conference on Tangible, Embedded and Embodied Interaction* (Association for Computing Machinery, New York, 2014), pp. 245–246. doi: [10.1145/2540930.2540967](#)
- H. Profita, N. Farrow, N. Correll, Flutter: An exploration of an assistive garment using distributed sensing, computation and actuation. *Proceedings of the 9th International Conference on Tangible, Embedded and Embodied Interaction* (Association for Computing Machinery, New York, USA, 2015), pp. 359–362. doi: [10.1145/2677199.2680586](#)
- M. A. McEvoy, N. Correll, “Shape change through programmable stiffness,” International Symposium on Experimental Robotics (ISER), Marrakech, Morocco, 2014.
- D. Hughes, N. Correll, “A soft, amorphous skin that can sense and localize texture,” IEEE International Conference on Robotics and Automation (ICRA), Hong Kong, 2014. doi: [10.1109/ICRA.2014.6907101](#)
- A. A. Berlin, K. J. Gabriel, Distributed MEMS: New challenges for computation. *IEEE Comput. Science Eng.* **4**, 12–16 (1997). doi: [10.1109/99.590851](#)
- S. C. Goldstein, J. D. Campbell, T. C. Mowry, Programmable matter. *Computer* **38**, 99–101 (2005). doi: [10.1109/MC.2005.198](#)
- H. Abelson et al., Amorphous computing. *Commun. ACM* **43**, 74–82 (2000). doi: [10.1145/332833.332842](#)
- W. Butera, Text display and graphics control on a paintable computer, self-adaptive and self-organizing systems. *First International Conference on Self-Adaptive and Self-Organizing Systems*. SASO'07 (IEEE, New York, 2007), pp. 45–54. doi: [10.1109/SASO.2007.60](#)
- S. Basu, Y. Gerchman, C. H. Collins, F. H. Arnold, R. Weiss, A synthetic multicellular system for programmed pattern formation. *Nature* **434**, 1130–1134 (2005). doi: [10.1038/nature03461](#); pmid: [15858574](#)
- M. Yim et al., Modular self-reconfigurable robot systems. *IEEE Robotics & Automation Magazine* **14**, 43–52 (2007). doi: [10.1109/MRA.2007.339623](#)
- C.-H. Yu, F.-X. Willems, D. Ingber, R. Nagpal, Self-organization of environmentally-adaptive shapes on a modular robot. *IEEE/RSJ International Conference on Intelligent Robots and Systems (IROS)* (IEEE, New York, 2007), pp. 2353–2360. doi: [10.1109/IROS.2007.4399491](#)
- P. Levis et al., in *TinyOS: An Operating System for Sensor Networks, Ambient Intelligence* (Springer, Berlin, 2005), pp. 115–148. doi: [10.1007/3-540-27139-2\\_7](#)
- H. Ishii, B. Ullmer, Tangible bits: Towards seamless interfaces between people, bits and atoms. *Proceedings of the ACM SIGCHI Conference on Human Factors in Computing Systems* (Association of Computing Machinery, New York, 1997), pp. 234–241. doi: [10.1145/258549.258715](#)
- H. Ishii, D. Lakatos, L. Bonanni, J.-B. Labruno, Radical atoms: Beyond tangible bits, toward transformable materials. *Interaction* **19**, 38 (2012). doi: [10.1145/2065327.2065337](#)
- J. Lifton, D. Seetharam, M. Broxton, J. Paradiso, *Pushpin Computing System Overview: A Platform for Distributed, Embedded, Ubiquitous Sensor Networks, Pervasive Computing* (Springer, 2002), pp. 139–151. doi: [10.1007/3-540-45866-2\\_12](#)
- J. Ou et al., jamSheets: Thin interfaces with tunable stiffness enabled by layer jamming. *Proceedings of the 8th International Conference on Tangible, Embedded and Embodied Interaction* (Association of Computing Machinery, New York, 2014), pp. 65–72. doi: [10.1145/2540930.2540971](#)
- D. Leithinger, S. Follmer, A. Olwal, H. Ishii, Physical telepresence: Shape capture and display for embodied, computer-mediated remote collaboration. *Proceedings of the 27th annual ACM symposium on User Interface Software and Technology* (Association of Computing Machinery, New York, 2014), pp. 461–470. doi: [10.1145/2642918.2647377](#)
- R. Niyama, L. Yao, H. Ishii, Weight and volume changing device with liquid metal transfer. *Proceedings of the 8th International Conference on Tangible, Embedded and Embodied Interaction* (Association of Computing Machinery, New York, 2014), pp. 49–52. doi: [10.1145/2540930.2540953](#)
- R. F. Gibson, A review of recent research on mechanics of multifunctional composite materials and structures. *Compos. Struct.* **92**, 2793–2810 (2010). doi: [10.1016/j.comstruct.2010.05.003](#)
- J. M. Kahn, R. H. Katz, K. S. Pister, Next century challenges: Mobile networking for “Smart Dust.” *Proceedings of the 5th annual ACM/IEEE International Conference on Mobile computing and Networking* (Association of Computing Machinery, New York, 1999), pp. 271–278. doi: [10.1145/313451.313558](#)
- R. M. Walser, Electromagnetic metamaterials. *Proc. SPIE* **4467**, Complex Mediums II: Beyond Linear Isotropic Dielectrics (San Diego, CA, 2001), pp. 1–15 (2001). doi: [10.1117/12.432921](#)
- N. Franceschini, J.-M. Pichon, C. Blanes, J. Brady, From insect vision to robot vision. *Philos. Trans. R. Soc. Lond. B Biol. Sci.* **337**, 283–294 (1992). doi: [10.1098/rstb.1992.0106](#)
- R. Pfeifer, F. lida, Morphological computation: Connecting body, brain and environment. *Japanese Scientific Monthly* **58**, 48 (2005). doi: [10.1007/978-3-642-00616-6\\_5](#)
- X. Sheng, Y.-H. Hu, Maximum likelihood multiple-source localization using acoustic energy measurements with wireless sensor networks. *IEEE Trans. Signal Processing* **53**, 44–53 (2005). doi: [10.1109/TSP.2004.838930](#)
- M. N. Ghasemi-Nejhad, R. Russ, S. Pourjalali, Manufacturing and testing of active composite panels with embedded piezoelectric sensors and actuators. *J. Intell. Mater. Syst. Struct.* **16**, 319–333 (2005). doi: [10.1177/1045389X05050103](#)
- S. Jang et al., Structural health monitoring of a cable-stayed bridge using smart sensor technology: Deployment and evaluation. *Smart Structures and Systems* **6**, 439–459 (2010). doi: [10.12989/sss.2010.6.5.439](#)
- J.-B. Ihn, F.-K. Chang, Detection and monitoring of hidden fatigue crack growth using a built-in piezoelectric sensor/actuator network: I. Diagnostics. *Smart Mater. Struct.* **13**, 609–620 (2004). doi: [10.1088/0964-1726/13/3/020](#)
- X. Zhao et al., Active health monitoring of an aircraft wing with embedded piezoelectric sensor/actuator network: I. Defect detection, localization and growth monitoring. *Smart Mater. Struct.* **16**, 1208–1217 (2007). doi: [10.1088/0964-1726/16/4/032](#)
- X. Zhao et al., Active health monitoring of an aircraft wing with an embedded piezoelectric sensor/actuator network: II. Wireless approaches. *Smart Mater. Struct.* **16**, 1218–1225 (2007). doi: [10.1088/0964-1726/16/4/033](#)
- T. Someya et al., Conformable, flexible, large-area networks of pressure and thermal sensors with organic transistor active matrixes. *Proc. Natl. Acad. Sci. U.S.A.* **102**, 12321–12325 (2005). doi: [10.1073/pnas.0502392102](#); pmid: [16107541](#)
- M. A. McEvoy, N. Correll, Thermoplastic variable stiffness composites with embedded, networked sensing, actuation, and control. *J. Composite Mater.* doi: [10.1177/0021998314525982](#) (2014).
- Y.-L. Park, C. Majidi, R. Kramer, P. Bérard, R. J. Wood, Hyperelastic pressure sensing with a liquid-embedded elastomer. *J. Micromech. Microeng.* **20**, 125029 (2010). doi: [10.1088/0960-1317/20/12/125029](#)
- H. Z. Tan, L. A. Slivovsky, A. Pentland, A sensing chair using pressure distribution sensors. *IEEE/ASME Trans. Mechatronics* **6**, 261 (2001). doi: [10.1109/3516.951364](#)
- J. Zhou et al., Flexible piezotronic strain sensor. *Nano Lett.* **8**, 3035–3040 (2008). doi: [10.1021/nl802367t](#); pmid: [18707178](#)
- T. Yamada et al., A stretchable carbon nanotube strain sensor for human-motion detection. *Nat. Nanotechnol.* **6**, 296–301 (2011). doi: [10.1038/nnano.2011.36](#); pmid: [21441912](#)
- C. Majidi, R. Kramer, R. Wood, A non-differential elastomer curvature sensor for softer-than-skin electronics. *Smart Mater. Struct.* **20**, 105017 (2011). doi: [10.1088/0964-1726/20/10/105017](#)
- F. Gandhi, S.-G. Kang, Beams with controllable flexural stiffness. *Smart Mater. Struct.* **16**, 1179–1184 (2007). doi: [10.1088/0964-1726/16/4/028](#)
- G. Murray, F. Gandhi, Multi-layered controllable stiffness beams for morphing: Energy, actuation force, and material strain considerations. *Smart Mater. Struct.* **19**, 045002 (2010). doi: [10.1088/0964-1726/19/4/045002](#)
- G. McKnight, C. Henry, “Variable stiffness materials for reconfigurable surface applications,” *Proc. SPIE* **5761** Smart Structures and Materials 2005: Active Materials: Behavior and Mechanics (20 May 2005), pp. 119–126. doi: [10.1117/12.601495](#)
- G. McKnight, R. Doty, A. Keefe, G. Herrera, C. Henry, Segmented reinforcement variable stiffness materials for reconfigurable surfaces. *J. Intell. Mater. Syst. Struct.* **21**, 1783–1793 (2010). doi: [10.1177/1045389X10386399](#)
- Q. Meng, J. Hu, A review of shape memory polymer composites and blends. *Compos., Part A Appl. Sci. Manuf.* **40**, 1661–1672 (2009). doi: [10.1016/j.compositesa.2009.08.011](#)
- E. Brown et al., Universal robotic gripper based on the jamming of granular material. *Proc. Natl. Acad. Sci. U.S.A.* **107**, 18809–18814 (2010). doi: [10.1073/pnas.1003250107](#)
- C. S. Haines et al., Artificial muscles from fishing line and sewing thread. *Science* **343**, 868–872 (2014). doi: [10.1126/science.1246906](#); pmid: [24558156](#)
- A. Nespoli, S. Besseghini, S. Pittaccio, E. Villa, S. Viscuso, The high potential of shape memory alloys in developing miniature mechanical devices: A review on shape memory alloy mini-actuators. *Sens. Actuators A Phys.* **158**, 149–160 (2010). doi: [10.1016/j.sna.2009.12.020](#)
- S. J. Furst, G. Bunget, S. Seelecke, Design and fabrication of a bat-inspired flapping-flight platform using shape memory alloy muscles and joints. *Smart Mater. Struct.* **22**, 014011 (2013). doi: [10.1088/0964-1726/22/1/014011](#)
- C. D. Onal, R. J. Wood, D. Rus, Towards printable robotics: Origami-inspired planar fabrication of three-dimensional mechanisms. *IEEE International Conference on Robotics and Automation* (IEEE, New York, 2011), pp. 4608–4613. doi: [10.1109/ICRA.2011.5980139](#)
- G. K. Klute, J. M. Czerniecki, B. Hannaford, McKibben artificial muscles: Pneumatic actuators with biomechanical intelligence. *Proceedings of IEEE/ASME International Conference on Advanced Intelligent Mechatronics* (IEEE, New York, 1999), pp. 221–226. doi: [10.1109/AIM.1999.803170](#)
- K. Takashima, J. Rossiter, T. Mukai, McKibben artificial muscle using shape-memory polymer. *Sens. Actuators A Phys.* **164**, 116–124 (2010). doi: [10.1016/j.sna.2010.09.010](#)
- M. De Volder, D. Reynaerts, Pneumatic and hydraulic microactuators: A review. *J. Micromech. Microeng.* **20**, 043001 (2010). doi: [10.1088/0960-1317/20/4/043001](#)
- R. F. Shepherd et al., Multigait soft robot. *Proc. Natl. Acad. Sci. U.S.A.* **108**, 20400–20403 (2011). doi: [10.1073/pnas.1116564108](#); pmid: [22123978](#)
- N. Correll, C. D. Onal, H. Liang, E. Schoenfeld, D. Rus, Soft autonomous materials—Using active elasticity and embedded distributed computation. *12th International Symposium on Experimental Robotics*, Springer Tracts in Advanced Robotics (2014), vol. 79, pp. 227–240. doi: [10.1007/978-3-642-28572-1\\_16](#)
- A. D. Marchese, K. Konrad, C. D. Onal, D. Rus, Design, curvature control, and autonomous positioning of a soft and highly compliant 2D robotic manipulator. *IEEE International Conference on Robotics and Automation* (IEEE, New York, 2014). doi: [10.1109/ICRA.2014.6907161](#)
- R. K. Katzschmann, A. D. Marchese, D. Rus, “Hydraulic autonomous soft robotic fish for 3D swimming,” International Symposium on Experimental Robotics (ISER), Marrakech, Morocco, 2014.
- K. Yoshida, K. Kamiyama, J.-Kim, S. Yokota, An intelligent microactuator robust against disturbance using electro-rheological fluid. *Sens. Actuators A Phys.* **175**, 101–107 (2012). doi: [10.1016/j.sna.2011.12.049](#)

66. K. A. Shaikh, S. Li, C. Liu, Development of a latching microvalve employing a low-melting-temperature metal alloy. *J. Microelectromech. Syst.* **17**, 1195–1203 (2008). doi: [10.1109/JMEMS.2008.2003055](https://doi.org/10.1109/JMEMS.2008.2003055)
67. G. N. Greaves, A. L. Greer, R. S. Lakes, T. Rouxel, Poisson's ratio and modern materials. *Nat. Mater.* **10**, 823–837 (2011). doi: [10.1038/nmat3134](https://doi.org/10.1038/nmat3134); pmid: [22020006](https://pubmed.ncbi.nlm.nih.gov/22020006/)
68. C. Henry, G. McKnight, Cellular variable stiffness materials for ultra-large reversible deformations in reconfigurable structures. *Proc. SPIE, Smart Structures and Materials 2006: Active Materials: Behavior and Mechanics* (2006), vol. 6170, p. 12. doi: [10.1117/12.659633](https://doi.org/10.1117/12.659633)
69. J. Suomela, Survey of local algorithms. *ACM Comput. Surv.* **45**, 24 (2013). doi: [10.1145/2431211.2431223](https://doi.org/10.1145/2431211.2431223)
70. M. Duckham, *Decentralized Spatial Computing: Foundations of Geosensor Networks* (Springer, Berlin, 2012).
71. G. Werner-Allen, G. Tewari, A. Patel, M. Welsh, R. Nagpal, Firefly-inspired sensor network synchronicity with realistic radio effects. *Proceedings of the 3rd International Conference on Embedded networked Sensor systems* (Association of Computing Machinery, New York, 2005), pp. 142–153. doi: [10.1145/1098918.1098934](https://doi.org/10.1145/1098918.1098934)
72. J. Beal et al., in *Formal and Practical Aspects of Domain-Specific Languages: Recent Developments* (IGI Global, 2012), pp. 436–501. doi: [10.4018/978-1-4666-2092-6.ch016](https://doi.org/10.4018/978-1-4666-2092-6.ch016)
73. S. Tilak, N. B. Abu-Ghazaleh, W. Heinzelman, A taxonomy of wireless micro-sensor network models. *Mob. Comput. Commun. Rev.* **6**, 28–36 (2002). doi: [10.1145/565702.565708](https://doi.org/10.1145/565702.565708)
74. J. N. Al-Karaki, A. E. Kamal, Routing techniques in wireless sensor networks: A survey. *IEEE Wireless Commun.* **11**, 6 (2004). doi: [10.1109/MWC.2004.1368893](https://doi.org/10.1109/MWC.2004.1368893)
75. P. Santi, Topology control in wireless ad hoc and sensor networks. *ACM Comput. Surv.* **37**, 164 (2005). doi: [10.1145/1089733.1089736](https://doi.org/10.1145/1089733.1089736)
76. C. Intanagonwiwat, D. Estrin, R. Govindan, J. Heidemann, Impact of network density on data aggregation in wireless sensor networks. *Proceedings of the 22nd International Conference on Distributed Computing Systems* (IEEE, New York, 2002), pp. 457–458. doi: [10.1109/ICDCS.2002.1022289](https://doi.org/10.1109/ICDCS.2002.1022289)
77. T. He, J. A. Stankovic, C. Lu, T. Abdelzaher, SPEED: A stateless protocol for real-time communication in sensor networks. *Proceedings. 23rd International Conference on Distributed Computing Systems* (IEEE, New York, 2003), pp. 46–55. doi: [10.1109/ICDCS.2003.1203451](https://doi.org/10.1109/ICDCS.2003.1203451)
78. S. Ma, H. Hosseinmardi, N. Farrow, R. Han, N. Correll, Establishing multi-cast groups in computational robotic materials. *IEEE International Conference on Cyber, Physical and Social Computing* (IEEE, New York, 2012), pp. 311–316. doi: [10.1109/GreenCom.2012.74](https://doi.org/10.1109/GreenCom.2012.74)
79. H. Hosseinmardi, N. Correll, R. Han, *Bloom Filter-Based Ad Hoc Multicast Communication in Cyber-Physical Systems and Computational Materials, Wireless Algorithms, Systems, and Applications* (Springer, 2012), pp. 595–606. doi: [10.1007/978-3-642-31869-6\\_52](https://doi.org/10.1007/978-3-642-31869-6_52)
80. C. Budelmann, B. Krieg-Brückner, From sensorial to smart materials: Intelligent optical sensor network for embedded applications. *J. Intell. Mater. Syst. Struct.* **24**, 2183–2188 (2013). doi: [10.1177/1045389X12462647](https://doi.org/10.1177/1045389X12462647)
81. G. Lanzara, N. Salowitz, Z. Guo, F.-K. Chang, A spider-web-like highly expandable sensor network for multifunctional materials. *Adv. Mater.* **22**, 4643–4648 (2010). doi: [10.1002/adma.201000661](https://doi.org/10.1002/adma.201000661); pmid: [20824665](https://pubmed.ncbi.nlm.nih.gov/20824665/)
82. N. Salowitz et al., Biol.-inspired stretchable network-based intelligent composites. *J. Composite Mater.* **47**, 97–105 (2012). doi: [10.1177/0021998312442900](https://doi.org/10.1177/0021998312442900)
83. P. J. Skabara, N. J. Findlay, *Polymer Electronics. Oxford Master Series in Physics 22. By Mark Geoghegan and Georges Hadzioannou.* (Wiley Online Library, 2014). doi: [10.1002/anle.201310074](https://doi.org/10.1002/anle.201310074)
84. A. Teichler, J. Perelaer, U. S. Schubert, Inkjet printing of organic electronics—comparison of deposition techniques and state-of-the-art developments. *J. Mater. Chem. C* **1**, 1910 (2013). doi: [10.1039/c2tc00255h](https://doi.org/10.1039/c2tc00255h)
85. Y. Menguc et al., Wearable soft sensing suit for human gait measurement. *Int. J. Robot. Res.* **33**, 1748–1764 (2014). doi: [10.1177/0278364914543793](https://doi.org/10.1177/0278364914543793)
86. A. Islam, H. N. Hansen, P. T. Tang, J. Sun, Process chains for the manufacturing of molded interconnect devices. *Int. J. Adv. Manuf. Technol.* **42**, 831–841 (2009). doi: [10.1007/s00170-008-1660-9](https://doi.org/10.1007/s00170-008-1660-9)
87. R. Merz, F. Prinz, K. Ramaswami, M. Terk, L. Weiss, *Shape Deposition Manufacturing* (Engineering Design Research Center, Carnegie Mellon Univ., Pittsburgh, PA, 1994).
88. S. J. Leigh, R. J. Bradley, C. P. Purssell, D. R. Billson, D. A. Hutchins, A simple, low-cost conductive composite material for 3D printing of electronic sensors. *PLOS ONE* **7**, e49365 (2012). doi: [10.1371/journal.pone.0049365](https://doi.org/10.1371/journal.pone.0049365); pmid: [23185319](https://pubmed.ncbi.nlm.nih.gov/23185319/)
89. K. Y. Ma, P. Chirarattananon, S. B. Fuller, R. J. Wood, Controlled flight of a biologically inspired, insect-scale robot. *Science* **340**, 603–607 (2013). doi: [10.1126/science.1231806](https://doi.org/10.1126/science.1231806); pmid: [23641114](https://pubmed.ncbi.nlm.nih.gov/23641114/)
90. J. E. Marsden, G. W. Patrick, S. Shkoller, Multisymplectic geometry, variational integrators, and nonlinear PDEs. *Commun. Math. Phys.* **199**, 351–395 (1998). doi: [10.1007/s002200050505](https://doi.org/10.1007/s002200050505)
91. E. R. Johnson, T. D. Murphey, Scalable variational integrators for constrained mechanical systems in generalized coordinates. *IEEE Trans. Robotics* **25**, 1249 (2009). doi: [10.1109/TRO.2009.2032955](https://doi.org/10.1109/TRO.2009.2032955)
92. T. Toffoli, N. Margolus, Programmable matter: Concepts and realization. *Physica D* **47**, 263–272 (1991). doi: [10.1016/0167-2789\(91\)90296-L](https://doi.org/10.1016/0167-2789(91)90296-L)
93. R. D'Andrea, G. E. Dullerud, Distributed control design for spatially interconnected systems. *IEEE Trans. Automatic Control* **48**, 1478 (2003). doi: [10.1109/TAC.2003.816954](https://doi.org/10.1109/TAC.2003.816954)
94. C. Langbort, R. S. Chandra, R. D'Andrea, Distributed control design for systems interconnected over an arbitrary graph. *IEEE Trans. Automatic Control* **49**, 1502 (2004). doi: [10.1109/TAC.2004.834123](https://doi.org/10.1109/TAC.2004.834123)
95. R. Scattolini, Architectures for distributed and hierarchical model predictive control—a review. *J. Process Contr.* **19**, 723–731 (2009). doi: [10.1016/j.jprocont.2009.02.003](https://doi.org/10.1016/j.jprocont.2009.02.003)
96. A. Hofstein, V. N. Lunetta, The laboratory in science education: Foundations for the twenty-first century. *Sci. Educ.* **88**, 28–54 (2004). doi: [10.1002/sce.10106](https://doi.org/10.1002/sce.10106)

#### ACKNOWLEDGMENTS

We are grateful to the Air Force Office of Scientific Research, NASA, NSF, Defense Advanced Research Projects Agency, and Army Research Office for support of this work.

10.1126/science.1261689



## REPORTS

## MICELLE ASSEMBLY

# Multidimensional hierarchical self-assembly of amphiphilic cylindrical block comicelles

Huibin Qiu,<sup>1</sup> Zachary M. Hudson,<sup>1</sup> Mitchell A. Winnik,<sup>2\*</sup> Ian Manners<sup>1\*</sup>

Self-assembly of molecular and block copolymer amphiphiles represents a well-established route to micelles with a wide variety of shapes and gel-like phases. We demonstrate an analogous process, but on a longer length scale, in which amphiphilic P-H-P and H-P-H cylindrical triblock comicelles with hydrophobic (H) or polar (P) segments that are monodisperse in length are able to self-assemble side by side or end to end in nonsolvents for the central or terminal segments, respectively. This allows the formation of cylindrical supermicelles and one-dimensional (1D) or 3D superstructures that persist in both solution and the solid state. These assemblies possess multiple levels of structural hierarchy in combination with existence on a multimicrometer-length scale, features that are generally only found in natural materials.

**A**mphiphiles such as molecular surfactants and block copolymers have been shown to form a rich variety of self-assembled nanoscopic structures, including spherical micelles, cylinders, nanotubes, bilayers, and vesicles as well as gel-like phases (1, 2). The construction of hierarchical colloidal materials on a longer length scale by use of spherical nanoparticles (3, 4), branched nanocrystals (5), nano-

rods (6), and nanocubes (7) has also recently been the subject of intense investigation. Control over the size, shape, and composition of these nanoscopic building blocks has enabled the formation of superstructures with substantial structural diversity (3, 7). Self-assembly of Janus and patchy nanoparticles formed by surface modification (8, 9) or from block copolymers (10), including diblock (11) and star (12) or linear triblock copolymers (13–15), has further broadened the range of superstructures that can be prepared. Nevertheless, despite these impressive recent advances, the use of anisotropic amphiphilic building blocks derived from soft matter

remains limited; examples include polymer-based (16) and polymer-metal hybrid nanorods (17, 18) and self-assembled nanotubes and cylinders (19, 20). These approaches represent the first steps toward the creation of tailored, functional hierarchical structures on the multimicrometer-length scale, a size domain currently dominated by biological assemblies.

We focused on the hierarchical self-assembly of amphiphilic cylindrical P-H-P triblock comicelles, as well as H-P-H triblock comicelles with an inverse sequence of the hydrophobic (H) and polar (P) segments. Their hierarchical self-assembly was controlled by means of solvent composition by using nonpolar hydrophobic hexane (or decane) and polar hydrophilic isopropanol (iPrOH). When added alone, these miscible solvents induce the stacking of the P or H segments, respectively. The triblock comicelles were prepared by means of living crystallization-driven self-assembly (CDSA) in a mixture of hexane and iPrOH (1:3 v/v), a medium in which the comicelles are individually dispersed. Block copolymers with a crystallizable poly(ferrocenyldimethylsilane) (PFS) core-forming block were used as precursors and possessed either a nonpolar, corona-forming H block [poly(dimethylsiloxane) (PDMS)] or poly(methylvinylsiloxane) (PMVS)], or a complementary P block [poly(2-vinylpyridine) (P2VP)], to form the micelle periphery (Fig. 1 and fig. S1). The triblock comicelle building blocks were monodisperse in both the H and P segment lengths, a feature that is characteristic of the living CDSA method (21–23).

Noncentrosymmetric H-H-P (24) and centrosymmetric P-H-P (25) amphiphilic triblock comicelles self-assemble in polar media to form spherical supermicelles of size 1 to 5  $\mu\text{m}$  with various aggregation numbers. However, attempts to prepare cylindrical morphologies from P-H-P triblock comicelles by the use of a hydrophobic

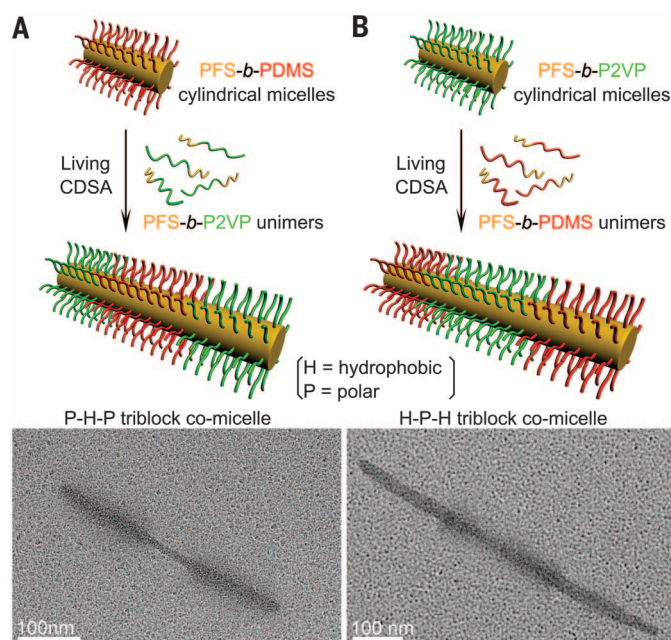


**Fig. 1. Formation of amphiphilic cylindrical P-H-P and H-P-H triblock comicelle building blocks via living CDSA.** (A) P-H-P triblock comicelles with a nonpolar, hydrophobic central segment (H) and two polar terminal segments (P) formed by the addition of PFS<sub>48</sub>-b-P2VP<sub>414</sub> unimers to a solution of monodisperse cylindrical seed micelles of PFS<sub>48</sub>-b-PDMS<sub>504</sub>. (B) H-P-H triblock comicelles with an inverse sequence of the hydrophobic and polar segments formed by the addition of PFS<sub>49</sub>-b-PDMS<sub>504</sub> unimers to a solution of monodisperse cylindrical seed micelles of PFS<sub>48</sub>-b-P2VP<sub>414</sub>. PDMS corona regions are not visible in the TEM image because of insufficient electron density contrast. The widths of the PFS cores are different for the H and P segments, which is often a feature of living CDSA processes that involve compositionally different block copolymer structures. The PFS core-forming block and the PDMS and P2VP corona-forming blocks are indicated by orange, red, and green colors, respectively.

segment of increased length led only to poorly defined elongated structures (fig. S2). This is likely a result of the use of a terminal P segment with a large degree of polymerization (P2VP<sub>414</sub>),

which generates a voluminous hydrophilic corona [overall diameter as observed with transmission electron microscopy (TEM) in dry state, ~70 nm (fig. S3A)] that disrupts the stacking of

the hydrophobic segments through repulsive interactions (fig. S2C) (25). We envisaged that efficient side-by-side stacking of the central core-forming segment of the triblock comicelle

## Fig. 2. 1D supermicelles through side-by-side stacking of P-H-P triblock comicelles.

(A) TEM images of train track–like superstructures formed by P<sub>55 nm</sub>-H<sub>35 nm</sub>-P<sub>55 nm</sub> (H = PFS<sub>55</sub>-*b*-PMVS<sub>825</sub>, P = PFS<sub>34</sub>-*b*-P2VP<sub>272</sub>) triblock comicelles formed on drying from a mixture of hexane and iPrOH (1:3 v/v). (B) TEM images of supermicelles with a tighter parallel stacking of P<sub>80 nm</sub>-H<sub>55 nm</sub>-P<sub>80 nm</sub> (P = PFS<sub>34</sub>-*b*-P2VP<sub>272</sub>) triblock comicelles formed in iPrOH. (C) TEM images of a cylindrical brushlike supermicelle formed by P<sub>340 nm</sub>-H<sub>35 nm</sub>-P<sub>340 nm</sub> (P = PFS<sub>20</sub>-*b*-P2VP<sub>140</sub>) triblock comicelles in iPrOH. (D) TEM (left) and optical microscopy (right) images of cylindrical brushlike supermicelles formed by P<sub>560 nm</sub>-H<sub>35 nm</sub>-P<sub>560 nm</sub> (P = PFS<sub>20</sub>-*b*-P2VP<sub>140</sub>) triblock comicelles formed in iPrOH. (E) TEM and optical microscopy (inset) images of longer cylindrical supermicelles formed by P<sub>220 nm</sub>-H<sub>55 nm</sub>-P<sub>220 nm</sub> (P = PFS<sub>20</sub>-*b*-P2VP<sub>140</sub>) triblock comicelles in iPrOH. TEM analysis was performed after solvent evaporation. Optical microscopy characterization of the solutions was performed in sealed rectangular capillary tubes. Because of repulsions between the solvated coronas of the P sections, in solution the supermicelles in (C) to (E) likely take up a twisted structure in which the parallel stacking of the H sections is slightly compromised, rather than the 2D structure revealed by TEM in the dry state.

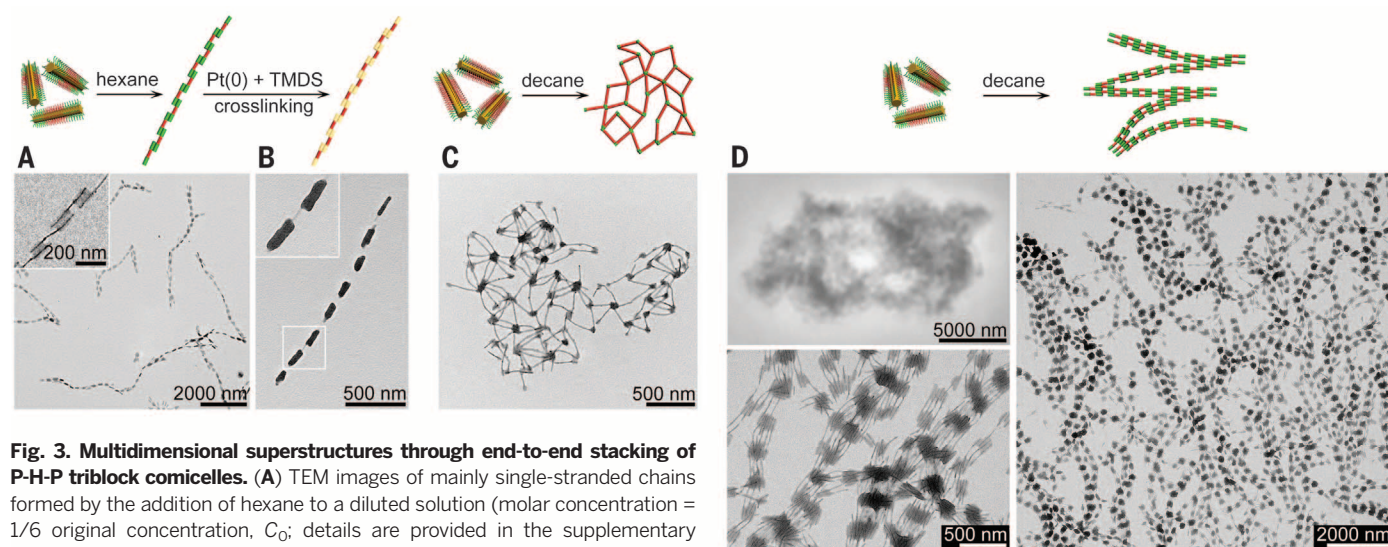
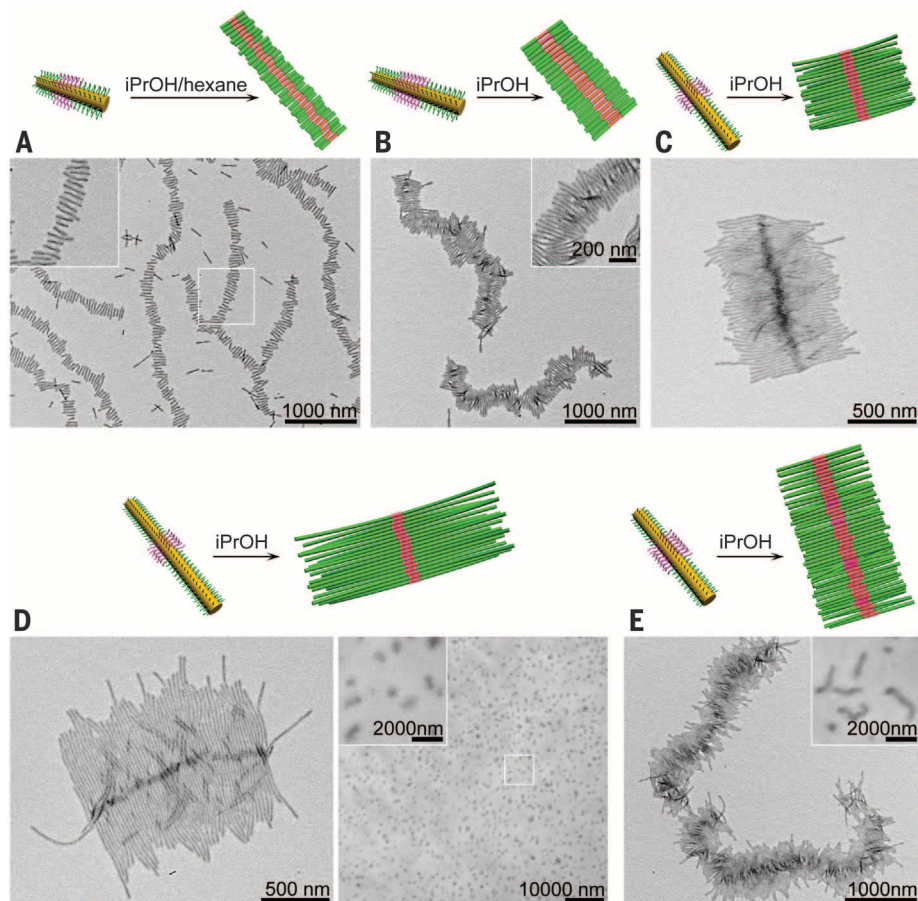


## Fig. 3. Multidimensional superstructures through end-to-end stacking of P-H-P triblock comicelles.

(A) TEM images of mainly single-stranded chains formed by the addition of hexane to a diluted solution (molar concentration = 1/6 original concentration,  $C_0$ ; details are provided in the supplementary materials) of P<sub>145 nm</sub>-H<sub>110 nm</sub>-P<sub>145 nm</sub> (H = PFS<sub>49</sub>-*b*-PDMS<sub>504</sub>, P = PFS<sub>48</sub>-*b*-P2VP<sub>414</sub>) triblock comicelles in 1:3 (v/v) hexane/iPrOH. (B) TEM images of an immobilized chain formed by intermicellar cross-linking of P2VP coronas of stacked terminal segments. (C) TEM image of an irregular network formed by the addition of decane to a solution (concentration =  $C_0$ ) of P<sub>50 nm</sub>-H<sub>190 nm</sub>-P<sub>50 nm</sub> triblock comicelles in 1:3 (v/v) hexane/iPrOH. (D) Optical microscopy (top left) and TEM (bottom left and right) images of chain networks formed by the addition of decane to a diluted solution (concentration = 1/10  $C_0$ ) of P<sub>145 nm</sub>-H<sub>110 nm</sub>-P<sub>145 nm</sub> triblock comicelles in 1:3 (v/v) hexane/iPrOH.



is necessary to form well-defined and robust cylindrical structures. Two block copolymers with shorter P2VP blocks, PFS<sub>34</sub>-*b*-P2VP<sub>272</sub> and PFS<sub>20</sub>-*b*-P2VP<sub>140</sub>, were therefore used. The resulting P-H-P triblock comicelles were shown by TEM to possess substantially smaller overall terminal P segment diameters (~40 nm and 20 nm in dry state, respectively) (fig. S3), indicating that the corresponding intermicellar steric interactions in supermicelle coronas should be appreciably reduced. Indeed, on formation of a polar colloidal solution (hexane, iPrOH 1:3 v/v) of the triblock comicelles P<sub>55 nm</sub>-H<sub>35 nm</sub>-P<sub>55 nm</sub> (H<sub>p</sub> = PFS<sub>55</sub>-*b*-PMVS<sub>825</sub> and P<sub>p</sub> = PFS<sub>34</sub>-*b*-P2VP<sub>272</sub>; the subscripts “*h*” and “*p*” depict the segment length in nanometers) with a P segment of ~40 nm diameter, well-defined “train track-like” superstructures were observed by means of TEM after solvent evaporation due to side-by-side packing (Fig. 2A and fig. S4). The average separation between two parallel triblock comicelles as observed with TEM (corresponding to a low electron density and therefore an invisible region of coronal overlap for the H segments) was found to be ~44 nm, which is slightly larger

than the overall diameter of the terminal segments (~40 nm). Longer P<sub>80 nm</sub>-H<sub>55 nm</sub>-P<sub>80 nm</sub> triblock comicelles with a slightly larger *h/p* ratio (0.69 versus 0.64) from the same block copolymer constituents were found to afford supermicelles with a significantly tighter packing (average separation, ~30 nm) (Fig. 2B). However, to increase the stacking interactions still further so as to create robust cylindrical architectures, we studied the self-assembly of P-H-P (P = PFS<sub>20</sub>-*b*-P2VP<sub>140</sub>) triblock comicelles with terminal P segments ~20 nm in diameter and various segment lengths and *h/p* ratios in iPrOH. This afforded a variety of well-defined supermicelles of length 1 to 10 μm with a cylindrical morphology (Fig. 2, C to E). Presumably with terminal P segments of even smaller diameter, the steric repulsions are further reduced, and the central H segments were very tightly stacked, as revealed by an apparent dark thread via TEM. The formation of persistent cylindrical supermicelles was confirmed by their existence in solution, as demonstrated with optical microscopy in iPrOH (Fig. 2, D and E, inset; fig. S5).

We also explored the formation of multi-dimensional superstructures by the intermicellar association of terminal segments using P-H-P triblock comicelles with spatially demanding ~70-nm-diameter P2VP<sub>414</sub> coronas for the terminal P segments so as to favor intermicellar association. To trigger assembly, hexane or decane was rapidly added to a colloidal solution of the triblock comicelles (in 1:3 v/v hexane/iPrOH) so that the volume ratio of nonpolar to polar solvent reached 3:1 v/v.

When hexane was used, the end-to-end association yielded discrete superstructures. For the triblock comicelles with relatively short terminal P segments (*p* = 50 nm), the association predominantly gave irregular loops (for example, for P<sub>50 nm</sub>-H<sub>260 nm</sub>-P<sub>50 nm</sub>) (fig. S7). The terminal segments became fully overlapped at *p* > 100 nm, and the assembly was restricted to a single direction, favoring the formation of linear chainlike superstructures (for example, for P<sub>145 nm</sub>-H<sub>110 nm</sub>-P<sub>145 nm</sub>) (Fig. 3A and fig. S8A). Multiply stranded chains were formed by using more concentrated triblock comicelle solutions (fig. S8A), whereas single-stranded structures resulted when under

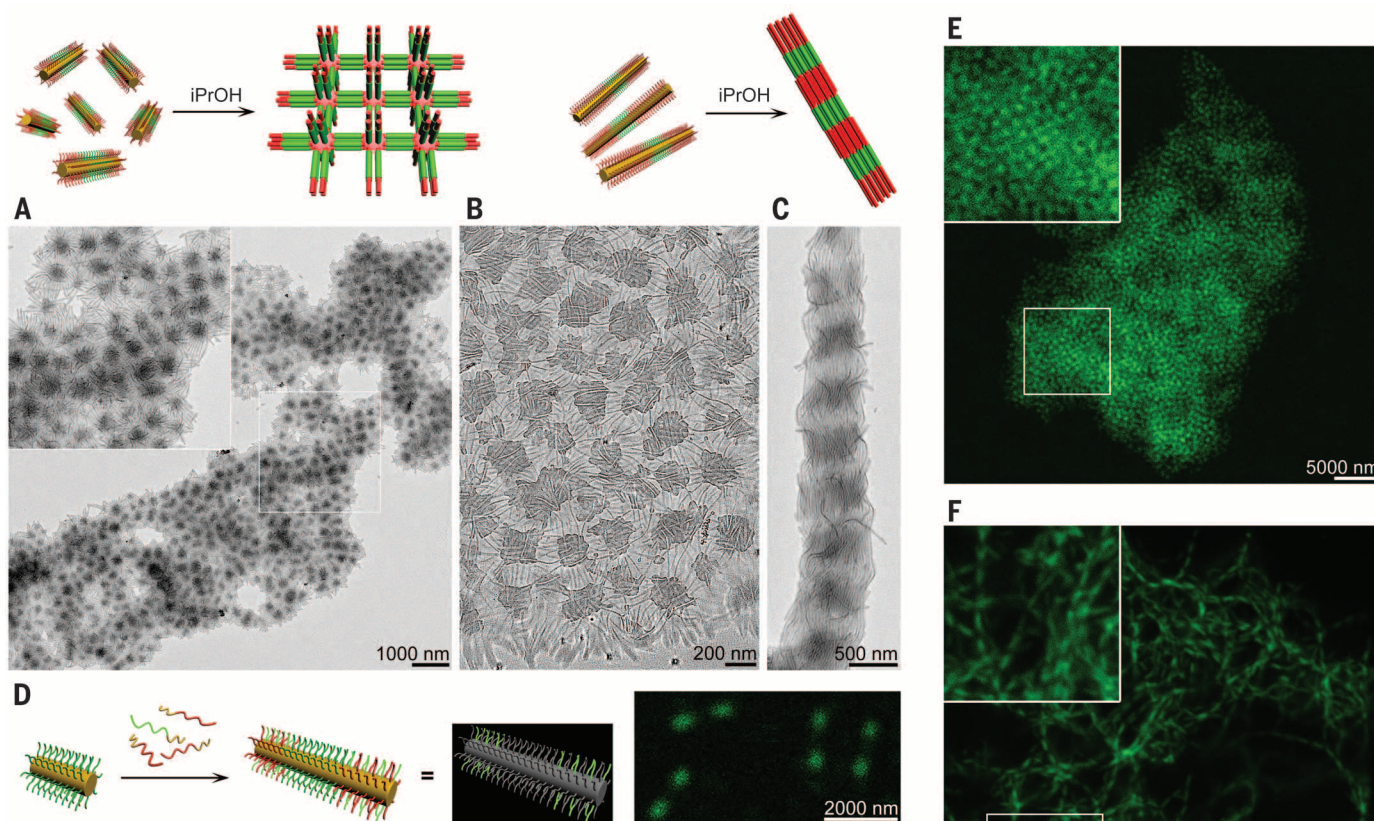


**Fig. 4. 3D and 1D superlattices through end-to-end stacking of H-P-H triblock comicelles.** (A) TEM images of a 3D superlattice formed by H<sub>105 nm</sub>-P<sub>160 nm</sub>-H<sub>105 nm</sub> (P = PFS<sub>48</sub>-*b*-P2VP<sub>414</sub>, H = PFS<sub>49</sub>-*b*-PDMS<sub>504</sub>) triblock comicelles. (B) A 3D superlattice revealed with electron tomography and 3D structural reconstruction. (C) TEM image of a 1D superlattice formed by H<sub>410 nm</sub>-P<sub>160 nm</sub>-H<sub>410 nm</sub> triblock comicelles. (D) Preparation of fluorescent (H/H<sub>G</sub>)-P-(H/H<sub>G</sub>) triblock comicelles and CLSM image of (H/H<sub>G</sub>)<sub>300 nm</sub>-P<sub>570 nm</sub>-(H/H<sub>G</sub>)<sub>300 nm</sub> triblock comicelles. The fluorescent corona-forming block of PFS<sub>62</sub>-*b*-(PDMS<sub>605</sub>-*r*-G<sub>21</sub>) is indicated in bright green. (E) CLSM images of a 3D superlattice formed by (H/H<sub>G</sub>)<sub>300 nm</sub>-P<sub>570 nm</sub>-(H/H<sub>G</sub>)<sub>300 nm</sub> triblock comicelles in iPrOH. (F) CLSM images of a 1D superlattice formed by (H/H<sub>G</sub>)<sub>745 nm</sub>-P<sub>570 nm</sub>-(H/H<sub>G</sub>)<sub>745 nm</sub> triblock comicelles in iPrOH.

dilute conditions (Fig. 3A). These chainlike superstructures can be readily made permanent through intermicellar cross-linking of the P2VP coronas of the interacting terminal segments, via coordination of the P2VP pyridyl groups with small Pt nanoparticles (Fig. 3B) (26, 27). The ends of the triblock comicelles also remained active toward living CDSA, as demonstrated by the addition of further unimer, enabling the subsequent growth of cylindrical micelle brushes (fig. S10).

The degree of end-to-end association dramatically increased when decane was used as the nonpolar solvent. This led to an additional level of hierarchical self-assembly, yielding large superstructures that extended in more than one dimension. For example, the triblock comicelles with short terminal segments ( $p = 50$  nm) formed irregular multidimensional architectures in decane [for example, for  $P_{50\text{ nm}}\text{-H}_{100\text{ nm}}\text{-P}_{50\text{ nm}}$  (Fig. 3C) and  $P_{50\text{ nm}}\text{-H}_{110\text{ nm}}\text{-P}_{50\text{ nm}}$  (fig. S11)], in which the end-to-end association was random in direction, giving superstructures composed of cross looplike units. In contrast, the association of micelles with longer terminal segments (such as  $P_{145\text{ nm}}\text{-H}_{110\text{ nm}}\text{-P}_{145\text{ nm}}$ ) produced disordered superstructures in more concentrated solutions (fig. S8B) but large and continuous networks of chains, with long, multiply stranded subunits connected by “bridging” micelle chains in dilute solution (Fig. 3D and fig. S12).

In previous studies (25), the nonpolar central H segments of P-H-P triblock comicelles stacked crosswise during the self-assembly in polar media to form spherical supermicelles (fig. S2, A and B). This type of organization for terminal H segments yields higher-dimensional assemblies. For example, we found that H-P-H triblock comicelle cylinders ( $P = \text{PFS}_{48}\text{-}b\text{-P2VP}_{414}$ ,  $H = \text{PFS}_{49}\text{-}b\text{-PDMS}_{504}$ ) self-assemble into a variety of multidimensional superlattices in iPrOH (for  $H_h\text{-P}_{160\text{ nm}}\text{-H}_h$  where  $h = 70, 105, 250$ , or  $410$  nm) (Fig. 4 and fig. S13). When the terminal segments were relatively short (such as  $h = 105$  nm), the H-P-H triblock comicelles preferred to form regular 3D superstructures. TEM analysis revealed dark (electron-dense) regions derived from intermicellar association of the H segments and lighter regions with relatively loosely bundled central P segments (Fig. 4A and fig. S13B). TEM images acquired in a thinner region of the sample showed that the darker dots formed an array with a  $d$ -spacing of  $\sim 310$  nm (Fig. 4A). Further insight into the organization of the triblock comicelles in the superlattices was revealed through structural reconstruction based on electron tomography (Fig. 4B, fig. S14, and movie S1). The darker areas consisting of cross-stacked terminal H segments were woven together by the central P segments across several layers. As the length of the terminal segments was increased, the three-dimensional (3D) superlattices started to deform, and the darker regions began to fuse into strips (for example, for  $h = 250$  nm) (fig. S13C). In contrast, 1D superstructures formed as the length of the terminal H segments was increased to above  $400$  nm (for

example,  $h = 410$  nm) (Fig. 4C and fig. S13D), and the triblock comicelles aligned in a parallel fashion, forming periodically segmented 1D columnlike structures. Analogous experiments for triblock comicelle cylinders with a longer central segment ( $p = 325$  nm) revealed similar 3D to 1D structural changes, with an increase in the length of the terminal segments ( $h \leq 350$  nm for 3D and  $h \geq 550$  nm for 1D superlattices) (fig. S15). In this case, values of  $h/p < \sim 1$  favored 3D assemblies, whereas  $h/p$  ratios  $> \sim 1.5$  led to a preference for 1D superstructures (table S4).

To enable direct characterization of the superlattices in solution, green fluorescent dye-labeled  $\text{PFS}_{62}\text{-}b\text{-}(\text{PDMS}_{605}\text{-}T\text{-}G_{21})$  (28) was blended with  $\text{PFS}_{49}\text{-}b\text{-}PDMS_{504}$  to form fluorescent hydrophobic terminal segments,  $H/H_G$  (Fig. 4D and fig. S1). The resulting  $(H/H_G)_h\text{-}P_p\text{-}(H/H_G)_h$  ( $H/H_G = 3:1$  by mass) triblock comicelles were readily visualized in solution by means of confocal laser scanning microscopy (CLSM) (Fig. 4D). Because of the resolution limits of CLSM (fig. S16), we focused on the superlattices formed by the triblock comicelles with longer central segments ( $p = 570$  nm) (Fig. 4D and figs. S17 and S19). CLSM images (Fig. 4, E and F; figs. S18 and S19; and movie S2) clearly showed that the  $(H/H_G)_{300\text{ nm}}\text{-}P_{570\text{ nm}}\text{-}(H/H_G)_{300\text{ nm}}$  triblock comicelles with  $h/p \sim 0.5$  formed 3D superlattices, whereas the  $(H/H_G)_{745\text{ nm}}\text{-}P_{570\text{ nm}}\text{-}(H/H_G)_{745\text{ nm}}$  triblock comicelles, with longer terminal segments and  $h/p \sim 1.3$ , formed segmented 1D superstructures. It was also apparent that in several domains of the 3D superlattices, the fluorescent dots were arranged in a pseudorectangular lattice with repeat spacing of  $\sim 760$  nm (Fig. 4E, inset). The use of triblock comicelles with either green- or red fluorescent dye-labeled central hydrophobic segments ( $H/H_G$  or  $H/H_R$ ) also provided evidence for the lack of micelle building block exchange in solution for both cylindrical supermicelles (fig. S6) and 1D chainlike superstructures (fig. S9) over 7 days at  $22^\circ\text{C}$ . This indicated that the assemblies formed should be regarded as kinetically trapped rather than equilibrium structures.

Amphiphilic cylindrical triblock comicelles afford a wide variety of superstructures through side-by-side stacking and end-to-end intermicellar association (tables S1, S3, and S4). The process is readily controlled by altering the comicelle architecture in terms of the sequence, chemistries, lengths, and diameters of the various segments, as well as the nature of the solvent used. Despite the observation that the self-assembled materials are not formed under equilibrium conditions, the spherical and cylindrical morphologies generated by side-by-side assembly can be qualitatively rationalized through trends in the critical packing parameter, a concept developed for molecular surfactants (table S2). The formation of 1D or 3D superlattices by means of end-to-end assembly is related to the  $h/p$  ratio where a larger value favors parallel (1D) stacking (table S4). The coronal blocks can be readily functionalized (as illustrated with fluorescent dyes) and cross-linked; moreover, the CDSA method is applicable to a variety of crystallizable

block copolymers and related species (28, 29), including those based on semiconducting (2, 30) and biodegradable materials (31). The approach described therefore offers opportunities to develop functional and robust micrometer-scale assemblies with potential applications in areas such as sensing and biomedicine and also in optoelectronics and as photonic crystals.

## REFERENCES AND NOTES

1. D. Myers, *Surfactant Science and Technology* (Wiley, Hoboken, NJ, ed. 3, 2005).
2. W. Zhang et al., *Science* **334**, 340–343 (2011).
3. F. Li, D. P. Josephson, A. Stein, *Angew. Chem. Int. Ed. Engl.* **50**, 360–388 (2011).
4. I.-H. Lee et al., *J. Am. Chem. Soc.* **135**, 17695–17698 (2013).
5. K. Misztal et al., *Nat. Mater.* **10**, 872–876 (2011).
6. T. Wang et al., *Science* **338**, 358–363 (2012).
7. Z. Quan, J. Fang, *Nano Today* **5**, 390–411 (2010).
8. Q. Chen, S. C. Bae, S. Granick, *Nature* **469**, 381–384 (2011).
9. Q. Chen et al., *Science* **331**, 199–202 (2011).
10. A. Walther, A. H. E. Müller, *Chem. Rev.* **113**, 5194–5261 (2013).
11. K.-Y. Yoon et al., *J. Am. Chem. Soc.* **134**, 14291–14294 (2012).
12. Z. Li, E. Kesselman, Y. Talmon, M. A. Hillmyer, T. P. Lodge, *Science* **306**, 98–101 (2004).
13. H. Cui, Z. Chen, S. Zhong, K. L. Wooley, D. J. Pochan, *Science* **317**, 647–650 (2007).
14. J. Dupont, G. Liu, *Soft Matter* **6**, 3654–3661 (2010).
15. A. H. Gröschel et al., *Nature* **503**, 247–251 (2013).
16. J.-Y. Wang, Y. Wang, S. S. Sheiko, D. E. Betts, J. M. DeSimone, *J. Am. Chem. Soc.* **134**, 5801–5806 (2012).
17. K. Liu et al., *Science* **329**, 197–200 (2010).
18. Z. Nie et al., *Nat. Mater.* **6**, 609–614 (2007).
19. X. Yan, G. Liu, Z. Li, *J. Am. Chem. Soc.* **126**, 10059–10066 (2004).
20. A. Walther et al., *J. Am. Chem. Soc.* **131**, 4720–4728 (2009).
21. X. Wang et al., *Science* **317**, 644–647 (2007).
22. J. B. Gilroy et al., *Nat. Chem.* **2**, 566–570 (2010).
23. J. Qian et al., *ACS Nano* **7**, 3754–3766 (2013).
24. P. A. Ruper, L. Chabanne, M. A. Winnik, I. Manners, *Science* **337**, 559–562 (2012).
25. H. Qiu et al., *Angew. Chem. Int. Ed. Engl.* **51**, 11882–11885 (2012).
26. R. K. O'Reilly, C. J. Hawker, K. L. Wooley, *Chem. Soc. Rev.* **35**, 1068–1083 (2006).
27. H. Qiu, V. A. Du, M. A. Winnik, I. Manners, *J. Am. Chem. Soc.* **135**, 17739–17742 (2013).
28. Z. M. Hudson, D. J. Lunn, M. A. Winnik, I. Manners, *Nat. Commun.* **5**, 3372 (2014).
29. J. Schmelz, A. E. Schedl, C. Steinlein, I. Manners, H. Schmalz, *J. Am. Chem. Soc.* **134**, 14217–14225 (2012).
30. J. Qian et al., *J. Am. Chem. Soc.* **136**, 4121–4124 (2014).
31. L. Sun et al., *Nat. Commun.* **5**, 5746 (2014).

## ACKNOWLEDGMENTS

H.Q. acknowledges the European Union (EU) for a Marie Curie Postdoctoral Fellowship and the European Research Council (ERC) for a Postdoctoral Fellowship. Z.M.H. is grateful to the EU for a Marie Curie Postdoctoral Fellowship. I.M. thanks the EU for an ERC Advanced Investigator Grant. M.A.W. thanks the Natural Sciences and Engineering Research Council of Canada for financial support. The authors also thank J. Mantell and A. Leard (Wolfson Biomaging Facility, University of Bristol) for TEM, CLSM, and optical microscopy imaging and tomography analysis. H.Q. and I.M. conceived the project, and H.Q. performed the experiments. Z.M.H. prepared the fluorescent PFS block copolymers. H.Q., Z.M.H., and I.M. prepared the manuscript with input from M.A.W. The project was supervised by I.M., with input from M.A.W.

## SUPPLEMENTARY MATERIALS

www.sciencemag.org/content/347/6228/1329/suppl/DC1  
Materials and Methods  
Figs. S1 to S19  
Movies S1 and S2  
References (32–37)

29 September 2014; accepted 5 February 2015  
10.1126/science.1261816



## SOLAR PHYSICS

# The crucial role of surface magnetic fields for the solar dynamo

Robert Cameron\* and Manfred Schüssler

Sunspots and the plethora of other phenomena occurring in the course of the 11-year cycle of solar activity are a consequence of the emergence of magnetic flux at the solar surface. The observed orientations of bipolar sunspot groups imply that they originate from toroidal (azimuthally orientated) magnetic flux in the convective envelope of the Sun. We show that the net toroidal magnetic flux generated by differential rotation within a hemisphere of the convection zone is determined by the emerged magnetic flux at the solar surface and thus can be calculated from the observed magnetic field distribution. The main source of the toroidal flux is the roughly dipolar surface magnetic field at the polar caps, which peaks around the minima of the activity cycle.

**T**he basic concept for the large-scale solar dynamo involves a cycle during which the poloidal field and the toroidal field are mutually generated by one another (1, 2). The winding of the poloidal field by differential rotation creates a toroidal field. A reversed poloidal field results from the formation of magnetic loops in the toroidal field, which become twisted by the Coriolis force owing to solar rotation. In turn, the reversed poloidal field then becomes the source of a reversed toroidal field. In this way, the 11-year cycle of solar activity is connected to a 22-year cycle of magnetic polarity.

Hale *et al.* (3) discovered that the magnetic orientations of the eastward and westward parts of bipolar sunspot groups in one solar hemisphere are the same during an 11-year cycle and opposite in the other hemisphere. This implies that the sunspot groups originate from a toroidal field of fixed orientation during a cycle. Toroidal flux of the opposite polarity would lead to sunspot groups violating Hale's law. Because only a small minority of the sunspot groups are actually observed to violate this rule (4), opposite-polarity toroidal field is largely irrelevant as a source of sunspot groups. In other words, it is the hemispheric net toroidal magnetic flux given by the azimuthal average of the toroidal field that is relevant for the formation of sunspot groups.

Here we use a simple method based on Stokes' theorem to show that the emerged surface fields determine the net toroidal flux generated by differential rotation in a solar hemisphere. The time evolution of the net toroidal flux in the convection zone can thus be calculated with only observed quantities (differential rotation and field distribution at the surface). We compare the resulting net toroidal flux with the observed large-scale unsigned surface flux and find that they vary in a similar manner.

We consider spherical polar coordinates,  $(r, \theta, \phi)$ , and the azimuthally averaged induction equation of magnetohydrodynamics

$$\frac{\partial \mathbf{B}}{\partial t} = \nabla \times (\mathbf{U} \times \mathbf{B} + \langle \mathbf{u} \times \mathbf{b} \rangle - \eta \nabla \times \mathbf{B}) \quad (1)$$

where  $\mathbf{B}(r, \theta)$  and  $\mathbf{U}(r, \theta)$  are the  $\phi$ -averaged magnetic field and plasma velocity, respectively, and  $\eta$  is the magnetic diffusivity. Angular brackets indicate the azimuthal average. The term  $\langle \mathbf{u} \times \mathbf{b} \rangle$  denotes the correlation of the fluctuating quantities with respect to the azimuthal averages, which gives rise to the  $\alpha$ -effect and to enhanced ("turbulent") magnetic diffusivity (5).

We define the contour  $\delta\Sigma$  enclosing the area  $\Sigma$  in a meridional plane of the Sun as shown in Fig. 1. The direction of the contour is chosen such that the vectorial surface element of  $\Sigma$  points into the direction of positive azimuthal field,  $B_\phi$ . Applying Stokes' theorem to the integral of the induction equation over  $\Sigma$  yields the time derivative of the net toroidal flux,  $\Phi_{\text{tor}}^N$ , in the northern hemisphere of the convection zone,

$$\begin{aligned} \frac{d\Phi_{\text{tor}}^N}{dt} &= \frac{d}{dt} \left( \int_{\Sigma} B_\phi dS \right) \\ &= \int_{\delta\Sigma} (\mathbf{U} \times \mathbf{B} + \langle \mathbf{u} \times \mathbf{b} \rangle - \eta \nabla \times \mathbf{B}) \cdot d\mathbf{l} \quad (2) \end{aligned}$$

where  $dS$  is the surface element of  $\Sigma$  and  $d\mathbf{l}$  is the line element along  $\delta\Sigma$ . An analogous procedure provides the net toroidal flux in the southern hemisphere,  $\Phi_{\text{tor}}^S$ .

Rotation is by far the dominant component of the azimuthally averaged velocity, so that we write  $\mathbf{U} = U_\phi \hat{\phi} = (\Omega r \sin \theta) \hat{\phi}$ , where  $\Omega(r, \theta)$  is the angular velocity and  $\hat{\phi}$  the unit vector in the azimuthal direction. The effect of  $\int_{\delta\Sigma} \langle \mathbf{u} \times \mathbf{b} \rangle \cdot d\mathbf{l}$  reduces to that of the turbulent magnetic diffusivity,  $\eta_t$ , since the contribution of the  $\alpha$ -effect

to the generation of the toroidal field can be neglected against that of differential rotation (1). With  $\eta_t \gg \eta$ , we thus obtain

$$\frac{d\Phi_{\text{tor}}^N}{dt} = \int_{\delta\Sigma} (\mathbf{U} \times \mathbf{B} - \eta_t \nabla \times \mathbf{B}) \cdot d\mathbf{l} \quad (3)$$

Guided by empirical results from helioseismology (6, 7), we take  $\Omega$  to be independent of  $r$  in the equatorial plane throughout the convection zone (8), i.e.,  $\Omega(r, \pi/2) = \Omega_{\text{eq}}$ . This allows us to work in a reference frame rotating with angular velocity  $\Omega_{\text{eq}}$ , for which  $U_\phi = 0$  in the equatorial plane. We can further assume that the magnetic field does not penetrate the low-diffusivity radiative zone below the convection zone. Together with  $U_\phi = 0$  along the rotational axis, these assumptions imply that only the surface segment (d) in Fig. 1 contributes to the line integral of  $\mathbf{U} \times \mathbf{B}$  along the contour  $\delta\Sigma$ . We obtain

$$\begin{aligned} \int_{\delta\Sigma} (\mathbf{U} \times \mathbf{B}) \cdot d\mathbf{l} &= \int_0^{\pi/2} U_\phi B_r R_\odot d\theta \\ &= \int_0^1 (\Omega - \Omega_{\text{eq}}) B_r R_\odot^2 d(\cos \theta) \quad (4) \end{aligned}$$

where  $U_\phi$ ,  $\Omega$ , and  $B_r$  are to be taken at the solar surface,  $r = R_\odot$ . This shows that the net toroidal flux generated in the convection zone by the action of differential rotation is determined by the poloidal field threading the solar surface. Any additional poloidal flux that is fully contained within the convection zone would lead to equal amounts of east-west- and west-east-orientated toroidal flux, which do not contribute to the net toroidal flux required by Hale's law.

The diffusion term in Eq. 3 is most relevant along the rotational axis, where toroidal flux can be destroyed, and also in the equatorial segment

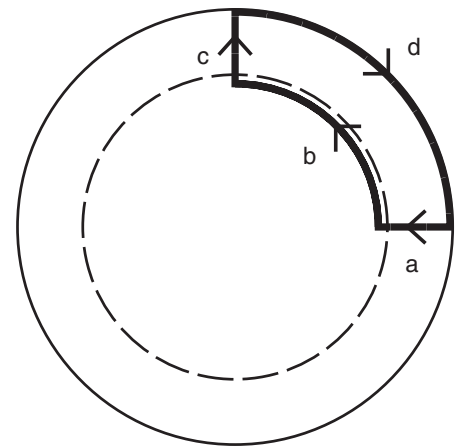


**Fig. 1. Integration contour for the application of Stokes' theorem.** The contour (thick solid line) on a meridional plane of the Sun is used to calculate the net toroidal flux in the northern hemisphere generated by the action of differential rotation on the poloidal field. The thin solid line represents the solar surface, the dashed line the bottom of the convection zone. The rotation poles are at the top and bottom. The contour consists of a radial segment in the equatorial plane (a), a circular arc slightly below the bottom of the convection zone (b), a part along the axis of rotation (c), and the solar surface (d).

Max-Planck-Institut für Sonnensystemforschung, Göttingen 37077, Germany.

\*Corresponding author. E-mail: cameron@mps.mpg.de

of  $\delta\Sigma$ , where flux can be transported between the hemispheres. These processes, which decrease the net magnetic flux, are difficult to quantify. To estimate their effect, we approximate them with an exponential decay term with  $e$ -folding time  $\tau$ . Altogether, we then obtain

$$\frac{d\Phi_{\text{tor}}^N}{dt} = \int_0^1 (\Omega - \Omega_{\text{eq}}) B_r R_\odot^2 d(\cos\theta) - \frac{\Phi_{\text{tor}}^N}{\tau} \quad (5)$$

and an analogous equation for the net toroidal flux generation in the southern hemisphere of the convection zone.

To evaluate the inductive part of Eq. 5, we use the synoptic magnetograms from the Kitt Peak National Observatory from 1975 to the present (9). The azimuthally averaged radial component of the magnetic field,  $B_r$ , as a function of time and  $\cos\theta$  is shown in Fig. 2A, where  $\cos\theta = 0$  represents the equator and  $\cos\theta = \pm 1$  the poles. The profile of the surface differential rotation taken from (10)

$$\Omega - \Omega_{\text{eq}} = -2.3\cos^2\theta - 1.62\cos^4\theta [^\circ/\text{day}] \quad (6)$$

given in Fig. 2B is combined with  $B_r$  to obtain the quantity  $(\Omega - \Omega_{\text{eq}})B_r$  (Fig. 2C), which determines the generation of toroidal flux by differential rotation in Eq. 5. It is dominated by the contribution from the polar regions.

We calculated the time integral of the inductive part of Eq. 5, as well as its counterpart for the southern hemisphere, to obtain the net toroidal flux in both hemispheres as a function of time. The integration begins with zero flux in February 1975, the starting time of the synoptic observations. This is near solar activity minimum, during which time we expect the toroidal flux to change sign. The result given in Fig. 3 shows that the modulus of the toroidal flux generated from the polar fields reaches peak values on the order of  $1 \times 10^{23}$  to  $6 \times 10^{23}$  Mx per hemisphere during recent activity cycles. Note that the net flux generated for the new cycle first has to cancel the opposite-polarity flux from the old cycle, so that it reaches its peak value around activity maximum of the new cycle.

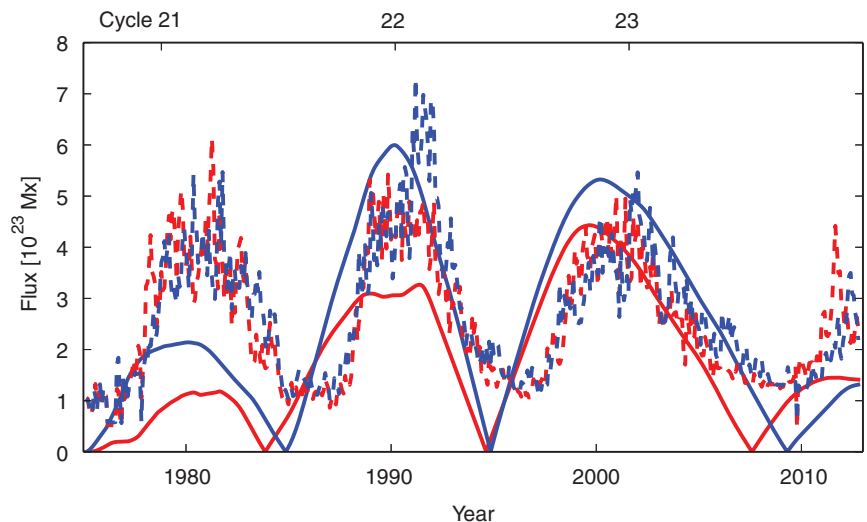
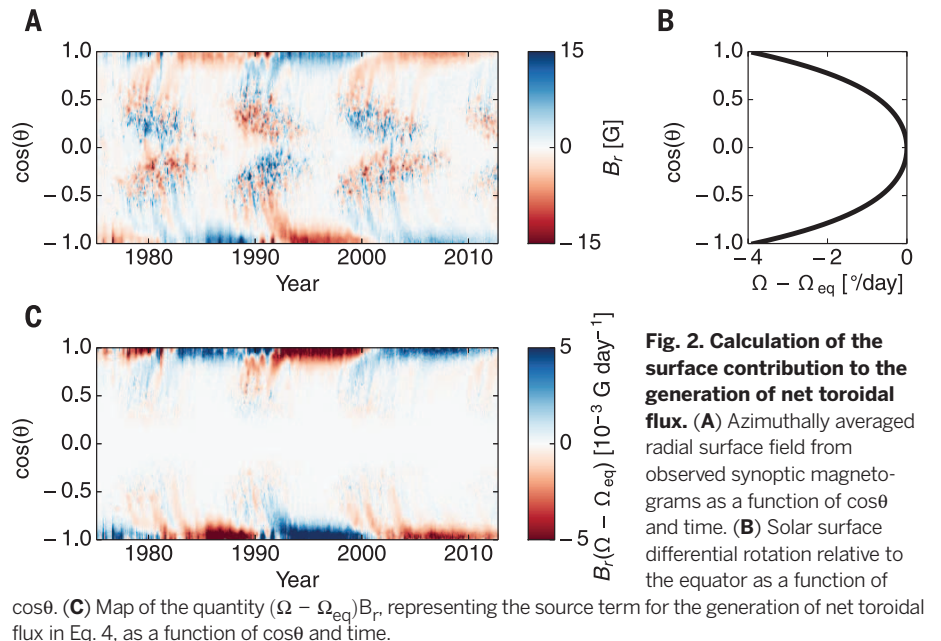
The exponential decay term in Eq. 5 mainly leads to a phase shift of the time evolution: The sign reversals and the maximum values of the toroidal flux occur earlier because the flux from the previous cycle is continuously reduced by the decay. At the same time, the newly generated flux is also subject to the decay, so that the amplitude of the toroidal flux is only weakly affected: Even for the extreme case of  $\tau = 4$  years, the peak values for cycles 22 and 23 are reduced by at most 20 to 30%. Plots analogous to Fig. 3 for various values of  $\tau$  are provided in the supplementary materials.

Is the inferred amount of net toroidal flux sufficient to provide the magnetic flux actually emerging in the form of bigger bipolar magnetic regions and sunspot groups at the solar surface? To estimate their combined fluxes, which provide a rough measure of the subsurface toroidal flux, we calculated the integrated unsigned radial surface flux,  $\Phi_U = \int |B_r| dA$  (where  $dA$  represents the solar surface element), for each hemisphere

on the basis of the Kitt Peak synoptic magnetograms. Because the spatial resolution element of the synoptic magnetograms is on average about  $12 \times 12 \text{ Mm}^2$  on the solar surface,  $\Phi_U$  represents the large-scale flux originating from the emergence of bigger bipolar magnetic regions. Figure 3 shows that the time evolution of  $\Phi_U$  for both hemispheres is very similar to that of the inferred toroidal flux, both with respect to phase as well as to amplitude (11). A short decay time,  $\tau$ , would lead to a notable phase shift, suggesting that the decay term in Eq. 5 has no strong effect on the net flux. Figure 3 indicates that the toroidal flux generated from the polar fields is sufficient to explain the observed time profile and amount of flux emerging in the resolved bipolar regions and

sunspot groups in the course of the solar cycle. Because there is probably considerable randomness in the flux emergence process, leading to elements of toroidal flux emerging more than once at various longitudes or not emerging at all, we cannot expect more than an order-of-magnitude agreement.

Our results demonstrate that the emerged magnetic flux and particularly the polar fields are by far the dominating source of the net toroidal flux in the convection zone, from which the sunspot groups of the subsequent cycle originate. The solenoidality of the magnetic field means that the flux associated with the polar fields threads through the Sun's convection zone, where it is wound up by differential rotation to generate toroidal magnetic flux. We thus confirm the





conjecture of H. W. Babcock (12) that the observed polar fields represent the poloidal field source for the subsurface toroidal field.

As also first suggested by Babcock, the net axial dipole moment represented by the polar fields results from the north-south dipole moments contributed by the individual sunspot groups and bipolar magnetic regions at the surface as a result of their systematic tilt with respect to the east-west direction (3). The tilt probably originates in one way or another from rotation via the Coriolis force: either by providing helicity to convective flows bringing magnetic flux to the surface or by twisting buoyantly rising flux loops. The concept of Babcock was further developed by Leighton (13), who introduced the notion of surface flux transport for the buildup of the polar fields in connection with the dynamo process. More recently, surface flux transport models successfully reproduced the observed evolution of the surface fields and, in particular, the polar fields on the basis of the observed records of sunspot groups as flux input (14–18). This implies that the tilt of the larger bipolar magnetic regions determines the polar fields. Small bipolar regions and small-scale correlations are irrelevant in this respect. Together with the results shown here, this establishes the key part of the surface fields in the solar dynamo process and thus corroborates the basic dynamo concept of Babcock (12) and Leighton (13).

The key role played by the polar fields in the generation of toroidal flux explains the strong empirical correlation between the strength of the polar field (19) and the Sun's open flux (20) around activity minimum with the number of sunspots of the subsequent activity cycle, which can be taken as a proxy for the underlying toroidal flux. Although the correlation is not perfect, which can be ascribed to randomness associated with the flux emergence process, it provides the best available method to predict the strength of the next cycle (21, 22). Our results put this method on a firm physical basis.

## REFERENCES AND NOTES

1. P. Charbonneau, *Living Rev. Sol. Phys.* **7**, 3 (2010); [www.livingreviews.org/lrsp-2010-3](http://www.livingreviews.org/lrsp-2010-3) (accessed 26 January 2015).
2. H. C. Spruit, *The Sun, the Solar Wind, and the Heliosphere*, M. P. Miralles, J. Sánchez Almeida, Eds. (Springer, Berlin, 2011), p. 39.
3. G. E. Hale, F. Ellerman, S. B. Nicholson, A. H. Joy, *Astrophys. J.* **49**, 153 (1919).
4. J. O. Stenflo, A. G. Kosovichev, *Astrophys. J.* **745**, 129 (2012).
5. F. Krause, K. H. Rädler, *Mean-Field Magnetohydrodynamics and Dynamo Theory* (Pergamon, Oxford, 1980).
6. J. Schou et al., *Astrophys. J.* **505**, 390–417 (1998).
7. R. Howe et al., *J. Phys. Conf. Ser.* **271**, 012074 (2011).
8. The effect of the slight radial variation of  $\Omega$  in the near-surface shear layer and in the convection-zone part of the tachocline (6, 7) on the net flux is on the level of a few percent as shown in the supplementary materials.
9. The National Solar Observatory (NSO)–Kitt Peak data used here are produced cooperatively by NSF–NOAO, NASA–Goddard Space Flight Center, and National Oceanic and Atmospheric Administration Space Environment Laboratory. This work utilizes SOLIS data obtained by the NSO Integrated Synoptic Program (NISIP), managed by the NSO, which is operated by the Association of Universities for Research in Astronomy

- (AURA), Inc., under a cooperative agreement with the NSF. The synoptic magnetograms were downloaded from the NSO digital library; <http://digilib.nso.edu/ftp.html>.
10. H. B. Snodgrass, *Astrophys. J.* **270**, 288 (1983).
11. The low values of the toroidal flux for cycle 21 are presumably due to the poorer quality of the earlier synoptic magnetograms before substantial improvements of the instrumentation were implemented.
12. H. W. Babcock, *Astrophys. J.* **133**, 572 (1961).
13. R. B. Leighton, *Astrophys. J.* **156**, 1 (1969).
14. Y.-M. Wang, J. Lean, N. R. Sheeley Jr., *Astrophys. J.* **577**, L53–L57 (2002).
15. J. Jiang, R. H. Cameron, D. Schmitt, M. Schüssler, *Astron. Astrophys.* **528**, A83 (2011).
16. R. H. Cameron, M. Schüssler, *Astron. Astrophys.* **548**, A57 (2012).
17. D. Mackay, A. Yeates, *Living Rev. Sol. Phys.* **9**, 6 (2012); [www.livingreviews.org/lrsp-2012-6](http://www.livingreviews.org/lrsp-2012-6) (accessed 26 January 2015).
18. J. Jiang et al., *Space Sci. Rev.* **186**, 491–523 (2014).
19. A. Muñoz-Jaramillo, M. Dasi-Espuig, L. A. Balmaceda, E. E. DeLuca, *Astrophys. J.* **767**, L25 (2013).

20. Y.-M. Wang, N. R. Sheeley, *Astrophys. J.* **694**, L11–L15 (2009).
21. K. H. Schatten, P. H. Scherrer, L. Svalgaard, J. M. Wilcox, *Geophys. Res. Lett.* **5**, 411–414 (1978).
22. K. Petrovay, *Living Rev. Sol. Phys.* **7**, 6 (2010); [www.livingreviews.org/lrsp-2010-6](http://www.livingreviews.org/lrsp-2010-6) (accessed 26 January 2015).

## ACKNOWLEDGMENTS

We are grateful to M. Rempel for enlightening discussions that led to substantial improvement of the manuscript. This work was carried out in the context of Deutsche Forschungsgemeinschaft SFB 963 “Astrophysical Flow Instabilities and Turbulence” (Project A16).

## SUPPLEMENTARY MATERIALS

[www.sciencemag.org/content/347/6228/1333/suppl/DC1](http://www.sciencemag.org/content/347/6228/1333/suppl/DC1)  
Supplementary Text  
Figs. S1 and S2

19 September 2014; accepted 6 February 2015  
10.1126/science.1261470

## SUPERCONDUCTIVITY

# Broken translational and rotational symmetry via charge stripe order in underdoped $\text{YBa}_2\text{Cu}_3\text{O}_{6+y}$

R. Comin,<sup>1,2\*</sup> R. Sutarto,<sup>3</sup> E. H. da Silva Neto,<sup>1,2,4,5</sup> L. Chauviere,<sup>1,2,5</sup> R. Liang,<sup>1,2</sup> W. N. Hardy,<sup>1,2</sup> D. A. Bonn,<sup>1,2</sup> F. He,<sup>3</sup> G. A. Sawatzky,<sup>1,2</sup> A. Damascelli<sup>1,2,\*</sup>

After the discovery of striplike order in lanthanum-based copper oxide superconductors, charge-ordering instabilities were observed in all cuprate families. However, it has proven difficult to distinguish between unidirectional (stripes) and bidirectional (checkerboard) charge order in yttrium- and bismuth-based materials. We used resonant x-ray scattering to measure the two-dimensional structure factor in the superconductor  $\text{YBa}_2\text{Cu}_3\text{O}_{6+y}$  in reciprocal space. Our data reveal the presence of charge stripe order (i.e., locally unidirectional density waves), which may represent the true microscopic nature of charge modulation in cuprates. At the same time, we find that the well-established competition between charge order and superconductivity is stronger for charge correlations across the stripes than along them, which provides additional evidence for the intrinsic unidirectional nature of the charge order.

Recent studies of Y-based copper oxides have highlighted the importance of a charge-ordered electronic ground state, also termed a charge density wave (CDW), for the phenomenology of high-temperature superconductors (1–14). Experiments on the family of  $\text{YBa}_2\text{Cu}_3\text{O}_{6+y}$  (YBCO) compounds have yielded a wealth of experimental results that have enabled advancements in our understanding of CDW instabilities and their interplay with superconductivity (9–11, 15–22).

<sup>1</sup>Department of Physics and Astronomy, University of British Columbia, Vancouver, British Columbia V6T 1Z1, Canada.

<sup>2</sup>Quantum Matter Institute, University of British Columbia, Vancouver, British Columbia V6T 1Z4, Canada. <sup>3</sup>Canadian Light Source, Saskatoon, Saskatchewan S7N 2V3, Canada.

<sup>4</sup>Quantum Materials Program, Canadian Institute for Advanced Research, Toronto, Ontario M5G 1Z8, Canada.

<sup>5</sup>Max Planck Institute for Solid State Research, D-70569 Stuttgart, Germany.

\*Corresponding author. E-mail: r.comin@utoronto.ca (R.C.); damascelli@physics.ubc.ca (A.D.)

YBCO is a layered copper oxide–based material in which hole doping is controlled by the oxygen stoichiometry in the chain layer, characterized by uniaxial  $\text{CuO}$  chains running along the crystallographic  $\mathbf{b}$  axis. In addition to ordering within the chain layer—attained via the periodic alternation of fully oxygenated and fully depleted  $\text{CuO}$  chains—recent experiments have extensively shown the presence of charge ordering in the  $\text{CuO}_2$  planes, with an incommensurate wave vector  $Q \approx 0.31$  reciprocal lattice units (23), corresponding to a period of approximately three unit cells in real space (9–11). Although the stripy nature of La-based cuprates is long established (1–3), the local symmetry of the CDW in YBCO has not yet been resolved. Both charge stripes (in the presence of  $90^\circ$  rotated domains) and a checkerboard pattern are consistent with the globally bidirectional structure of the CDW, which is characterized by wave vectors along both the  $\mathbf{a}$  and  $\mathbf{b}$  axes, at  $\mathbf{Q}_a \approx (0.31, 0)$  and  $\mathbf{Q}_b \approx (0, 0.31)$ , respectively (10, 11, 24–26).

This leaves open the fundamental question of whether stripes are the underlying charge instability in the whole class of hole-doped cuprates.

We used resonant x-ray scattering (RXS) to study the local density correlations of the charge-ordered state and the interaction of this state with superconductivity (SC) in underdoped YBCO. The RXS technique, which is now at full maturity, represents a unique combination of diffraction (to probe reciprocal space) and resonant absorption (allowing element specificity and therefore site selectivity). RXS directly measures the structure factor  $S(Q_x, Q_y)$ , where  $Q_x$  and  $Q_y$  represent the momenta along the reciprocal axes  $H$  and  $K$ , respectively. The structure factor is linked to the density-density correlation function and therefore to the CDW order parameter in momentum space (27). To reconstruct the two-dimensional (2D) structure factor with high resolution, we used a specifically devised RXS probing scheme whereby a charge-ordering peak is sliced along different directions in the  $(Q_x, Q_y)$  plane, parameterized by the azimuthal angle  $\alpha$  (Fig. 1). The resulting 2D shape of the CDW peaks rules out checkerboard order and is instead consistent with a stripy nature of charge modulations in YBCO (28). We carried out RXS

measurements in the vicinity of the CDW wave vectors  $\mathbf{Q}_a \approx (0.31, 0)$  and  $\mathbf{Q}_b \approx (0, 0.31)$  for three detwinned, oxygen-ordered YBCO samples:  $\text{YBa}_2\text{Cu}_3\text{O}_{6.51}$  (Y651, with hole doping  $p \approx 0.10$ ),  $\text{YBa}_2\text{Cu}_3\text{O}_{6.67}$  (Y667,  $p \approx 0.12$ ), and  $\text{YBa}_2\text{Cu}_3\text{O}_{6.75}$  (Y675,  $p \approx 0.13$ ).

In our experimental scheme, the CDW peaks are scanned in a radial geometry via control of the azimuthal angle  $\alpha$  (29) (Fig. 1A). At the  $\text{Cu-L}_{3\beta}$  edge, the measured signal is mainly sensitive to periodic variations in the  $\text{Cu-2p} \rightarrow 3d$  transition energy (30, 31), which is a scalar quantity, even though the detailed contribution of a pure charge modulation versus ionic displacements to the RXS signal cannot be decoupled (32). In addition, the poor coherence of the CDW across the  $\text{CuO}_2$  planes (11, 24, 26) qualifies this electronic ordering as a 2D phenomenon, thus motivating our focus on the structure factor in the  $(Q_x, Q_y)$  plane. Representative scans of the CDW peak for different  $\alpha$  values and at the superconducting critical temperature  $T \approx T_c$  are shown in the insets to Fig. 1A, for the  $\mathbf{Q}_b$  and  $\mathbf{Q}_a$  CDW peaks of a Y667 sample. A change in the peak half width at half maximum (HWHM)  $\Delta Q$  between  $\alpha = 0^\circ$  and  $\alpha = 90^\circ$  is already apparent but is even better visualized in

the color map of Fig. 1B, which shows the sequence of  $Q$ -scans versus azimuthal angle and the corresponding variation of  $\Delta Q$  for  $\mathbf{Q}_b$  in the range  $\alpha = -90^\circ$  to  $90^\circ$ . This same procedure is applied to all three YBCO doping levels, for both the  $\mathbf{Q}_a$  and  $\mathbf{Q}_b$  CDW peaks; polar plots of  $\Delta Q$  versus  $\alpha$  are shown in Fig. 1, C to E, for Y651, Y667, and Y675, respectively. With the aid of the ellipse fits to the CDW profiles (continuous lines), four key aspects of these data stand out: (i) All peaks show a clear anisotropy between the two perpendicular directions  $\alpha = 0^\circ$  and  $\alpha = 90^\circ$ ; (ii) for each doping, the  $\mathbf{Q}_a$  and  $\mathbf{Q}_b$  peaks have different shapes, and in the case of Y651 and Y667 this is more evident as the peaks are elongated along two different directions; (iii) the departure from an isotropic case, quantified by the elongation of the CDW ellipses, increases toward the underdoped regime and is opposite to the evolution of orthorhombicity, which is instead maximized at optimal doping [see (27) and fig. S4 for a more detailed discussion]; and (iv) the peak elongation at  $\mathbf{Q}_a$  and  $\mathbf{Q}_b$ , evolving from biaxial (Y651 and Y667) to uniaxial (Y675), is inconsistent with the doping independence of the uniaxial symmetry of the  $\text{CuO}$  chain layer, which rules out the

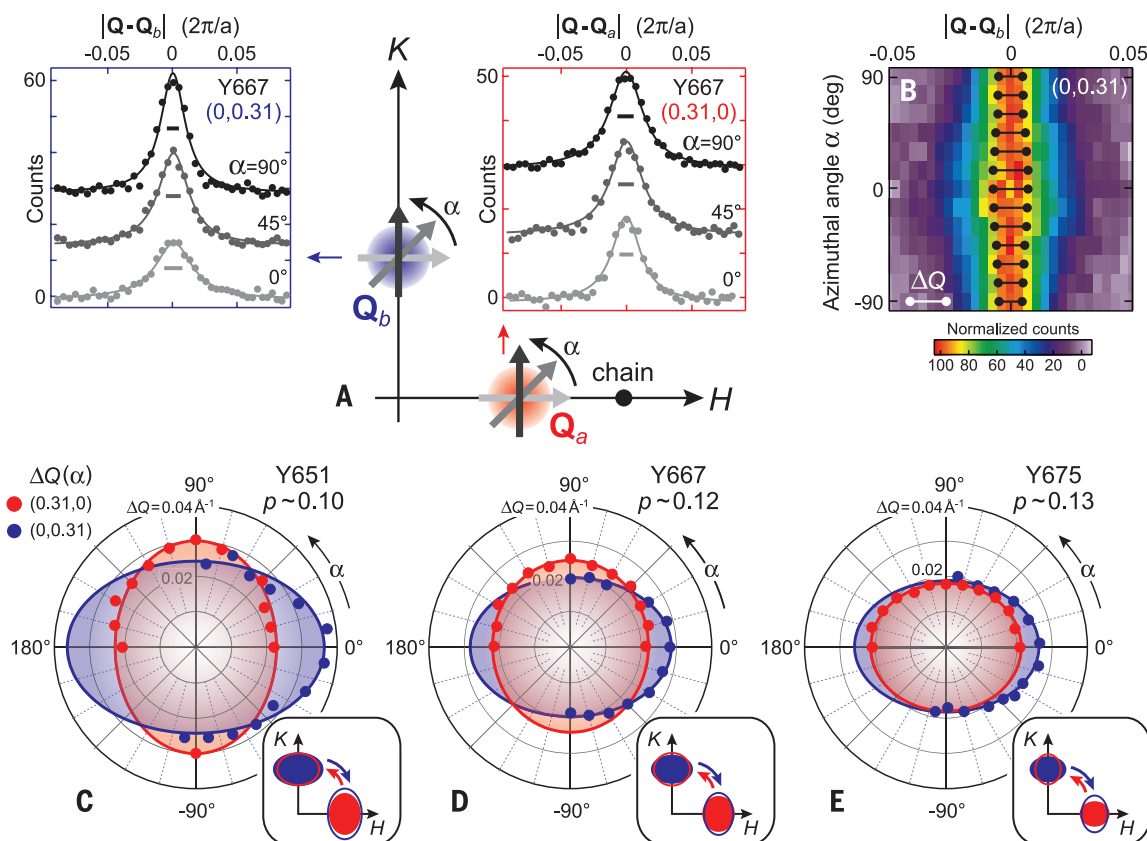


**Fig. 1. Charge order topology in momentum space.** (A) Schematic representation of the momentum structure of charge modulations in YBCO. Left inset: Selected momentum scans of the CDW peak along the  $\mathbf{b}$  axis at  $\mathbf{Q}_b = (0, 0.31)$ , for different azimuthal angles ( $\alpha = 0^\circ, 45^\circ, 90^\circ$ ). Continuous lines represent Lorentzian fits; horizontal bars denote the linewidth  $\Delta Q$  (HWHM). Right inset: Same as for the left inset, but for the CDW peak along the  $\mathbf{a}$  axis at  $\mathbf{Q}_a \approx (0.31, 0)$ . (B) Color map of a series of  $Q$ -scans (normalized to the peak

height) slicing the  $\mathbf{Q}_b$  peak between  $\alpha = -90^\circ$  and  $\alpha = 90^\circ$ ; black bars represent the linewidth  $\Delta Q$ , which is largest at  $\alpha = 0^\circ$ . (C to E) Polar plots of  $\Delta Q$  as a function of the azimuthal angle  $\alpha$  for  $\mathbf{Q}_a$  (red) and  $\mathbf{Q}_b$  (blue) in  $\text{YBa}_2\text{Cu}_3\text{O}_{6.51}$  (Y651),  $\text{YBa}_2\text{Cu}_3\text{O}_{6.67}$  (Y667), and  $\text{YBa}_2\text{Cu}_3\text{O}_{6.75}$  (Y675), respectively. Concentric gray circles are spaced by  $0.01 \text{ \AA}^{-1}$ ; continuous lines are fits to an elliptical profile. Bottom right insets: CDW peaks represented as solid ellipses and compared with their rotated versions (hollow ellipses) for each doping.



possibility that the observed CDW peak structure is exclusively controlled by the crystal's orthorhombic structure [however, the uniaxial anisotropy observed for Y675 might reflect a more pronounced interaction between the Cu-O planes and chains in this compound, possibly caused by the increase in orthorhombicity upon hole doping (27)].

The observed 2D peak shape indicates that the four-fold ( $C_4$ ) symmetry is broken at both the macro- and nanoscale, which is consistent with the emergence of a stripe-ordered state. In fact, under  $C_4$  symmetry the electronic density would be invariant under a  $90^\circ$  rotation in real space ( $x \rightarrow y, y \rightarrow -x$ ), which is equivalent to a  $90^\circ$  rotation in momentum space ( $Q_x \rightarrow Q_y, Q_y \rightarrow -Q_x$ ). Instead, the CDW structure factor  $S(Q_x, Q_y)$  is clearly not invariant under such operation, as shown in the insets of Fig. 1, C to E, which compare the original  $S(Q_x, Q_y)$  factors to their  $90^\circ$  rotated versions  $S(Q_y, -Q_x)$ . This finding demonstrates an unambiguous breaking of global  $C_4$  symmetry in all investigated samples and might elucidate the origin of the anisotropy observed in the Nernst effect (20) and in optical birefringence measurements (33).

The real-space representation of charge order branches off into two possible scenarios: (i) a biaxial anisotropy, where both  $x$ - and  $y$ -elongated domains (34) are present (Fig. 2, A and C); (ii) a uniaxial anisotropy, where only  $y$ -elongated (or, equivalently,  $x$ -elongated) domains are found (Fig. 2, B and D). Note that these domains need

not necessarily lie in the same layer, but they need to be present at the same time within the bulk of the material (e.g., they can be present in alternating layers while still leading to the same momentum structure). The momentum-space representation of the order parameter—and therefore of the electronic density fluctuations—is shown in the corresponding panels in Fig. 2, E to H, where  $S_a(\mathbf{Q})$  (red ellipses) and  $S_b(\mathbf{Q})$  (blue ellipses) represent the structure factor associated to the charge modulations along  $\mathbf{a}$  and  $\mathbf{b}$ , respectively. The profile of a single structure-factor peak is the result of two contributions: the underlying CDW symmetry as well as its 2D correlation length, which can also be anisotropic.

As a net result, the anisotropy of a single peak in  $\mathbf{Q}$ -space cannot be used to discriminate between different CDW symmetries. Instead, the latter can be resolved by probing the 2D CDW structure factor—that is, by comparing the CDW peak shapes for  $\mathbf{Q}_a$  and  $\mathbf{Q}_b$ . Inspection of the diagrams in Fig. 2, E to H, reveals a common trait of checkerboard structures in momentum space, in that the following conditions (Fig. 2, G and H) must always hold by symmetry:  $\Delta Q_x^a = \Delta Q_x^b$  and  $\Delta Q_y^a = \Delta Q_y^b$ . That is, the peak broadening along a given direction must coincide for  $\mathbf{Q}_a$  and  $\mathbf{Q}_b$  (see bottom of Fig. 2, E to H, for case-specific conditions on the peak linewidths). Intuitively, this follows from the fact that for the checkerboard case, the charge modulations along  $\mathbf{a}$  and  $\mathbf{b}$  axes must be subject to the same correlation

lengths within each domain—irrespective of its orientation—and must therefore lead to an equivalent peak broadening along the same direction in reciprocal space, in contrast to our findings for the CDW linewidths (27). From this symmetry analysis, we can conclude that for both uniaxial and biaxial anisotropy it is in principle possible (35) to discriminate between a pure checkerboard and a pure stripe charge order, even in the presence of a distribution of canted domains (see tables S1 to S3 for a complete classification). Ultimately, the inequivalence of the peak broadening  $\Delta Q$  along different directions for all studied YBCO samples, combined with the macroscopic  $C_4$  symmetry breaking, provides clear evidence for the unidirectional (stripe) intrinsic nature of the charge order (28).

Having established the underlying stripelike character of charge modulations in the  $\text{CuO}_2$  planes, we turn to the temperature dependence of the longitudinal and transverse correlation lengths, respectively parallel and perpendicular to the specific ordering wave vector. These can be extracted by inverting the momentum HWHM  $\Delta Q$ , as illustrated in Fig. 3A. Longitudinal correlations are then given by  $\xi_{||} = \Delta Q_{||}^{-1}$ , where  $\Delta Q_{||}$  represents the momentum linewidth in the direction parallel to the ordering wave vector; transverse correlations are given by  $\xi_{\perp} = \Delta Q_{\perp}^{-1}$ , where  $\Delta Q_{\perp}$  represents the momentum linewidth in the direction perpendicular to the ordering wave vector.

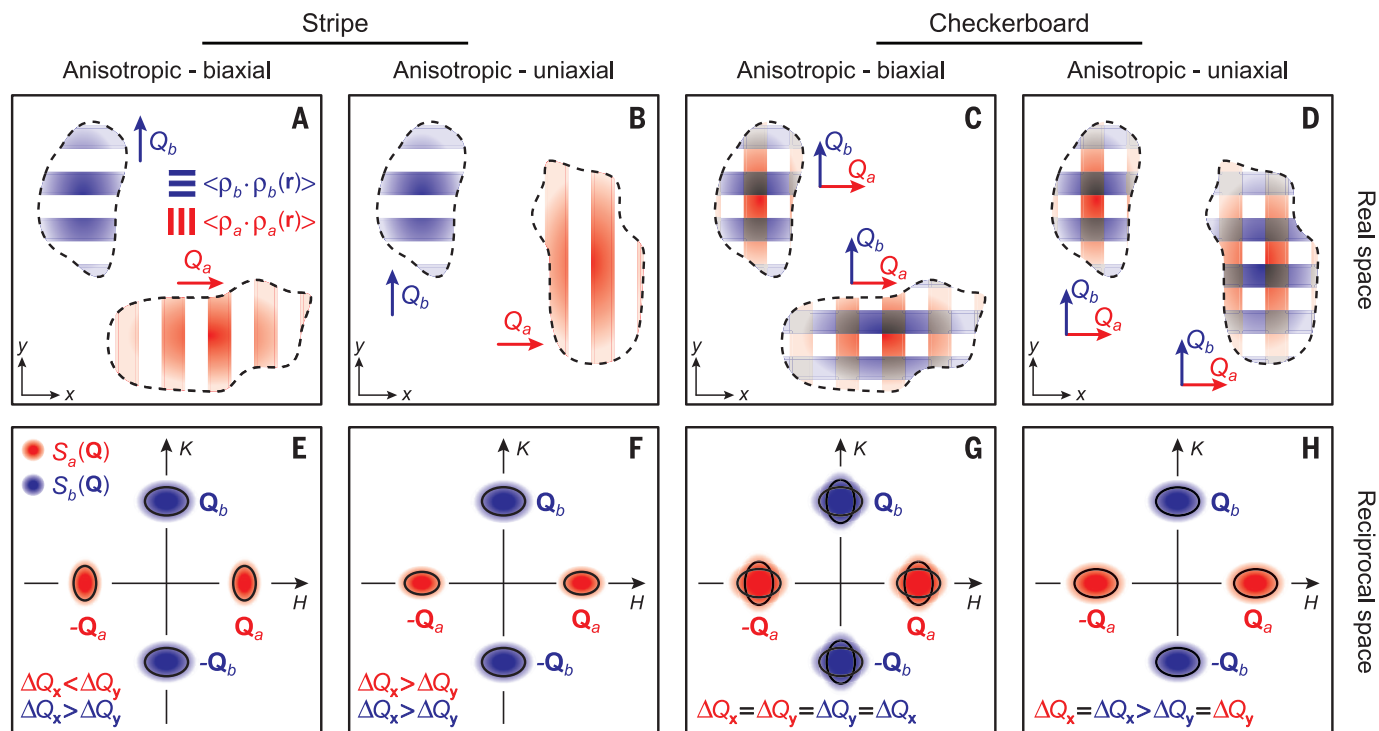
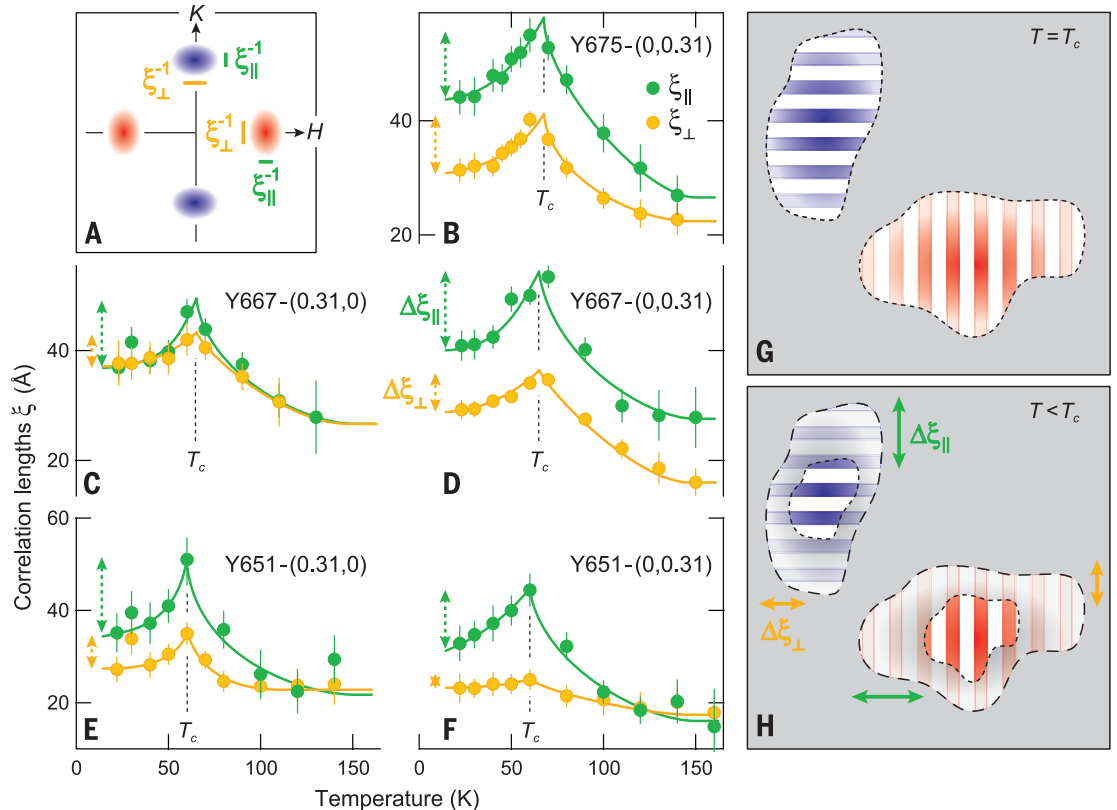


**Fig. 2. Domain mesostructure in real and reciprocal space.** (A and B) Stripy domains along  $\mathbf{a}$  (red stripes) and  $\mathbf{b}$  (blue stripes) in the presence of biaxial (A) and uniaxial (B) anisotropic correlations. The domains are visualized in the same layer, although a situation in which they are present in alternating layers in a  $90^\circ$ -rotated arrangement is equally possible. (C and D) Checkerboard

domains in the presence of biaxial (C) and uniaxial (D) anisotropic correlations. (E to H) Corresponding structure factors in reciprocal ( $\mathbf{Q}$ ) space. In case of the simultaneous presence of both CDW components (checkerboard), the imprinted correlations must be equal for the density wave along  $\mathbf{a}$  and  $\mathbf{b}$ , thus imposing an equivalent peak structure at  $\mathbf{Q}_a$  and  $\mathbf{Q}_b$  as seen in (G) and (H).

**Fig. 3. Interplay between stripe order and the superconducting state.** (A) Schematics of the CDW structure factor in Q-space, illustrating how longitudinal ( $\xi_{||}$ ) and transverse ( $\xi_{\perp}$ ) correlation lengths are extracted from the data by taking the inverse of the peak HWHM  $\Delta Q$ . (B to F) Temperature dependence of  $\xi_{||}$  (green markers) and  $\xi_{\perp}$  (orange markers) for the various samples (where data are available) and CDW peaks investigated. Continuous lines are guides to the eye; double arrows highlight the drop in correlation lengths  $\Delta\xi_{||}$  and  $\Delta\xi_{\perp}$  below  $T_c$ . (G and H) Cartoons representing the evolution of the stripy nanodomains from above  $T_c$  (G) to below  $T_c$  (H), illustrating how longitudinal correlations undergo a larger suppression in the presence of superconducting order.



We subsequently studied the temperature dependence of  $\xi_{||}$  and  $\xi_{\perp}$  for both the  $\mathbf{Q}_a$  and  $\mathbf{Q}_b$  ordering wave vectors (Fig. 3, B to F). We observed a rise of correlation lengths below the CDW onset near 150 K, followed by their suppression below the SC transition temperature  $T_c$ ; this confirms the competition between these two orders, in agreement with recent energy-integrated as well as energy-resolved RXS studies (10, 11, 24, 25, 30). However, the drop in the correlation lengths below  $T_c$  ( $\Delta\xi$ ) was in all instances larger for the longitudinal correlations, or  $\Delta\xi_{||} > \Delta\xi_{\perp}$ . In particular, the discrepancy between  $\Delta\xi_{||}$  and  $\Delta\xi_{\perp}$ , although small for Y675, was quite substantial for the more underdoped Y667 and Y651. This anisotropy provides additional evidence for the unidirectional nature of the charge ordering and thus the breaking of  $C_4$  symmetry, because a bidirectional order would be expected to exhibit an isotropic drop in correlation length across  $T_c$ . The anisotropy has an opposite doping trend from the crystal orthorhombicity, whose associated anomalies across  $T_c$  increase with hole doping [as revealed, for example, by lattice expansivity measurements (27, 36)].

The inferred real-space representation of the evolution across  $T_c$  is schematically illustrated in Fig. 3, G and H, where nanodomains are used to pictorially represent a charge-ordered state with finite correlation lengths. We conclude that the largest change occurs along the direction perpendicular to the stripes. This reflects the tendency of the SC order to gain strength as temperature is lowered, primarily at the expense of longitudinal CDW correlations; the implication is that the

mechanism responsible for the density fluctuations across the periodically modulated stripes might be the main one competing with the Cooper pairing process.

Our results may explain many common aspects between CDW physics in YBCO and the stripy cuprates from the La-based family, such as thermoelectric transport (37, 38), strength of the order parameter (39), out-of-equilibrium response (40, 41), and energy-dependent RXS response (30, 31). The nanoscopic nature of the stripe instability and the presence of both **a**- and **b**-oriented domains also clarify why this broken symmetry has been difficult to disentangle from a native bidirectional order (10, 11, 42), therefore requiring a tailored experimental scheme to resolve the 2D CDW structure factor  $S(\mathbf{Q}_a, \mathbf{Q}_b)$ . The pronounced directionality in the competition between superconductivity and stripe order reveals the underlying interplay between particle-particle and particle-hole pairing in high-temperature superconductors and provides insights for an ultimate understanding of these materials.

#### REFERENCES AND NOTES

1. J. M. Tranquada, B. J. Sternlieb, J. D. Axe, Y. Nakamura, S. Uchida, *Nature* **375**, 561–563 (1995).
2. M. Zimmermann et al., *Europhys. Lett.* **41**, 629–634 (1998).
3. P. Abbamonte et al., *Nat. Phys.* **1**, 155–158 (2005).
4. J. E. Hoffman et al., *Science* **295**, 466–469 (2002).
5. C. Howald, H. Eisaki, N. Kaneko, A. Kapitulnik, *Proc. Natl. Acad. Sci. U.S.A.* **100**, 9705–9709 (2003).
6. T. Hanaguri et al., *Nature* **430**, 1001–1005 (2004).
7. W. D. Wise et al., *Nat. Phys.* **4**, 696–699 (2008).
8. C. V. Parker et al., *Nature* **468**, 677–680 (2010).
9. T. Wu et al., *Nature* **477**, 191–194 (2011).
10. G. Ghiringhelli et al., *Science* **337**, 821–825 (2012).

11. J. Chang et al., *Nat. Phys.* **8**, 871–876 (2012).
12. R. Comin et al., *Science* **343**, 390–392 (2014).
13. E. H. da Silva Neto et al., *Science* **343**, 393–396 (2014).
14. W. Tabis et al., *Nat. Commun.* **5**, 5875 (2014).
15. V. Hinkov et al., *Nature* **430**, 650–654 (2004).
16. N. Doiron-Leyraud et al., *Nature* **447**, 565–568 (2007).
17. M. A. Hossain et al., *Nat. Phys.* **4**, 527 (2008).
18. D. LeBoeuf et al., *Nature* **450**, 533–536 (2007).
19. V. Hinkov et al., *Science* **319**, 597–600 (2008).
20. R. Daou et al., *Nature* **463**, 519–522 (2010).
21. D. Fournier et al., *Nat. Phys.* **6**, 905–911 (2010).
22. B. Ramshaw et al., *Nat. Phys.* **7**, 234–238 (2011).
23. The small but finite doping dependence of the ordering wave vector is here neglected, because it is not the focus of our investigation. For more details, see (24, 25, 43).
24. E. Blackburn et al., *Phys. Rev. Lett.* **110**, 137004 (2013).
25. S. Blanco-Canosa et al., *Phys. Rev. Lett.* **110**, 187001 (2013).
26. M. Le Tacon et al., *Nat. Phys.* **10**, 52–58 (2014).
27. See supplementary materials on Science Online.
28. Because of our inability to measure magnetic ordering, our concept of stripes only applies to the charge modulations, unlike the canonical definition used in La-based cuprates, which also implies concomitant magnetic order.
29. R. Comin et al., <http://arxiv.org/abs/1402.5415> (2014).
30. A. J. Achkar et al., *Phys. Rev. Lett.* **109**, 167001 (2012).
31. A. J. Achkar et al., *Phys. Rev. Lett.* **110**, 017001 (2013).
32. However, x-ray diffraction experiments estimate the upper bound for ionic displacements to be around  $7 \times 10^{-4}$  Å, or  $\sim 2.7 \times 10^{-3}$  Å (11).
33. Y. Lubashevsky, L. Pan, T. Kirzhner, G. Koren, N. P. Armitage, *Phys. Rev. Lett.* **112**, 147001 (2014).
34. We use the concept of domain to indicate a coherence subregion (i.e., a portion of space where density modulations are largely in phase); in this sense, the size of the domains is intended to reflect the magnitude of correlation lengths.
35. Unless  $\Delta Q_{||}^{\text{CDW}} = \Delta Q_{||}^{\text{SC}}$ , in which case the patterns shown in Fig. 2, F and H, become indistinguishable. This situation, however, is not encountered in our study.
36. C. Meingast et al., *Phys. Rev. Lett.* **86**, 1606–1609 (2001).
37. O. Cyr-Choinière et al., *Nature* **458**, 743–745 (2009).
38. F. Laliberté et al., *Nat. Commun.* **2**, 432 (2011).
39. V. Thampy et al., *Phys. Rev. B* **88**, 024505 (2013).



40. D. H. Torchinsky, F. Mahmood, A. T. Bollinger, I. Božović, N. Gedik, *Nat. Mater.* **12**, 387–391 (2013).  
 41. J. P. Hinton *et al.*, *Phys. Rev. B* **88**, 060508(R) (2013).  
 42. D. LeBoeuf *et al.*, *Nat. Phys.* **9**, 79–83 (2013).  
 43. S. Blanco-Canosa *et al.*, *Phys. Rev. B* **90**, 054513 (2014).

## ACKNOWLEDGMENTS

We thank P. Abbamonte, E. Blackburn, L. Braicovich, J. Geck, G. Ghiringhelli, B. Keimer, S. Kivelson, M. Le Tacon, and S. Sachdev for insightful discussions. Supported by the

Max Planck–UBC Centre for Quantum Materials, fellowships from the Killam, Alfred P. Sloan, and Alexander von Humboldt Foundations, and a Natural Sciences and Engineering Research Council (NSERC) Steacie Memorial Fellowship (A.D.); the Canada Research Chairs Program (A.D., G.A.S.); and NSERC, CFI, and CIFAR Quantum Materials. All of the experiments were performed at beamline REIXS of the Canadian Light Source, which is funded by the CFI, NSERC, NRC, CIHR, the Government of Saskatchewan, WD Canada, and the University of Saskatchewan. R.C. acknowledges the receipt of support from the CLS Graduate Student Travel Support Program. E.H.d.S.N. acknowledges support from the CIFAR Global Academy.

## SUPPLEMENTARY MATERIALS

www.sciencemag.org/content/347/6228/1335/suppl/DC1  
 Materials and Methods  
 Supplementary Text  
 Figs. S1 to S9  
 Tables S1 to S3  
 References (44–48)

7 July 2014; accepted 8 February 2015  
 10.1126/science.1258399

## HEAVY FERMIONS

# Chirality density wave of the “hidden order” phase in URu<sub>2</sub>Si<sub>2</sub>

H.-H. Kung,<sup>1,\*</sup> R. E. Baumbach,<sup>2,†</sup> E. D. Bauer,<sup>2</sup> V. K. Thorsmølle,<sup>1,‡</sup> W.-L. Zhang,<sup>1</sup>  
 K. Haule,<sup>1,\*</sup> J. A. Mydosh,<sup>3</sup> G. Blumberg<sup>1,4,\*</sup>

A second-order phase transition in a physical system is associated with the emergence of an “order parameter” and a spontaneous symmetry breaking. The heavy fermion superconductor URu<sub>2</sub>Si<sub>2</sub> has a “hidden order” (HO) phase below the temperature of 17.5 kelvin; the symmetry of the associated order parameter has remained ambiguous. Here we use polarization-resolved Raman spectroscopy to specify the symmetry of the low-energy excitations above and below the HO transition. We determine that the HO parameter breaks local vertical and diagonal reflection symmetries at the uranium sites, resulting in crystal field states with distinct chiral properties, which order to a commensurate chirality density wave ground state.

In solids, electrons occupying 5f orbitals often have a partly itinerant and partly localized character, which leads to a rich variety of low-temperature phases, such as magnetism and superconductivity (1). Generally, these ordered states are characterized by the symmetry they break, and an order parameter may be constructed to describe the state with reduced symmetry. In a solid, the order parameter reflects the microscopic interactions among electrons that lead to the phase transition. In materials containing f-electrons, exchange interactions of the lanthanide or actinide magnetic moments typically generate long-range antiferromagnetic or ferromagnetic order at low temperatures, but multipolar ordering such as quadrupolar, octupolar, and hexadecapolar is also possible (2).

One particularly interesting example is the uranium-based intermetallic compound URu<sub>2</sub>Si<sub>2</sub>. It displays a nonmagnetic second-order phase transition into an electronically ordered state at  $T_{\text{HO}} = 17.5$  K, and then becomes superconduct-

ing below 1.5 K (3, 4). Despite numerous theoretical proposals to explain the properties below  $T_{\text{HO}}$  in the past 30 years (5–10), the symmetry and microscopic mechanism for the order parameter remain ambiguous, hence the term “hidden order” (HO) (11). In this ordered state, an energy gap in both the spin and the charge response has been reported (12–18). In addition, an in-gap collective excitation at a commensurate wave vector has been observed in neutron scattering experiments (13, 14, 16). Recently, fourfold rotational symmetry breaking under an in-plane magnetic field (19) and a lattice distortion along the crystallographic *a* axis (20) have been reported in high-quality small crystals. However, the available experimental works cannot yet conclusively determine the symmetry of the order parameter in the HO phase.

URu<sub>2</sub>Si<sub>2</sub> crystallizes in a body-centered tetragonal structure belonging to the  $\mathbb{D}_{4h}$  point group (space group no. 139 *I*<sub>4</sub>/*mmm*, Fig. 1A). The uniqueness of URu<sub>2</sub>Si<sub>2</sub> is rooted in the coexistence of the broad conduction bands, composed mostly of Si-p and Ru-d electronic states, and more localized U-5f orbitals, which are in a mixed-valent configuration between tetravalent 5f<sup>2</sup> and trivalent 5f<sup>3</sup> (21). When the temperature is lowered below ~70 K, the hybridization with the conduction band allows a small fraction of each U-5f electron to participate in formation of a narrow quasiparticle band at the Fermi level, whereas the rest of the electron remains better described as localized on the uranium site.

In the dominant atomic configuration, the orbital angular momentum and spin of the two quasi-localized U-5f electrons add up to total momentum  $4\hbar$ , having ninefold degeneracy (6, 22). In the crystal environment of URu<sub>2</sub>Si<sub>2</sub>, these states split into seven energy levels denoted by irreducible representations of the  $\mathbb{D}_{4h}$  group: five singlet states  $2A_{1g} \oplus A_{2g} \oplus B_{1g} \oplus B_{2g}$  and two doublet states  $2E_g$ . Each irreducible representation possesses distinct symmetry properties under operations such as reflection, inversion, and rotation. For example, the  $A_{1g}$  states are invariant under all symmetry operations of the  $\mathbb{D}_{4h}$  group, whereas the  $A_{2g}$  state changes sign under all diagonal and vertical reflections, and thereby has eight nodes (Fig. 1A). Most of the physical observables, such as density-density and stress tensors, or one-particle spectral functions, are symmetric under exchange of *x* and *y* axis in tetragonal structure and therefore are impervious to the  $A_{2g}$  excitations, whereas these  $A_{2g}$  excitations can be probed by Raman spectroscopy (23–28).

Raman scattering is an inelastic process that promotes excitations of controlled symmetry defined by the scattering geometries, namely, polarizations of the incident and scattered light (22, 23). Polarization-resolved Raman spectroscopy enables separation of the spectra of excitations into distinct symmetry representations, such as  $A_{1g}$ ,  $A_{2g}$ ,  $B_{1g}$ ,  $B_{2g}$ , and  $E_g$  in the  $\mathbb{D}_{4h}$  group, thereby classifying the symmetry of the collective excitations (22, 26). The temperature evolution of these excitations across a phase transition provides an unambiguous identification of the broken symmetries; furthermore, the photon field used by the Raman probe is weak, which avoids introducing external symmetry-breaking perturbations.

We use linearly and circularly polarized light to acquire the temperature evolution of the Raman response functions in all symmetry channels. In Fig. 2, we plot the Raman susceptibility in the  $A_{2g}$  channel, where the most significant temperature dependence was observed. The Raman susceptibility above  $T_{\text{HO}}$  can be described within a low-energy minimal model suggested in (6) (illustrated in Fig. 1B) that contains two singlet states of  $A_{2g}$  and  $A_{1g}$  symmetries, split by an energy  $\omega_0$ , and a conduction band of predominantly  $A_{1g}$  symmetry. In the following, we denote the singlet states of  $A_{2g}$  and  $A_{1g}$  symmetries by  $|0\rangle$  and  $|1\rangle$ ; the conduction band is labeled  $|CB\rangle$ .

At high temperatures, the Raman spectra exhibit a Drude-like line shape, which in (25) was attributed to quasi-elastic scattering. The maximum in the Raman response function decreases

<sup>1</sup>Department of Physics and Astronomy, Rutgers University, Piscataway, NJ 08854, USA. <sup>2</sup>Los Alamos National Laboratory, Los Alamos, NM 87545, USA. <sup>3</sup>Kamerlingh Onnes Laboratory, Leiden University, 2300 RA Leiden, Netherlands. <sup>4</sup>National Institute of Chemical Physics and Biophysics, 12618 Tallinn, Estonia.  
 \*Corresponding author. E-mail: girsh@physics.rutgers.edu (G.B.); haule@physics.rutgers.edu (K.H.); skung@physics.rutgers.edu (H.-H.K.) <sup>†</sup>Present address: National High Magnetic Field Laboratory, Florida State University, Tallahassee, FL 32310, USA. <sup>‡</sup>Present address: Department of Physics, University of California, San Diego, La Jolla, CA 92093, USA, and Department of Physics, Boston University, Boston, MA 02215, USA.

**Fig. 1. Schematics of the local symmetry of the quasi-localized states.** (A) The crystal structure of URu<sub>2</sub>Si<sub>2</sub> above  $T_{\text{HO}}$ , belonging to the  $\mathbb{D}_{4h}$  point group. Presented in three dimensions and xy-plane cut are illustrations showing the symmetry of the  $A_{2g}$  state  $|0\rangle$  and  $A_{1g}$  state  $|1\rangle$ , where the positive (negative) amplitude is denoted by red (blue) color. The  $A_{1g}$  state is symmetric with respect to the vertical ( $\sigma_v$ ) and diagonal ( $\sigma_d$ ) reflections, whereas the  $A_{2g}$  state is antisymmetric with respect to these reflections. (B) Schematic of the band structure of a low-energy minimal model. The green dashed line denotes the conduction band  $|CB\rangle$ ; the red and black dashed lines denote crystal field states of the U-5f electrons: the ground state  $|0\rangle$  and the first excited state  $|1\rangle$  (22). Blue and red arrows denote the incident and scattered light in a Raman process, respectively.  $\omega_L = 1.65$  eV is the incoming photon energy (energy levels not to scale),  $\mathbb{W}$  is the hybridization strength between  $|1\rangle$  and  $|CB\rangle$ ;  $\omega_0$  and  $\epsilon_k$  are the resonance energies for  $|0\rangle \rightarrow |1\rangle$  and  $|0\rangle \rightarrow |CB\rangle$  excitations, respectively. (C) The crystal structure of URu<sub>2</sub>Si<sub>2</sub> in the HO phase, and illustrations showing the symmetry of the chiral states  $|\mathbf{N}^+\rangle$  and  $|\mathbf{N}^-\rangle$ , and the excited state  $|\mathbf{J}\rangle$ . The left- and right-handed states, denoted by red and blue atoms, respectively, are staggered in the lattice.  $U^L$  and  $U^R$  denotes the two nonequivalent uranium sites in the HO phase. (D) Schematics of the chirality density wave in the HO phase. The uranium sites  $U^L$  and  $U^R$  are occupied by  $|\mathbf{N}^-\rangle$  and  $|\mathbf{N}^+\rangle$  states, respectively.

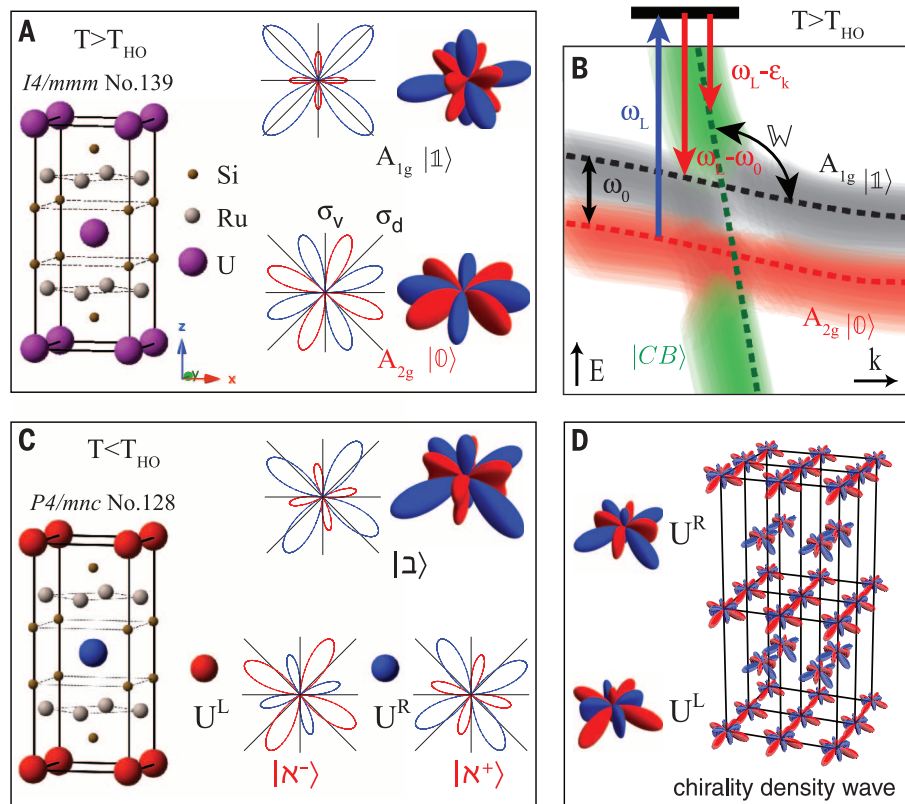
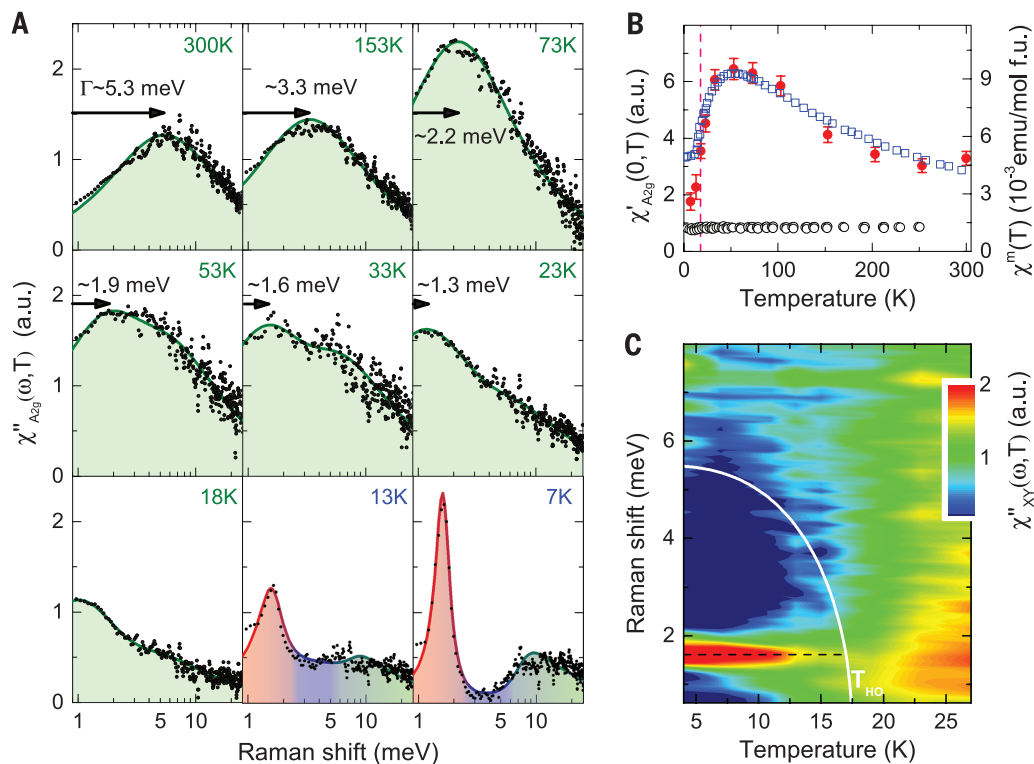


**Fig. 2. Temperature dependence of the  $A_{2g}$  Raman susceptibility.**

(A) The  $A_{2g}$  Raman response function decomposed from the spectra measured in the XY, X'Y', and RL scattering geometries (22). The solid lines are a guide to the eye, illustrating the narrowing of the Drude function (25):  $\chi''_{A_{2g}}(\omega, T) \propto \text{Im}[\Gamma(T) - i\omega]^{-1}$ , where  $\Gamma(T)$  is the Drude scattering rate (indicated by the arrows), which decreases on cooling. Below 70 K, the Raman response deviates from the Drude function. Below  $T_{\text{HO}}$ , the Raman response shows spectral weight suppression below 6 meV and the appearance of an in-gap mode at 1.6 meV (7 and 13 K). (B) Temperature dependence of the static Raman susceptibility in  $A_{2g}$  channel

$$\chi'_{A_{2g}}(0, T) = \frac{2}{\pi} \int_0^{25 \text{ meV}} \frac{\chi''_{A_{2g}}(\omega, T)}{\omega} d\omega$$

(red dots), and the static magnetic susceptibility along  $c$  and  $a$  axis from (3) are plotted as blue squares and black circles, respectively.  $T_{\text{HO}}$  is marked by the dashed line. (C) Temperature dependence of the low-frequency Raman response in the XY scattering geometry, dominantly composed of  $A_{2g}$  excitations. A gaplike suppression develops on cooling, and an in-gap mode at 1.6 meV (black dashed line) emerges below  $T_{\text{HO}}$ . The full width at half-maximum of the mode decreases on cooling from  $\sim 0.75$  meV at 13 K to  $\sim 0.3$  meV at 7 K. The white line shows the temperature dependence of the BCS gap function.





from 5 meV at room temperature to 1 meV just above  $T_{\text{HO}}$  (Fig. 2A). Below 70 K, the line shape deviates slightly from the Drude function, tracking the formation of the heavy fermion states by the hybridization of the itinerant conduction band and the U-5f states. Below 17.5 K, the  $A_{2g}$  Raman response function shows suppression of low-energy spectral weight resembling the temperature dependence of the Bardeen-Cooper-Schrieffer (BCS) gap function, and the emergence of a sharp in-gap mode at 1.6 meV (Fig. 2, A and C).

Figure 2B displays a comparison between the static Raman susceptibility  $\chi'_{A_{2g}}(0, T)$  (left axis) and the  $c$ -axis static magnetic susceptibility  $\chi'_c(T)$  (right axis), showing that the responses are proportional to each other at temperatures above  $T_{\text{HO}}$ . This proportionality can be understood by noting that both susceptibilities probe  $A_{2g}$ -like excitations, as given by the minimal model of Fig. 1B. The extreme anisotropy of the magnetic susceptibility (Fig. 2B) also follows from this minimal model (22).

Having established the Raman response of  $A_{2g}$  symmetry and its correspondence with the magnetic susceptibility, we now present our main results describing the symmetry breaking in the HO state. Figure 3 shows the Raman response in six scattering geometries at 7 K. The intense in-gap mode is observed in all scattering geometries

containing  $A_{2g}$  symmetry. The mode can be interpreted as a  $\omega_0 = 1.6$  meV resonance between the  $|0\rangle$  and  $|1\rangle$  quasi-localized states, which can only appear in the  $A_{2g}$  channel of the  $\mathbb{D}_{4h}$  group. A weaker intensity is also observed at the same energy in XX and  $X'X'$  geometries commonly containing the excitations of the  $A_{1g}$  symmetry, and a much weaker intensity is barely seen within the experimental uncertainty in RL geometry.

The observation of this intensity “leakage” into forbidden scattering geometries marks the lowering of symmetry in the HO phase, indicating the reduction in the number of irreducible representations of the parent point group,  $\mathbb{D}_{4h}$ . For example, the  $\omega_0$  mode intensity “leakage” from the  $A_{2g}$  into the  $A_{1g}$  channel implies that the irreducible representation  $A_{1g}$  and  $A_{2g}$  of the  $\mathbb{D}_{4h}$  point group merge into the  $A_g$  representation of the lower group  $\mathbb{C}_{4h}$ . This signifies the removal of the local vertical and diagonal reflection symmetry operators at the uranium sites in the HO phase. Similarly, the tiny intensity leakage into the RL scattering geometry measures the strength of orthorhombic distortion caused by broken fourfold rotational symmetry.

When the reflection symmetries are broken, an  $A_{2g}$ -like interaction operator  $\Psi_{\text{HO}} \equiv V|1\rangle\langle 0|$  mixes the  $|0\rangle$  and  $|1\rangle$  states, leading to two new local states

$$|\mathbf{N}^+\rangle \approx (1 - \frac{V^2}{2\omega_0^2})|0\rangle + \frac{V}{\omega_0}|1\rangle \quad (1)$$

$$|\mathbf{N}^-\rangle \approx (1 - \frac{V^2}{2\omega_0^2})|0\rangle - \frac{V}{\omega_0}|1\rangle \quad (2)$$

with  $V$  being the interaction strength (6). A pair of such states cannot be transformed into one another by any remaining  $\mathbb{C}_{4h}$  group operators: a property known as chirality (or handedness). The choice of either the right-handed or the left-handed state on a given uranium site,  $|\mathbf{N}^+\rangle$  or  $|\mathbf{N}^-\rangle$ , defines the local chirality in the HO phase (Fig. 1C). Notice that these two degenerate states both preserve the time-reversal symmetry, carry no spin, and contain the same charge, but differ only in handedness.

The same 1.6-meV sharp resonance has also been observed by inelastic neutron scattering at momentum commensurate with the reciprocal lattice vector, but only in the HO state (14, 16, 29). The Raman measurement proves that this resonance is a long-wavelength excitation of  $A_{2g}$  character. The appearance of the same resonance in neutron scattering at a different wavelength, corresponding to the  $c$ -axis lattice constant, requires HO to be a staggered alternating electronic order along the  $c$  direction. Such order with alternating left- and right-handed states at the uranium sites for neighboring basal planes has no modulation of charge or spin and does not couple to the tetragonal lattice; hence, it is hidden to all probes but the scattering of  $A_{2g}$  symmetry. We reveal this hidden order to be a chirality density wave depicted in Fig. 1D.

The chirality density wave doubles the translational periodicity of the phase above  $T_{\text{HO}}$ ; hence, it folds the electronic Brillouin zone, as recently observed by angle-resolved photoemission spectroscopy (30). It also gives rise to an energy gap, as previously observed in optics (12, 17, 18) and tunneling experiments (15, 31) and shown in Fig. 2C to originate in expelling the continuum of  $A_{2g}$  excitations. The sharp resonance is explained by excitation from the ground state, in which a chirality density wave staggers  $|\mathbf{N}^+\rangle$  and  $|\mathbf{N}^-\rangle$ , to the excited collective state (22).

A local order parameter of primary  $A_{2g}$  symmetry, breaking vertical and diagonal reflections, with a subdominant  $B_{1g}$  component, breaking fourfold rotational symmetry, can be expressed in terms of the composite hexadecapole local order parameter of the form (6, 22)

$$\pm V(\overline{J_x - J_y})(J_x + J_y)(J_x J_y + J_y J_x) \quad (3)$$

where  $J_x, J_y$  are in-plane angular momentum operators and the overline stands for symmetrization. A spatial order alternating the sign of this hexadecapole for neighboring basal planes is the chirality density wave (Fig. 1D) that consistently explains the HO phenomena as it is observed by Raman and neutron scattering (13, 14, 16, 29), magnetic torque (19), x-ray diffraction (20), and other data (11, 12, 17, 18, 30). Our finding is an example of exotic electronic ordering emerging from strong interaction among f electrons, which

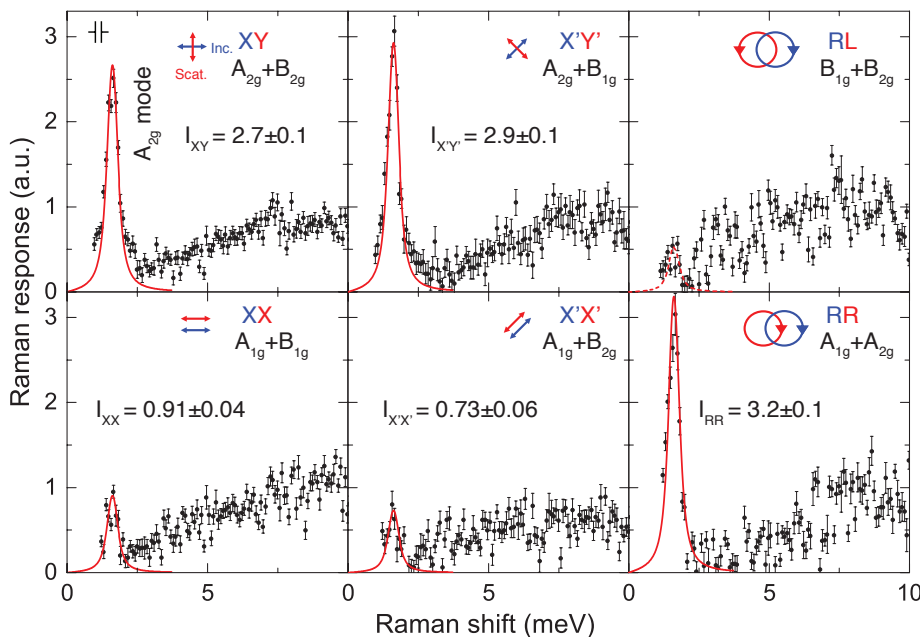


**Fig. 3. The Raman response function in six scattering geometries at 7 K.** The arrows in each panel show the linear or circular polarizations for incident (blue) and scattered (red) light. The six scattering geometries are denoted as  $\mathbf{e}_i \mathbf{e}_s = \text{XX, XY, X'X', X'Y', RR, and RL}$ , with  $\mathbf{e}_i$  being the direction vector for incident light polarization and  $\mathbf{e}_s$  being the scattered light polarization.  $X = [100]$ ,  $Y = [010]$  are aligned along crystallographic axes;  $X' = [110]$ ,  $Y' = [\bar{1}\bar{1}0]$  are at  $45^\circ$  to the  $a$  axes;  $R = (X + iY)/\sqrt{2}$  and  $L = (X - iY)/\sqrt{2}$  are right and left circularly polarized light, respectively (22). The irreducible representations for each scattering geometry are shown within the  $\mathbb{D}_{4h}$  point group. The data are shown in black circles, where the error bars show 1 SD. The red solid lines are fits of the in-gap mode to a Lorentzian, and the fitted intensity using the method of maximum likelihood is noted in each panel. By decomposition, the in-gap mode intensity in each symmetry channels are  $I_{A_{2g}} = 2.6 \pm 0.1$ ,  $I_{A_{1g}} = 0.7 \pm 0.1$ ,  $I_{B_{1g}} = 0.3 \pm 0.1$ , and  $I_{B_{2g}} = 0.1 \pm 0.1$ . The full width at half-maximum of the in-gap mode is about 0.3 meV at 7 K (instrumental resolution of 0.17 meV is shown in the XY panel).

should be a more generic phenomenon relevant to other intermetallic compounds.

**Note added in proof:** While this paper was being reviewed, J. Buhot *et al.* (32) reproduced the  $A_{2g}$  symmetry in-gap mode in a Raman experiment with 561-nm laser excitation and showed that the mode does not split in up to 10 T magnetic field.

## REFERENCES AND NOTES

- G. R. Stewart, *Rev. Mod. Phys.* **56**, 755–787 (1984).
- P. Santini *et al.*, *Rev. Mod. Phys.* **81**, 807–863 (2009).
- T. T. M. Palstra *et al.*, *Phys. Rev. Lett.* **55**, 2727–2730 (1985).
- M. B. Maple *et al.*, *Phys. Rev. Lett.* **56**, 185–188 (1986).
- P. Santini, G. Amoretti, *Phys. Rev. Lett.* **73**, 1027–1030 (1994).
- K. Haule, G. Kotliar, *Nat. Phys.* **5**, 796–799 (2009).
- S. Elgazzar, J. Ruzs, M. Amft, P. M. Oppeneer, J. A. Mydosh, *Nat. Mater.* **8**, 337–341 (2009).
- P. Chandra, P. Coleman, J. A. Mydosh, V. Tripathi, *Nature* **417**, 831–834 (2002).
- H. Ikeda *et al.*, *Nat. Phys.* **8**, 528–533 (2012).
- P. Chandra, P. Coleman, R. Flint, *Nature* **493**, 621–626 (2013).
- J. A. Mydosh, P. M. Oppeneer, *Rev. Mod. Phys.* **83**, 1301–1322 (2011) and references therein.
- D. A. Bonn, J. D. Garrett, T. Timusk, *Phys. Rev. Lett.* **61**, 1305–1308 (1988).
- C. Broholm *et al.*, *Phys. Rev. B* **43**, 12809–12822 (1991).
- C. R. Wiebe *et al.*, *Nat. Phys.* **3**, 96–99 (2007).
- P. Aynajian *et al.*, *Proc. Natl. Acad. Sci. U.S.A.* **107**, 10383–10388 (2010).
- F. Bourdarot *et al.*, *J. Phys. Soc. Jpn.* **79**, 064719 (2010).
- J. S. Hall *et al.*, *Phys. Rev. B* **86**, 035132 (2012).
- W. T. Guo *et al.*, *Phys. Rev. B* **85**, 195105 (2012).
- R. Okazaki *et al.*, *Science* **331**, 439–442 (2011).
- S. Tonegawa *et al.*, *Nat. Commun.* **5**, 4188 (2014).
- J. R. Jeffries, K. T. Moore, N. P. Butch, M. B. Maple, *Phys. Rev. B* **82**, 033103 (2010).
- See supplementary materials on Science Online.
- L. N. Ovander, *Opt. Spectrosc.* **9**, 302 (1960).
- J. A. Koningstein, O. S. Mortensen, *Nature* **217**, 445–446 (1968).
- S. L. Cooper, M. V. Klein, M. B. Maple, M. S. Torikachvili, *Phys. Rev. B* **36**, 5743–5746 (1987).
- B. S. Shastry, B. I. Shraiman, *Int. J. Mod. Phys. B* **5**, 365–388 (1991).
- D. V. Khveshchenko, P. B. Wiegmann, *Phys. Rev. Lett.* **73**, 500–503 (1994).
- H. Rho, M. V. Klein, P. C. Canfield, *Phys. Rev. B* **69**, 144420 (2004).
- F. Bourdarot, B. Fåk, K. Habicht, K. Prokeš, *Phys. Rev. Lett.* **90**, 067203 (2003).
- C. Bareille *et al.*, *Nat. Commun.* **5**, 4326 (2014).
- A. R. Schmidt *et al.*, *Nature* **465**, 570–576 (2010).
- J. Buhot *et al.*, *Phys. Rev. Lett.* **113**, 266405 (2014).

## ACKNOWLEDGMENTS

We thank J. Buhot, P. Chandra, P. Coleman, G. Kotliar, M.-A. Méasson, D. K. Morr, L. Pascut, A. Sacuto, J. Thompson, and V. M. Yakovenko for discussions. G.B. and V.K.T. acknowledge support from the U.S. Department of Energy, Office of Basic Energy Sciences, Division of Materials Sciences and Engineering under Award DE-SC0005463. H.-H.K. acknowledges support from the National Science Foundation under Award NSF DMR-1104884. K.H. acknowledges support by NSF DMR-1405303. W.-L.Z. acknowledges support by the Institute for Complex Adaptive Matter (NSF-IMI grant DMR-0844115). Work at Los Alamos National Laboratory was performed under the auspices of the U.S. Department of Energy, Office of Basic Energy Sciences, Division of Materials Sciences and Engineering.

## SUPPLEMENTARY MATERIALS

www.sciencemag.org/content/347/6228/1339/suppl/DC1  
Material and Methods  
Figs. S1 to S4  
References (33–46)

3 March 2014; accepted 30 January 2015  
Published online 12 February 2015;  
10.1126/science.1259729

## APPLIED OPTICS

# Multiwavelength achromatic metasurfaces by dispersive phase compensation

Francesco Aieta,<sup>\*</sup> Mikhail A. Kats,<sup>†</sup> Patrice Genevet,<sup>‡</sup> Federico Capasso<sup>§</sup>

The replacement of bulk refractive optical elements with diffractive planar components enables the miniaturization of optical systems. However, diffractive optics suffers from large chromatic aberrations due to the dispersion of the phase accumulated by light during propagation. We show that this limitation can be overcome with an engineered wavelength-dependent phase shift imparted by a metasurface, and we demonstrate a design that deflects three wavelengths by the same angle. A planar lens without chromatic aberrations at three wavelengths is also presented. Our designs are based on low-loss dielectric resonators, which introduce a dense spectrum of optical modes to enable dispersive phase compensation. The suppression of chromatic aberrations in metasurface-based planar photonics will find applications in lightweight collimators for displays, as well as chromatically corrected imaging systems.

Refractive and diffractive optical components have fundamentally different responses to broadband light. For a material with normal dispersion, refractive lenses have larger focal distances for red light than for blue and prisms deflect longer wavelengths by a smaller angle; the contrary occurs for diffractive lenses and gratings (1, 2). This contrasting behavior arises because two different principles are used to shape the light: Refractive optics relies on the phase gradually accumulated through propagation, whereas diffractive optics operates by means of interference of light transmitted through an amplitude or phase mask. In most transparent materials in the visible, the refractive index  $n$  decreases with increasing wavelength ( $\lambda$ ) (normal dispersion). Because the deflection angle  $\theta$  of a prism increases with  $n$  and a lens focal length  $f$  is inversely proportional to  $n - 1$ , the resulting effect is the one shown in Fig. 1, A and B. In a diffractive optical element (DOE), the beam deflection angle and the focal length instead increase and decrease with  $\lambda$ , respectively (Fig. 1, C and D), generating an opposite dispersion compared with standard refractive devices. Although for many applications a spatial separation of different wavelengths is desirable, in many others this represents a problem. For example, the dependence of the focal distance on  $\lambda$  produces chromatic aberrations and is responsible for the degradation of the quality of an imaging system. Another difference between these technologies is the efficiency that is generally lower for

diffractive optics due to the presence of higher diffraction orders. The wavelength dependence is typically much more pronounced in diffractive optics than in refractive optics, when low-dispersion materials are used in the latter (2). In refractive lenses, complete elimination of chromatic aberrations at two and three wavelengths is accomplished using, respectively, two and three elements (achromatic doublet and apochromatic triplet) arranged to achieve the same focal length at the wavelengths of interest (3). Superachromatic lenses are practically achromatic for all colors by correcting aberrations at four suitable wavelengths (4). Although successful, these strategies add weight, complexity, and cost to optical systems. On the other hand, DOEs have the advantage of being relatively flat, light, and often low cost. Blazed gratings and Fresnel lenses are diffractive optical devices with an analog phase profile and integrate some benefits of both technologies (e.g., small footprint and high efficiency), but they still suffer from strong chromatic aberrations. Multiorder diffractive lenses overcome this limitation by using thicker phase profiles to achieve chromatic correction for a discrete set of wavelengths (1). However, the realization of thick, analog phase profiles is challenging for conventional fabrication technologies.

Metasurfaces are thin optical components that rely on a different approach for light control: A dense arrangement of subwavelength resonators is designed to modify the optical response of the interface. The resonant nature of the scatterers introduces an abrupt phase shift in the incident wavefront, making it possible to mold the scattered wavefront at will and enabling a new class of planar photonics components (flat optics) (5–8). Different types of resonators (metallic or dielectric antennas, apertures, etc.) have been used to demonstrate various flat optical devices, including blazed gratings (9–11), lenses (12–14), holographic plates (15), polarizers, and wave plates

School of Engineering and Applied Sciences, Harvard University, Cambridge, MA 02138, USA.

<sup>\*</sup>Present address: Hewlett-Packard Laboratories, Palo Alto, CA 94304, USA.

<sup>†</sup>Present address: Department of Electrical and Computer Engineering, University of Wisconsin, Madison, WI 53706, USA.

<sup>‡</sup>Present address: Singapore Institute of Manufacturing Technology (SIMTech), Singapore 638075, Singapore. <sup>§</sup>Corresponding author. E-mail: capasso@seas.harvard.edu



(6, 16). The metasurface approach is distinct in that it provides continuous control of the phase profile (i.e., from 0 to  $2\pi$ ) with a binary structure (only two levels of thickness), circumventing the

fundamental limitation of multiple diffraction orders while maintaining the size, weight, and ease-of-fabrication advantages of planar diffractive optics (5–8). However, the metasurface-based

optical devices demonstrated so far are affected by large chromatic aberrations, though research efforts have shown that relatively broadband optical metasurfaces can be achieved (6, 10, 11, 13–15). This claim of large bandwidth refers to the broadband response of the resonators, which is the result of the high radiation losses necessary for high scattering efficiency and, to a lesser extent, of the absorption losses (6, 17). As a consequence, the phase function implemented by the metasurface can be relatively constant over a range of wavelengths. However, this is not sufficient to eliminate chromatic aberrations. In this Report, we demonstrate a new approach to planar optics based on metasurfaces that achieves achromatic behavior at multiple wavelengths and offers a potentially practical route to circumventing the limitations of both refractive and standard diffractive optics.

Any desired functionality (focusing, beaming, etc.) requires constructive interference between multiple light paths separating the interface and the desired wavefront [i.e., same total accumulated phase  $\varphi_{\text{tot}}$  modulo  $2\pi$  for all light paths (Fig. 1, E and F)]. The total accumulated phase is the sum of two contributions:  $\varphi_{\text{tot}}(r, \lambda) = \varphi_m(r, \lambda) + \varphi_p(r, \lambda)$ , where  $\varphi_m$  is the phase shift imparted at point  $r$  by the metasurface and  $\varphi_p$  is the phase accumulated via propagation through free space. The first term is characterized by a large variation across the resonance. The second is given by  $\varphi_p(r, \lambda) = \frac{2\pi}{\lambda} l(r)$ , where  $l(r)$  is the physical distance between the interface and the desired wavefront (Fig. 1, E and F). To ensure achromatic behavior of the device (e.g., deflection angle or focal length independent of wavelength), the condition of constructive interference should be preserved at different wavelengths by keeping  $\varphi_{\text{tot}}$  constant. The dispersion of  $\varphi_m$  has to be designed to compensate for the wavelength dependence of  $\varphi_p$

$$\varphi_m(r, \lambda) = -\frac{2\pi}{\lambda} l(r) \quad (1)$$

where  $l(r)$  contains information on the device function [i.e., beam deflector (5, 6), lens, axicon (12), etc.]. Equation 1 is the cornerstone for the design of an achromatic metasurface. This approach to flat optics features the advantages of diffractive optics, such as flatness and small footprint, while achieving achromatic operation at selected design wavelengths (Fig. 1). As an example of an achromatic metasurface, we demonstrate a beam deflector based on dielectric resonators: Whereas the typical function of a diffractive grating is the angular separation of different wavelengths, we show beam deflection with a wavelength-independent angle of deflection  $\theta$  for three discrete telecom wavelengths.

The basic unit of the achromatic multiwavelength metasurface is a subwavelength-size resonator designed to adjust the scattering phase shift at different wavelengths  $\varphi_m(r, \lambda)$  to satisfy Eq. 1. In this work, coupled rectangular dielectric resonators (RDRs) are used as building blocks

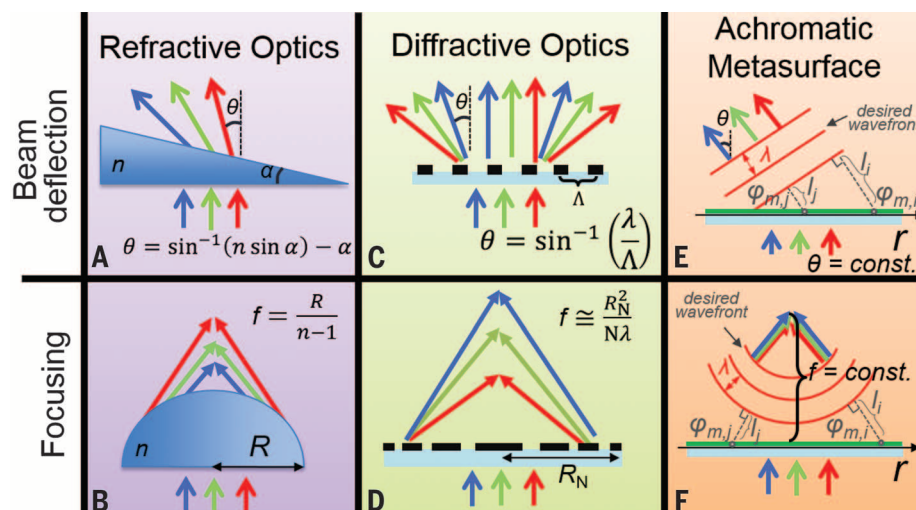


**Fig. 1. Comparison between refractive optics, diffractive optics, and achromatic metasurfaces.** In the first two cases (A to D), the angle of deflection  $\theta$  and the focal length  $f$  change as a function of wavelength. The achromatic metasurface (E and F) consisting of subwavelength spaced resonators is designed to preserve its operation (same  $\theta$  and  $f$ ) for multiple wavelengths. To achieve this, the phase shifts  $\varphi_{m,i}$  and  $\varphi_{m,j}$  imparted by the metasurface at points  $r_i$  and  $r_j$  of the interface are designed so that the paths  $l_i = l(r_i)$  and  $l_j = l(r_j)$  are optically equivalent at different wavelengths.  $\alpha$ , apex angle of the prism;  $R$ , radius of curvature of the refractive lens;  $\Lambda$ , period of the grating;  $R_N$  and  $N$ , radius and number of rings of the diffractive lens, respectively.

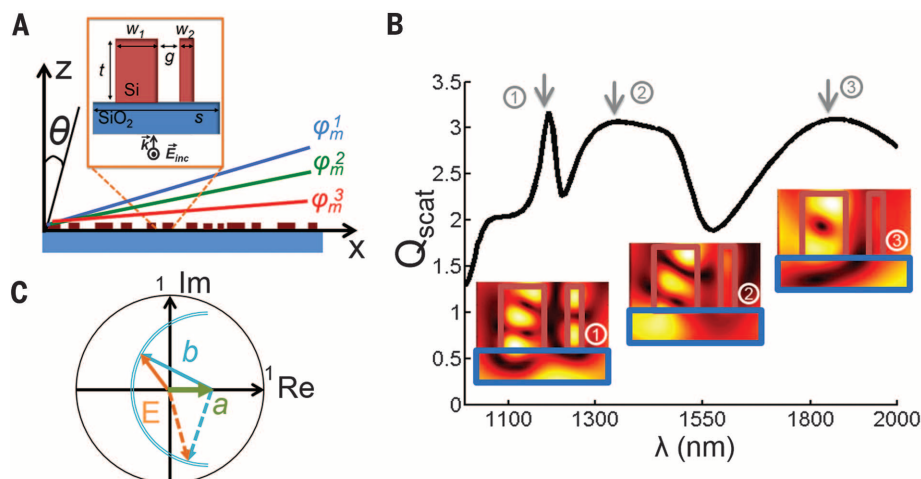


**Fig. 2. Achromatic metasurface.** (A) Side view of the metasurface made of 240 unit cells, each consisting of a slot of the same width  $s$ , comprising two coupled rectangular dielectric resonators of fixed height  $t$  and varying widths  $w_1$  and  $w_2$  (inset). The resonators are assumed to be 2D in the simulations because their length ( $240 \mu\text{m}$ ) is much larger than the other dimensions. The metasurface is designed to diffract normally incident plane waves at three wavelengths ( $\lambda_1 = 1300 \text{ nm}$ ,  $\lambda_2 = 1550 \text{ nm}$ ,  $\lambda_3 = 1800 \text{ nm}$ ) by the same angle ( $\theta_0 = -17^\circ$ ) by implementing a wavelength-dependent linear phase profile  $\varphi_m$ .  $\vec{k}_0$  and  $\vec{E}_{\text{inc}}$ , incident wave vector and electric field, respectively. (B) Scattering efficiency  $Q_{\text{scat}}$  (defined as the ratio of the 2D scattering cross section, which has the dimension of a length, and the geometric length  $w_1 + w_2$ ) for one unit cell with geometry  $s = 1 \mu\text{m}$ ,  $t = 400 \text{ nm}$ ,  $w_1 = 300 \text{ nm}$ ,  $w_2 = 100 \text{ nm}$ , and  $g = 175 \text{ nm}$ . The spectrum has resonances due to the individual resonators (2 and 3) and to the coupling between the resonators (1), as shown by the electric field intensity ( $|E|^2$ ) distributions. (C) Vector representation of the interference between the electric fields scattered by the slot and by the resonators, proportional to  $a$  and  $b$ , respectively. The vector sum of  $a$  (green) and  $b$  (blue) is represented by the phasor  $E$  (orange) for two different wavelengths (solid and dashed lines). Im, imaginary; Re, real.

(18). Figure 2A shows the side view of the metasurface: A 240- $\mu\text{m}$ -wide collection of 240- $\mu\text{m}$ -long silicon (Si) RDRs patterned on a fused silica ( $\text{SiO}_2$ ) substrate is designed to deflect normally incident light at an angle  $\theta_0 = -17^\circ$  for three different wavelengths ( $\lambda_1 = 1300$  nm,  $\lambda_2 = 1550$  nm,

$\lambda_3 = 1800$  nm). The target spatially varying phase functions (Fig. 2A) are defined by (where  $x$  is the spatial coordinate of the metasurface)

$$\varphi_m(x, \lambda_i) = -\frac{2\pi}{\lambda_i} \sin\theta_0 x \text{ for } i = 1, 2, 3 \quad (2)$$

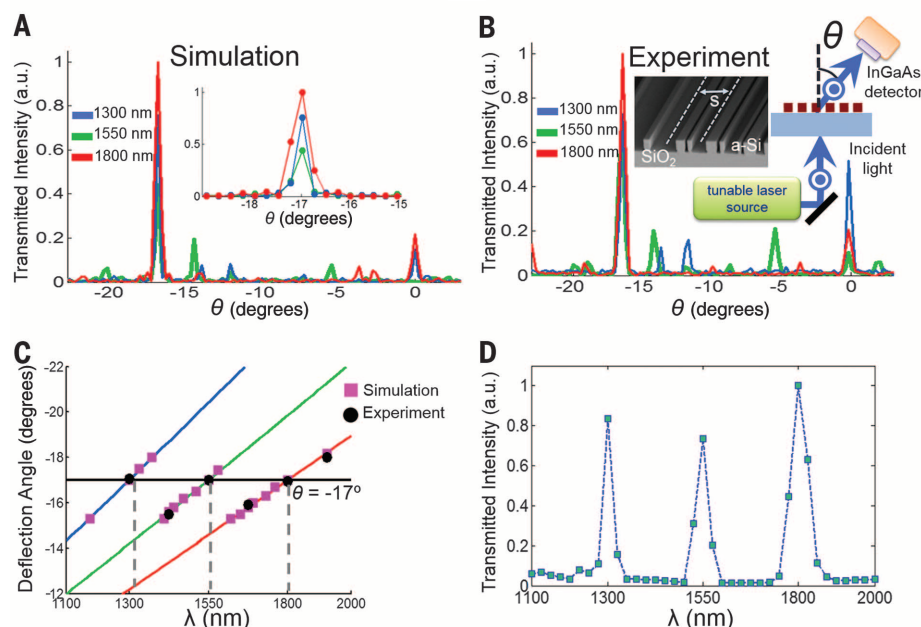


**Fig. 3. Dispersion-free beam deflector.** (A) Simulated far-field intensity (normalized to the maximum value for each of the three wavelengths) as a function of the angle  $\theta$  from the normal to the interface. a.u., arbitrary units. (Inset) Zoomed-in view around the angle  $\theta_0 = -17^\circ$ . (B) Far-field transmission measurements. (Inset) Schematic of the experimental setup and scanning electron microscopy image of a portion of the metasurface ( $s = 1 \mu\text{m}$ ). (C) Measured (black circles) and simulated (pink squares) deflection angles for wavelengths from 1100 to 1950 nm. The colored lines are calculated from Eq. 2 for fixed phase gradients designed for  $\theta_0 = -17^\circ$  and  $\lambda = 1300$  nm (blue), 1550 nm (green), and 1800 nm (red), respectively. (D) Intensity measured by the detector at  $\theta_0$  as a function of wavelength.

The metasurface is divided into 240 subwavelength unit cells of equal width  $s$ , and for each section we choose two RDRs of fixed height  $t$ , varying widths  $w_1$  and  $w_2$ , and separation  $g$  so that the phase response follows Eq. 2. Each unit cell, comprising a slot of width  $s$  with two RDRs (Fig. 2A), is different from the others, and therefore the metasurface is completely aperiodic, unlike other gradient metasurfaces (5, 11) (fig. S7A).

Figure 2B shows the scattering cross section of an isolated unit cell excited with transverse-electric polarization. Given a plane wave traveling along the  $z$  axis and incident on the unit cell, at large distance from the interface ( $\rho \gg \lambda$ ) the field amplitude is given by two contributions: the light diffracted by the slot of width  $s$  and the field scattered by the coupled resonators (19, 20)

$$E(\rho) \approx \frac{e^{jk\rho}}{\rho} [a + b(\theta)] \quad (3)$$

where  $j$  is the imaginary unit,  $k$  is the wave number of the light,  $a$  is the diffraction amplitude assuming the absence of the resonators and is in phase with the incident light,  $\theta$  is the angle between  $\rho$  and the  $z$  axis, and  $b(\theta)$  is the complex scattering function. Equation 3 is valid when the slot size  $s$  is much smaller than the free-space wavelength  $\lambda$ . This is not entirely applicable for our feature size; however, this approximation is sufficient to demonstrate the concept. The interference described by Eq. 3 makes it possible to adjust the phase values at several wavelengths simultaneously within a large range. This effect can be visualized using the complex field (phasors) representation in Fig. 2C. Whereas  $a$  is in phase with the incident field, the phase of  $b$ —associated with the scattered light due to the resonances of the dielectric resonators—spans the range  $(\pi/2, 3\pi/2)$  (11, 21). The vector sum  $E$

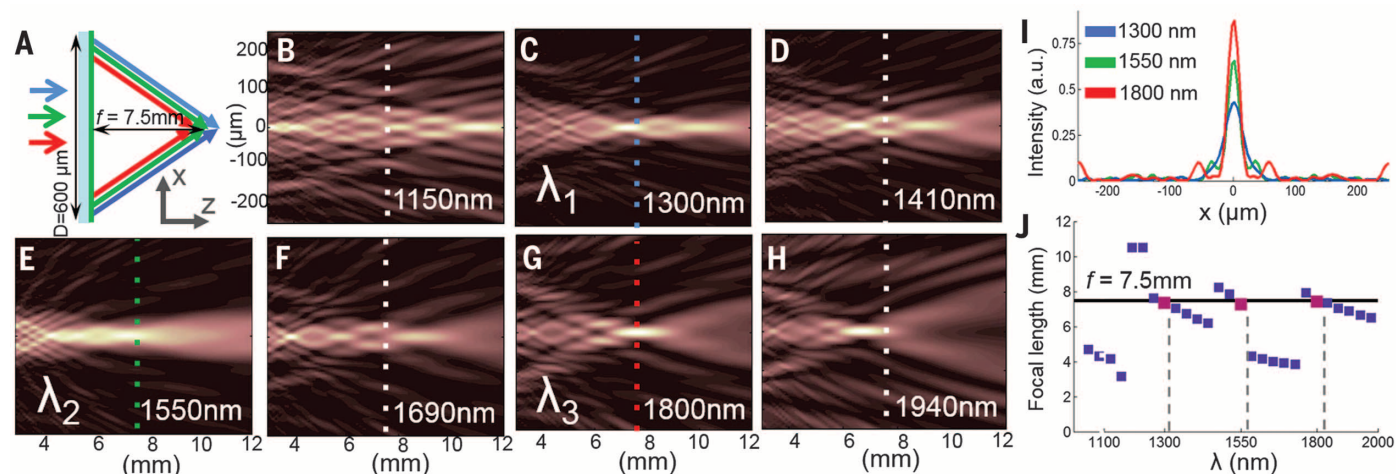


**Fig. 4. Performance of a simulated achromatic flat lens.** (A) A broadband plane wave illuminates the backside of the lens with side  $D = 600 \mu\text{m}$  and focal distance  $f = 7.5$  mm. (B to H) Far-field intensity distribution for different wavelengths. The dashed lines correspond to the desired focal planes. (I) Cross section across the focal plane for  $\lambda_1$ ,  $\lambda_2$ , and  $\lambda_3$ . (J) Focal lengths as a function of wavelength, calculated as the distance between the lens center and highest-intensity point on the optical axis. The three pink squares correspond to the wavelengths of interest.



can thus cover all four quadrants. Note that the scattering cross section  $Q_{\text{scat}}$  (Fig. 2B) used to visualize the resonance of the structure is related to the forward scattering amplitude  $b(0)$  by the optical theorem (20).

Finite-difference time-domain (FDTD) simulations were performed to optimize the geometry of each unit cell to obtain the desired phase response  $\varphi_m(x, \lambda)$  and approximately uniform transmitted amplitude for all unit cells at the three design wavelengths (18). We also simulated the entire structure and calculated the far-field distribution of light transmitted through the interface at several wavelengths. The fabrication procedure involving chemical vapor deposition of amorphous silicon, electron-beam lithography, and reactive ion etching, is described in the supplementary materials (18). Both the simulation and the experimental results show the multiwavelength achromatic behavior of the metasurface (Fig. 3): Whereas the dispersive nature of conventional flat and diffractive optical components would produce an angular separation of the three wavelengths, the angle of deflection at  $\lambda_1$ ,  $\lambda_2$ , and  $\lambda_3$  is the same ( $\theta = -17^\circ$ ). The diffraction order at the opposite side ( $-\theta_0$ ) is completely suppressed (fig. S7), confirming that the structure does not present any periodicity and that the steering effect is the result of the phase gradient introduced by the subwavelength resonators. Simulations for different angles of incidence are presented in fig. S8. Figure 3C shows the simulated and measured deflection angles for normal incidence in the entire spectral range from 1150 to 1950 nm. As expected from the modeling, the device deflects the incident light by an angle  $\theta_0$  only for the designed wavelengths. The three colored lines in Fig. 3C are the theoretical angular dispersion curves obtained from Eq. 2 for metasurfaces designed for fixed wavelengths  $\lambda_1$ ,  $\lambda_2$ , and  $\lambda_3$ . The overlap of the experimental and simulated data with these curves indicates that wavelengths other than  $\lambda_1$ ,  $\lambda_2$ , and  $\lambda_3$  tend to follow the dispersion curve of the closest designed wavelengths. Based on the same type of resonators with identical number of degrees of freedom ( $w_1$ ,  $w_2$ , and  $g$ ), we also designed four other metasurfaces with one, two, four, and five corrected wavelengths, respectively; each metasurface deflects the design wavelengths by the same angle,  $\theta_0 = -17^\circ$  (fig. S9). These results show that our design is wavelength scalable, paving the way for the creation of broadband metasurfaces that are able to suppress chromatic aberrations for a large number of wavelengths, using a reduced number of components compared with achromatic refractive optics (3, 4). An important requirement for an achromatic optical device is uniform efficiency within the bandwidth (1). We measured the intensity at the angular position  $\theta = -17^\circ$  as a function of wavelength from 1100 to 2000 nm (Fig. 3D) and observed intensity variations of less than 13% at  $\lambda_1$ ,  $\lambda_2$ , and  $\lambda_3$  and large suppression ratios with respect to the other wavelengths (50:1). These properties suggest that this device can be used as an optical filter with multiple pass-bands [the full width at half maximum for

each band is  $\sim 30$  nm (fig. S10)]. The measured absolute efficiency of the device (power at  $\theta_0$  divided by the incident power) for the three wavelengths is 9.8%, 10.3%, and 12.6% for  $\lambda_1$ ,  $\lambda_2$ , and  $\lambda_3$ , respectively. From the analysis of the FDTD simulations, we can understand the origin of the limited efficiency and how it can be improved (18).

The design of a flat lens based on RDRs for the same three wavelengths is also presented. This device is functionally equivalent to the bulk refractive lens known as apochromatic triplet or apochromat (3). The parameters  $s$  and  $t$  are the same as in the previous demonstration, and the values of  $w_1$ ,  $w_2$ , and  $g$  for 600 unit cells are chosen so that the target phase functions are (12)

$$\varphi_m(x, \lambda_i) = -\frac{2\pi}{\lambda_i} (\sqrt{x^2 + f^2} - f) \text{ for } i = 1, 2, 3 \quad (4)$$

where the focal distance  $f = 7.5$  mm. Because we are using two-dimensional (2D) RDRs, the hyperbolic phase gradient is applied only in one dimension, imitating a cylindrical lens. The multiwavelength properties of the lens are demonstrated with FDTD simulations (Fig. 4). As expected, we observe good focusing at  $f = 7.5$  mm for  $\lambda_1$ ,  $\lambda_2$ , and  $\lambda_3$  (Fig. 4, C, E, and G) and focusing with aberrations at other wavelengths (Fig. 4, B, D, F, and H). The diameters of the Airy disks at the focal spots are 50, 66, and 59  $\mu\text{m}$  for  $\lambda_1$ ,  $\lambda_2$ , and  $\lambda_3$ , respectively, achieving focusing close to the diffraction limit (40, 47, 55  $\mu\text{m}$ ; numerical aperture = 0.05) (Fig. 4I). For the wavelengths close to  $\lambda_1$ ,  $\lambda_2$ , and  $\lambda_3$ , the focal distance follows the dispersion curve associated with the closest corrected wavelength (Fig. 4J). Recently, it was pointed out that to achieve broadband focusing, the phase shift distribution of a metasurface should satisfy a wavelength-dependent function, though a general approach to overcome this inherent dispersive effect was not provided (22).

In general, the phase function is defined up to an arbitrary additive constant. Therefore, Eq. 1 can be generalized as

$$\varphi_m(r, \lambda) = -\frac{2\pi}{\lambda} l(r) + C(\lambda) \quad (5)$$

For linear optics applications, the quantity  $C(\lambda)$  can take on any value and thus can be used as a free parameter in the optimization of the metasurface elements. More generally,  $C(\lambda)$  can be a relevant design variable in the regime of nonlinear optics, where the interaction between light of different wavelengths becomes important.

Metasurfaces have potential as flat, thin, and lightweight optical components that can combine several functionalities into a single device, making them good candidates to augment conventional refractive or diffractive optics (5–8). The multiwavelength metasurfaces demonstrated here circumvent one of the most critical limitations of planar optical components: the strong wavelength dependence of their operation (focusing, deflection, etc.). These devices could find appli-

cation in digital cameras and holographic 3D displays, in which a red-green-blue filter is used to create a color image. Multiwavelength achromatic metasurfaces could also be implemented in compact and integrated devices for nonlinear processes. Our metasurface design is scalable from the ultraviolet to the terahertz and beyond and can be realized with conventional fabrication processes. Finally, the versatility in the choice of the wavelength-dependent phase allows for functionalities that are very different (even opposite) from the achromatic behavior discussed in this paper. For example, an optical device with enhanced dispersion (e.g., a grating able to separate different colors further apart) can be useful for ultracompact spectrometers.

## REFERENCES AND NOTES

- B. Kress, P. Meyrueis, *Applied Digital Optics* (Wiley, Hoboken, NJ, 2009).
- E. Hecht, *Optics* (Addison Wesley, Boston, ed. 3, 1997).
- F. L. Pedrotti, L. S. Pedrotti, *Introduction to Optics* (Prentice-Hall, Upper Saddle River, NJ, 1987).
- R. Mercado, L. Ryzhikov, *Proc. SPIE* **3482**, 321–331 (1998).
- N. Yu et al., *Science* **334**, 333–337 (2011).
- N. Yu et al., *IEEE J. Sel. Top. Quantum Electron.* **19**, 4700423 (2013).
- N. Yu, F. Capasso, *Nat. Mater.* **13**, 139–150 (2014).
- A. V. Kildishev, A. Boltasseva, V. M. Shalae, *Science* **339**, 1232009 (2013).
- F. Aieta et al., *Nano Lett.* **12**, 1702–1706 (2012).
- X. Ni, N. K. Emani, A. V. Kildishev, A. Boltasseva, V. M. Shalae, *Science* **335**, 427 (2012).
- D. Lin, P. Fan, E. Hasman, M. L. Brongersma, *Science* **345**, 298–302 (2014).
- F. Aieta et al., *Nano Lett.* **12**, 4932–4936 (2012).
- A. Pors, M. G. Nielsen, R. L. Eriksen, S. I. Bozhevolnyi, *Nano Lett.* **13**, 829–834 (2013).
- S. Vo et al., *IEEE Photon. Technol. Lett.* **26**, 1375–1378 (2014).
- W. T. Chen et al., *Nano Lett.* **14**, 225–230 (2014).
- B. Yang, W. M. Ye, X. D. Yuan, Z. H. Zhu, C. Zeng, *Opt. Lett.* **38**, 679–681 (2013).
- M. Kats et al., *Proc. Natl. Acad. Sci. U.S.A.* **109**, 12364–12368 (2012).
- See supplementary materials on Science Online.
- M. Born, E. Wolf, *Principles of Optics* (Cambridge Univ. Press, New York, ed. 7, 1999).
- H. C. van de Hulst, *Light Scattering by Small Particles* (Dover, New York, 1981).
- A. E. Krasnok, A. E. Miroshnichenko, P. A. Belov, Y. S. Kivshar, *Opt. Express* **20**, 20599–20604 (2012).
- C. Saeidi, D. van der Weide, *Appl. Phys. Lett.* **105**, 053107 (2014).

## ACKNOWLEDGMENTS

We acknowledge partial financial support from the Air Force Office of Scientific Research under grant FA9550-12-1-0389 (Multidisciplinary University Initiative), Draper Laboratory under program SC001-0000000731, and the NSF under program ECCS-1347251 (EAGER). We thank B. Kress (Google) for insightful remarks and suggestions; S. Kalchmair, R. Khorasaninejad, and J. P. Laine (Draper Laboratory) for helpful discussions; and E. Hu for the supercontinuum laser (NKT “SuperK”). The fabrication was performed at the Harvard Center for Nanoscale Systems, which is a member of the National Nanotechnology Infrastructure Network. The thin-film characterization of the amorphous silicon was done by Accurion.

## SUPPLEMENTARY MATERIALS

www.sciencemag.org/content/347/6228/1342/suppl/DC1  
Materials and Methods  
Supplementary Text  
Figs. S1 to S10  
References (23–29)

14 November 2014; accepted 6 February 2015  
Published online 19 February 2015;  
10.1126/science.aaa2494

## VIBRATIONAL DYNAMICS

# Experimental ground-state combination differences of $\text{CH}_5^+$

Oskar Asvany,<sup>1</sup> Koichi M. T. Yamada,<sup>2</sup> Sandra Brünken,<sup>1</sup>  
Alexey Potapov,<sup>1</sup> Stephan Schlemmer<sup>1\*</sup>

Protonation of methane ( $\text{CH}_4$ ), a rather rigid molecule well described by quantum mechanics, produces  $\text{CH}_5^+$ , a prototypical floppy molecule that has eluded definitive spectroscopic description. Experimental measurement of high-resolution spectra of pure  $\text{CH}_5^+$  samples poses a formidable challenge. By applying two types of action spectroscopy predicated on photoinduced reaction with  $\text{CO}_2$  and photoinhibition of helium cluster growth, we obtained low-temperature, high-resolution spectra of mass-selected  $\text{CH}_5^+$ . On the basis of the very high accuracy of the line positions, we determined a spectrum of combination differences. Analysis of this spectrum enabled derivation of equally accurate ground state–level schemes of the corresponding nuclear spin isomers of  $\text{CH}_5^+$ , as well as tentative quantum number assignment of this enfant terrible of molecular spectroscopy.

For stable molecules, rotational-vibrational spectra are unique fingerprints of their geometry and chemical bonding. Therefore, high-resolution spectroscopy is the classical tool to determine the moments of inertia and the distances between the nuclei, as well as the frequencies of the vibrational motions and thus the forces underlying the bonds. For example, the electrons in methane ( $\text{CH}_4$ ) mediate four equivalent bonds from the central carbon to the four protons in a tetrahedral configuration that is a global minimum of the multidimensional potential energy surface (PES). Around this minimum, methane performs only small-amplitude motions, making its ro-vibrational spectrum well understood. This simple picture breaks down for very floppy but rather stable molecules such as protonated methane ( $\text{CH}_5^+$ ), known from mass spectra since the early 1950s (1), which accommodates the extra proton via three-center-two-electron (3c-2e) bonding (2).  $\text{CH}_5^+$  is thus a prototype of one class of hypercoordinated carbocations (3).

$\text{CH}_5^+$  has challenged theory for a long time, as it requires the inclusion of higher-level interactions [e.g., electron correlation (4)] to reproduce even low-lying transition states on the PES correctly. Until the 1990s there was debate over whether  $\text{CH}_5^+$  had a structure at all (5). Today (6–8) there is consensus that  $\text{CH}_5^+$  has 120 equivalent global minima on the PES. The minimum energy configuration consists of a  $\text{CH}_3$  tripod and a 3c-2e-bonded  $\text{H}_2$  moiety (Fig. 1, inset). The high zero-point vibrational energy of  $\text{CH}_5^+$  exceeds the potential barriers that arise on the path from one minimum to another. This induces a delocalization of the vibrational wave function among all these equivalent minima

by large-amplitude internal rotation and flip motions, even at low temperature, resulting in a very complicated and hitherto poorly understood spectrum. Not a single transition in the only published high-resolution line list (9) could be assigned, and only the gross features of the spectrum are qualitatively known (8, 10).

Nonetheless, the high-resolution spectra (9) demonstrate that  $\text{CH}_5^+$  has a well-defined ro-vibrational energy level structure. Here, we decipher this level structure by recording cryogenic

spectra of the CH-stretching vibrations in the range where the  $\text{CH}_3$  tripod modes are expected (10). The enabling experimental technologies have been documented in (11–13), with further details given in the supplementary material. Two different action spectroscopy methods were applied to a few thousand mass-selected and trapped  $\text{CH}_5^+$  ions at two different temperatures: laser-induced reaction (LIR) (10, 14, 15) with  $\text{CO}_2$  at a nominal temperature of 10 K, followed by laser-induced inhibition of complex growth (LIICG) at a nominal temperature of 4 K. In LIICG (13, 16, 17), the attachment of helium is hindered by resonant excitation of the bare ion. Besides the cryogenic temperatures, the usage of a narrow-band optical parametric oscillator as the light source and a frequency comb (12) for frequency determination allowed measurement of all line centers of the ro-vibrational transitions with high accuracy and precision, often below 1 MHz. In the obtained spectra, 2897 lines are in the range 2886 to 3116  $\text{cm}^{-1}$  comprising the LIR spectrum (Fig. 1A), and, upon further cooling, only 185 lines are in the LIICG spectrum (Fig. 1B).

The  $\text{CH}_5^+$  spectrum changes markedly upon cooling, and therefore our cryogenic spectra differ substantially from those measured by the Oka group (9), indicated as black bars in the exemplary 0.9  $\text{cm}^{-1}$ -wide experimental spectrum (Fig. 1, inset). In general, many of the strongest lines from their study do not appear in our spectra, but of their 770 lines contained in our measurement range, 215 are present in our 10 K spectrum (within 0.003  $\text{cm}^{-1}$  tolerance) and 14 are present in our 4 K spectrum. This simplification

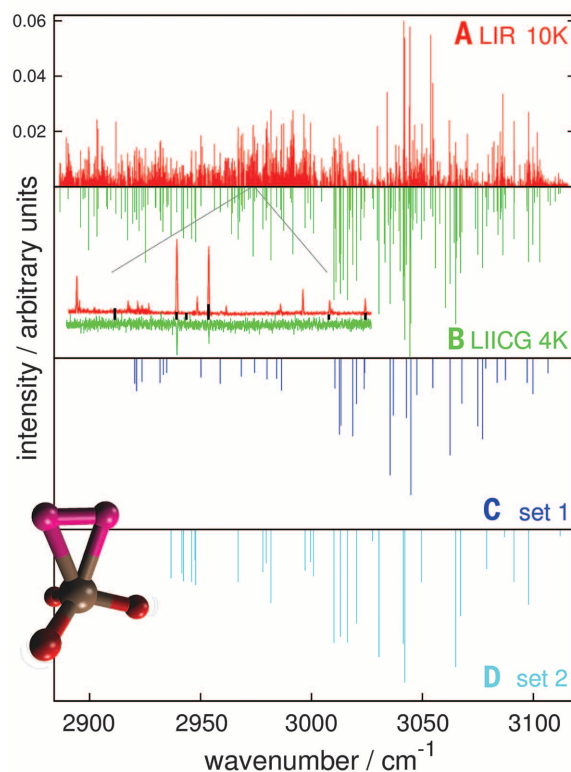


**Fig. 1. High-resolution CH-stretching vibrational spectrum of  $\text{CH}_5^+$ .** The vibrations mainly involve the three tripod hydrogens (see inset molecule sketch). (A) Experimental stick spectrum recorded by LIR at a nominal temperature of 10 K. (B) Stick spectrum recorded by LIICG nominally at 4 K. The inset shows an experimental scan (2973.34 to 2974.26  $\text{cm}^{-1}$ ) that demonstrates the high density of lines at 10 K and the simplification upon cooling. From our 19 lines and six lines reported by Oka's group (9) (shown as black bars) in that range, only two survive in the 4 K spectrum. (C and D) Two disjunct sets of lines extracted from the 4 K line list, likely belonging to the different nuclear spin symmetry species (see text).

<sup>1</sup>Physikalisches Institut, Universität zu Köln, 50937 Köln, Germany. <sup>2</sup>Environmental Molecular Science Group, EMTech, AIST Tsukuba West, Onogawa 16-1, Tsukuba, Ibaraki 305-8569, Japan.

\*Corresponding author. E-mail: schlemmer@ph1.uni-koeln.de



upon cooling allows the band centers to become more apparent. In both the 10 K and 4 K spectra, the strongest lines gather around  $3043\text{ cm}^{-1}$ , which implies that this is one of the CH-stretching band centers. This finding is also supported by the density of lines peaking there. However, it becomes obvious that even at 4 K, where only the lowest rotational levels are populated, the bands are still very numerous and heavily overlapping. This is caused by combination bands with low-lying vibrational levels (18), as well as large rotational constants due to the light protons rotating around the heavy carbon nucleus. The wide spread of the lines and the very irregular patterns make an assignment of the band centers by simple inspection impossible. Moreover, there is no realistic model prediction for the spectrum of this enigmatic molecule. However, we make use of the first principles of quantum mechanics for the assignment of the rich spectra taken at different temperatures.

The narrow ro-vibrational lines in our spectra are connected to a well-defined energy level diagram by the basic formula  $h\nu_{fi} = E_f - E_i$ , where  $E_i$  and  $E_f$  denote the initial and final states of the transition, respectively. The transitions shown in Fig. 2 as arrows share the same energy level diagram. The energy levels are labeled 0 through 3 for the lowest-energy states ( $E_i$ ) and  $a$  through  $d$  for states with one quantum of C-H stretch vibration excited ( $E_f$ ). The arrows (transitions)

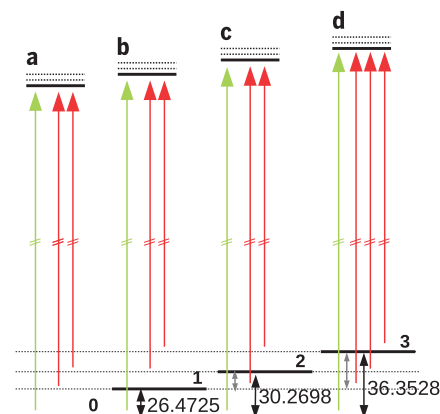


**Fig. 2. Energy level diagram of ground and vibrational excited states connected by the observed ro-vibrational transitions.** The green arrows indicate transitions from the lowest level, which should thus be contained in the 4 K line list shown in Fig. 1B. The multitude of upper levels (a through d) is indicated by dashed lines. If two transitions share a common upper level—for example, the transitions from level 0 to a and from level 1 to a—the difference of the two transition frequencies is the energy difference of levels 0 and 1, which is called a ground-state combination difference. Such CoDiffs reveal themselves by their multiple appearance. The energy values (in  $\text{cm}^{-1}$ ) shown exemplarily for the ground-state levels are those of set 1 (marked “x” in Fig. 3). There is one or more such diagram for each set (symmetry species) of  $\text{CH}_5^+$ .

drawn in blocks share the same upper level. As a consequence, the energy differences between these transitions, the so-called combination differences (CoDiffs), will reveal the relative energy structure of the lower states of this term diagram. As indicated by the many bands observed in the present experiment, the upper states accessed are numerous. Therefore, CoDiff values belonging to such energy differences will appear many times. Derived from the experimental spectrum, each CoDiff has a frequency uncertainty. Neighboring CoDiffs are considered to coincide with this CoDiff value when their values overlap within the frequency uncertainties (see supplementary materials).

Accordingly, we constructed a CoDiff coincidence spectrum. Figure 3A shows the number of coincidences of CoDiffs up to  $60\text{ cm}^{-1}$ , as derived from the 1617 strongest lines of the 2897 lines in the 10 K spectrum (Fig. 1A). This CoDiff spectrum shows a tremendous number of very narrow peaks that appear from an almost noise-free background (Fig. 3, inset). The construction of the CoDiff spectrum is such that coincidence peaks associated with the energy differences of the term diagram exhibit a bell-shaped probability distribution (Fig. 3, inset). For some peaks, the number of coincidences significantly exceeds a statistical average value. These are the CoDiffs that we clearly associate with the desired energy structure.

To assign the observed CoDiff peaks to differences in the ground state or the excited state, we make use of the fact that we measured the spectrum at two temperatures. The 4 K line list contains only  $N = 185$  lines, originating from the lowest level (green arrows originating from level 0 in Fig. 2); higher levels (denoted 1 through 3 in Fig. 2) may not be populated under the conditions of the LIICG experiment. Thus, if we require both lines of a CoDiff to be contained in the 4 K LIICG spectrum, the number of CoDiffs is reduced considerably to  $N(N - 1)/2 = 17,020$ , although we risk missing ground-state CoDiffs. In order to exploit the full information of our spectra, we therefore created another list of CoDiffs based on both line lists. For CoDiffs from the full 10 K spectrum (rejecting only 134 weak lines), we required that the higher-frequency transition also appear in the 4 K spectrum (Fig. 2, green arrows) because the lower initial state should be populated. The resulting CoDiff spectrum is shown as the green trace in Fig. 3B. This spectrum has far fewer CoDiffs than the 10 K spectrum in Fig. 3A, and strong peaks appear only for CoDiff values larger than  $20\text{ cm}^{-1}$ . These are the energy differences that we associate with the differences between state 0 and states 1 to 3 in Fig. 2. The prominent peaks in the low-frequency part of Fig. 3A, on the other hand, belong to transitions from states that are populated at 10 K but not at 4 K (Fig. 2, gray arrows). The

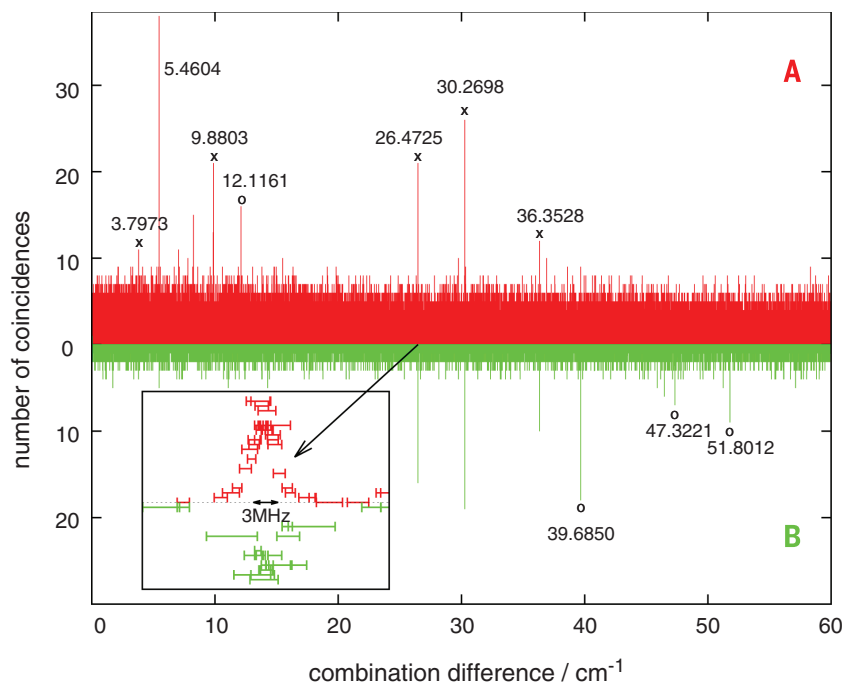


**Fig. 3. Number of coincidences of combination differences (CoDiffs) as a function of their energy difference.** Strong peaks arise from nonaccidental CoDiffs based on the numerous bands observed and are associated with ground-state CoDiffs (see text). (A) Coincidence spectrum based on a selection of the 1617 strongest lines from the 2897 lines of the 10 K spectrum. (B) Coincidence spectrum based on nearly all 2897 lines of the 10 K spectrum, but with the additional condition that the higher-frequency transition of the CoDiff be contained in the 4 K spectrum (see supplementary text for details). The inset is a magnification of the CoDiff peak at  $26.4725\text{ cm}^{-1}$ . The CoDiff peak positions are summarized in Table 1.

strong peaks found in the CoDiff spectra are summarized in Table 1.

According to Fig. 2, all ground-state CoDiffs participating in such a level scheme, called a set in the following, should be linked by common 4 K lines. By checking these lines, we could clearly identify two such distinct sets that do not share common transitions (“x” and “o” in Fig. 3; sets 1 and 2 in Table 1), with the obtained ground state-level energies of set 1 given explicitly in Fig. 2. The extracted 4 K lines belonging to these two distinct sets are plotted in Fig. 1, C and D, respectively. The distinction of the sets arises from the selection rules of the corresponding transitions. These selection rules are dictated by the symmetry of the  $\text{CH}_5^+$  molecule (see supplementary material). We associate the distinct sets with the three different nuclear spin isomers ( $I = 5/2$ ,  $3/2$ , and  $1/2$ ) that are formed by the five protons ( $I = 1/2$ ) in  $\text{CH}_5^+$ , analogous to the ortho ( $I = 1$ ) and para ( $I = 0$ ) spin isomers in  $\text{H}_2$ . Transitions between these different nuclear spin isomers are forbidden because the nuclear spin does not flip in ro-vibrational transitions. Therefore, upon cooling to 4 K, only the three lowest levels of the different spin isomers will remain. Apparently we only found two of these levels, denoted as 0 in Fig. 2 and Table 1. The third set of CoDiffs we expect is not as easily identified in our data because the number of lines, and thus the number of CoDiffs, appears to be too small to emerge as a strong peak in the coincidence spectrum.

Because of the Pauli exclusion principle, the three nuclear spin configurations ( $A_1$  for  $I = 5/2$ ,  $G_1$  for  $I = 3/2$ , and  $H_1$  for  $I = 1/2$ ) are each associated with exactly one symmetry species ( $A_2$ ,  $G_2$ , and  $H_2$ ) of the ro-vibrational states in the molecular symmetry group  $G_{240}$  for  $\text{CH}_5^+$ . Applying the rules of group theory, it therefore becomes possible to identify the nuclear spin configuration associated with the sets appearing in our spectra, and thus to address the symmetry of the ro-vibrational states denoted as 0 through 3 in Fig. 2 and Table 1. This is of

fundamental importance when trying to find the lowest rotational state  $J'' = 0$  and for comparison with theoretical spectra. The intensity of the lines observed in our spectra is governed by the nuclear spin statistical weights ( $2I + 1$ ), which are 6, 4, and 2 for the ro-vibrational states  $A_2$ ,  $G_2$ , and  $H_2$ , respectively. Likewise, the numbers of states of  $A_2$ ,  $G_2$ , and  $H_2$  symmetry are 1:4:5 [see (9, 19) or supplementary materials], and we therefore expect the proportions of the corresponding CoDiff coincidences to be approximately the square of this ratio, namely 1:16:25. As a result of these considerations, the lines of set 1 (Fig. 1C) are associated with  $G_2$  states, and those of set 2 (Fig. 1D) likely belong to the  $H_2$  symmetry. For the latter state, the number of CoDiffs is quite numerous (Fig. 3B) but the intensity is rather small, and thus the CoDiff peaks arise only when lower-intensity lines of the 10 K spectrum are considered in combination with the 4 K spectrum. In contrast, the transitions of the  $A_2$  ro-vibrational states are rather intense but create few CoDiffs. Therefore, we are certain that the missing CoDiff set 3 is associated with this state.

The  $G_2$  spectrum shown in Fig. 1C comprises transitions from the rotationless state  $J'' = R'' = 0$  (20), as pointed out before (21). Therefore, one might assign this quantum number and molecular symmetry label ( $G_2$ ) to the lowest-energy state denoted 0 in Fig. 2. Because of the construction of the CoDiffs and a  $\Delta R = \pm 1$  propensity rule for the observed transitions, the state denoted 1 in Fig. 2 might then be associated with  $R'' = 2$ . For a more rigid molecule, one would predict a value of  $6B$  for the spacing of these two states, where  $B$  would be an effective rotational constant. For a reasonable value of  $B \approx 4 \text{ cm}^{-1}$  [see, e.g., (21)] for the almost spherical  $\text{CH}_5^+$ , this agrees well with the first peak of set 1 at  $26.4725 \text{ cm}^{-1}$  (Fig. 3A). Likewise, the smallest combination difference,  $39.6850 \text{ cm}^{-1}$ , found for set 2 (Fig. 3B) is close to  $10B$ , which corresponds to the energy difference between  $J'' = 1$  and  $J'' = 3$  (22). Provided these last assumptions are cor-

rect, our findings may support the unexpected notion that  $\text{CH}_5^+$ , even though highly fluxional in the bending and torsional degrees of freedom, behaves more rigidly in the stretching coordinates, thus giving rise to an effective rotational constant. This idea was suggested some years ago (23), as the C-H bond lengths remain almost constant in the PES.

However, the assignments of the rotational states have to be taken with care, as the ordering of the states may be irregular because of splittings of the  $J'' \geq 1$  states to the extent that levels with higher  $J''$  are lower in energy. This has already been predicted in the particle-on-a-sphere (POS) model of Deskevich *et al.* (24) for  $\text{CH}_5^+$ . This stands in contrast to the regular energy level schemes of more rigid molecules. Because of the complex ro-tunneling structure of  $\text{CH}_5^+$ , the exact positions of the individual CoDiffs are a result of its PES, as discussed in detail by Wang and Carrington (18) for the  $J'' = 0$  ground state. Future work for  $J'' > 0$  may unfold the detailed structure of the lowest-energy states. More sophisticated tools are needed to find more transitions, more CoDiffs, and more complex spectroscopic patterns that are linked by the symmetry of  $\text{CH}_5^+$ . Also, some of the strongest peaks in the CoDiff spectrum (e.g., at  $5.46036 \text{ cm}^{-1}$ ) still need to be assigned. Even so, the values in Table 1 will challenge theoretical predictions at the highest level of sophistication. The analysis of the wealth of experimental data allowed a tentative assignment of the lowest-energy levels of this enigmatic molecule based on the high-resolution spectra taken at two low temperatures. Transitions from the rotational ground state are likely identified. The problem is not solved, but the method of LIR is ready to take on the next experimental challenge—to directly test the lowest ro-vibrational transitions in the quest for a proper description of  $\text{CH}_5^+$ .

## REFERENCES AND NOTES

- V. Tal'roze, A. Lyubimova, *Dokl. Akad. Nauk SSSR* **86**, 909 (1952).
- D. Marx, M. Parrinello, *Nature* **375**, 216–218 (1995).
- G. A. Olah, N. Hartz, G. Rasul, G. K. S. Prakash, *J. Am. Chem. Soc.* **117**, 1336–1343 (1995).
- V. Dyczmons, W. Kutzelnigg, *Theor. Chim. Acta* **33**, 239–247 (1974).
- P. R. Schreiner, S. Kim, H. F. Schaefer, P. von Ragué Schleyer, *J. Chem. Phys.* **99**, 3716 (1993).
- P. Kumar P., D. Marx, *Phys. Chem. Chem. Phys.* **8**, 573–586 (2006).
- Z. Jin, B. J. Braams, J. M. Bowman, *J. Phys. Chem. A* **110**, 1569–1574 (2006).
- X. Huang *et al.*, *Science* **311**, 60–63 (2006).
- E. T. White, J. Tang, T. Oka, *Science* **284**, 135–137 (1999).
- O. Asvany *et al.*, *Science* **309**, 1219–1222 (2005).
- O. Asvany, F. Biellau, D. Moratschke, J. Krause, S. Schlemmer, *Rev. Sci. Instrum.* **81**, 076102 (2010).
- O. Asvany, J. Krieg, S. Schlemmer, *Rev. Sci. Instrum.* **83**, 093110 (2012).
- O. Asvany, S. Brünken, L. Kluge, S. Schlemmer, *Appl. Phys. B* **114**, 203–211 (2014).
- S. Schlemmer, E. Lescop, J. von Richthofen, D. Gerlich, M. A. Smith, *J. Chem. Phys.* **117**, 2068 (2002).
- O. Asvany *et al.*, *Phys. Rev. Lett.* **100**, 233004 (2008).
- S. Chakrabarty *et al.*, *J. Phys. Chem. Lett.* **4**, 4051–4054 (2013).
- S. Brünken, L. Kluge, A. Stoffels, O. Asvany, S. Schlemmer, *Astrophys. J.* **783**, L4 (2014).

**Table 1. CoDiff positions obtained by fitting the most prominent peaks in the two spectra of Fig. 3.** Errors are SD. The involved levels are labeled 0 through 3, as in Fig. 2.

Position ( $\text{cm}^{-1}$ )	Symmetry	Upper	Lower
$3.79734 \pm 0.00004$	Set 1	2	1
$5.46036 \pm 0.00006$			
$7.04935 \pm 0.00008$			
$8.25267 \pm 0.00004$			
$9.88029 \pm 0.00005$	Set 1	3	1
$12.11611 \pm 0.00005$	Set 2	3	1
$26.47251 \pm 0.00005$	Set 1	1	0
$29.76214 \pm 0.00007$	Set 1	2	0
$30.26982 \pm 0.00006$			
$36.35281 \pm 0.00003$			
$36.91995 \pm 0.00009$			
$39.68506 \pm 0.00007$	Set 2	1	0
$46.46478 \pm 0.00010$			
$47.32219 \pm 0.00005$	Set 2	2	0
$51.80120 \pm 0.00006$	Set 2	3	0



18. X.-G. Wang, T. Carrington Jr., *J. Chem. Phys.* **129**, 234102 (2008).
19. T. Oka, *J. Mol. Spectrosc.* **228**, 635–639 (2004).
20. Here  $J$  denotes the rotational quantum number comprising end-over-end rotation  $R$  and internal rotation.
21. P. Bunker, B. Ostojić, S. Yurchenko, *J. Mol. Struct.* **695–696**, 253 (2004).
22. Here we use the quantum number  $J$  instead of  $R$ , because the rotational motion in the state is not purely the end-over-end rotation.
23. M. Kolbuszewski, P. R. Bunker, *J. Chem. Phys.* **105**, 3649 (1996).

24. M. P. Deskevich, A. B. McCoy, J. M. Hutson, D. J. Nesbitt, *J. Chem. Phys.* **128**, 094306 (2008).

#### ACKNOWLEDGMENTS

We thank T. Carrington, P. Bunker, D. Nesbitt, P. Jensen, and U. Manthe for fruitful discussions on theoretical aspects of  $\text{CH}_5^+$ , as well as J. Krieg in the initial stage of the experiment. Supported by Deutsche Forschungsgemeinschaft grant SCHL 341/6-1. We gratefully acknowledge the support of the workshops of the I. Physikalisches Institut. The two line lists (for 10 K and 4 K) associated with Fig. 1 are available as supplementary material;

the raw data are archived at the University of Cologne and are available upon request.

#### SUPPLEMENTARY MATERIALS

[www.sciencemag.org/content/347/6228/1346/suppl/DC1](http://www.sciencemag.org/content/347/6228/1346/suppl/DC1)  
Materials and Methods  
Tables S1 and S2  
Reference (25)

21 November 2014; accepted 21 January 2015  
10.1126/science.aaa3304

## ADDITIVE MANUFACTURING

# Continuous liquid interface production of 3D objects

John R. Tumbleston,<sup>1</sup> David Shirvanyants,<sup>1</sup> Nikita Ermoshkin,<sup>1</sup> Rima Januszewicz,<sup>2</sup> Ashley R. Johnson,<sup>3</sup> David Kelly,<sup>1</sup> Kai Chen,<sup>1</sup> Robert Pinschmidt,<sup>1</sup> Jason P. Rolland,<sup>1</sup> Alexander Ermoshkin,<sup>1\*</sup> Edward T. Samulski,<sup>1,2\*</sup> Joseph M. DeSimone<sup>1,2,4\*</sup>

Additive manufacturing processes such as 3D printing use time-consuming, stepwise layer-by-layer approaches to object fabrication. We demonstrate the continuous generation of monolithic polymeric parts up to tens of centimeters in size with feature resolution below 100 micrometers. Continuous liquid interface production is achieved with an oxygen-permeable window below the ultraviolet image projection plane, which creates a “dead zone” (persistent liquid interface) where photopolymerization is inhibited between the window and the polymerizing part. We delineate critical control parameters and show that complex solid parts can be drawn out of the resin at rates of hundreds of millimeters per hour. These print speeds allow parts to be produced in minutes instead of hours.

Additive manufacturing has become a useful technique in a wide variety of applications, including do-it-yourself 3D printing (1, 2), tissue engineering (3–5), materials for energy (6, 7), chemistry reactionware (8), molecular visualization (9, 10), microfluidics (11), and low-density, high-strength materials (12–15). Current additive manufacturing methods such as fused deposition modeling, selective laser sintering, and stereolithography (2, 16) are inordinately slow because they rely on layer-by-layer printing processes. A macroscopic object several centimeters in height can take hours to construct. For additive manufacturing to be viable in mass production, print speeds must increase by at least an order of magnitude while maintaining excellent part accuracy. Although oxygen inhibition of free radical polymerization is a widely encountered obstacle to photopolymerizing UV-curable resins in air, we show how controlled oxygen inhibition can be used to enable simpler and faster stereolithography.

Typically, oxygen inhibition leads to incomplete cure and surface tackiness when photopolymerization is conducted in air (17, 18). Oxygen

can either quench the photoexcited photoinitiator or create peroxides by combining with the free radical from the photocleaved photoinitiator (fig. S1). If these oxygen inhibition pathways can be avoided, efficient initiation and propagation of polymer chains will result. When stereolithography is conducted above an oxygen-permeable build window, continuous liquid interface production (CLIP) is enabled by creating an oxygen-containing “dead zone,” a thin uncured liquid layer between the window and the cured part surface. We show that dead zone thicknesses on the order of tens of micrometers are maintained by judicious selection of control parameters (e.g., photon flux and resin optical and curing properties). Simple relationships describe the dead zone thickness and resin curing process, and, in turn, result in a straightforward relationship between print speed and part resolution. We demonstrate that CLIP can be applied to a range of part sizes from undercut micropaddles with stem diameters of 50  $\mu\text{m}$  to complex handheld objects greater than 25 cm in size.

Figure 1A illustrates the simple architecture and operation of a 3D printer that takes advantage of an oxygen-inhibited dead zone. CLIP proceeds via projecting a continuous sequence of UV images (generated by a digital light-processing imaging unit) through an oxygen-permeable, UV-transparent window below a liquid resin bath. The dead zone created above the window maintains a liquid interface below the advancing part. Above the dead zone, the curing part is continuously drawn out of the resin bath, thereby creat-

ing suction forces that constantly renew reactive liquid resin. This nonstop process is fundamentally different from traditional bottom-up stereolithography printers, where UV exposure, resin renewal, and part movement must be conducted in separate and discrete steps (fig. S2). Even for inverted top-down approaches in which photopolymerization occurs at an air-resin interface [i.e., the part is successively lowered into a resin bath during printing (16, 19)], these steps must be conducted sequentially for the formation of each layer. Because each step takes several seconds to implement for each layer, and because each layer of a part has a typical thickness of 50 to 100  $\mu\text{m}$ , vertical print speeds are restricted to a few millimeters per hour (16). By contrast, the print speed for CLIP is limited by resin cure rates and viscosity (discussed below), not by stepwise layer formation. For example, the gyroid and argyle structures shown in Fig. 1B were printed at 500 mm/hour, reaching a height of  $\sim 5$  cm in less than 10 min (movies S1 and S2). An additional benefit of a continual process is that the choice of 3D model slicing thickness, which affects part resolution, does not influence print speed, as shown in the ramp test patterns in Fig. 1C. Because CLIP is continuous, the refresh rate of projected images can be increased without altering print speed, ultimately allowing for smooth 3D objects with no model slicing artifacts.

Establishing an oxygen-inhibited dead zone is fundamental to the CLIP process. CLIP uses an amorphous fluoropolymer window (Teflon AF 2400) with excellent oxygen permeability (1000 barrers; 1 barrer =  $10^{-10}$   $\text{cm}^3(\text{STP}) \text{ cm cm}^{-2} \text{ s}^{-1} \text{ cmHg}^{-1}$ ) (20), UV transparency, and chemical inertness. Dead zone thickness measurements using a differential thickness technique (fig. S3) demonstrate the importance of both oxygen supply and oxygen permeability of the window in establishing the dead zone. Figure 2 shows that the dead zone thickness when pure oxygen is used below the window is about twice the thickness when air is used, with the dead zone becoming thinner as the incident photon flux increases (see below). When nitrogen is used below the window, the dead zone vanishes. A dead zone also does not form when Teflon AF 2400 is replaced by a material with very poor oxygen permeability, such as glass or polyethylene, even if oxygen is present below the window. Without a suitable dead zone, continuous part production is not possible.

For the case of ambient air below the window, Fig. 3A shows the dependence of dead zone thickness on incident photon flux ( $\Phi_0$ ), photoinitiator

<sup>1</sup>Carbon3D Inc., Redwood City, CA 94063, USA. <sup>2</sup>Department of Chemistry, University of North Carolina, Chapel Hill, NC 27599, USA. <sup>3</sup>Joint Department of Biomedical Engineering, University of North Carolina at Chapel Hill and North Carolina State University. <sup>4</sup>Department of Chemical and Biomolecular Engineering, North Carolina State University, Raleigh, NC 27695, USA.

\*Corresponding author. E-mail: alex@carbon3d.com (A.E.); et@unc.edu (E.T.S.); desimone@email.unc.edu (J.M.D.)

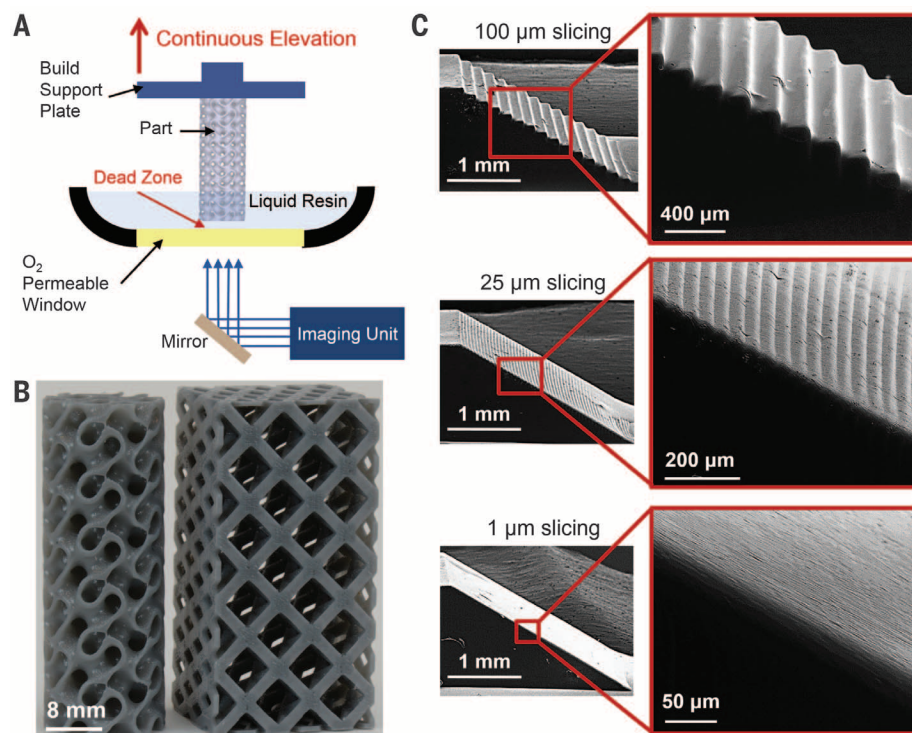


**Fig. 1. CLIP enables fast print speeds and layerless part construction.** (A) Schematic of CLIP printer where the part (gyroid) is produced continuously by simultaneously elevating the build support plate while changing the 2D cross-sectional UV images from the imaging unit. The oxygen-permeable window creates a dead zone (persistent liquid interface) between the elevating part and the window. (B) Resulting parts via CLIP, a gyroid (left) and an argyle (right), were elevated at print speeds of 500 mm/hour (movies S1 and S2). (C) Ramp test patterns produced at the same print speed regardless of 3D model slicing thickness (100  $\mu\text{m}$ , 25  $\mu\text{m}$ , and 1  $\mu\text{m}$ ).

absorption coefficient ( $\alpha_{\text{PI}}$ ), and resin curing dosage ( $D_{\text{co}}$ ). These three control parameters are related to dead zone thickness according to

$$\text{Dead zone thickness} = C \left( \frac{\Phi_0 \alpha_{\text{PI}}}{D_{\text{co}}} \right)^{-0.5} \quad (1)$$

where  $\Phi_0$  is the number of incident photons at the image plane per area per time,  $\alpha_{\text{PI}}$  is the product of photoinitiator concentration and the wavelength-dependent absorptivity,  $D_{\text{co}}$  quantifies the resin reactivity of a monomer-photoinitiator combination (fig. S4), and  $C$  is a proportionality constant. This relationship is similar to the one that describes photopolymerizable particle formation in microfluidic devices that use oxygen-permeable channel walls (21, 22). The dead zone thickness behaves as follows: Increasing either  $\Phi_0$  or  $\alpha_{\text{PI}}$  increases the concentration of free radicals in the resin (fig. S1) and decreases the initial oxygen concentration by reaction. Additional oxygen diffuses through the window and into the resin but decays with distance from the window, so that free radicals will overpower inhibiting oxygen at some distance from the window. At the threshold distance where all oxygen is consumed and free radicals still exist, polymerization will begin. Increasing the reactivity of the resin (i.e., decreasing  $D_{\text{co}}$ ) causes the polymerization threshold distance from the window to also

shrink, thus making the dead zone thinner. The proportionality constant  $C$  in Eq. 1 has a value of  $\sim 30$  for our case of 100- $\mu\text{m}$ -thick Teflon AF 2400 with air below the window, and has units of the square root of diffusivity. The flux of oxygen through the window is also important in maintaining a stable dead zone over time, which is commonly described in terms of the ratio of film permeability to film thickness (23). Using these relationships enables careful control of the dead zone, which provides a critical resin renewal layer between the window and the advancing part.

Above the dead zone, photopolymerization occurs to a certain cured thickness that depends on  $\Phi_0 \alpha_{\text{PI}} / D_{\text{co}}$  along with exposure time ( $t$ ) and the resin absorption coefficient ( $\alpha$ ) according to the relationship

$$\text{Cured thickness} = \frac{1}{\alpha} \ln \left( \frac{\Phi_0 \alpha_{\text{PI}} t}{D_{\text{co}}} \right) \quad (2)$$

Figure 3B shows cured thickness for three different resins with varying  $\alpha$  (holding  $\alpha_{\text{PI}}$  constant) where thicknesses were measured for different UV photon dosages (products of  $\Phi_0$  and  $t$ ) (fig. S3). These curves are akin to the so-called “working curves” used in stereolithography resin characterization (16, 19). For these resins,  $\alpha$  is varied by adjusting the concentration of an absorbing dye or pigment that passively absorbs light (i.e.,

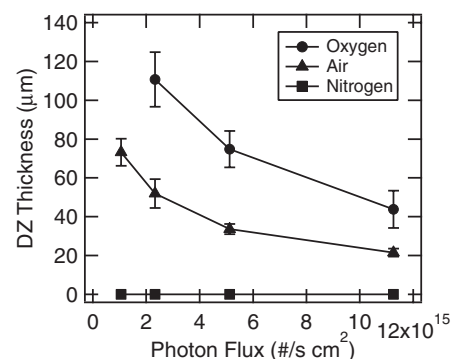


**Fig. 2. The dead zone is created by oxygen permeation through the window.** Dead zone thickness is shown as a function of incident photon flux. When pure oxygen is used below the gas-permeable window, the dead zone thickness increases. If nitrogen is used, the dead zone vanishes, resulting in adhesion of the cured resin to the window. Error bars represent SD of 10 measurements of the same conditions.

does not produce radicals) but contributes to overall resin absorption via  $\alpha = \alpha_{\text{PI}} + \alpha_{\text{dye}}$ . Note that  $\alpha$  is the inverse of the characteristic optical absorption height ( $h_A$ ) of the resin:

$$h_A = \frac{1}{\alpha} \quad (3)$$

The value of  $h_A$ , in conjunction with the model slicing thickness (Fig. 1C), projected pixel size, and image quality, determines the part resolution. The projected pixel size (typically between 10 and 100  $\mu\text{m}$ ) and image quality are functions of the imaging setup and determine lateral part resolution. As with slicing thickness,  $h_A$  affects vertical resolution but is a property of the resin. If  $h_A$  is high, then previously cured 2D patterns will continue to be exposed, causing unintentional overcuring and “print-through,” which in turn results in defects for undercut and overhang geometries.

From the expressions for dead zone thickness and cured thickness, a simple relationship among print speed,  $h_A$  (i.e., resolution), and  $\Phi_0 \alpha_{\text{PI}} / D_{\text{co}}$  is derived:

$$\frac{\text{Speed}}{h_A} \propto \frac{\Phi_0 \alpha_{\text{PI}}}{D_{\text{co}}} \quad (4)$$

(see supplementary materials). Figure 3C shows a contour plot of speed as a function of  $h_A$  and the ratio  $\Phi_0 \alpha_{\text{PI}} / D_{\text{co}}$ ; the dead zone thickness (Eq. 1) is indicated. For a given  $h_A$ , speed can be increased by increasing  $\Phi_0$  or  $\alpha_{\text{PI}}$  or by using a resin with lower  $D_{\text{co}}$ . However, as speed increases, dead zone thickness decreases and will eventually become too thin for the process to remain stable. For CLIP, the empirically determined minimum dead zone thickness is  $\sim 20$  to 30  $\mu\text{m}$ . Part production with a dead zone thickness below this minimum is possible but can lead to window adhesion-related defects. Once the minimum dead zone thickness is reached, the print speed can only be increased by relaxing the resolution (i.e., using a resin with higher  $h_A$ ).



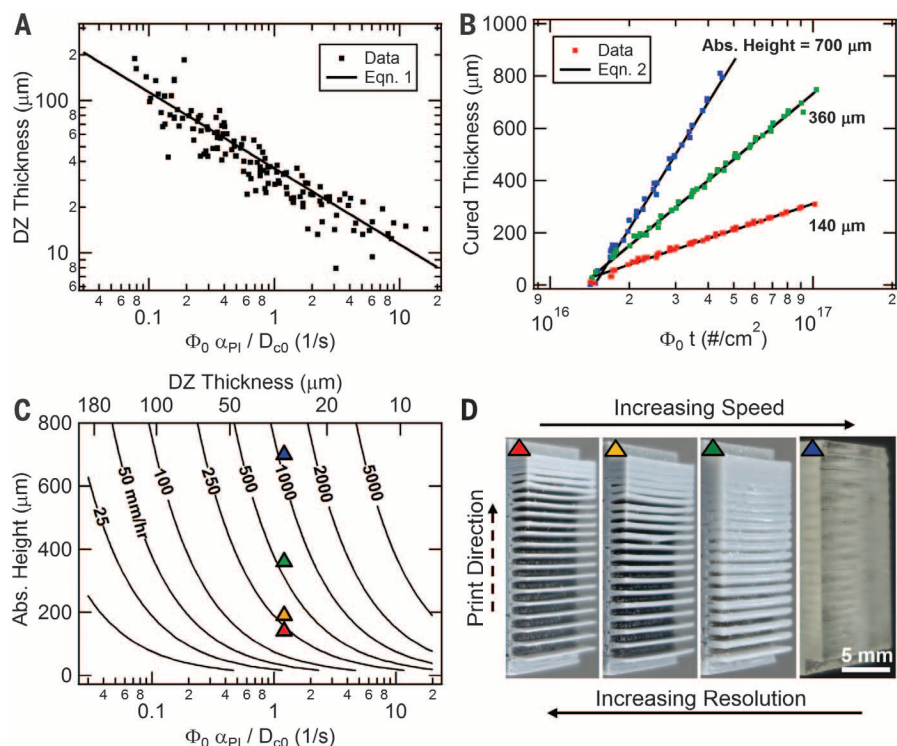


**Fig. 3. A trade off exists between print speed and part resolution.** (A) Liquid interface dead zone (DZ) thickness as a function of  $\Phi_0 \alpha_{PI} / D_{CO}$ . These parameters have typical ranges:  $5 \times 10^{14} \text{ cm}^2 \text{ s}^{-1} < \Phi_0 < 2 \times 10^{16} \text{ cm}^2 \text{ s}^{-1}$ ;  $2 \times 10^{-4} \mu\text{m}^{-1} < \alpha_{PI} < 1 \times 10^{-2} \mu\text{m}^{-1}$ ;  $5 \times 10^{12} \text{ cm}^2 \mu\text{m}^{-1} < D_{CO} < 5 \times 10^{13} \text{ cm}^2 \mu\text{m}^{-1}$ . (B) Cured thickness as a function of UV photon dosage ( $\Phi_0 t$ ) for three resins with different  $h_A$  controlled with dye loading. (C) CLIP print speed contours as functions of  $h_A$  and  $\Phi_0 \alpha_{PI} / D_{CO}$ . (D) Photographs of resolution test patterns using resins with different  $h_A$  from (B). Colored triangles correspond to process conditions in (C). The dye-free test pattern produced at highest print speed (blue triangle) is semitransparent.

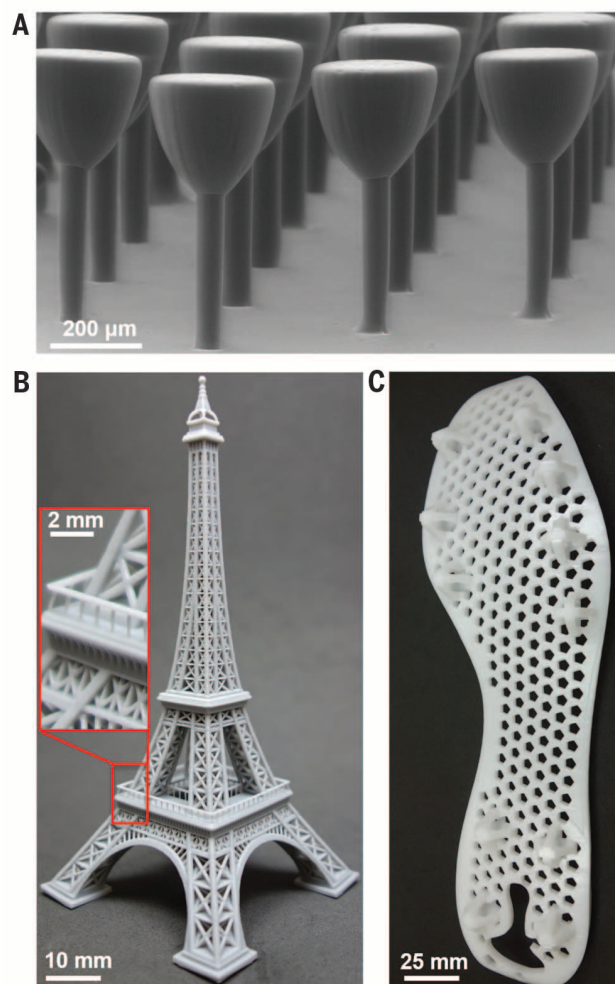


**Fig. 4. A variety of parts can be fabricated using CLIP.** (A) Micropaddles with stems 50 μm in diameter. (B) Eiffel Tower model, 10 cm tall. (C) A shoe cleat >20 cm in length. Even in large parts, fine detail is achieved, as shown in the inset of (B) where features <1 mm in size are obtained. The micropaddles were printed at 25 mm/hour; the Eiffel Tower model and shoe cleat were printed at 100 mm/hour.

This analysis shows that for a dead zone thickness of 20 μm, speeds in excess of 300 mm/hour with  $h_A = 100 \mu\text{m}$  are accessible. By increasing  $h_A$  to 300 μm and sacrificing resolution, speeds greater than 1000 mm/hour are readily achieved. The trade off between speed and resolution is demonstrated in Fig. 3D with resolution test patterns using the resins with different  $h_A$  from Fig. 3B (all have equivalent  $\Phi_0 \alpha_{PI} / D_{CO}$  and dead zone thickness). As dye loading is increased,  $h_A$  is reduced, leading to less print-through and ultimately higher resolution. However, dye absorption does not produce free radicals, so resins with lower  $h_A$  require greater dosages to adequately solidify; that is, parts must be elevated more slowly for constant photon flux. On the other hand, the resin without dye and with the highest  $h_A$  can be printed at the greatest speed but with poor resolution (as shown by unintentional curing of the overhangs in the test pattern).

Using this process control framework, Fig. 4 shows an array of expediently produced parts ranging in size from undercut micropaddles with stem diameters of 50 μm (Fig. 4A) to full-size shoe cleats 25 cm in length (Fig. 4C). The Eiffel Tower model in Fig. 4B illustrates that fine detail is achieved even in macroscale parts: The horizontal railing posts (diameter <500 μm) are resolved on this 10-cm-tall model. This ratio of scales (1:200) confirms that the CLIP process enables rapid production of arbitrary microscopic features over parts having macroscopic dimensions. For these parts, the speed-limiting process is resin curing (Eq. 4); however, for other part geometries, the speed-limiting process is resin flow into the build area. For such geometries with comparatively wide solid cross sections, parameters that affect

resin flow (e.g., resin viscosity, suction pressure gradient) become important to optimize.

Preliminary studies show that the CLIP process is compatible with producing parts from soft elastic materials (24, 25), ceramics (26), and biological materials (27, 28). CLIP has the potential to extend the utility of additive manufacturing to many areas of science and technology, and to lower the manufacturing costs of complex polymer-based objects.

## REFERENCES AND NOTES

1. J. M. Pearce, *Science* **337**, 1303–1304 (2012).
2. H. Lipson, M. Kurman, *Fabricated: The New World of 3D Printing* (Wiley, Indianapolis, 2013).
3. B. Derby, *Science* **338**, 921–926 (2012).
4. A. Atala, F. K. Kasper, A. G. Mikos, *Sci. Transl. Med.* **4**, 160rv12 (2012).
5. B. C. Gross, J. L. Erkal, S. Y. Lockwood, C. Chen, D. M. Spence, *Anal. Chem.* **86**, 3240–3253 (2014).
6. K. Sun et al., *Adv. Mater.* **25**, 4539–4543 (2013).
7. G. Chisholm, P. J. Kitson, N. D. Kirkaldy, L. G. Bloor, L. Cronin, *Energy Environ. Sci.* **7**, 3026–3032 (2014).
8. M. D. Symes et al., *Nat. Chem.* **4**, 349–354 (2012).
9. P. Chakraborty, R. N. Zuckermann, *Proc. Natl. Acad. Sci. U.S.A.* **110**, 13368–13373 (2013).
10. P. J. Kitson et al., *Cryst. Growth Des.* **14**, 2720–2724 (2014).
11. J. L. Erkal et al., *Lab Chip* **14**, 2023–2032 (2014).
12. X. Zheng et al., *Science* **344**, 1373–1377 (2014).
13. T. A. Schaedler et al., *Science* **334**, 962–965 (2011).
14. J. Bauer, S. Hengsbach, I. Tesari, R. Schwaiger, O. Kraft, *Proc. Natl. Acad. Sci. U.S.A.* **111**, 2453–2458 (2014).
15. E. B. Duoss et al., *Adv. Funct. Mater.* **24**, 4905–4913 (2014).
16. I. Gibson, D. W. Rosen, B. Stucker, *Additive Manufacturing Technologies: Rapid Prototyping to Direct Digital Manufacturing* (Springer, New York, 2010).
17. S. C. Ligon, B. Húsár, H. Wutzler, R. Holman, R. Liska, *Chem. Rev.* **114**, 557–589 (2014).
18. Y. Yagci, S. Jockusch, N. J. Turro, *Macromolecules* **43**, 6245–6260 (2010).
19. P. F. Jacobs, *Rapid Prototyping & Manufacturing: Fundamentals of Stereolithography* (Society of Manufacturing Engineers, Dearborn, MI, 1992).
20. T. C. Merkel, I. Pinnau, R. Prabhakar, B. D. Freeman, *Materials Science of Membranes for Gas and Vapor Separation* (Wiley, West Sussex, UK, 2006), pp. 251–270.
21. D. Dendukuri et al., *Macromolecules* **41**, 8547–8556 (2008).
22. D. Dendukuri, D. C. Pregibon, J. Collins, T. A. Hatton, P. S. Doyle, *Nat. Mater.* **5**, 365–369 (2006).
23. J. M. Gonzalez-Mejome, V. Compañ-Moreno, E. Riande, *Ind. Eng. Chem. Res.* **47**, 3619–3629 (2008).
24. J. A. Rogers, T. Someya, Y. Huang, *Science* **327**, 1603–1607 (2010).
25. S. Bauer et al., *Adv. Mater.* **26**, 149–161 (2014).
26. N. Trivitzky et al., *Adv. Eng. Mater.* **16**, 729–754 (2014).
27. C. Cvetkovic et al., *Proc. Natl. Acad. Sci. U.S.A.* **111**, 10125–10130 (2014).
28. Y. Lu, G. Mapili, G. Suhali, S. Chen, K. Roy, *J. Biomed. Mater. Res. A* **77**, 396–405 (2006).

## ACKNOWLEDGMENTS

This work was sponsored by Carbon3D Inc. J.R.T., D.S., N.E., D.K., R.P., J.P.R., A.E., E.T.S., and J.M.D. all have an equity stake in Carbon3D Inc., which is a venture-backed startup company. Continuous liquid interface printing is the subject of patent protection including Patent Cooperation Treaty publication numbers WO 2014/126837 A2, WO 2014/126830 A2, and WO 2014/126834 A2, and others.

## SUPPLEMENTARY MATERIALS

www.sciencemag.org/content/347/6228/1349/suppl/DC1  
Materials and Methods  
Supplementary Text  
Figs. S1 to S4  
Movies S1 and S2  
Reference (29)

5 November 2014; accepted 3 February 2015  
10.1126/science.aaa2397

## PALEOANTHROPOLOGY

# Early *Homo* at 2.8 Ma from Ledi-Geraru, Afar, Ethiopia

Brian Villmoare,<sup>1,4,6\*</sup> William H. Kimbel,<sup>2\*</sup> Chalachew Seyoum,<sup>2,7</sup>  
Christopher J. Campisano,<sup>2</sup> Erin N. DiMaggio,<sup>3</sup> John Rowan,<sup>2</sup> David R. Braun,<sup>4</sup>  
J. Ramón Arrowsmith,<sup>5</sup> Kaye E. Reed<sup>2</sup>

Our understanding of the origin of the genus *Homo* has been hampered by a limited fossil record in eastern Africa between 2.0 and 3.0 million years ago (Ma). Here we report the discovery of a partial hominin mandible with teeth from the Ledi-Geraru research area, Afar Regional State, Ethiopia, that establishes the presence of *Homo* at 2.80 to 2.75 Ma. This specimen combines primitive traits seen in early *Australopithecus* with derived morphology observed in later *Homo*, confirming that dentognathic departures from the australopith pattern occurred early in the *Homo* lineage. The Ledi-Geraru discovery has implications for hypotheses about the timing and place of origin of the genus *Homo*.

Fifty years after the recognition of the species *Homo habilis* as the earliest known representative of our genus (1), the origin of *Homo* remains clouded. This uncertainty stems in large part from a limited fossil record between 2.0 and 3.0 million years ago (Ma), especially in eastern Africa. Some taxa from this time period, such as *Australopithecus africanus* (~2.8 to 2.3 Ma) and the less well known *A. garhi* (~2.5 Ma) and *A. aethiopicus* (~2.7 to 2.3 Ma), appear too specialized cranially and/or dentally to represent the probable proximate ancestral conditions for *Homo* species known in Africa by ~2.0 Ma (*H. habilis* and *H. rudolfensis*). This leaves a thin scatter of isolated, variably informative specimens dated to 2.4 to 2.3 Ma as the only credible fossil evidence bearing on the earliest known populations of the genus *Homo* (2, 3).

Here we describe a recently recovered partial hominin mandible, LD 350-1, from the Ledi-Geraru research area, Afar Regional State, Ethiopia, that extends the fossil record of *Homo* back in time a further 0.4 million years. The specimen, securely dated to 2.80 to 2.75 Ma, combines derived morphology observed in later *Homo* with primitive traits seen in early *Australopithecus*. The discovery has implications for hypotheses concerning the timing and place of *Homo* origins.

The LD 350 locality resides in the Lee Adoyta region of the Ledi-Geraru research area (Fig. 1). Geologic research at Lee Adoyta (4) identified fault-bounded sedimentary packages dated 2.84 to 2.58 Ma. The LD 350-1 mandible was recovered on the surface of finely bedded fossiliferous

silts 10 m conformably above the Gurumaha Tuff (Fig. 1). The matrix adherent to the specimen is consistent with it having eroded from these silts [for details on stratigraphy and depositional environment, see (4)]. The Gurumaha Tuff is radiometrically dated to  $2.822 \pm 0.006$  Ma (4), a date that is consistent with the normal magnetic polarity of the Gurumaha section, presumably the Gauss Chron. An upper bounding age for LD 350-1 is provided by an adjacent down-faulted younger block that contains the  $2.669 \pm 0.011$  Ma Lee Adoyta Tuff. A magnetostratigraphic reversal 12 m conformably above the Lee Adoyta Tuff is inferred to be the Gauss/Matuyama boundary at 2.58 Ma (4). Because no significant erosional events intervene between the Gurumaha Tuff and the fossiliferous horizon, the age of LD 350-1 can be further constrained by stratigraphic scaling. Applying a sedimentation rate of either 14 cm per thousand years (ky) from the Lee Adoyta fault block or 30 cm/ky from the Hadar Formation (5) provides age estimates of 2.77 and 2.80 million years (My), respectively, for LD 350-1. Based on the current chronostratigraphic framework for Ledi-Geraru, we consider the age of LD 350-1 to be 2.80 to 2.75 My.

The hominin specimen, found by Chalachew Seyoum on 29 January 2013, comprises the left side of an adult mandibular corpus that preserves the partial or complete crowns and roots of the canine, both premolars, and all three molars. The corpus is well preserved from the symphysis to the root of the ascending ramus and retromolar platform. Surface detail is very good to excellent, and there is no evidence of significant transport. The inferior margin of the corpus and the lingual alveolar margin are intact, but the buccal alveolar margin is chipped between P<sub>3</sub> and M<sub>1</sub>. The P<sub>4</sub>, M<sub>2</sub>, and M<sub>3</sub> crowns are complete and well preserved, but the C, P<sub>3</sub>, and M<sub>1</sub> crowns are incomplete (Fig. 2 and text S2). The anterior dentition is represented by the broken root of the lateral incisor and the alveolus of the central incisor.

Given its location and age, it is natural to ask whether the LD 350-1 mandible represents a late-surviving population of *A. afarensis*, whose

<sup>1</sup>Department of Anthropology, University of Nevada Las Vegas, Las Vegas, NV 89154, USA. <sup>2</sup>Institute of Human Origins and School of Human Evolution and Social Change, Arizona State University, Tempe, AZ 85287, USA. <sup>3</sup>Department of Geosciences, Pennsylvania State University, University Park, PA 16802, USA. <sup>4</sup>Center for the Advanced Study of Hominin Paleobiology, George Washington University, Washington, DC 20052, USA. <sup>5</sup>School of Earth and Space Exploration, Arizona State University, Tempe, AZ 85281, USA. <sup>6</sup>Department of Anthropology, University College London, London WC1H 0BW, UK. <sup>7</sup>Authority for Research and Conservation of Cultural Heritage, Addis Ababa, Ethiopia.

\*Corresponding author. E-mail: brian.villmoare@unlv.edu (B.V.); wkimbel.ih@asu.edu (W.H.K.)



youngest known samples date to ~3.0 Ma at the neighboring Hadar site (6). Indeed, in overall dental and mandibular size, LD 350-1 matches

smaller specimens of *A. afarensis* (figs. S1 to S4 and tables S1 to S3). In addition, LD 350-1 shares with *A. afarensis* a primitive anterior corpus, in-

cluding an inclined symphyseal cross section, a bulbous anterior symphyseal face, and a projecting inferior transverse torus that is only slightly elevated above the corpus base (Fig. 2A). There are, however, substantial differences between LD 350-1 and the mandibles and teeth of *A. afarensis*. LD 350-1 lacks the lateral corpus hollow in which the mental foramen is located, which distinguishes *A. afarensis* mandibles across their size range. Instead, the LD 350-1 corpus is slightly convex inferosuperiorly, with the mental foramen located lateralmost on this arc (fig. S5). Unlike in *A. afarensis*, the anterior corpus of LD 350-1 bears a distinct symphyseal keel, accentuated by a flattened area between it and a pronounced canine jugum (Fig. 2). It lacks both an incisura mandibulae anterior and a mentum osseum, and thus does not have a chin. The  $P_3$  buccal crown profile is symmetrical in occlusal view, lacking the prominent mesiobuccal extension that skews the  $P_3$  crown outline in *A. afarensis*. The  $P_3$  occlusal enamel is worn through to dentine buccally, yet the moderately worn molars retain considerable occlusal relief. In *A. afarensis*, a reversed wear pattern is typical: The canine and mesial moiety of  $P_3$  remain relatively unscathed by wear even when molar occlusal enamel is exhausted (6). The wear disparity in LD 350-1 may signal modification of the relatively primitive  $C/P_3$  complex of *A. afarensis*, which, while non-honing, retained apelike aspects of crown shape and occlusal wear (6, 7). The basally expanded hypoconid that creates the characteristic “bilobate” buccal crown contour in *A. afarensis*  $M_2$ s and  $M_3$ s is not evident in LD 350-1 (7). Finally, there is a distinct C7 cusp on the LD 350-1  $M_1$  (Fig. 2), yet no such cusp has been recorded for an *A. afarensis*  $M_1$  ( $n = 18$ ) (8, 9).

Despite a well-developed lateral prominence that swells the corpus anterior to the ascending ramus, LD 350-1 lacks the great corpus thickening, inflated corpus contours beneath  $P_3$ - $M_1$ , and anterior dental arch constriction seen in robust australopith mandibles, including Omo 18-1967-18 (holotype of *A. aethiopicus*, ~2.6 Ma). Postcanine dental expansion, including the differential enlargement of lower molar entoconids typical of robust australopiths, is also absent (8) (figs. S1 to S3 and table S4).

LD 350-1 also differs from *Australopithecus* in features that align it with early *Homo*. The inferior and alveolar margins of the corpus are subparallel, resulting in similar corpus depths at  $P_3$  and  $M_2$  (Fig. 2), whereas in *A. afarensis*, *A. africanus*, and *A. sediba*, the corpus is typically deepest under the premolars (10, 11). Some specimens of early *Homo*, such as SK 45 and KNM-ER 60000 (10, 12), have a deeper corpus anteriorly, but LD 350-1 resembles many others that are relatively uniform in depth along the corpus (10, 13–16) (figs. S5 and S6 and table S5). In LD 350-1, the mental foramen opens directly posteriorly into a short groove on the corpus. A posteriorly opening foramen is the most common condition in early and modern *Homo* (13, 17). The foramen always opens anteriorly or anterosuperiorly in *A. afarensis* mandibles, whereas in

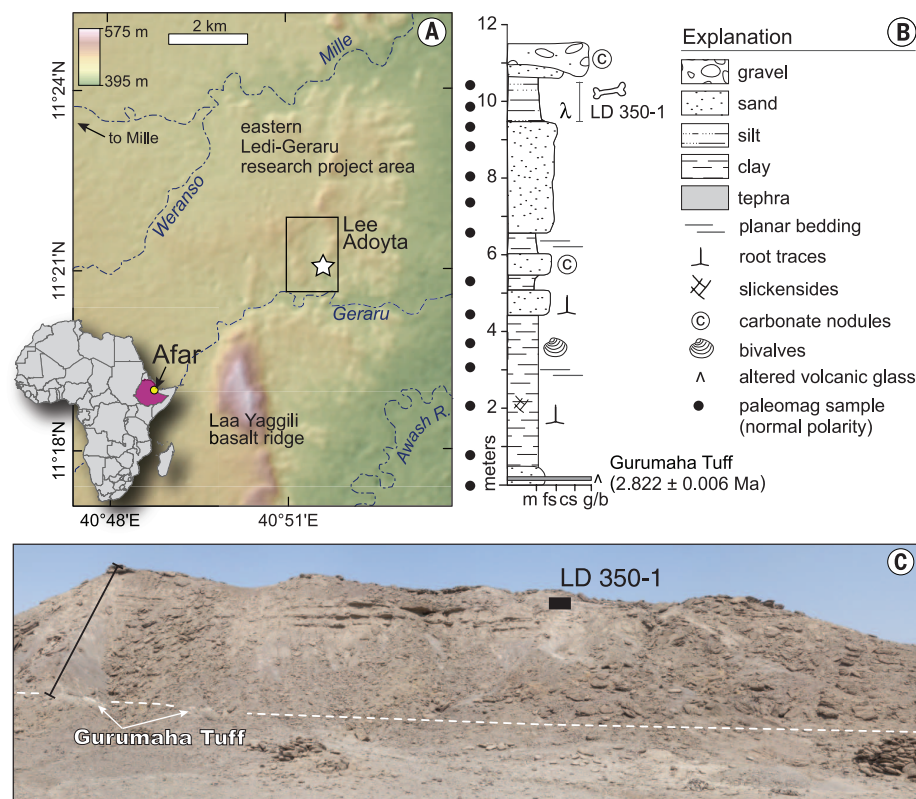
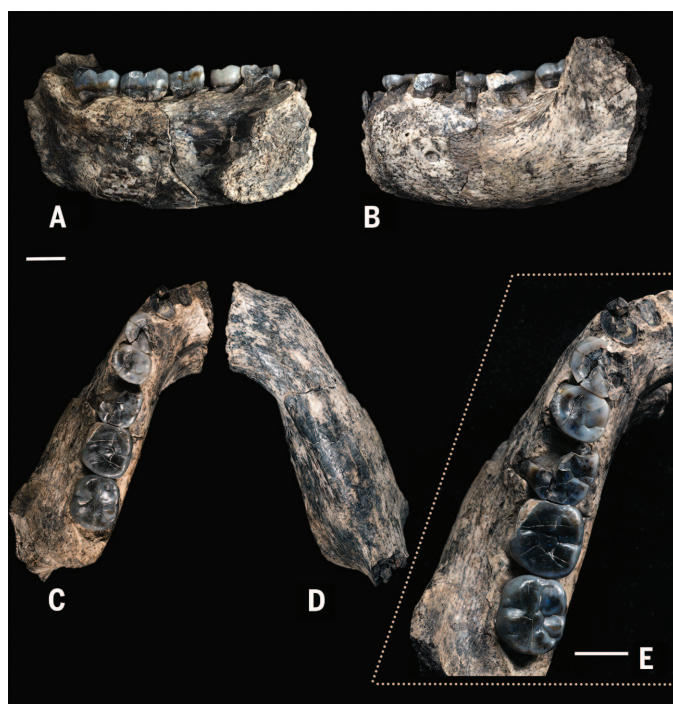


**Fig. 1. The geographic and geologic setting of the LD 350-1 hominin mandible.** (A) Map of the Lee Adoyta region in the Ledi-Geraru research area. (B) Stratigraphic section of the Lee Adoyta sequence indicating the provenience of LD 350-1. (C) The LD 350 locality, with the position of the LD 350-1 mandible on the surface in relation to the Gurumaha Tuff. Resistant ledges in the center of the photo are localized cemented sand and carbonate nodule pebble conglomerate. The section in (B) is indicated by the black line at left in (C). Details in (6).

**Fig. 2. The LD 350-1 mandible.** (A) Medial view. (B) Lateral view. (C) Occlusal view. (D) Basal view. (E) Enlarged occlusal view of dentition. Scale bars, 1 cm.



*A. africanus* its orientation ranges from antero-inferior to directly lateral. The anterior margin of the ascending ramus in LD 350-1 becomes independent from the corpus opposite the middle of the  $M_3$  crown, and in lateral view only the distalmost part of this crown is hidden (Fig. 2 and fig. S5). In the great majority of *Australopithecus* mandibles, the anterior margin of the ramus is positioned further anteriorly, between mid- and distal  $M_2$ . A posterior origin of the ramus margin is most common in specimens of early *Homo* (fig. S7 and table S6).

The LD 350-1 molars have simple occlusal surfaces, with salient, marginally positioned cusp apices and broad occlusal basins. With the exception of a tiny protostylid on  $M_3$ , the crowns are devoid of circular remnants. Estimated  $M_1$  length is small (fig. S4). The breadth across the mesial aspect of  $M_2$  and  $M_3$  measures less than the distal breadth, giving these crowns a mesially tapered occlusal outline. This distinctive outline is due in part to a relatively confined mesiolingual cusp (metaconid) on these teeth (Fig. 2 and table S4). In *A. afarensis* and *A. africanus*, and also in *A. sediba* specimen MH1,  $M_2$  and  $M_3$  crown outlines are square or distally tapered (especially  $M_3$ ) (fig. S8). Although some early *Homo* distal molars show reduced mesial breadths, there is significant overlap with *Australopithecus* in mesial:distal breadth ratio, and none approaches the uniquely tapered outline of LD 350-1 (table S7). Whereas *Australopithecus*  $M_2$  and  $M_3$  crowns usually have a sloping buccal face up to the point of advanced occlusal wear, the buccal walls of these teeth in LD 350-1 descend almost vertically from the occlusal rim, as frequently observed in early and later *Homo* (fig. S8). LD 350-1 departs from the *A. africanus* dental pattern, which includes buccolingually expanded postcanine teeth (especially  $M_{2,3}$ ) and flattened molar occlusal surfaces in specimens with similar degrees of premolar wear (6, 7). LD 350-1 possesses a mesiodistally shorter  $M_3$  than  $M_2$ , which is common in *Homo* but occurs only in 1 out of 16 *A. afarensis* and 3 out of 14 *A. africanus* specimens in our sample. In crown length, the LD 350-1  $M_3$  falls outside the distribution of 20 *A. africanus* and 19 *A. afarensis*  $M_{3s}$  (fig. S3).

With an age of 2.80 to 2.75 My, the Ledi-Geraru mandible is younger than the youngest known *A. afarensis* fossils from Hadar, ~3.0 Ma. Although it shares with *A. afarensis* primitive anterior corpus morphology, the specimen falls outside the range of variation for most other diagnostic mandibular and dental traits of this species. In the majority of traits that distinguish it from this species, LD 350-1 presents morphology that we interpret as transitional between *Australopithecus* and *Homo*.

The *Homo* postcanine dental pattern (18) is present in members E through G of the Shungura Formation of Ethiopia (~2.4 to 2.0 Ma) and is best represented by mandible Omo 75-14, which has a reduced  $M_3$  crown and a C7 cusp on  $M_1$  (18), features shared with LD 350-1. The A.L. 666-1 maxilla from the Busidima Formation at Hadar also establishes the *Homo* dentognathic pat-

tern by ~2.3 Ma (19). A small collection of postcanine teeth from members B and C (~2.9 to 2.6 Ma) of the Shungura Formation evinces more derived morphology than *A. afarensis* and has been affiliated with *A. africanus/Homo* (18, 20). Although *A. africanus* is usually thought to have been endemic to southern Africa, the corresponding time period in the East African record is notoriously poor in hominin fossils. At ~2.80 to 2.75 Ma, LD 350-1 falls within the member B-C temporal interval and is broadly contemporaneous with *A. africanus* samples from Makapansgat and Sterkfontein (21). Morphologically, however, it is distinguished from *A. africanus* by its subequal anterior and posterior corpus heights, posterior position of the anterior ramus margin, posteriorly oriented mental foramen, steeper premolar-molar wear gradient, vertical buccal walls of  $M_{2,3}$ , and reduced  $M_3$ . In the combination of these features, LD 350-1 resembles younger East African *Homo* specimens more than it does geologically contemporaneous or older *Australopithecus*. Summarizing the Shungura Formation dental evidence, Suwa *et al.* [(18) pp. 270–271] identified the 2.9- to 2.7-Ma interval as “the transitional period when evolution occurred from an *A. afarensis*-like to a more advanced species...close in overall dental morphology to the *A. africanus* condition but also mostly within the *A. afarensis* and/or early *Homo* ranges of variation.” We consider the Ledi-Geraru mandible to sample a population from this transition and to point to a close phyletic relationship with *Homo* at 2.4 to 2.3 Ma.

A set of teeth comprising the isolated left and right  $P_3$ - $M_2$  crowns of a single individual (KNM-ER 5431) from the upper Tulu Bor Member at Koobi Fora, Kenya (22), is germane to the status of LD 350-1. Constrained in age between ~2.7 and ~3.0 Ma (23), these teeth show a mix of australopith (premolar cusp morphology) and early *Homo*-like (C7 cusp on  $M_1$  and  $M_2$ ) characters (15), whereas its  $P_3$  form has been characterized as “intermediate between *A. afarensis*...and *A. africanus* or early *Homo*” [(24), p. 199]. The KNM-ER 5431 teeth could represent the same East African transitional form as the LD 350-1 mandible.

Arguments for the role of 2.5-Ma *A. garhi* as the direct ancestor of *Homo* are relevant to interpretations of LD 350-1 (25). The tremendous postcanine dental size and differentially enlarged  $P^3$  of *A. garhi* holotype cranium BOU-VP 12/130 are a poor match for the modest-size teeth of the Ledi jaw (in resampling analyses, the LD 350-1 lower second molar and the BOU-VP 12/130 upper second molar were found to be diminishingly unlikely to sample the same species; see text S3). To include LD 350-1 and BOU-VP 12/130 in the same species lineage and simultaneously postulate an ancestor-descendant relationship between *A. garhi* and *Homo* would require a dramatic increase in tooth size between ~2.8 and ~2.5 Ma, and then an equally dramatic decrease in tooth size in a ~2.5- to 2.3-Ma transition to *Homo*. Although nonrobust mandibles with derived corpus morphology and smaller

teeth are approximately contemporaneous with *A. garhi* in the Middle Awash of Ethiopia (25, 26), it is unclear whether these represent *A. garhi* or a second lineage, potentially of *Homo*. For all of these reasons, we consider the hypothesis that posits LD 350-1 as representing a population ancestral to ~2.4- to 2.3-Ma *Homo*, to the exclusion of *A. garhi*, to be more parsimonious than ones that include this taxon in the *Homo* lineage [consistent with the phylogenetic analysis in (27); see text S3].

By ~2.0 Ma, at least two species of the genus *Homo* were present in Africa, *H. habilis* and *H. rudolfensis* (3, 28), but primitive anterior corpus morphology distinguishes LD 350-1 from both of them. These species are distinct from one another in dental arcade shape (12, 29), and LD 350-1 suggests the primitively arched canine/incisor row seen in *H. habilis* *sensu stricto* (fig. S9). For the present, pending further discoveries, we assign LD 350-1 to *Homo*, species indeterminate. The identification of the 2.80- to 2.75-Ma Ledi-Geraru mandible as representing a likely phyletic predecessor to early Pleistocene *Homo* implies that phylogenetic schemes positing the origin of the *Homo* lineage from *A. sediba* as late as 1.98 Ma are likely to be incorrect [contra (30); see text S3].

The time period 2.8 to 2.5 Ma witnessed climatic shifts that are frequently hypothesized to have led to the origin of the *Homo* lineage (3, 31–33). Although the open habitats reconstructed for the Lee Adoyta faunal assemblages provide a new window on these changes (4), too little is known of the pattern of hominin evolution during this period to forge causal links to specific evolutionary events. The Ledi-Geraru specimen confirms that divergence from australopith dental and mandibular anatomy was an early hallmark of the *Homo* lineage. Additional discoveries are needed to determine whether or not these dentognathic changes were accompanied by neurocranial expansion, technological innovation, or shifts in other anatomical/behavioral systems that are familiar components of the *Homo* adaptive pattern.

## REFERENCES AND NOTES

1. L. S. B. Leakey, P. V. Tobias, J. R. Napier, *Nature* **202**, 7–9 (1964).
2. W. H. Kimbel, in *The First Humans: Origin and Early Evolution of the Genus Homo*, F. E. Grine, J. G. Fleagle, R. E. Leakey, Eds. (Springer, Dordrecht, Netherlands, 2009), pp. 31–38.
3. S. C. Antón, R. Potts, L. C. Aiello, *Science* **345**, 1236828 (2014).
4. E. N. DiMaggio *et al.*, *Science* **347**, 1355 (2015).
5. C. J. Campisano, C. S. Feibel, *J. Hum. Evol.* **53**, 515–527 (2007).
6. W. H. Kimbel, L. K. Deleze, *Am. J. Phys. Anthropol.* **140**, 2–48 (2009).
7. T. D. White, D. C. Johanson, W. H. Kimbel, *S. Afr. J. Sci.* **77**, 445–470 (1981).
8. G. Suwa, B. A. Wood, T. D. White, *Am. J. Phys. Anthropol.* **93**, 407–426 (1994).
9. D. Guatelli-Steinberg, J. D. Irish, *Am. J. Phys. Anthropol.* **128**, 477–484 (2005).
10. T. D. White, *The Anterior Mandibular Corpus of Early Hominidae: Functional Significance of Shape and Size*. Thesis, University of Michigan, Ann Arbor, MI (1977).
11. W. H. Kimbel, Y. Rak, D. C. Johanson, *The Skull of Australopithecus afarensis* (Oxford Univ. Press, New York, 2004).
12. M. G. Leakey *et al.*, *Nature* **488**, 201–204 (2012).
13. F. Weidenreich, *Palaeontol. Sin. Ser. D* **7**, 1–132 (1936).



14. P. V. Tobias, *Olduvai Gorge Volume 4: The Skulls and Endocasts of Homo habilis* (Cambridge Univ. Press, Cambridge, 1991).
15. B. A. Wood, *Koobi Fora Research Project Volume 4, Hominid Cranial Remains* (Clarendon, Oxford, 1991).
16. B. A. Wood, F. L. Van Noten, *Am. J. Phys. Anthropol.* **69**, 117–127 (1986).
17. M. F. A. Montagu, *Am. J. Phys. Anthropol.* **12**, 503–518 (1954).
18. G. Suwa, T. D. White, F. C. Howell, *Am. J. Phys. Anthropol.* **101**, 247–282 (1996).
19. W. H. Kimbel, D. C. Johanson, Y. Rak, *Am. J. Phys. Anthropol.* **103**, 235–262 (1997).
20. J.-R. Boisserie *et al.*, *C. R. Palevol* **7**, 429–439 (2008).
21. A. I. R. Herries *et al.*, in *The Paleobiology of Australopithecus*. K. E. Reed, J. G. Fleagle, R. E. Leakey, Eds. (Springer, Dordrecht, Netherlands, 2013), pp. 21–40.
22. R. E. Leakey, A. C. Walker, *Am. J. Phys. Anthropol.* **67**, 135–163 (1985).
23. I. McDougall *et al.*, *J. Geol. Soc. London* **169**, 213–226 (2012).
24. G. Suwa, *A Comparative Analysis of Hominid Dental Remains from the Shingura and Usno Formations, Omo Valley, Ethiopia*. Thesis, University of California, Berkeley, CA (1990).
25. B. Asfaw *et al.*, *Science* **284**, 629–635 (1999).
26. T. D. White, B. Asfaw, G. Suwa, *Trans. R. Soc. S. Afr.* **60**, 79–83 (2005).
27. D. S. Strait, F. E. Grine, *J. Hum. Evol.* **47**, 399–452 (2004).
28. B. A. Wood, J. Baker, *Annu. Rev. Ecol. Evol. Syst.* **42**, 47–69 (2011).
29. F. Spoor *et al.*, *Nature* **519**, 83–86 (2015).
30. L. R. Berger *et al.*, *Science* **328**, 195–204 (2010).
31. E. S. Vrba, in *The Evolutionary History of the “Robust” Australopithecines*, F. E. Grine, Ed. (Aldine, Chicago, 1988), pp. 405–426.
32. P. B. deMenocal, *Science* **331**, 540–542 (2011).
33. R. Potts, *Quat. Sci. Rev.* **73**, 1–13 (2013).

# ACKNOWLEDGMENTS

We thank the Authority for Research and Conservation of Cultural Heritage, Ethiopian Ministry of Culture and Tourism, for permission to conduct field work at Ledi-Geraru and laboratory research in the National Museum of Ethiopia, Addis Ababa, in which the LD 350-1 mandible is housed. Research funding provided by the National Science Foundation (NSF) (grant no.

BCS-1157351), and the Institute of Human Origins at Arizona State University is gratefully acknowledged. B.A.V. also thanks NSF (BCS-0725122 HOMINID grant) and the George Washington University Selective Excellence Program for support during this research project. We thank Z. Alemseged, B. Asfaw, L. Berger, F. Brown, C. Feibel, D. Johanson, F. Spoor, G. Suwa, C. Ward, T. White, and B. Wood for discussion, assistance, and/or permission to examine fossils. Constructive comments by F. Spoor, B. Wood, and three anonymous referees substantially improved the manuscript. Supporting data for this paper are presented in the supplementary materials.

# SUPPLEMENTARY MATERIALS

www.sciencemag.org/content/347/6228/1352/suppl/DC1  
Text S1 to S3  
Figs. S1 to S10  
Tables S1 to S7  
References (34–47)

23 October 2014; accepted 13 February 2015  
Published online 5 March 2015;  
10.1126/science.1234343

## PALEOANTHROPOLOGY

# Late Pliocene fossiliferous sedimentary record and the environmental context of early *Homo* from Afar, Ethiopia

Erin N. DiMaggio,<sup>1\*</sup> Christopher J. Campisano,<sup>2</sup> John Rowan,<sup>2</sup> Guillaume Dupont-Nivet,<sup>3†</sup> Alan L. Deino,<sup>4</sup> Faysal Bibi,<sup>5</sup> Margaret E. Lewis,<sup>6</sup> Antoine Souron,<sup>7</sup> Dominique Garello,<sup>8</sup> Lars Werdelin,<sup>9</sup> Kaye E. Reed,<sup>2</sup> J Ramón Arrowsmith<sup>8</sup>

Sedimentary basins in eastern Africa preserve a record of continental rifting and contain important fossil assemblages for interpreting hominin evolution. However, the record of hominin evolution between 3 and 2.5 million years ago (Ma) is poorly documented in surface outcrops, particularly in Afar, Ethiopia. Here we present the discovery of a 2.84– to 2.58-million-year-old fossil and hominin-bearing sediments in the Ledi-Geraru research area of Afar, Ethiopia, that have produced the earliest record of the genus *Homo*. Vertebrate fossils record a faunal turnover indicative of more open and probably arid habitats than those reconstructed earlier in this region, which is in broad agreement with hypotheses addressing the role of environmental forcing in hominin evolution at this time. Geological analyses constrain depositional and structural models of Afar and date the LD 350-1 *Homo* mandible to 2.80 to 2.75 Ma.

Surface exposures of fossiliferous sedimentary rocks dated between 3.0 and 2.5 million years ago (Ma) are rare throughout Africa, yet are of great interest because this interval overlaps with shifts in African climate (1–5), corresponds to faunal turnover (6–8), and represents an important gap in our knowledge of evolutionary events in the human lineage (9). The time period coincides with changing geologic conditions in eastern Africa, as rifting processes (10, 11) and extensive volcanism (12) altered the architecture of sedimentary basins (13–15), controlling the paleogeography of hominin and other mammalian habitats. In tectonically active areas such as the lower Awash Valley (LAV), Afar, Ethiopia, rift-basin dynamics create spatially variable and often incomplete records of deposition. At other fossil sites in the LAV, the fluvio-lacustrine

sediments of the Hadar Formation (~3.8 to 2.9 Ma) are separated from the younger fluvial sediments of the Busidima Formation (~2.7 to 0.16 Ma) by an erosional unconformity (14, 16). The Hadar region contains early *Homo* dated to ~2.35 Ma (9) and an excellent record of *Australopithecus afarensis* from 3.5 to 2.95 Ma (17). However, the absence of fossiliferous sediments in the Hadar region due to the unconformity has impeded efforts to document a continuous record of hominin and other faunal evolution, and limits our understanding of regional habitat change in the LAV. Recent field investigations and geochronological analysis of sedimentary deposits at Ledi-Geraru (LG), located northeast of Hadar, Gona, and Dikika (Fig. 1), confirm the presence of late Pliocene fossiliferous sedimentary rocks dated to the interval represented elsewhere in the region by the erosional unconformity

(18). Here we present the geology, chronostratigraphy, and paleontology of the Lee Adoyta region of LG, where the LD 350-1 early *Homo* mandible (19) and 614 other mammal specimens were recovered from sediments dated 2.84 to 2.58 Ma (Fig. 1).

The Lee Adoyta region preserves an ~70-m-thick sedimentary sequence that is cut by multiple closely spaced NW-SE (320° to 340°)-trending faults that postdate deposition (Figs. 1 and 2). Geologic mapping documents drag folds and stratigraphic juxtaposition to define the normal sense of motion along the faults, which is consistent with faulting patterns oriented NW-SE associated with Red Sea rift extension (14). There are four major fault-bounded blocks, each of which comprises a discrete sedimentary package (Fig. 2).

The Bulinan sedimentary package is 10 m thick and consists of lacustrine deposits (laminated silty claystone with dispersed gastropod shells) with five intercalated 2- to 12-cm-thick altered tuffs (Fig. 3). The crystal-rich Bulinan Tuff lies 4 m above the base of the section. It is 2 to 3 cm thick, light pink in color, and composed of altered volcanic glass with <15% subangular lithic fragments and feldspar grains. The Bulinan Tuff was dated by the laser single-crystal incremental heating

<sup>1</sup>Department of Geosciences, Pennsylvania State University, University Park, PA 16802, USA. <sup>2</sup>Institute of Human Origins, School of Human Evolution and Social Change, Arizona State University, Tempe, AZ 85287, USA. <sup>3</sup>CNRS Géosciences Rennes, Campus de Beaulieu, 35042 Rennes, France. <sup>4</sup>Berkeley Geochronology Center, 2455 Ridge Road, Berkeley, CA 94709, USA. <sup>5</sup>Museum für Naturkunde, Leibniz Institute for Evolution and Biodiversity Science, Invalidenstrasse 43, 10115 Berlin, Germany. <sup>6</sup>Biology Program, Stockton University, 101 Vera King Farris Drive, Galloway, NJ 08205, USA. <sup>7</sup>Human Evolution Research Center, University of California, Berkeley, 3101 Valley Life Sciences Building, Berkeley, CA, 94720-3160, USA. <sup>8</sup>School of Earth and Space Exploration, Arizona State University, Tempe, AZ 85287, USA. <sup>9</sup>Swedish Museum of Natural History, Department of Palaeobiology, Box 50007, SE-10405 Stockholm, Sweden.

\*Corresponding author. E-mail: dimaggio@psu.edu (E.N.D.); kreed@asu.edu (K.E.R.) †Present address: Institute of Earth and Environmental Science, Potsdam University, Karl-Liebknecht-Strasse 24-25, 14476 Potsdam-Golm, Germany.

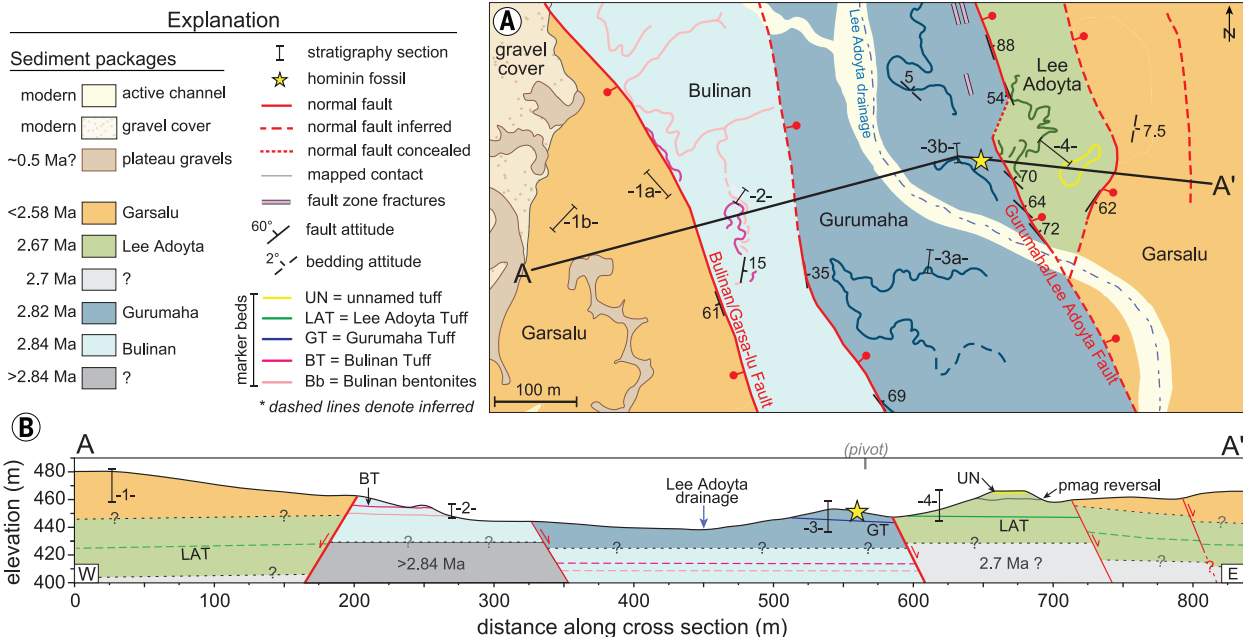
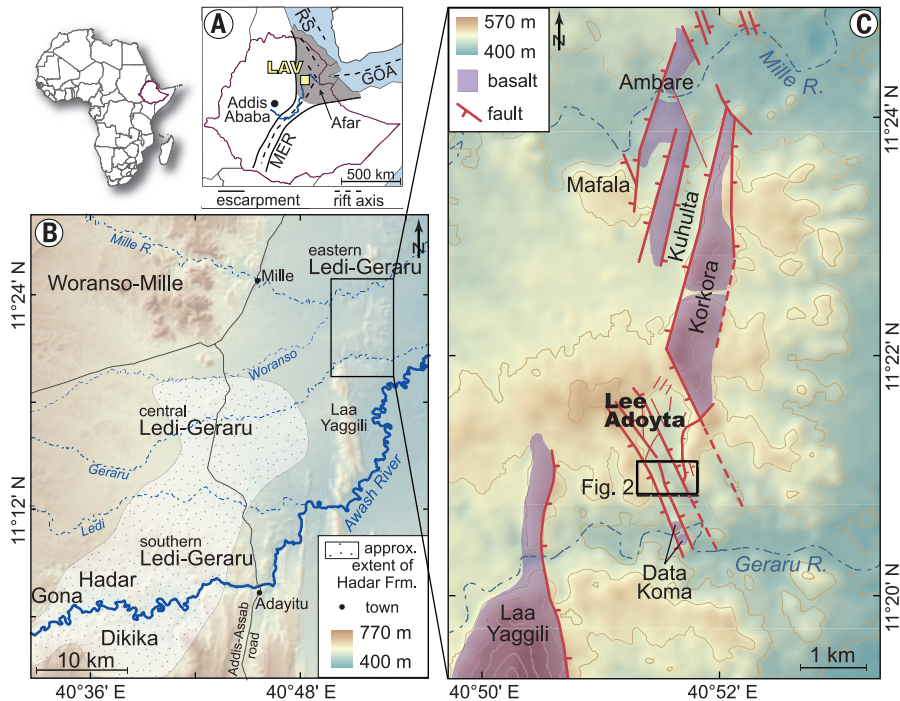
(SCIH)  $^{40}\text{Ar}/^{39}\text{Ar}$  technique on individual grains of phenocrystic Na-plagioclase feldspar from a single sample. Age “plateaus” as revealed in  $^{39}\text{Ar}$  release spectra indicate the characteristic age of the feldspars. The population of those ages yielded a weighted-mean result of  $2.842 \pm 0.010$  Ma ( $1\sigma$  internal error;  $\pm 0.014$  Ma external error;  $n = 4$  grains) (figs. S2 to S4 and table S2). Just four fos-

sils have been recovered from this fault block, and therefore an inference of habitat based on fauna is precluded.

The Gurumaha sedimentary package, which yielded the LD 350-1 hominin, is ~21 m thick and dips 3° to 5° E-SE. Gurumaha sediments coarsen up-section and include laminated mudstone with thin, fine sandstones, siltstone, and coarse cross-

bedded sandstone with pebble lags. The package is capped by a fluvial sequence composed of a carbonate nodule-rich, cross-bedded pebble conglomerate and overlying sands with minimal basal scour. The Gurumaha Tuff is a crystal-rich lapilli tephra-fall deposit that contains pumice (table S5) and forms a continuous white to light gray stratigraphic marker 8 to 10 cm thick (Fig. 2).

**Fig. 1. Geographic and geologic setting of the Lee Adayta hominin site.** (A) The LAV (yellow square), Afar Depression (gray area), Ethiopia. RS, Red Sea; GOA, Gulf of Aden; MER, Main Ethiopian Rift. (B) LAV project areas and the approximate mapped extent of the Hadar Formation *sensu stricto*. The Busidima Formation is largely exposed in the areas of Hadar, Gona, and Dikika. (C) Sediments and volcanic rocks in the eastern LG research project area are cut by two sets of faults striking NW and NNE, indicating the influence of both the RS and MER extensional systems, respectively. At Lee Adayta, NW-trending faults are most significant and appear to cross-cut NNE faults. Regions referred to in the text are labeled in black.





The Gurumaha Tuff was dated by the SCIH technique applied to four samples containing anorthoclase to Na-plagioclase feldspar phenocrysts. A weighted mean of the plateau ages yielded  $2.822 \pm 0.006$  Ma ( $\pm 0.015$  Ma external error;  $n = 23$  grains) (figs. S2 to S4 and table S2). This age falls within chron C2An.1n (Gauss) of the astronomical polarity time scale (20), consistent with the normal paleomagnetic polarity measured for the entire Gurumaha sequence (Fig. 3). The age on the tuff provides a maximum age for the LD 350-1 hominin fossil, which was recovered from a vertebrate fossil-rich silt horizon 10 m conformably above the Gurumaha Tuff and 1 m below the base of the capping pebble conglomerate (19). Based on local and regional sedimentation rates, a refined age estimate of 2.80 to 2.75 million years is calculated for the fossiliferous horizon (19).

Ecological community structure analysis based on mammalian fauna recovered from the Gurumaha fault block indicates a more open habitat (mostly mixed grasslands/shrublands with gallery forest) that probably experienced less rainfall than any

of those reconstructed for the members of the Hadar Formation (6). The landscape was similar to modern African open habitats, such as the Serengeti Plains, Kalahari, and other African open grasslands, given the abundance of grazing species and lack of arboreal taxa, although the presence of *Deinotherium bozasi* and tragelaphins probably indicates a gallery forest (fig. S6). The existence of *Kobus sigmoidalis*, aff. *Hippopotamus afarensis*, crocodiles, and fish in this package reflects the presence of rivers and/or lakes. Approximately one-third of the mammalian taxa present are shared with those in the youngest Hadar Formation (~3 Ma), whereas one-third are first appearances of these taxa in the LAV (Table 1). The remaining one-third of mammals recovered can only be identified to the genus level.

The Lee Adoyta sedimentary package is ~22 m thick and approximately horizontal. Two tuffs separated stratigraphically by ~8 to 10 cm approximate the base of the Lee Adoyta package. The lower tuff is a 5- to 6-cm-thick basaltic ash typically altered to a yellowish bentonite. The upper

unit is a 4- to 5-cm-thick light gray vitric-crystal tuff (table S6). The Lee Adoyta Tuffs are encased in brown fissile mudstone that directly overlies a green Vertisol. The overlying sedimentary units include brown mudstone, basalt-rich sandstone, and a pebble conglomerate. A 1.5-m-thick, cross-laminated, unnamed glassy tuff caps the section (table S6). Na-plagioclase phenocrysts from the upper Lee Adoyta Tuff have a weighted-mean SCIH age of  $2.669 \pm 0.011$  Ma ( $\pm 0.03$  Ma external;  $n = 5$  grains) (figs. S2 to S4 and table S2). Paleomagnetic measurements record a transition from normal to reverse polarity ~12 m above the Lee Adoyta Tuffs (Fig. 3), which is probably the Gauss/Matuyama reversal at 2.581 Ma (20). The date and stratigraphic position of the Lee Adoyta Tuffs are consistent with its assignment to the C2An.1n chron (Gauss), and provide a minimum age constraint for the LD 350-1 fossil. The Lee Adoyta fault block yielded mammalian fauna with ~80% taxonomic overlap with the Gurumaha fauna, and the ecological community structure also reconstructs an open habitat (fig. S6 and Table 1).

The Garsalu sedimentary package encompasses strata exposed along the margins of the Lee Adoyta drainage (Fig. 2). We correlate these packages based on the similarity of sedimentary facies and downfaulting against adjacent fault blocks. These fluvial deposits are ~26 m thick, gently dipping, and include paleosols, sandstones, siltstones, and conglomerates (Fig. 3). The Garsalu sedimentary package is the youngest (<2.58 Ma) in the Lee Adoyta region, based on faulting relationships and the presence of *Connochaetes gentryi*.

The combined 70-m-thick section at Lee Adoyta is placed within the chronostratigraphic framework of the LAV in an interval previously undocumented in the regional sedimentary record (fig. S8). In general, the sedimentary deposits at Lee Adoyta coarsen upward and represent a variety of depositional environments. At Lee Adoyta, a paleolake (~2.84 Ma) extended at least 6 km north to Ambare and Mafala (Fig. 1C), where lacustrine deposits are present in similarly aged strata (18). The depositional environment progressed to a nearshore delta plain by 2.82 Ma, as indicated by sandy channel bodies and the presence of crocodiles, fish, and mammals in the Gurumaha sediments. At present, sedimentary deposits between the top of the Gurumaha sedimentary package (2.80 to 2.75 Ma) and the Lee Adoyta Tuffs (2.67 Ma) have not been observed. The Lee Adoyta fault block strata (<2.67 Ma) are coeval with a portion of the Busidima Formation and similarly capture a fluvial record probably deposited by tributaries to the ancestral Awash River system (16).

Geological investigations at Lee Adoyta allow us to place constraints on regional basin models. The presence of deposits dated to 2.8 Ma in eastern LG is consistent with continued deposition in the Hadar Basin as a result of northeastern migration of paleo Lake Hadar during the late Pliocene to early Pleistocene (14, 21–23). Some time between 2.95 and 2.7 Ma, changes in base level associated with Main Ethiopian Rift extension

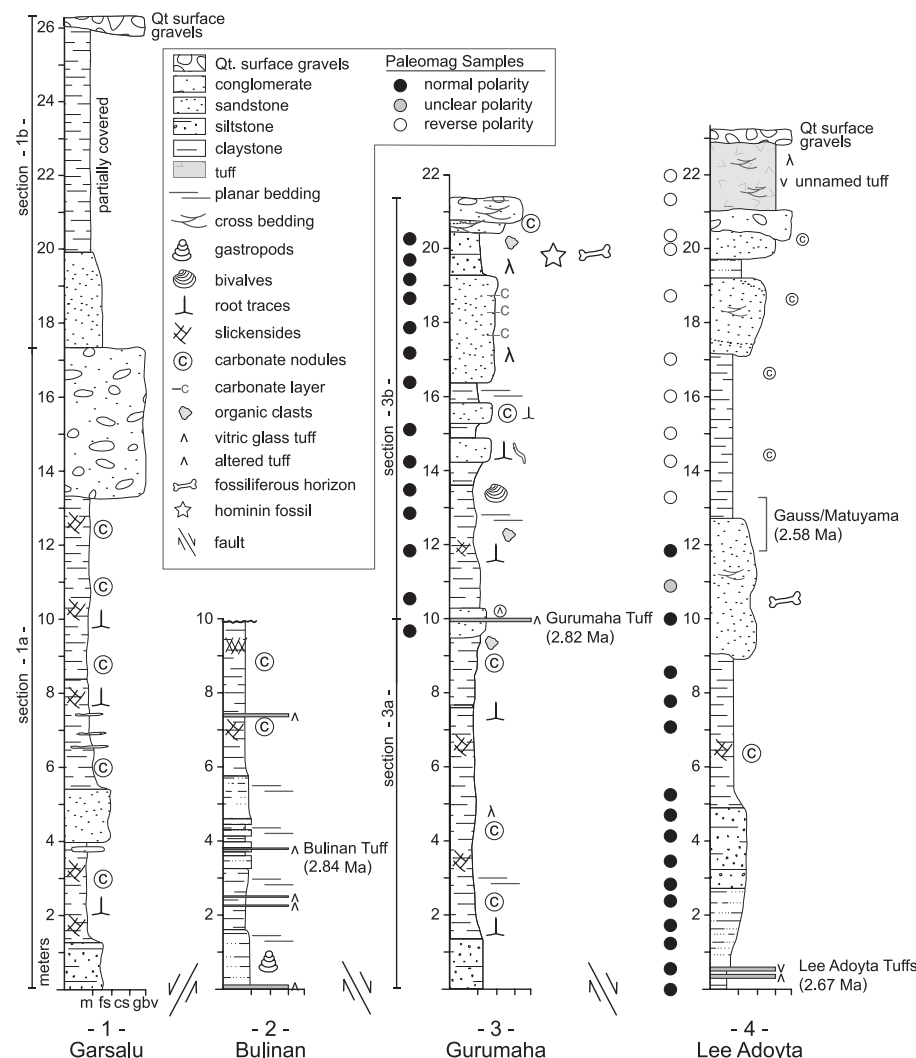


**Fig. 3. Stratigraphy and magnetostratigraphy of the sedimentary packages at Lee Adoyta.** The dip and sense of motion along each fault bounding the sediment packages are shown to separate the packages and thus establish relative ages. Section locations (numbered) are provided in Fig. 2.

eroded Hadar Basin sedimentary deposits in the areas of Gona, Hadar, Dikika, and central and southern LG, creating an erosional unconformity (Fig. 1B and fig. S8) (14, 15, 18, 24). The preservation of 2.8-Ma sediments in eastern LG, but not elsewhere in the lower Awash, suggests that the unconformity did not extend as far east as Lee Adoyta (or at least was not as long in duration). This may be related to the proximity of

Lee Adoyta to border faults, spatial variability of base level changes, or localized downfaulting of eastern LG before erosion. Lee Adoyta lies beyond the proposed eastern margin of the Busidima half-graben (14, 15). Therefore, the <2.7-Ma deposits at Lee Adoyta were either deposited in a different basin, or the Busidima half-graben was larger and more variable than proposed. After ~2.6 Ma, NW-SE trending faults that cross-cut

all sedimentary packages (Fig. 1C) indicate that Red Sea rifting was the dominant extensional regime.

Global climate change at ~2.8 Ma and resultant increases in African climatic variability and aridity are hypothesized to have spurred cladogenetic events in various mammalian lineages, including hominins (1, 2, 7). The faunal changes evident at Lee Adoyta appear to be in accord with these hypotheses, because the 2.8-Ma record shows a mammalian species turnover that includes first appearance datums and the dispersal of immigrant taxa previously unknown in Afar. Additionally, mammal communities in the Gurumaha and Lee Adoyta sedimentary packages indicate open habitats, with most vegetation cover consisting of grasses or low shrubs, a pattern that contrasts with the older, *Australopithecus afarensis*-bearing, Hadar Formation. Although the Lee Adoyta data provide enticing evidence for a correlation between open habitats linked to African aridification and the origins of the genus *Homo*, evidence from other sites in eastern Africa shortly after 3 Ma does not show a uniform transition toward open habitats (8, 25–27). Ongoing research efforts in the eastern LG continue to explore previously undocumented sedimentary exposures that may allow us to test the hypothesis that the Lee Adoyta record samples a drier habitat of a larger, more variable ecosystem or represents a distinct arid phase in Afar during the late Pliocene.

**Table 1. Preliminary faunal lists for the Gurumaha (GU), Lee Adoyta (LA), and Garsalu (GA) sedimentary packages from the Lee Adoyta Drainage.** Key: X, present; 0, absent; \*, taxa shared with the Kada Hadar submember 2; †, species previously unrecorded in the LAV, including chronospecies.

	GU	LA	GA
<b>Mammalia</b>			
Artiodactyla			
Bovidae			
<i>Aepyceros</i> sp.	X	X	0
<i>Beatragus</i> sp. nov.†	X	X	0
<i>Connochaetes gentryi</i> †	0	0	X
cf. <i>Damaliscus</i> sp.	X	X	0
cf. <i>Damalibore</i> sp. A	X	0	0
<i>Parmularius</i> cf. <i>pachyceras</i> *	0	X	0
<i>Gazella</i> sp.	X	0	0
"Neotragini" Gen et. sp. indet.	0	X	0
aff. <i>Syncerus acoelotus</i> †	0	X	0
<i>Ugandax coryndonae</i> *	X	0	0
<i>Kobus sigmoidalis</i> †	X	0	0
<i>Tragelaphus</i> cf. <i>gaudryi</i> †	0	X	0
<i>Tragelaphus nakuae</i> †	X	X	0
Giraffidae			
<i>Giraffa gracilis</i> †	X	0	0
<i>Sivatherium maurusium</i> *	X	X	0
Hippopotamidae sp.	X	X	X
Suidae			
<i>Kolpochoerus</i> cf. <i>phillipi</i> †	X	0	0
cf. <i>Kolpochoerus</i> sp.	0	X	X
<i>Metridiochoerus</i> cf. <i>andrewsi</i>	X	0	0
cf. <i>Metridiochoerus</i> sp.	X	0	X
<i>Notochoerus</i> sp.	X	0	X
cf. <i>Notochoerus</i> sp.	X	X	0
Carnivora			
cf. <i>Dinofelis</i> sp.	X	0	0
<i>Homotherium</i> sp.	X	0	0
Gen et. sp. indet.	X	0	0
<i>Crocota dietrichi</i> *	X	0	0
Perissodactyla			
Equidae			
<i>Eurygnathohippus hasumense</i> *	X	X	X
<i>Eurygnathohippus afarensis</i> *	X	X	X
Rhinocerotidae			
<i>Ceratotherium</i> sp.	0	X	0
Primates			
Cercopithecidae			
<i>Theropithecus darti</i> *	X	X	0
Hominini			
<i>Homo</i> sp.†	X	0	0
Proboscidea			
<i>Deinotherium bozasi</i> *	X	X	X
<i>Elephas recki</i> *	X	X	0
Tubulidentata			
<i>Orycteropus</i> sp.	X	0	0
<b>Osteichthyes</b>			
Siluriformes			
<i>Clarias</i> sp.	X	X	0
<b>"Reptilia"</b>			
Crocodylia			
<i>Crocodylus</i> sp.	X	X	0

## REFERENCES AND NOTES

1. P. B. deMenocal, *Earth Planet. Sci. Lett.* **220**, 3–24 (2004).
2. P. B. deMenocal, *Science* **270**, 53–59 (1995).
3. J. G. Wynn, *Am. J. Phys. Anthropol.* **123**, 106–118 (2004).
4. T. E. Cerling, *Palaeogeogr. Palaeoclimatol. Palaeoecol.* **97**, 241–247 (1992).
5. A. C. Ravelo, D. H. Andreasen, M. Lyle, A. Olivarez Lyle, M. W. Wara, *Nature* **429**, 263–267 (2004).
6. K. E. Reed, *J. Hum. Evol.* **54**, 743–768 (2008).
7. E. S. Vrba, in *Paleoclimate and Evolution, with Emphasis on Human Origins*, E. S. Vrba, G. H. Denton, T. C. Partridge, L. H. Burckle, Eds. (Yale Univ. Press, New Haven, CT, 1995), pp. 385–424.
8. R. Boe, A. K. Behrensmeyer, *Palaeogeogr. Palaeoclimatol. Palaeoecol.* **207**, 399–420 (2004).
9. W. H. Kimbel et al., *J. Hum. Evol.* **31**, 549–561 (1996).
10. E. Wolfenden, C. Ebinger, G. Yirgu, A. Deino, D. Ayalew, *Earth Planet. Sci. Lett.* **224**, 213–228 (2004).
11. T. Kidane et al., *J. Geophys. Res.* **108**, 2102 (2003).
12. P. Lahitte, P.-Y. Gillot, T. Kidane, V. Courtillot, A. Bekele, *J. Geophys. Res.* **108** (B2), 2123 (2003).
13. N. J. Hayward, C. J. Ebinger, *Tectonics* **15**, 244–257 (1996).
14. J. G. Wynn et al., *Spec. Pap. Geol. Soc. Am.* **446**, 87–118 (2008).
15. J. Quade et al., *Spec. Pap. Geol. Soc. Am.* **446**, 1–31 (2008).
16. J. Quade et al., *Geol. Soc. Am. Bull.* **116**, 1529–1544 (2004).
17. W. H. Kimbel, L. K. Delezenne, *Yearb. Phys. Anthropol.* **140**, 2–48 (2009).
18. E. DiMaggio, thesis, Arizona State University, Tempe, AZ (2013).
19. B. Villmoare et al., *Science* **347**, 1352–1355 (2015).
20. F. M. Gradstein, J. G. Ogg, M. D. Schmitz, G. M. Ogg, *The Geologic Time Scale 2012* (Elsevier, Oxford, 2012).
21. J. Aronson, M. Taieb, in *Hominid Sites: Their Geologic Settings*, G. J. Rapp, C. F. Vondra, Eds. (Westview Press, Boulder, CO, 1981), pp. 165–196.
22. J. E. Kalb, *Palaeogeogr. Palaeoclimatol. Palaeoecol.* **114**, 357–368 (1995).
23. C. Campisano, C. Feibel, *Spec. Pap. Geol. Soc. Am.* **446**, 179–201 (2008).
24. C. J. Campisano, *J. Hum. Evol.* **62**, 338–352 (2012).



25. F. Bibi, A. Souron, H. Bocherens, K. Uno, J.-R. Boisserie, *Biol. Lett.* **9**, 20120890 (2013).
26. J. Kingston, in *Late Cenozoic Environments and Hominid Evolution: A Tribute to Bill Bishop*, P. Andrews, P. Banham, Eds. (Geological Society, London, 1999), pp. 69–84.
27. N. E. Levin, F. H. Brown, A. K. Behrensmeyer, R. Bobe, T. E. Cerling, *Palaeogeogr. Palaeoclimatol. Palaeoecol.* **307**, 75–89 (2011).

## ACKNOWLEDGMENTS

We thank the Ethiopian Authority for Research and Conservation of Cultural Heritage, especially Y. Desta, D. Abebaw, G. Senishaw, T. Getachew, T. Assefa, and Y. Assefa. We also thank our Afar representative, M. Ahamedin, and our field crew and Afar friends,

especially M. Mekonnen Bekele, and M. Jungers for field assistance. The Arizona State University (ASU) LeRoy Eyring Center for Solid State Studies and NG<sup>3</sup>L laboratory personnel provided laboratory support. J. Kalb and E. B. Oswald generously shared their geological and paleontological data. Discussions with C. Ebinger, W. Kimbel, and D. Feary, and comments from two anonymous reviewers, have greatly improved this manuscript. This research was funded by NSF (grants BCS-1157351 and BCS-1322017); the Institute of Human Origins and School of Human Evolution and Social Change at ASU; grants to E.N.D. from American Association of Petroleum Geologists, Society for Sedimentary Geology, Geological Society of America, and the Philanthropic Education Organization; to G.D.-N. from the Marie Curie Actions and Alexander von Humboldt Foundation; and to A.S.

from the Fyssen Foundation and Human Evolution Research Center/University of California Berkeley. Supporting data for this paper are presented in the supplementary materials.

## SUPPLEMENTARY MATERIALS

www.sciencemag.org/content/347/6228/1355/suppl/DC1  
Materials and Methods  
Figs. S1 to S8  
Tables S1 to S6  
References (28–36)

23 October 2014; accepted 13 February 2015  
Published online 5 March 2015;  
10.1126/science.aaa1415

## CRYSTAL GROWTH

# Aqueous formation and manipulation of the iron-oxo Keggin ion

Omid Sadeghi, Lev N. Zakharov, May Nyman\*

There is emerging evidence that growth of synthetic and natural phases occurs by the aggregation of prenucleation clusters, rather than classical atom-by-atom growth. Ferrihydrite, an iron oxyhydroxide mineral, is the common form of Fe<sup>3+</sup> in soils and is also in the ferritin protein. We isolated a 10 angstrom discrete iron-oxo cluster (known as the Keggin ion, Fe<sub>13</sub>) that has the same structural features as ferrihydrite. The stabilization and manipulation of this highly reactive polyanion in water is controlled exclusively by its counterions. Upon dissolution of Fe<sub>13</sub> in water with precipitation of its protecting Bi<sup>3+</sup>-counterions, it rapidly aggregates to ~22 angstrom spherical ferrihydrite nanoparticles. Fe<sub>13</sub> may therefore also be a prenucleation cluster for ferrihydrite formation in natural systems, including by microbial and cellular processes.

Iron oxides and oxyhydroxides are ubiquitous in the environment and serve vital roles in interrelated phenomena of contaminant transport, pH control of surface and ground water, and microbial activity (1–4). Relevant phases include hematite, magnetite, goethite, and ferrihydrite. The structure of ferrihydrite,

the most common iron oxyhydroxide in soil and in the core of the ferritin protein, is isostructural to the Al-mineral akdalaite (5). The ferrihydrite structure has been highly debated (6–9), but the general framework contains linked and fused iron-oxyhydroxide Keggin units. The Keggin ion or molecule is a metal-oxo structural motif in natural and synthetic materials (10). Even before the proposed structure of ferrihydrite, an iron Keggin cluster (henceforth referred to as Fe<sub>13</sub>) was presumed to be synthetically attainable—analogueous to

the Al<sub>13</sub>-Keggin cluster [AlO<sub>4</sub>Al<sub>12</sub>(OH)<sub>24</sub>(H<sub>2</sub>O)<sub>12</sub>]<sup>7+</sup>, which was first crystallized and structurally characterized over 50 years ago. (11)

The identified nonclassical growth behavior of iron oxides in both nature (3) and the laboratory (12)—defined by the aggregation of prenucleation clusters rather than atom-by-atom growth—supports the existence of a discrete Fe<sub>13</sub> ion as a precursor to ferrihydrite and magnetite (Fig. 1). However, the higher reactivity (acidity) of Fe<sup>3+</sup>-bound H<sub>2</sub>O as compared with Al<sup>3+</sup>-bound H<sub>2</sub>O in the Al<sub>13</sub> Keggin ion has thus far thwarted all synthetic efforts to capture a discrete Fe<sub>13</sub> ion from water. Instead, iron oxyhydroxide nanoparticles and precipitates are obtained, bypassing the intermediate discrete cluster state. The closest specie to Fe<sub>13</sub> reported thus far is [FeO<sub>4</sub>Fe<sub>12</sub>F<sub>24</sub>(OCH<sub>3</sub>)<sub>12</sub>]<sup>5-</sup> (13). Although possessing the Keggin structure, this cluster was synthesized in anhydrous conditions and is surface-passivated entirely with nonaqua ligands; it is neither a likely precursor for iron oxide nucleation, nor provides identification of the aqua ligands and ion-charge of Fe<sub>13</sub> derived from water.

Here, we present strategies to stabilize and crystallize the discrete Fe<sub>13</sub> Keggin ion from water and redissolve it in water, both as unassociated and aggregated forms. Because Fe<sub>13</sub> is a very highly charged polyoxoanion, contrary to the analogous Al<sub>13</sub> polyoxocation, we chose likewise highly charged counteranions (Bi<sup>3+</sup>)

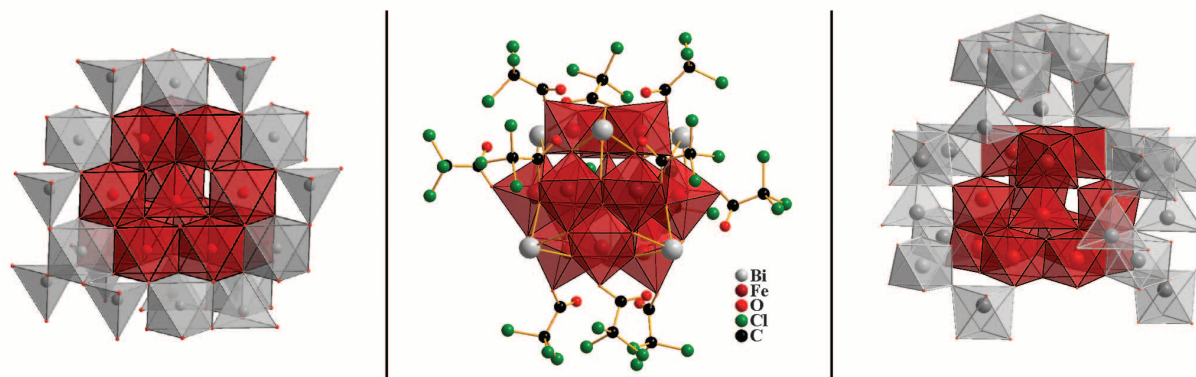


**Fig. 1. The iron Keggin ion.** Views of the iron Keggin ion in different structures. **(Left)** Magnetite, (Fe<sup>II</sup><sub>tet</sub>)(Fe<sup>III</sup><sub>oct</sub>)<sub>2</sub>O<sub>4</sub> emphasizing the ε-Keggin isomer building unit (red polyhedra). The four trimers of edge-sharing octahedra are likewise connected together by edge-sharing. **(Middle)** Bi<sub>6</sub>α-[FeO<sub>4</sub>Fe<sub>12</sub>O<sub>12</sub>(OH)<sub>12</sub>(O<sub>2</sub>C(CCl<sub>3</sub>)<sub>12</sub>)]<sup>7-</sup>, Bi<sub>6</sub>Fe<sub>13</sub>L<sub>12</sub>. In the α-isomer, the four trimers are linked together by corner-sharing. **(Right)** A view of ferrihydrite, structure determined from pair distribution function (5). The red polyhedra emphasize the δ-Fe<sub>13</sub> building block. In the δ-isomer, three of the trimers are edge-sharing, and the fourth is corner-linked.

for charge-stabilization. We used small-angle x-ray scattering (SAXS) to probe the self-assembly of  $\text{Fe}_{13}$  and its behavior in solution. In addition, we simulated scattering data (14) from the x-ray structure for “nude”  $\text{Fe}_{13}$ ,  $\text{Fe}_{13}$  with associated  $\text{Bi}^{3+}$  ( $\text{Bi}_6\text{Fe}_{13}$ ), and the complete cluster ligated with trichloroacetate ( $\text{Bi}_6\text{Fe}_{13}\text{L}_{12}$ ) (table S1), as well as Keggin-ion dimers, for comparison with the experimental data. Last, transmission electron microscopy (TEM) was used to support the x-ray scattering data.

$\text{Fe}_{13}$  crystallizes in a monoclinic lattice and is fully formulated  $\text{Bi}_6[\text{FeO}_4\text{Fe}_2\text{O}_{12}(\text{OH})_{12}(\text{O}_2\text{C}(\text{CCl}_3)_{12})\cdot[\text{O}_2\text{C}(\text{CCl}_3)_2]\cdot 14\text{H}_2\text{O}$  (Fig. 1 and table S2). The 13 Fe and six Bi of the cluster are all trivalent, as determined by bond valence sum (BVS) calculations (tables S3 to S5). The oxo and hydroxyl ligands were likewise identified by BVS, which provides a  $\text{Fe}_{13}$ -cluster charge of  $-17$ , balanced by six  $\text{Bi}^{3+}$  cations and a single lattice trichloroacetate (TCA) co-ion; TCA also serves as the ligand and cap to each octahedral iron. This  $-17$  charge represents the highest charge-density ever observed for Keggin ions, either polyoxocations or polyoxoanions. The closest is  $[\text{TNb}_{12}\text{O}_{40}]^{16-}$  ( $\text{T}=\text{Si}, \text{Ge}$ ) (15, 16). The  $\text{Fe}_{13}$  core is the  $\alpha$ -isomer (Fig. 1), with 12  $\text{Fe}^{3+}$  octahedra and a central  $\text{Fe}^{3+}$ -tetrahedron. The four octahedra-triads are linked together by corner-sharing. Within the triads, the bridging ligands of the edge-sharing octahedra are hydroxyls, and the ligands between the corner-sharing octahedra are oxos. In contrast, the  $\text{Al}_{13}$ -polycation has hydroxyl-ligands at all the bridging positions, related to the lower acidity of an aqua ligand bonded to  $\text{Al}^{3+}$ .

In contrast to the  $\alpha$ -isomer of  $\text{Fe}_{13}$ , the  $\text{Al}_{13}$  polycation has been synthesized as the  $\epsilon$  (17),  $\delta$  (17), and  $\gamma$  (18) isomers, and ferrihydrite is composed of  $\delta$ - $\text{Fe}_{13}$  Keggin units (Fig. 1). In the  $\delta$ -isomer of ferrihydrite, three of the triads are edge-sharing, and the fourth is corner-linked. The  $\epsilon$ -isomer of magnetite and  $\text{Al}_{13}$  features edge-sharing between all the triads. In a rare example from nature, the  $\alpha$ -aluminum Keggin ion

(with  $\text{Si}^{4+}$  in the tetrahedral site) is the building block for the mineral zunyite (19). Speculations (without structural evidence) reported a  $\text{Fe}_{13}$  polycation analogous to the  $\text{Al}_{13}$  polycation (20), presumed by similarities of aqueous Al and Fe chemistry. Understanding the multiple chemical and structural factors that dictate Keggin-isomer stability and interconversion in both discrete ions and frameworks is complex and will likely require computational studies to elucidate.

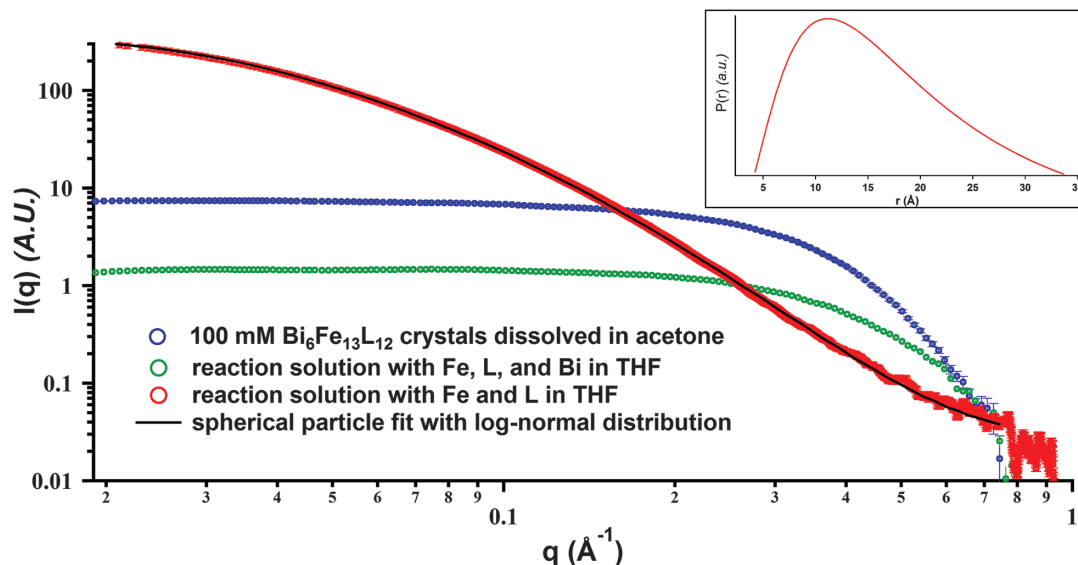
To synthesize  $\text{Fe}_{13}$  in water,  $\text{Fe}^{3+}$  and  $\text{Bi}^{3+}$  nitrate along with trichloroacetic acid and sodium bicarbonate (base) are dissolved in water to give a solution of pH  $\sim 1.4$ . With heating, a red-brown crude product precipitates. The precipitate is dissolved in tetrahydrofuran (THF), from which  $\text{Bi}_6\text{Fe}_{13}\text{L}_{12}$  crystallizes. SAXS analysis (Fig. 2, fig. S2, and table S1) of the crude product dissolved in THF suggests that the dominant form is discrete  $\text{Bi}_6\text{Fe}_{13}$  [based on radius of gyration ( $R_g$ ) and ( $q^{-1}$ ) slope at low  $q$  where  $q$  is the x-ray scattering vector, directly proportional to the scattering angle], without the TCA ligand coordinated. Rather, THF probably coordinates at the terminal site [ $\text{Bi}_6\text{Fe}_{13}\text{THF}_{12}$ ]. Although THF ligands are similar in size to TCA, they do not possess any heavy atoms that provide contrast to the solvent, whereas the chlorides of TCA do provide contrast, and a TCA-ligated cluster therefore appears larger via the x-ray scattering (fig. S2). This suggests that the role of TCA is not necessarily to stabilize  $\text{Fe}_{13}$  but perhaps to aid in crystallization by providing suitable packing and space-filling in a lattice; but it can be readily displaced, as demonstrated throughout this study.

SAXS of  $\text{Bi}_6\text{Fe}_{13}\text{L}_{12}$  dissolved in acetone benchmarks x-ray scattering of the fully intact cluster, for comparison with other derivatives observed in water (Fig. 1 and figs. S1 and S2). The  $\log(q)$ - $\log(I)$  plots of three different concentrations (Fig. 3 and fig. S1) show ideal nonaggregated, monodisperse solutions of spherical clusters

over the concentration range of 5 to 100 mM. Simulated scattering curves for  $\text{Fe}_{13}$ ,  $\text{Bi}_6\text{Fe}_{13}$ , and  $\text{Bi}_6\text{Fe}_{13}\text{L}_{12}$  along with normalized intensity scattering curves of 5, 50, and 100 mmol  $\text{Bi}_6\text{Fe}_{13}\text{L}_{12}$  dissolved in acetone show clearly the specie dissolved in acetone is intact  $\text{Bi}_6\text{Fe}_{13}\text{L}_{12}$ , with minimal deligation or dissociation of Bi (fig. S2). This is in contrast to other conditions discussed later, in which Bi and the ligand are displaced to provide a nude  $\text{Fe}_{13}$  cluster. Additionally, the  $R_g$  determined from the Guinier analysis of all three concentrations agrees well with the  $R_g$  of the simulated scattering curve of  $\text{Bi}_6\text{Fe}_{13}\text{L}_{12}$  (table S1). Last, the pair distance distribution function (PDDF) real-space representation (27) of simulated and experimental  $\text{Bi}_6\text{Fe}_{13}\text{L}_{12}$  dissolved in acetone (Fig. 3, right) are identical in radius and maximum linear extent. The small difference in the  $P(r)$  in the “tail” of the curve likely relates to the difference in conformation of the flexible and mobile ligands in a rigid lattice as compared with in solution.

In the solid-state structure of  $\text{Bi}_6\text{Fe}_{13}\text{L}_{12}$ , the six  $\text{Bi}^{3+}$ -cations cap the square “windows” of the Keggin ion with four Bi-O bonds each ( $\sim 2.1$  to  $2.3$  Å). To assess the role of  $\text{Bi}^{3+}$  in stabilizing  $\text{Fe}_{13}$  clusters during self-assembly, we performed the synthesis with only iron and TCA. Again, a precipitate formed that was dissolved in THF, and the scattering curve is shown in Fig. 2. The difference between this product and that containing bismuth is evident. The substantially higher scattering intensity and slope at low- $q$  indicates a polydisperse system with larger particles, which was modeled with a log-normal distribution of spherical particles (Fig. 2, inset) with a mean radius of  $16.8$  Å and a mode radius of  $11.2$  Å (maximum population of the log-normal distribution). This is in good agreement with prior studies on ferrihydrite nanoparticles, in which a radius of  $\sim 12$  Å for a freshly prepared sample was reported (22). This control study shows that  $\text{Bi}^{3+}$  is necessary for stabilizing  $\text{Fe}_{13}$

**Fig. 2. SAXS data illustrating the effect of Bi on isolation of  $\text{Fe}_{13}$ .** The crude product of  $\text{Fe}_{13}$  dissolved in THF, made with (green curve) and without (red curve) bismuth, and pure crystals of  $\text{Bi}_6\text{Fe}_{13}\text{L}_{12}$  dissolved in acetone for comparison. The black curve-fit model is a log-normal distribution of spherical particles. (Inset) Log-normal size distribution of particles from Bi-free synthesis with a mean particle size of  $16.8$  Å, and mode size of  $11.2$  Å. A.U., arbitrary units for all SAXS data presented.





in solution by both neutralizing the high negative cluster charge and preventing linkage and eventual precipitation of iron oxyhydroxide. Both the high cation charge of  $\text{Bi}^{3+}$  and the inert pair effect contribute to this stabilization.

$\text{Bi}_6\text{Fe}_{13}\text{L}_{12}$  cannot dissolve in water without an electrolyte that partially or fully displaces the strongly associated  $\text{Bi}^{3+}$  to yield a higher polyanion charge.  $\text{Bi}_6\text{Fe}_{13}\text{L}_{12}$  exhibits the same anomalous solubility behavior as polyoxoniobates in aqueous  $\text{ACl}$  solutions (A, alkali) (table S6) (16, 23). Solubility of  $\text{Bi}_6\text{Fe}_{13}\text{L}_{12}$  in  $\text{A}^+(\text{aq})$  trends  $\text{Cs} > \text{Rb} > \text{K} > \text{Na} > \text{Li}$ . SAXS of  $\text{Bi}_6\text{Fe}_{13}\text{L}_{12}$  dissolved in  $\text{CsCl}(\text{aq})$  reveals spherical clusters intermediate in size between  $\text{Bi}_6\text{Fe}_{13}$  and  $\text{Bi}_6\text{Fe}_{13}\text{L}_{12}$  (Fig. 3 and table S1). The ligand is hydrolyzed, replaced by aqua ligands, evident in the ultraviolet-visible (UV-vis) spectrum (fig. S3). Likely a mixture of Cs and Bi is bonded to the cluster in water, preventing direct association between  $\text{Fe}_{13}$  units, in contrast to experiments described below. Last, there is slight aggregation of the clusters in  $\text{CsCl}(\text{aq})$ , evidenced by the rise in  $I(q)$  between  $q = 0.03$  to  $0.07 \text{ \AA}^{-1}$ . Indeed, precipitates from

this solution contain Fe, Bi, and Cs, but no Cl, which is further evidence that the ligand is completely replaced by aqua ligands. The ability to replace TCA with aqua ligands provides access to well-defined and discrete  $\text{Fe}_{13}$ . Organic and inorganic carboxylic acids similar to TCA used in this study are plentiful in nature, suggesting that these too could coordinate and stabilize iron-oxyhydroxide prenucleation clusters during self-assembly in the environment.

Two solution conditions have been identified in which  $\text{Bi}_6\text{Fe}_{13}\text{L}_{12}$  dissolves with both removal of the ligand (hydrolysis) and complete precipitation of bismuth ( $\text{BiOCl}$  ICSD-24608): (i) wet ethanol and (ii) aqueous surfactant solution. Dissolution of  $\text{Bi}_6\text{Fe}_{13}\text{L}_{12}$  in ethanol gives both a scattering profile and PDDF typical of a dimer of clusters (Fig. 3, table S1, and fig. S4). Hydrolysis of the ligand was also identified by means of UV-vis spectroscopy (fig. S3). In fig. S4, we compare the scattering curves and PDDFs of  $\text{Bi}_6\text{Fe}_{13}\text{L}_{12}$  dissolved in ethanol with that of two simulated dimers. This comparison is limited to available structures; therefore, we used other polyoxme-

talate  $\alpha$ -Keggin compositions because the size and shape are essentially identical, regardless of the metal. One simulated dimer is two complete dodecaniobate  $\alpha$ -Keggin ions linked by a single alkali (15). The second dimer is a derived from the ferrihydrite structure, with some of the shared octahedra removed (fig. S4). The experimental and simulated scattering curves all have the same characteristic shape with an inflection at high  $q$  ( $0.6 \text{ \AA}^{-1}$  for the experimental scattering curve), a feature not present in the scattering curve of simulated  $\text{Fe}_{13}$  (fig. S4). Comparison of the PDDFs reveals that the experimental dimer is closer in size to the fragment from the ferrihydrite structure. This suggests that conversion from  $\text{Fe}_{13}$  to ferrihydrite (discussed below) takes place by first eliminating iron octahedra and joining the resulting lacunary fragments together. This would be consistent with decreasing the  $\text{Fe}_{\text{oct}}/\text{Fe}_{\text{tet}}$  ratio from the isolated cluster (12:1) to that of ferrihydrite (4:1). This is also consistent with the well-studied behavior of the Group V/VI polyoxometalates. Specifically, (i) lacunary clusters have coordinatively unsaturated oxo-ligands that

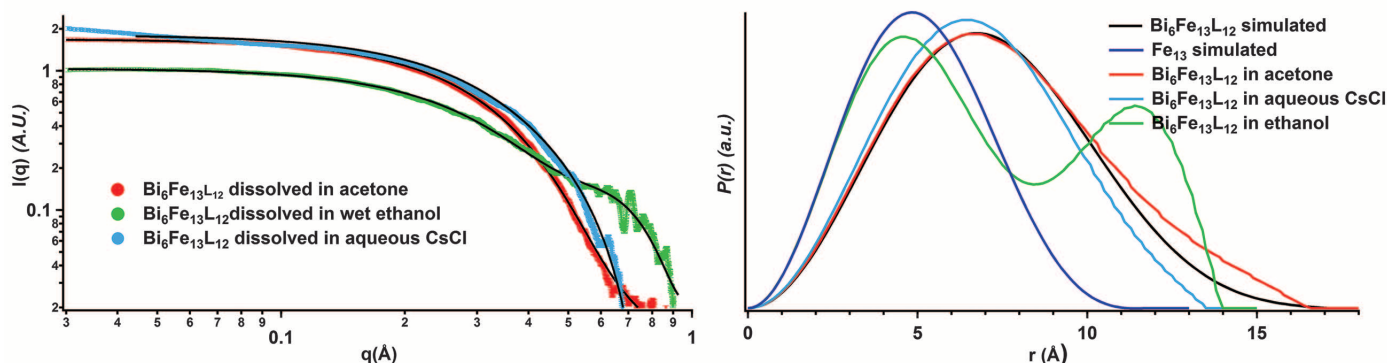


**Fig. 3. SAXS data of  $\text{Bi}_6\text{Fe}_{13}\text{L}_{12}$  in three solvents and associated PDDFs.** The scattering data shows in acetone the cluster is dissolved intact as  $\text{Bi}_6\text{Fe}_{13}\text{L}_{12}$ , with partial deligation and displacement of Bi in aqueous  $\text{CsCl}$ , and with dimer formation in wet ethanol (table S1 and figs. S3 and S4).

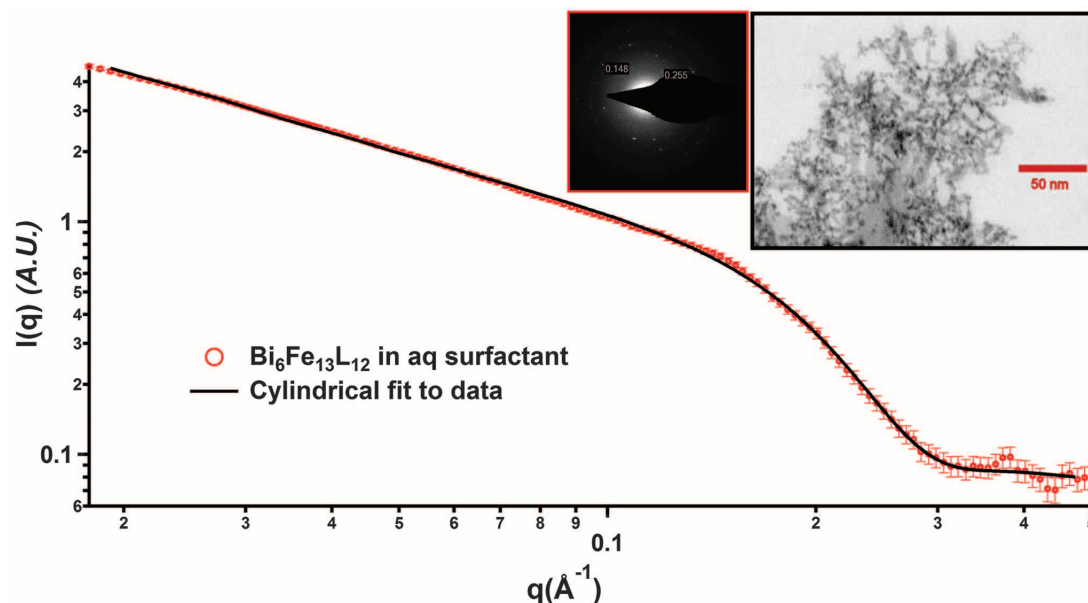


**Fig. 4. Ferrihydrite formation of  $\text{Bi}_6\text{Fe}_{13}\text{L}_{12}$  dissolved in aqueous surfactant.** The SAXS data (red symbols) indicate a linear arrangement of  $\sim 11 \text{ \AA}$  radius spherical particles. The black line is a cylindrical model fit to the experimental data. The TEM image and selected area electron diffraction respectively show spherical particles of this size, with a tendency toward a linear arrangement (fig. S5), and diffraction spots consistent with ferrihydrite (inset).

become more stable by linking together and (ii) lacunary clusters more readily undergo rotational isomerization (24)—for example, from  $\alpha$ -Fe<sub>13</sub> of the isolated cluster to  $\delta$ -Fe<sub>13</sub> of ferrihydrite. The limited amount of water in this experiment slowed the conversion to ferrihydrite, affording this possible intermediate state.

An aqueous solution of a cationic surfactant [cetyltrimethylammonium chloride (CTACl)] dissolves Bi<sub>6</sub>Fe<sub>13</sub>L<sub>12</sub> and persists for months, providing opportunity for extensive aqueous-phase studies of Fe<sub>13</sub> and its soluble derivatives. The dissolution occurs with complete precipitation of BiOCl (no Bi detected in solid obtained from drying the solution) and complete ligand hydrolysis (fig. S3). Fe<sub>13</sub> in this solution that is devoid of associating counteranions such as Bi or Cs undergoes rapid (within a few hours) transformation to resemble incipient ferrihydrite. The background solution containing only CTACl shows no significant scattering or “diffraction” peaks, indicating that CTACl is below the critical micelle concentration, and therefore features in the scattering data (Fig. 4) are from the metal-oxo clusters. The power-law dependence of the slope between  $q = 0.01$  to  $0.18 \text{ \AA}^{-1}$  is  $\sim q^{-1}$ , which is consistent with a linear arrangement of clusters. The scattering data fits well with a cylindrical model with a radius of  $\sim 11 \text{ \AA}$ , the same dominant size observed in the crude synthesis product without Bi (Fig. 1 and table S1), and the same size of synthetic ferrihydrite nanoparticles, which are likewise organized in chains (22, 25). Natural ferrihydrite nanoparticles are also observed in linear arrangements (3). With dialysis to remove the supporting surfactant ions, a precipitate is obtained (Fig. 4). Spherical particles, around 20 to 30  $\text{\AA}$  diameter, are observed than tend toward linear structures, and selected area electron diffraction (SAED) is consistent with natural (3) and synthetic (26) 2-line ferrihydrite. This precipitate can be redissolved in water and gives a solution with a self-buffering pH of 6 and a positive surface charge (zeta potential = +35 mV), which is also consistent with ferrihydrite (27).

The mild conditions of dissolution (neutral pH, room temperature) suggest that features of the Keggin isomers should be preserved upon transformation to the incipient ferrihydrite nanoparticles, strengthening the prior supposition that Fe<sub>13</sub> is a key prenucleation cluster for common iron-oxhydroxides in the environment. Our synthetic approach to Fe<sub>13</sub> provides a long-sought missing link between iron monomers and ferrihydrite nanoparticles that will enable a deeper understanding of one of the most ubiquitous phases in the geosphere and biosphere.

## REFERENCES AND NOTES

1. T. Borch et al., *Environ. Sci. Technol.* **44**, 15–23 (2010).
2. C. M. Hansel et al., *Geochim. Cosmochim. Acta* **67**, 2977–2992 (2003).
3. J. F. Banfield, S. A. Welch, H. Zhang, T. T. Ebert, R. L. Penn, *Science* **289**, 751–754 (2000).
4. S. Dixit, J. G. Hering, *Environ. Sci. Technol.* **37**, 4182–4189 (2003).
5. F. M. Michel et al., *Science* **316**, 1726–1729 (2007).
6. D. G. Rancourt, J. F. Meunier, *Am. Mineral.* **93**, 1412–1417 (2008).
7. A. Manceau, S. Skanthakumar, L. Soderholm, *Am. Mineral.* **99**, 102–108 (2014).
8. D. Paktunc, A. Manceau, J. Dutrizac, *Am. Mineral.* **98**, 848–858 (2013).
9. F. Maillot et al., *Geochim. Cosmochim. Acta* **75**, 2708–2720 (2011).
10. J. F. Keggin, *Proc. R. Soc.* **144**, 75 (1934).
11. G. Johansson, L.-O. Gullman, A. Kjekshus, R. Söderquist, *Acta Chem. Scand.* **14**, 771–773 (1960).
12. J. Baumgartner et al., *Nat. Mater.* **12**, 310–314 (2013).
13. A. Bino, M. Ardon, D. Lee, B. Spingler, S. J. Lippard, *J. Am. Chem. Soc.* **124**, 4578–4579 (2002).
14. R. T. Zhang, P. Thiagarajan, D. M. Tiede, *J. Appl. Cryst.* **33**, 565–568 (2000).
15. M. Nyman, F. Bonhomme, T. M. Alam, J. B. Parise, G. M. B. Vaughan, *Angew. Chem. Int. Ed. Engl.* **43**, 2787–2792 (2004).
16. M. Nyman, *Dalton Trans.* **40**, 8049–8058 (2011).
17. L. Allouche, C. Huguenard, F. Taulelle, *J. Phys. Chem. Solids* **62**, 1525–1531 (2001).
18. S. E. Smart, J. Vaughn, I. Pappas, L. Pan, *Chem. Commun. (Camb.)* **49**, 11352–11354 (2013).
19. W. H. Baur, T. Ohta, *Acta Crystallogr. B* **38**, 390–401 (1982).
20. J. D. Sudha, A. Pich, V. L. Reena, S. Sivakala, H. J. P. Adler, *J. Mater. Chem.* **21**, 16642 (2011).
21. P. B. Moore, *J. Appl. Cryst.* **13**, 168–175 (1980).
22. B. A. Legg, M. Zhu, L. R. Comolli, B. Gilbert, J. F. Banfield, *Langmuir* **30**, 9931–9940 (2014).
23. M. Nyman, P. C. Burns, *Chem. Soc. Rev.* **41**, 7354–7367 (2012).
24. T. M. Anderson, C. L. Hill, *Inorg. Chem.* **41**, 4252–4258 (2002).
25. V. M. Yuwono, N. D. Burrows, J. A. Soltis, R. L. Penn, *J. Am. Chem. Soc.* **132**, 2163–2165 (2010).
26. D. E. Janney, J. M. Cowley, P. R. Buseck, *Clays Clay Miner.* **48**, 111–119 (2000).
27. T. Hiemstra, W. H. Van Riemsdijk, *Geochim. Cosmochim. Acta* **73**, 4423–4436 (2009).

## ACKNOWLEDGMENTS

This work was supported by the U.S. Department of Energy, Office of Basic Energy Sciences, Division of Materials Sciences and Engineering under award DE-SC0010802TDD. We thank B. Gilbert for valuable technical discussions and P. Eschbach and T. Sawyer for help with sample preparation and TEM imaging. All data are available in the supplementary materials.

## SUPPLEMENTARY MATERIALS

www.sciencemag.org/content/347/6228/1359/suppl/DC1  
Materials and methods  
Supplementary Text  
Figs. S1 to S7  
Tables S1 to S6  
Crystallographic Information File

17 December 2014; accepted 17 February 2015  
Published online 26 February 2015;  
10.1126/science.aaa4620

## EPILEPSY TREATMENT

# Targeting LDH enzymes with a stiripentol analog to treat epilepsy

Nagisa Sada,<sup>1</sup> Suni Lee,<sup>2</sup> Takashi Katsu,<sup>1\*</sup> Takemi Otsuki,<sup>2</sup> Tsuyoshi Inoue<sup>1†</sup>

Neuronal excitation is regulated by energy metabolism, and drug-resistant epilepsy can be suppressed by special diets. Here, we report that seizures and epileptiform activity are reduced by inhibition of the metabolic pathway via lactate dehydrogenase (LDH), a component of the astrocyte-neuron lactate shuttle. Inhibition of the enzyme LDH hyperpolarized neurons, which was reversed by the downstream metabolite pyruvate. LDH inhibition also suppressed seizures in vivo in a mouse model of epilepsy. We further found that stiripentol, a clinically used antiepileptic drug, is an LDH inhibitor. By modifying its chemical structure, we identified a previously unknown LDH inhibitor, which potently suppressed seizures in vivo. We conclude that LDH inhibitors are a promising new group of antiepileptic drugs.

Approximately 1% of the world population suffers from epilepsy. Clinically available antiepileptic drugs are not effective for one third of epileptic patients (1); therefore, new medicines are needed for drug-resistant epilepsy. Surprisingly, the ketogenic diet was developed in the 1920s and is still in use today for some patients with drug-resistant epilepsy (2). Thus, it is theoretically possible to target metabolic systems, similar to the ketogenic diet.

The ketogenic diet is a high-fat and low-carbohydrate diet. The energy source for the

brain is switched from glucose to ketone bodies (acetoacetate and  $\beta$ -hydroxybutyrate). Ketone bodies directly regulate neural excitation and seizures via adenosine 5'-triphosphate (ATP)-sensitive K<sup>+</sup> channels (K<sub>ATP</sub> channels) (3–5) and vesicular glutamate transporters (6). Ketogenic diets also suppress seizures via adenosine A<sub>1</sub> receptors (7). These molecules are involved in generating electrical currents (ion channels, synaptic receptors, and neurotransmitter transporters) [reviewed in (8)]. Although ketogenic diets act on energy metabolism (for example, glycolysis and the TCA cycle), metabolic enzymes that control epilepsy have not yet been identified. Antiepileptic drugs that act on metabolic pathways are also not known (9).

We first examined how membrane potentials in neurons were changed by a switch from glucose to ketone bodies (Fig. 1A) because this metabolic switch is elicited by ketogenic diets (10).

<sup>1</sup>Department of Biophysical Chemistry, Graduate School of Medicine, Dentistry and Pharmaceutical Sciences, Okayama University, Okayama 700-8530, Japan. <sup>2</sup>Department of Hygiene, Kawasaki Medical School, Kurashiki 701-0192, Japan.

\*Present address: Department of Pharmacy, Graduate School of Pharmacy, Yasuda Women's University, Hiroshima 731-0153, Japan.  
†Corresponding author. E-mail: tinoue@pharm.okayama-u.ac.jp



We used patch-clamp recording from neurons in slices from the subthalamic nucleus (STN) of the basal ganglia (11). The basal ganglia [the STN and substantia nigra pars reticulata (SNr)] are important for the propagation of some forms of seizures (12, 13), and SNr cells are electrically responsive to ketone bodies (3). We also used 2.5 mM glucose in artificial cerebrospinal fluid

(ACSF) to study neuronal activities under in vivo-like metabolic conditions. This concentration is lower than that of commonly used ACSF for in vitro electrophysiology (10 to 25 mM). However, because brain glucose concentrations are ~2.4 mM in vivo (14), this in vivo-like glucose (2.5 mM) has been used for in vitro electrophysiology such as glucose sensors in the hypothalamus (15)

and metabolic state-dependent cortical activities (16).

STN cells were markedly hyperpolarized by a switch from 2.5 mM glucose in ACSF to 2.5 mM  $\beta$ -hydroxybutyrate, a ketone body (Fig. 1, B and C;  $n = 10$  cells), or to 2.5 mM acetoacetate, another ketone body (fig. S1, A and B;  $n = 9$  cells). Although mild neuronal inhibition by ketone bodies

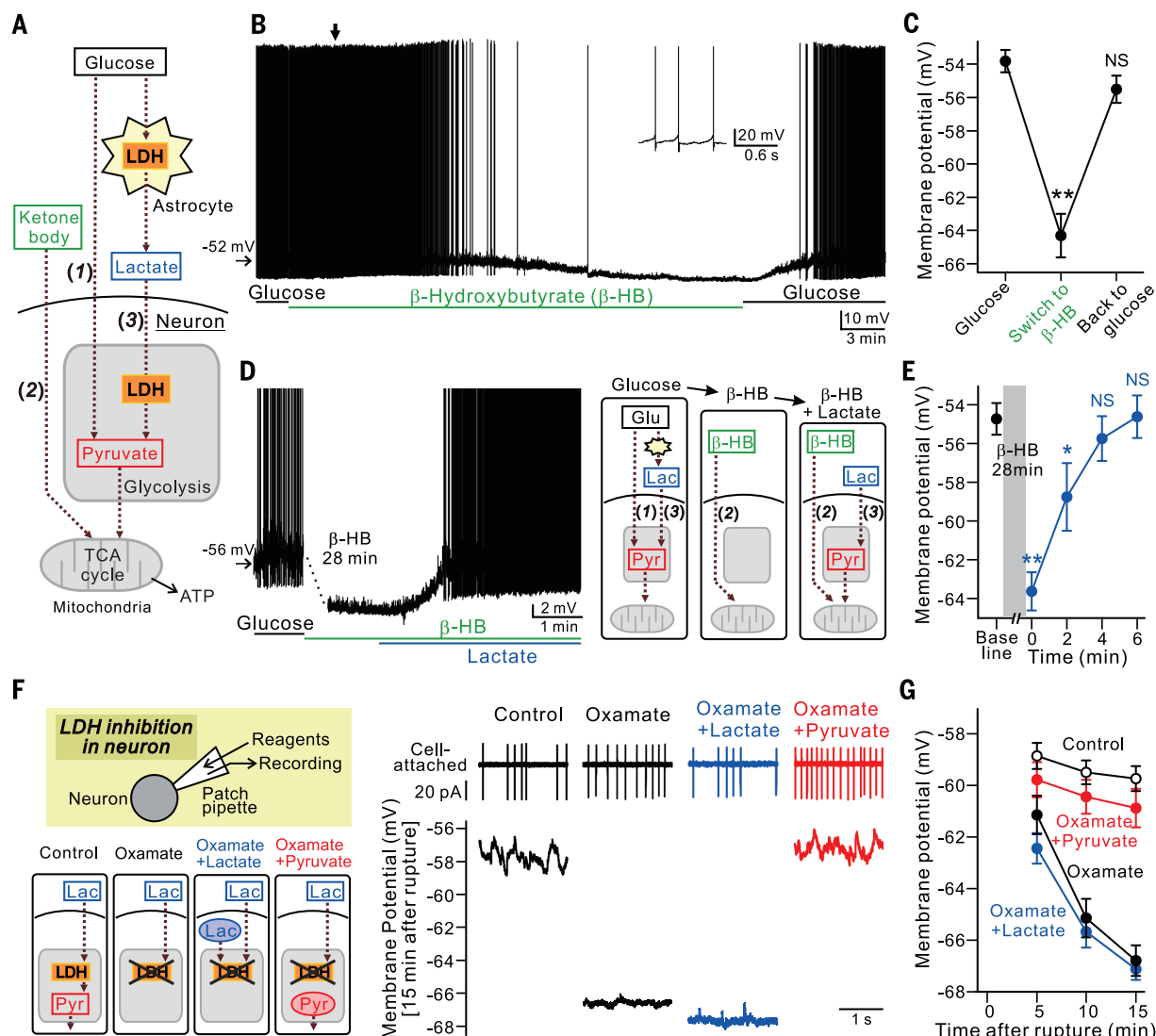


**Fig. 1. LDH regulates membrane potentials in neurons.** (A) A scheme of energy metabolic pathways. Glucose is transported into neurons and converted to pyruvate in glycolysis (pathway 1). Ketone bodies directly activate the TCA cycle in neurons (pathway 2). Glucose is also transported into astrocytes and converted to lactate by LDH, which is then released to neurons and converted to pyruvate by LDH (pathway 3, the astrocyte-neuron lactate shuttle). (B) Hyperpolarization in an STN cell induced by a switch from 2.5 mM glucose to 2.5 mM sodium  $\beta$ -hydroxybutyrate ( $\beta$ -HB) for 29 min. These reagents were bath-applied. (Inset) Horizontal expansion at the vertical arrow. (C) A summary of the data from (B) ( $n = 10$  cells). Data are mean  $\pm$  SEM. \*\* $P < 0.01$ ; NS, not significant from the data of glucose [one-way repeated measures analysis of variance (ANOVA) followed by Dunnett's test]. (D) This hyperpolarization by a switch from glucose to  $\beta$ -hydroxybutyrate was completely reversed by addition of 5 mM sodium lactate. Spikes are truncated for clarity. (Right) Schemes of metabolic pathways in the three experimental conditions. Glucose, lactate, and pyruvate are depicted as "Glu," "Lac," and

"Pyr," respectively. (E) A summary of the data from (D) ( $n = 8$  cells). Lactate was applied at 0 min. Data are mean  $\pm$  SEM. \*\* $P < 0.01$ ; \* $P < 0.05$ ; NS, not significant from the baseline (one-way repeated measures ANOVA followed by Dunnett's test). (F) Changes in the membrane potential of STN cells induced by intracellular application of 6 mM sodium oxamate (black), oxamate plus 6 mM sodium lactate (blue), or oxamate plus 6 mM sodium pyruvate (red). No reagents were applied in the control (black). These reagents were intracellularly applied for 15 min through a patch pipette. (Left) Schemes of metabolic pathways in the four experimental conditions. Although spikes were observed before the patch membrane was ruptured (Cell-attached), the intracellular application of oxamate hyperpolarized STN cells, and this hyperpolarization was blocked by the addition of pyruvate. Cell-attached spikes are truncated for clarity. (G) A summary of the data from (F) ( $n = 8$  cells for control,  $n = 14$  cells for oxamate,  $n = 9$  cells for oxamate + lactate,  $n = 9$  cells for oxamate + pyruvate). The patch membrane was ruptured at 0 min. Data are mean  $\pm$  SEM. The statistical evaluation is shown in fig. S2C.

has been reported (3), STN cells were not hyperpolarized by the addition of  $\beta$ -hydroxybutyrate to glucose-containing ACSF in our recording conditions (fig. S1, C and D;  $n = 8$  cells). However, STN cells were hyperpolarized by the removal of glucose from ketone body-containing ACSF (fig. S1, E and F;  $n = 9$  cells).

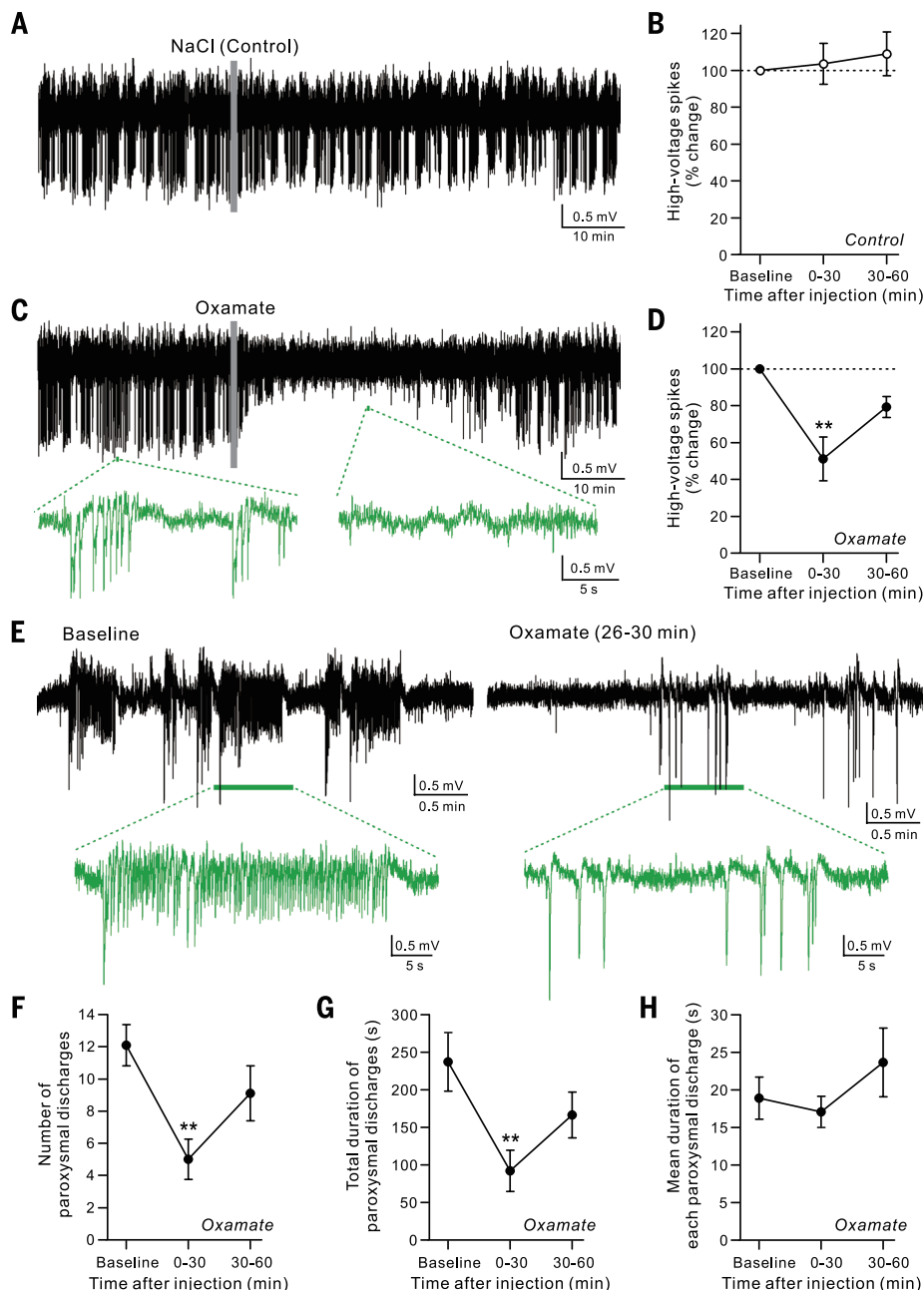
We further examined why neurons were hyperpolarized by decreases in glucose during the switch to ketone bodies. Glucose is transported into neurons and then converted to pyruvate in glycolysis (Fig. 1A, pathway 1), whereas ketone bodies directly activate the TCA cycle in neurons (Fig. 1A, pathway 2). Glucose is also converted to lactate in astrocytes, and this lactate is then converted to pyruvate in neurons [Fig.

1A, pathway 3; known as the astrocyte-neuron lactate shuttle (17)]. Thus, there are two pathways of glucose into neurons (pathways 1 and 3). This lactate shuttle directly regulates brain functions such as synaptic transmission (18), neuronal membrane potentials (19), memory acquisition (20), salt-intake behavior (21), and central nervous system (CNS) regulation of blood glucose (22). We found that the hyperpolarization by a switch from glucose to  $\beta$ -hydroxybutyrate (Fig. 1B) was completely reversed by the addition of lactate (Fig. 1, D and E;  $n = 8$  cells).

The lactate pathway is mediated by the enzyme LDH (Fig. 1A). We therefore examined the effects of LDH inhibition on membrane potentials in STN cells. Oxamate has been used to

inhibit LDH in the CNS (22). To inhibit LDH only in the recorded neuron, we intracellularly applied oxamate through a patch pipette (Fig. 1F, left scheme). Intracellular oxamate (6 mM) hyperpolarized STN cells, suppressed spike firing, and decreased input resistances ("Oxamate" in Fig. 1, F and G, and fig. S2;  $n = 14$  cells). To further confirm that oxamate selectively blocked LDH in neurons, the upstream metabolite (lactate) or downstream metabolite (pyruvate) was co-applied into the neuron (Fig. 1F, bottom left scheme). If oxamate is selective, the upstream lactate cannot reactivate the pathway, whereas the downstream pyruvate must reactivate the pathway. We found that the oxamate-induced hyperpolarization was recovered by the co-application of 6 mM pyruvate

**Fig. 2. LDH in the brain regulates epileptiform activity in the kainate model in vivo.** (A and C) Spontaneous high-voltage spikes in the hippocampus of mice 2 weeks after the kainate injection, changed by the intrahippocampal injection of (A) NaCl (control) or (C) sodium oxamate. Reagents (75 nmol in 100 nL) were directly injected into the hippocampus at the vertical gray bars. In (C), horizontal expansions of the trace are shown in green. (B and D) A summary of the data from (A) and (C), showing the number of high-voltage spikes changed after (B) NaCl ( $n = 7$  mice) or (D) oxamate ( $n = 7$  mice). The number of all spikes for every 30 min after the injection was normalized by that for 30 min before the injection (baseline). Data are mean  $\pm$  SEM.  $**P < 0.01$  from the baseline (one-way repeated measures ANOVA followed by Dunnett's test). (E) Spontaneous paroxysmal discharges in the hippocampus of mice  $>3$  weeks after the kainate injection, changed by the intrahippocampal injection of sodium oxamate (75 nmol in 100 nL). Horizontal expansions of the traces are shown in green, representing a clear paroxysmal discharge in baseline. (F to H) A summary of the data from (E). Changes in the number of paroxysmal discharges (F), the total duration of paroxysmal discharges (G), and the mean duration of each paroxysmal discharge (H) are shown in every 30-min time frame. Baseline events were calculated from 30-min recordings before the injection. Data were obtained from 10 mice, whereas data in (H) were from 9 mice because no paroxysmal discharges were observed in one mouse after the injection. Data are mean  $\pm$  SEM.  $**P < 0.01$  from the baseline (one-way repeated measures ANOVA followed by Dunnett's test).





(“Oxamate + Pyruvate” in Fig. 1, F and G;  $n = 9$  cells) or 600  $\mu\text{M}$  pyruvate (“Oxamate + Pyr” in fig. S3, B and E;  $n = 7$  cells) but not recovered by that of 6 mM lactate (“Oxamate + Lactate” in Fig. 1, F and G;  $n = 9$  cells). Oxamate-induced decreases in membrane excitability were also recovered by pyruvate but not by lactate (fig. S2).

The mechanism underlying the hyperpolarization by LDH inhibition was further examined (figs. S3 to S5 and supplementary text S1). We found that the hyperpolarization by LDH inhibition was recovered by pyruvate and oxaloacetate, downstream metabolites of LDH (fig. S3); however, it was not recovered by energy substrates (fig. S4). We also found that the hyperpolarization by LDH inhibition was recovered by  $\text{K}_{\text{ATP}}$  channel blockers (fig. S5).

We then explored which neurons in the brain were responsive to LDH inhibition. Oxamate markedly hyperpolarized neurons in the basal ganglia ( $n = 21$  STN cells and  $n = 8$  SNr cells) and pyramidal cells in the hippocampus ( $n = 8$  cells) (fig. S6). In CA1, excitatory pyramidal cells were strongly hyperpolarized by 2.5 to 10 mM oxamate, but inhibitory fast-spiking cells were not (fig. S7, A and B). The hyperpolarization was reversed by 5 mM pyruvate ( $n = 7$  cells) but not by lactate ( $n = 8$  cells) (fig. S7, C and D), which further supports electrical regulation by LDH. Oxamate hyperpolarized pyramidal cells by  $\sim 10$  mV (fig. S8, A and C) and decreased voltage deflection by current injection (fig. S8, A and D), which resulted in marked reduction in firing (fig. S8, B, E, and F;  $n = 9$  cells). The lack of hyperpolarization in inhibitory fast-spiking cells (fig. S7A) is possibly because there is no link between the downstream metabolites of LDH and  $\text{K}_{\text{ATP}}$  channels (fig. S9 and supplementary

text S2). In pyramidal cells, oxamate also reduced excitatory postsynaptic currents (EPSCs) ( $n = 7$  cells) more strongly than inhibitory postsynaptic currents (IPSCs) ( $n = 8$  cells) (fig. S10). The excitatory components (pyramidal cells and EPSCs) in the hippocampus are thus strongly responsive to LDH inhibition.

There are two LDHs in the astrocyte-neuron lactate shuttle (Fig. 1A). We next examined electrical regulation by LDH in astrocytes. In double recordings from neighboring pairs of pyramidal cells and astrocytes (fig. S11, A and B), pyramidal cells were recorded in whole-cell, whereas astrocytes were recorded in cell-attached configuration (fig. S11C, before “rupture”). Because oxamate was included in the patch pipette of astrocytes, we could selectively inhibit LDH in astrocytes by rupturing their patch membranes (“rupture” in fig. S11C) and examine its effects on neighboring pyramidal cells (fig. S11C, after “rupture”). Small molecules, such as oxamate, can easily diffuse to neighboring astrocytes via gap junctions but not to neurons (18, 23). We found that pyramidal cells were hyperpolarized by oxamate into neighboring astrocytes (fig. S11, C and D;  $n = 8$  pairs). This hyperpolarization was due to reduction in lactate release from astrocytes (fig. S11A) because pyramidal cells were not hyperpolarized by oxamate into astrocytes in lactate-containing ACSF (fig. S11, E and F;  $n = 6$  pairs). These results show that pyramidal cells are electrically regulated by the astrocyte-neuron lactate shuttle via LDH.

We then asked whether LDH inhibition could suppress seizures *in vivo*. We first examined an acute seizure model in mice (figs. S12 and S13 and supplementary text S3). Pilocarpine-induced paroxysmal discharges in the electroencephalo-

gram (EEG) (fig. S12) and pilocarpine-induced behavioral seizures (fig. S13) were both suppressed by LDH inhibition.

We then investigated whether LDH inhibition could suppress chronic seizures *in vivo* using a kainate model (supplementary text S4) (24). We injected kainate into the hippocampus and then placed electrodes at the injected site for the local field potential (LFP) recordings (fig. S14A). Spontaneous high-voltage spikes were evaluated in mice 2 weeks after the kainate injection, and spontaneous paroxysmal discharges were evaluated in mice  $>3$  weeks after the kainate injection (fig. S14C and supplementary text S4). Oxamate [500 mg/kg intraperitoneally (ip)] suppressed the spontaneous high-voltage spikes (fig. S15;  $n = 7$  mice) and paroxysmal discharges (fig. S16;  $n = 6$  mice). To confirm that LDH in the brain regulated these epileptiform activities, we directly injected the LDH inhibitor into the hippocampus. The spontaneous high-voltage spikes were not changed by a control solution (Fig. 2, A and B, and fig. S17A;  $n = 7$  mice) but were suppressed by the intrahippocampal injection of oxamate (75 nmol in 100 nL) (Fig. 2, C and D, and fig. S17B;  $n = 7$  mice). The spontaneous paroxysmal discharges were also not changed by a control solution (fig. S18;  $n = 9$  mice) but were suppressed by the injection of oxamate (Fig. 2E;  $n = 10$  mice). Quantitatively, the number of paroxysmal discharges (Fig. 2F) and total duration of paroxysmal discharges (Fig. 2G) were significantly reduced by the LDH inhibitor ( $n = 10$  mice).

We then knocked down LDHA, a subunit of LDH, by means of an intrahippocampal injection of antisense oligodeoxynucleotide (ODN). Expression of LDHA proteins in the hippocampus was decreased 2.5 to 3 hours after the

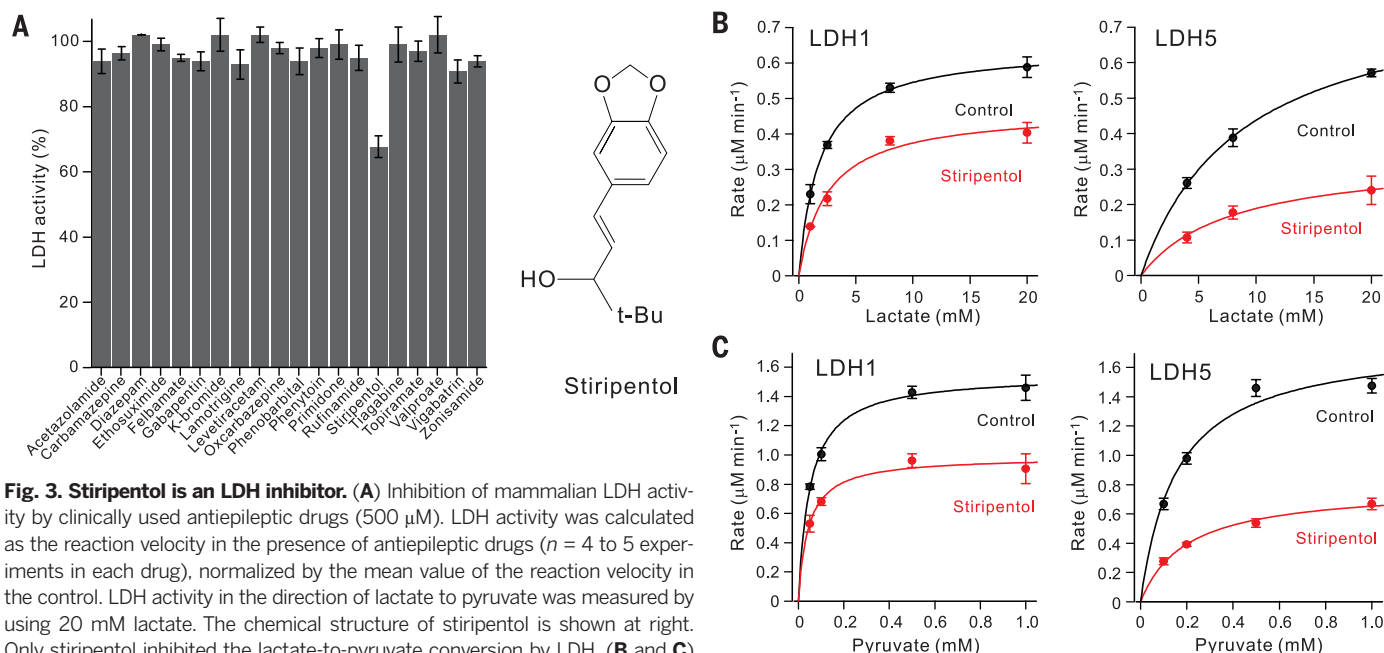


**Fig. 3. Stiripentol is an LDH inhibitor.** (A) Inhibition of mammalian LDH activity by clinically used antiepileptic drugs (500  $\mu\text{M}$ ). LDH activity was calculated as the reaction velocity in the presence of antiepileptic drugs ( $n = 4$  to 5 experiments in each drug), normalized by the mean value of the reaction velocity in the control. LDH activity in the direction of lactate to pyruvate was measured by using 20 mM lactate. The chemical structure of stiripentol is shown at right. Only stiripentol inhibited the lactate-to-pyruvate conversion by LDH. (B and C) Reaction velocities of the (B) lactate-to-pyruvate conversion and (C) pyruvate-to-lactate conversion by two human LDHs (LDH1 and LDH5) and their inhibition by 500  $\mu\text{M}$  stiripentol. The data in each point were from  $n = 3$  to 8 experiments. Data are mean  $\pm$  SEM.

injection of an antisense ODN to LDHA, compared with the injection of a control ODN (fig. S19A;  $n = 12$  mice in each group). Spontaneous high-voltage spikes in the kainate model were not changed by the control ODN but were suppressed by the LDHA antisense ODN (fig. S19, B to F;  $n = 7$  mice in each group).

On the basis of our *in vitro* and *in vivo* experiments, LDH inhibition weakens the lactate pathway, hyperpolarizes neurons, and suppresses seizures *in vivo*. We then asked whether LDH inhibition (or reduction in lactate, a mediator of the lactate pathway) was actually induced by ketogenic diets. Ketogenic diets reduce plasma glucose concentrations (10) and extracellular glucose concentrations in the brain (25). Lactate concentrations in the hippocampus were significantly lower in mice fed a ketogenic diet than in control mice (fig. S20A;  $n = 11$  mice in each group). LDH expression and activity in the hippocampus were not changed by the ketogenic diet (fig. S20, B and C).

Taken together, our results indicate that LDH is a molecular target to suppress epilepsy and mimic ketogenic diet treatment. As the next step,

we explored antiepileptic drugs acting on this enzyme. Although several dozen antiepileptic drugs have been used clinically, antiepileptic drugs acting on LDH are not known (9). We hypothesized that some antiepileptic drugs, which were clearly not designed to act on LDH, might actually inhibit LDH. If this hypothesis is correct, LDH inhibitors are relatively safe as antiepileptic drugs because partial LDH inhibition already has been used in humans.

We explored clinically used antiepileptic drugs that act on LDH. Inhibition of LDH activity by 20 antiepileptic drugs was measured as the conversion of lactate to pyruvate by purified mammalian LDH (Fig. 3A). Although most of the drugs did not influence LDH activity, we found that stiripentol had an inhibitory effect (Fig. 3A). Stiripentol is used for the treatment of Dravet syndrome, a rare form of epilepsy (26). We examined the effects of stiripentol on human LDH isoform 1 (hLDH1, composed of LDHB subunits) and human LDH isoform 5 (hLDH5, composed of LDHA subunits). Stiripentol (500  $\mu$ M) inhibited the lactate-to-pyruvate conversion as well

as the pyruvate-to-lactate conversion by both human LDHs (Fig. 3, B and C). Lineweaver-Burk plots revealed that the inhibition by stiripentol was noncompetitive (fig. S21), suggesting that stiripentol binds to the LDHs at a different site with lactate and pyruvate.

Stiripentol is a new-generation antiepileptic drug, and its chemical structure is unrelated to other antiepileptic drugs. Thus, it is highly important to further modify its chemical structure for developing new antiepileptic drugs. Stiripentol (300 mg/kg ip) had a small effect on high-voltage spikes in the kainate model (STP in Fig. 4, C and D, and fig. S22A;  $n = 8$  mice). We therefore explored stiripentol-like compounds that inhibit the LDH enzymes and strongly suppress seizures *in vivo*. By screening stiripentol derivatives, we found that isosafrole was a potent LDH inhibitor (Fig. 4, A and B). Isosafrole is a substructure of stiripentol that lacks the hydroxyl group and tertiary-butyl group of stiripentol (Fig. 4A). Isosafrole strongly inhibited the pyruvate-to-lactate conversion by both LDH1 and LDH5 (Fig. 4B), suggesting that it inhibits lactate production itself (Fig. 1A). Isosafrole (200 to 300 mg/kg ip) strongly suppressed spontaneous high-voltage spikes (ISO in Fig. 4, C and D, and fig. S22B;  $n = 8$  mice) and paroxysmal discharges (fig. S23;  $n = 9$  mice) in the kainate model *in vivo*. Major side effects were not observed (figs. S24 and S25 and supplementary text S5). Thus, the LDH-targeting stiripentol analog has antiepileptic actions *in vivo*.

In the present study, we found that neural activities and seizures can be suppressed by LDH inhibition and also found that LDH can be inhibited by stiripentol and its analog (fig. S26). This antiepileptic action was based on an antiepileptic mechanism of ketogenic diets (fig. S26 and supplementary text S6). There are no antiepileptic drugs that act on metabolic pathways (9); therefore, LDH inhibitors would be the first antiepileptic drug to mimic ketogenic diets. There are some candidates as LDH inhibitors. First, clinically used stiripentol is an LDH inhibitor (Fig. 3). Stiripentol is an antiepileptic drug for Dravet syndrome (26), and ketogenic diets are also effective in such cases (27). Second, LDH5 inhibitors have been chemically synthesized as antimalarial and antitumor drugs (28, 29). Third, a stiripentol analog (isosafrole) is an LDH inhibitor that suppresses seizures *in vivo* (Fig. 4). Going by the lactate reduction by ketogenic diets (fig. S20), LDH inhibitors for the pyruvate-to-lactate conversion, such as isosafrole (Fig. 4B), would be more effective for antiepileptic actions. Because antiepileptic drugs generally act on multiple molecular targets (9) [(30, 31) for stiripentol], it would be interesting to identify other targets of LDH inhibitors developed as antiepileptic drugs. Our study opens a realistic path to develop compounds for drug-resistant epilepsy by targeting LDH enzymes with stiripentol derivatives.

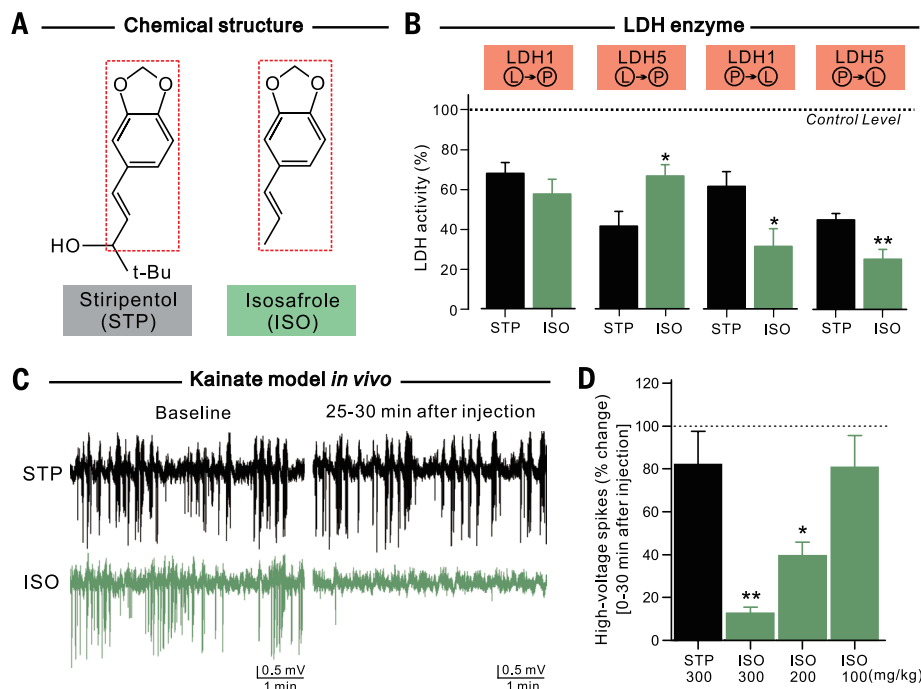


**Fig. 4. Suppression of epileptiform activity *in vivo* by an LDH-targeting stiripentol analog.** (A) The chemical structures of stiripentol and isosafrole. Their common structures are surrounded by red dotted lines. (B) Inhibition of LDH activity by stiripentol (STP; 500  $\mu$ M, black) or isosafrole (ISO; 500  $\mu$ M, green), measured with enzyme kinetic experiments. The lactate-to-pyruvate conversion (in 20 mM lactate; shown as "L" $\rightarrow$ "P") and pyruvate-to-lactate conversion (in 1 mM pyruvate; shown as "P" $\rightarrow$ "L") were measured by using two human LDHs (LDH1 and LDH5). LDH activity was calculated as the reaction velocity in the presence of stiripentol or isosafrole ( $n = 3$  to 6 experiments in each bar), normalized by the mean value of the reaction velocity in the control. The control level (100%) is indicated as a horizontal dotted line. Data are mean  $\pm$  SEM. \*\* $P < 0.01$ ; \* $P < 0.05$  from the data of stiripentol (unpaired  $t$  test). (C) Spontaneous high-voltage spikes in the hippocampus of mice 2 weeks after the kainate injection, changed by the intraperitoneal injection of stiripentol (STP; 300 mg/kg, black) or isosafrole (ISO; 300 mg/kg, green). (D) The number of high-voltage spikes was reduced by stiripentol (300 mg/kg ip,  $n = 8$  mice, black) or isosafrole (100 to 300 mg/kg ip,  $n = 8$  mice for all doses, green). The number of all spikes for 0 to 30 min after the injection was normalized by that for 30 min before the injection. Data are mean  $\pm$  SEM. \*\* $P < 0.01$ ; \* $P < 0.05$  from the data of stiripentol (one-way ANOVA followed by Dunnett's test).

#### REFERENCES AND NOTES

- P. Kwan, M. J. Brodie, *N. Engl. J. Med.* **342**, 314–319 (2000).
- E. G. Neal *et al.*, *Lancet Neurol.* **7**, 500–506 (2008).
- W. Ma, J. Berg, G. Yellen, *J. Neurosci.* **27**, 3618–3625 (2007).



4. G. R. Tanner, A. Lutas, J. R. Martínez-François, G. Yellen, *J. Neurosci.* **31**, 8689–8696 (2011).
5. A. Giménez-Cassina *et al.*, *Neuron* **74**, 719–730 (2012).
6. N. Juge *et al.*, *Neuron* **68**, 99–112 (2010).
7. S. A. Masino *et al.*, *J. Clin. Invest.* **121**, 2679–2683 (2011).
8. A. Lutas, G. Yellen, *Trends Neurosci.* **36**, 32–40 (2013).
9. B. S. Meldrum, M. A. Rogawski, *Neurotherapeutics* **4**, 18–61 (2007).
10. K. J. Bough *et al.*, *Ann. Neurol.* **60**, 223–235 (2006).
11. Materials and methods are available as supplementary materials on Science Online.
12. D. Dybdal, K. Gale, *J. Neurosci.* **20**, 6728–6733 (2000).
13. M. J. Iadarola, K. Gale, *Science* **218**, 1237–1240 (1982).
14. I. A. Silver, M. Erecińska, *J. Neurosci.* **14**, 5068–5076 (1994).
15. Z. Song, B. E. Levin, J. J. McArdle, N. Bakhos, V. H. Routh, *Diabetes* **50**, 2673–2681 (2001).
16. M. O. Cunningham *et al.*, *Proc. Natl. Acad. Sci. U.S.A.* **103**, 5597–5601 (2006).
17. M. Bélanger, I. Allaman, P. J. Magistretti, *Cell Metab.* **14**, 724–738 (2011).
18. N. Rouach, A. Koulakoff, V. Abudara, K. Willecke, C. Giaume, *Science* **322**, 1551–1555 (2008).
19. M. P. Parsons, M. Hirasawa, *J. Neurosci.* **30**, 8061–8070 (2010).
20. A. Suzuki *et al.*, *Cell* **144**, 810–823 (2011).
21. H. Shimizu *et al.*, *Neuron* **54**, 59–72 (2007).
22. T. K. Lam, R. Gutierrez-Juarez, A. Pocai, L. Rossetti, *Science* **309**, 943–947 (2005).
23. R. D'Ambrosio, J. Wenzel, P. A. Schwartzkroin, G. M. McKhann 2nd, D. Janigro, *J. Neurosci.* **18**, 4425–4438 (1998).
24. V. Riban *et al.*, *Neuroscience* **112**, 101–111 (2002).
25. R. Samala, J. Klein, K. Borges, *Neurochem. Int.* **58**, 5–8 (2011).
26. C. Chiron *et al.*, *Lancet* **356**, 1638–1642 (2000).
27. R. H. Caraballo *et al.*, *Epilepsia* **46**, 1539–1544 (2005).
28. L. M. Deck *et al.*, *J. Med. Chem.* **41**, 3879–3887 (1998).
29. C. Granchi *et al.*, *J. Med. Chem.* **54**, 1599–1612 (2011).
30. M. K. Trojnar, K. Wojtal, M. P. Trojnar, S. J. Czuczwar, *Pharmacol. Rep.* **57**, 154–160 (2005).
31. P. P. Quilichini, C. Chiron, Y. Ben-Ari, H. Gozlan, *Epilepsia* **47**, 704–716 (2006).

# ACKNOWLEDGMENTS

We thank K. Imoto for comments on this manuscript, D. Kase for technical advice on in vivo recordings at the initial stage, and

A. Wakasa and K. Urakawa for their technical support on the intrahippocampal kainate model. N.S., S.L., T.O., and T.I. are inventors on a patent (World Intellectual Property Organization WO2014/115764) related to clinical use of stiripentol as LDH inhibitors, and N.S. and T.I. are also inventors on a patent (Japan JP2015-023572) related to isosafrole as antiepileptic compounds. These patent applications have been filed by Okayama University. All data described in the paper are presented in this report and supplementary materials. This work was supported by grants from the Japan Society for the Promotion of Science (24590114) and by research grants from Takeda Science Foundation and Ryobi-Teien Memory Foundation.

# SUPPLEMENTARY MATERIALS

www.sciencemag.org/content/347/6228/1362/suppl/DC1  
Materials and Methods  
Supplementary Text  
Figs. S1 to S26  
References (32–59)

21 October 2014; accepted 9 February 2015  
10.1126/science.1299

## TRANSLATION

# An RNA biosensor for imaging the first round of translation from single cells to living animals

James M. Halstead,<sup>1,\*</sup> Timothée Lionnet,<sup>2,3,4,\*</sup> Johannes H. Wilbertz,<sup>1,5,\*</sup> Frank Wippich,<sup>6,\*</sup> Anne Ephrussi,<sup>6,†</sup> Robert H. Singer,<sup>2,3,4,†</sup> Jeffrey A. Chao<sup>1,2,†</sup>

Analysis of single molecules in living cells has provided quantitative insights into the kinetics of fundamental biological processes; however, the dynamics of messenger RNA (mRNA) translation have yet to be addressed. We have developed a fluorescence microscopy technique that reports on the first translation events of individual mRNA molecules. This allowed us to examine the spatiotemporal regulation of translation during normal growth and stress and during *Drosophila* oocyte development. We have shown that mRNAs are not translated in the nucleus but translate within minutes after export, that sequestration within P-bodies regulates translation, and that *oskar* mRNA is not translated until it reaches the posterior pole of the oocyte. This methodology provides a framework for studying initiation of protein synthesis on single mRNAs in living cells.

**D**uring translation, mRNAs are bound by the ribosome. Measurements of ribosome occupancy of mRNAs and protein abundance provide a genome-wide view of translation regulation (1, 2). Fluorescence microscopy complements these global approaches because it allows analysis of gene expression with single-molecule resolution in living cells and provides mechanistic insights obscured by ensemble mea-

surements (3, 4). Imaging methods have been developed that allow newly synthesized proteins to be discerned from the preexisting population or enable actively translating ribosomes to be identified within the cell; however, these approaches are limited by low signal-to-noise ratio and lack the resolution to correlate these events with specific mRNA molecules (5). Here, we describe a single-molecule assay that allows untranslated mRNAs to be distinguished unequivocally from previously translated ones and provides a foundation for investigating the spatiotemporal regulation of translation in living cells.

Because the ribosome or its associated factors must displace endogenous RNA-binding proteins during the first round of translation, we reasoned that it would be possible to construct an RNA biosensor whose fluorescent signal would depend on this process. The orthogonal bacteriophage PP7 and MS2 stem-loops were used to label a transcript within both the coding sequence (PP7) and

the 3' untranslated region (UTR) (MS2) with spectrally distinct fluorescent proteins (6). Simultaneous expression of the PP7 coat protein fused to a nuclear localization sequence (NLS) and green fluorescent protein (NLS-PCP-GFP) and the MS2 coat protein fused to an NLS and red fluorescent protein (NLS-MCP-RFP) resulted in nuclear transcripts labeled with both fluorescent proteins (Fig. 1A). Upon export of the reporter mRNA, the first round of translation displaces NLS-PCP-GFP from the transcript, as the ribosome traverses the coding region that contains the PP7 stem-loops. The NLS limits the concentration of free NLS-PCP-GFP in the cytoplasm, yielding translated mRNAs that are labeled with only NLS-MCP-RFP bound to the stem-loops in the 3' UTR (Fig. 1, A and B). We refer to this technique as translating RNA imaging by coat protein knock-off (TRICK).

Efficient translation of a 6xPP7 stem-loop cassette required optimization of the distance between adjacent stem-loops, stem-loop folding, and codon usage so that they would not block or stall elongation of the ribosome, which might elicit decay of the transcript (7) (Fig. 1C). The polypeptide encoded by the PP7 stem-loops has a molecular mass of ~14 kD and is not homologous to any known protein. Binding of NLS-MCP-RFP to the 3' UTR had no effect on translation, and binding of NLS-PCP-GFP to the PP7 stem-loop cassette in the coding region also did not result in reduced translation of the reporter mRNA (Fig. 1C and fig. S1). Similarly, binding of the fluorescent proteins to the reporter mRNA also did not alter the stability of the transcript (fig. S2).

The TRICK reporter mRNA was expressed in a U-2 OS human osteosarcoma cell line stably expressing NLS-PCP-GFP and NLS-MCP-RFP. Fluorescence-activated cell sorting isolated cells with small amounts of both fluorescent proteins, allowing detection of all reporter mRNAs (figs. S3 and S4). The cells were imaged on a fluorescence microscope equipped with two registered cameras, allowing simultaneous visualization of single mRNA molecules in both channels. In the nucleus, single mRNAs were fluorescently labeled with both red

<sup>1</sup>Friedrich Miescher Institute for Biomedical Research, CH-4058 Basel, Switzerland. <sup>2</sup>Department of Anatomy and Structural Biology, Albert Einstein College of Medicine, Bronx, NY 10461, USA. <sup>3</sup>Gruss-Lipper Biophotonics Center, Albert Einstein College of Medicine, Bronx, NY 10461, USA. <sup>4</sup>Transcription Imaging Consortium, Howard Hughes Medical Institute Janelia Farm Research Campus, Ashburn, VA 20147, USA. <sup>5</sup>University of Basel, CH-4003 Basel, Switzerland. <sup>6</sup>Developmental Biology Unit, European Molecular Biology Laboratory, 69117 Heidelberg, Germany. \*These authors contributed equally to this work. †Corresponding author. E-mail: ephrussi@embl.de (A.E.); robert.singer@einstein.yu.edu (R.H.S.); jeffrey.chao@fmi.ch (J.A.C.)

and green proteins and thus appeared yellow (Fig. 1D). In contrast, almost all of the mRNAs appeared as red particles in the cytoplasm, indicating that only NLS-MCP-RFP was bound (Fig. 1, D and E). Quantification of the steady-state number of yellow mRNAs in the cytoplasm revealed that ~94% of TRICK reporter mRNAs had been translated at least once (Fig. 1, E and H). To confirm that loss of NLS-PCP-GFP from cytoplasmic transcripts was translation-dependent, we induced transcription of the TRICK reporter by ponasterone A (ponA) in the presence of translational inhibitors (8). Adding either cycloheximide, which inhibits elongation, or puromycin, which causes premature termination, for 30 min before induction of TRICK reporter mRNA expression resulted in an increase in the number of untranslated mRNAs in the cytoplasm (Fig. 1, F to H, and movies S1 to S3). Consistent with the imaging, polysome analysis indicated that NLS-PCP-GFP was absent from actively translating mRNAs, whereas NLS-MCP-RFP could be detected within polysomes (fig. S5). This demonstrated that translation of the PP7 stem-loops by the ribosome was required for displacement of the green signal from the mRNA.

Although translation is thought to occur exclusively in the cytoplasm, recent studies suggest that protein synthesis can occur in the nucleus (9, 10). Because the TRICK assay can distinguish between untranslated and translated mRNAs, we imaged TRICK reporter mRNAs in the nucleus 30 min after ponA induction. Single-particle tracking (SPT) of nuclear mRNAs determined that they undergo both corralled ( $D = 0.02 \mu\text{m}^2 \text{s}^{-1}$ ) and random diffusion ( $D = 0.09 \mu\text{m}^2 \text{s}^{-1}$ ), similar to the movements observed for other nuclear mRNAs (11, 12). We found  $91.3 \pm 0.9\%$  of mRNAs labeled with both colors, which is not significantly different from the fraction of double-labeled mRNAs in the cytoplasm of cells treated with translational inhibitors ( $P = 0.75$ , unpaired  $t$  test) (fig. S6, A and B, and movie S4). We cannot, however, exclude the possibility that the fusion protein rebound the PP7 stem-loops immediately after translation. If translation were occurring in the nucleus, addition of small amounts of cycloheximide would increase polysome formation, causing occlusion of the PP7 stem-loops and thereby preventing NLS-PCP-GFP from rebinding (13) (fig. S7A). Similar to experiments in the absence of cycloheximide,  $90.7 \pm 0.6\%$  of nuclear mRNAs were labeled with

both colors when cells were treated with  $1 \mu\text{g ml}^{-1}$  cycloheximide ( $P = 0.44$ , unpaired  $t$  test) (fig. S7, B and C, and movie S5). Although it is possible that nuclear translation could occur for specific mRNAs, this was not observed for the TRICK reporter. These findings are consistent with the previous observation that mRNAs containing premature stop codons are exported before undergoing decay in the cytoplasm (14).

The rapid diffusion of mRNAs in the cytoplasm and photobleaching prevented us from imaging a single mRNA from the time it entered the cytoplasm until it was translated (figs. S8 and S9). Untranslated mRNAs, however, could be detected after export from the nucleus and were observed throughout the cytoplasm (fig. S8). To verify these live-cell observations, we measured the spatial distribution of untranslated reporter mRNAs in fixed cells, using a combined immunofluorescence-fluorescence in situ hybridization (IF-FISH) approach. FISH probes targeted to the MS2 stem-loops allowed detection of all reporter mRNAs, whereas a GFP nanobody was used to identify the untranslated ones (fig. S10, A and B). In agreement with live-cell results, we observed a large percentage of cytoplasmic translated mRNAs (93.7%). As mRNAs

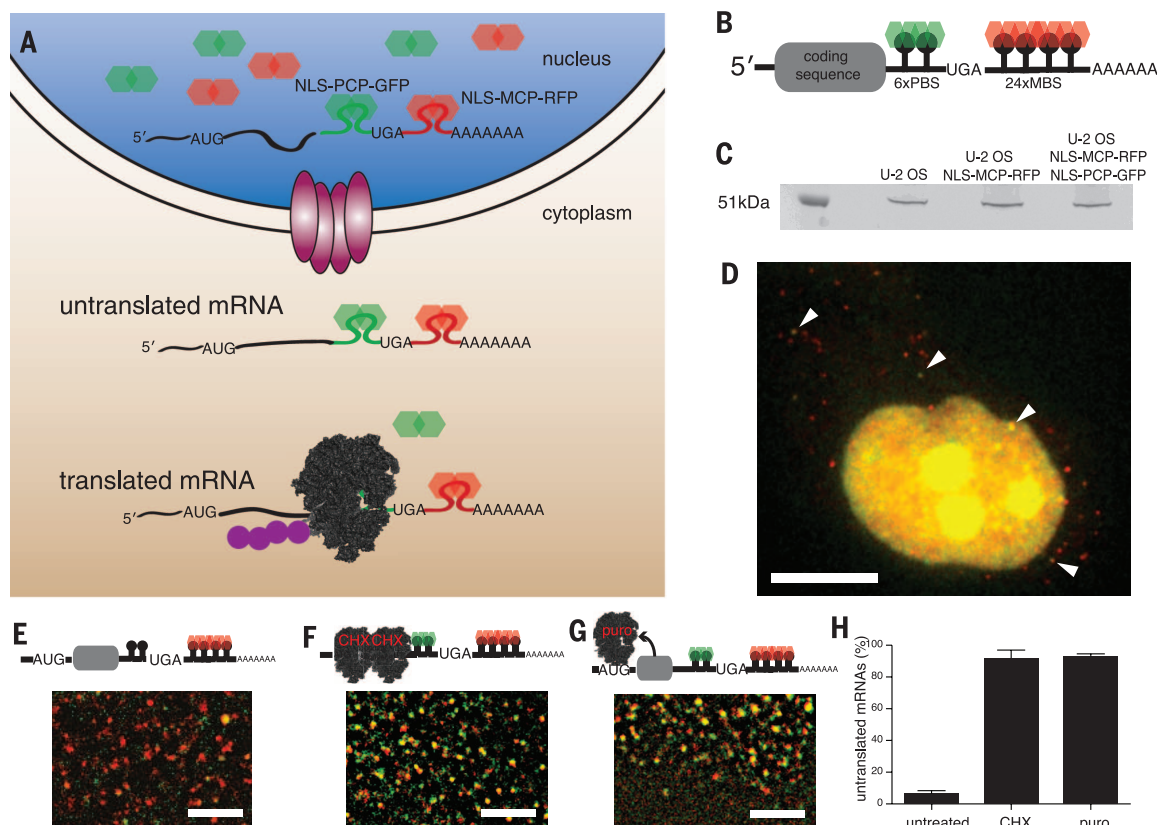


**Fig. 1. Imaging translation of mRNAs in living cells.** (A) Schematic of TRICK assay. (B) Schematic of TRICK reporter transcript. 6xPP7 stem-loops (PBS) inserted in-frame with the C terminus of a protein-coding sequence and 24xMS2 stem-loops (MBS) in the 3' UTR. (C) Expression of TRICK reporter mRNA in U-2 OS cells. The protein encoded by the TRICK reporter (51.4 kDa) is translated in U-2 OS cells, and expression is not affected by NLS-MCP-RFP and NLS-PCP-GFP. (D) U-2 OS cell expressing TRICK reporter. Arrows indicate untranslated nuclear mRNA and three untranslated mRNAs

detected in the cytoplasm. Scale bar, 10  $\mu\text{m}$ . (E) Cytoplasmic region of untreated U-2 OS cells. (F) Addition of cycloheximide ( $100 \mu\text{g ml}^{-1}$ ) and (G) addition of puromycin ( $100 \mu\text{g ml}^{-1}$ ) during ponA induction of TRICK reporter mRNAs. Scale bar (E to G), 2  $\mu\text{m}$ . (H) Percentage of untranslated TRICK mRNAs in U-2 OS cells. In untreated cells,  $5.8 \pm 1.4\%$  of mRNAs colocalize with both NLS-PCP-GFP and NLS-MCP-RFP compared to  $91.0 \pm 3.0\%$  for cycloheximide-treated and  $92.6 \pm 1.0\%$  for puromycin-treated cells.  $n = 5$  cells for each condition.



diffuse away from the nucleus, their chances to collide with the 43S preinitiation complex and become translated increase over time. Indeed, we observed that the fraction of untranslated mRNAs decreased gradually as the distance from the nucleus increased (fig. S10C). Spatial profiles of untranslated mRNAs demonstrated that some mRNAs diffused micrometers away from the nucleus before undergoing translation, indicating that translation does not occur immediately upon export, but occurs minutes after the mRNA has entered the cytoplasm (the time before an mRNA translates should scale as  $L^2/D$ , where  $L \sim 5 \mu\text{m}$  is the radial extent of the untranslated mRNA profile and  $D = 0.02$  to  $0.13 \mu\text{m}^2 \text{s}^{-1}$  is the range of diffusion coefficients; fig. S9). Furthermore, we find no evidence for enrichment or depletion at specific cytosolic locations, suggesting that translation can occur homogeneously throughout the cytoplasm.

We next investigated how stress conditions affect translation. Upon a variety of cellular stresses, signaling pathways inhibit translation through phosphorylation of eukaryotic translation initiation factor 2 $\alpha$  (eIF2 $\alpha$ ), resulting in disassembly of polysomes and formation of cytoplasmic stress granules and processing bodies (P-bodies), cyto-

plasmic organelles whose role in RNA metabolism is not well understood (15, 16). The mRNAs and proteins that constitute these organelles are dynamic and rapidly exchange with the cytosol (17, 18). However, mRNAs containing 5' terminal oligopyrimidine (TOP) motifs accumulate in stress granules upon amino acid starvation, suggesting that certain mRNA classes may be differentially regulated within these compartments (19). To characterize the spatiotemporal regulation of 5' TOP mRNA translation during stress, a tetracycline-inducible HeLa cell line expressing a 5' TOP TRICK reporter mRNA with green (NLS-PCP-GFP) and red (NLS-MCP-Halo; JF<sub>549</sub>) fluorescent proteins required for single-molecule RNA imaging were stressed with arsenite. 5' TOP TRICK mRNAs were detected as single molecules distributed throughout the cytosol or located within stress granules and P-bodies. Only mRNAs sequestered within P-bodies formed large clusters. This association with P-bodies was specific for the 5' TOP TRICK mRNAs because a reporter that lacked the 5' TOP motif did not form multimeric assemblies within these cytoplasmic foci (Fig. 2, A to C).

To address the translational regulation of cytosolic mRNAs and those clustered in P-bodies,

we induced transcription of the 5' TOP TRICK reporter mRNA for a short period before addition of arsenite. This resulted in an increase in the number of untranslated mRNAs in the cytoplasm to be detected compared to unstressed cells, consistent with an inhibition of eIF2.GTP.Met-tRNA<sup>Met</sup> formation (Fig. 2, D and F). The untranslated 5' TOP TRICK reporter mRNAs in the cytoplasm were detected as either single mobile mRNAs or static clusters within P-bodies. Photobleaching of the clustered mRNAs indicated that they were stably associated with P-bodies (fig. S11). Upon removal of arsenite, 5' TOP TRICK mRNAs in the cytosol underwent translation; however, the clustered transcripts retained in P-bodies remained untranslated, indicating that these cellular structures can provide a distinct level of regulation (Fig. 2, E and F, and movies S6 to S7).

Messenger ribonucleoprotein (mRNP) granules form not only during cellular stress, but also as part of normal regulatory pathways. In *Drosophila*, localized expression of Oskar protein at the posterior pole of the oocyte is essential for correct body patterning and germ cell formation (20). Precise spatiotemporal translational regulation is crucial during long-range transport of *oskar* mRNA (*osk*) from the nurse cells, where the mRNA

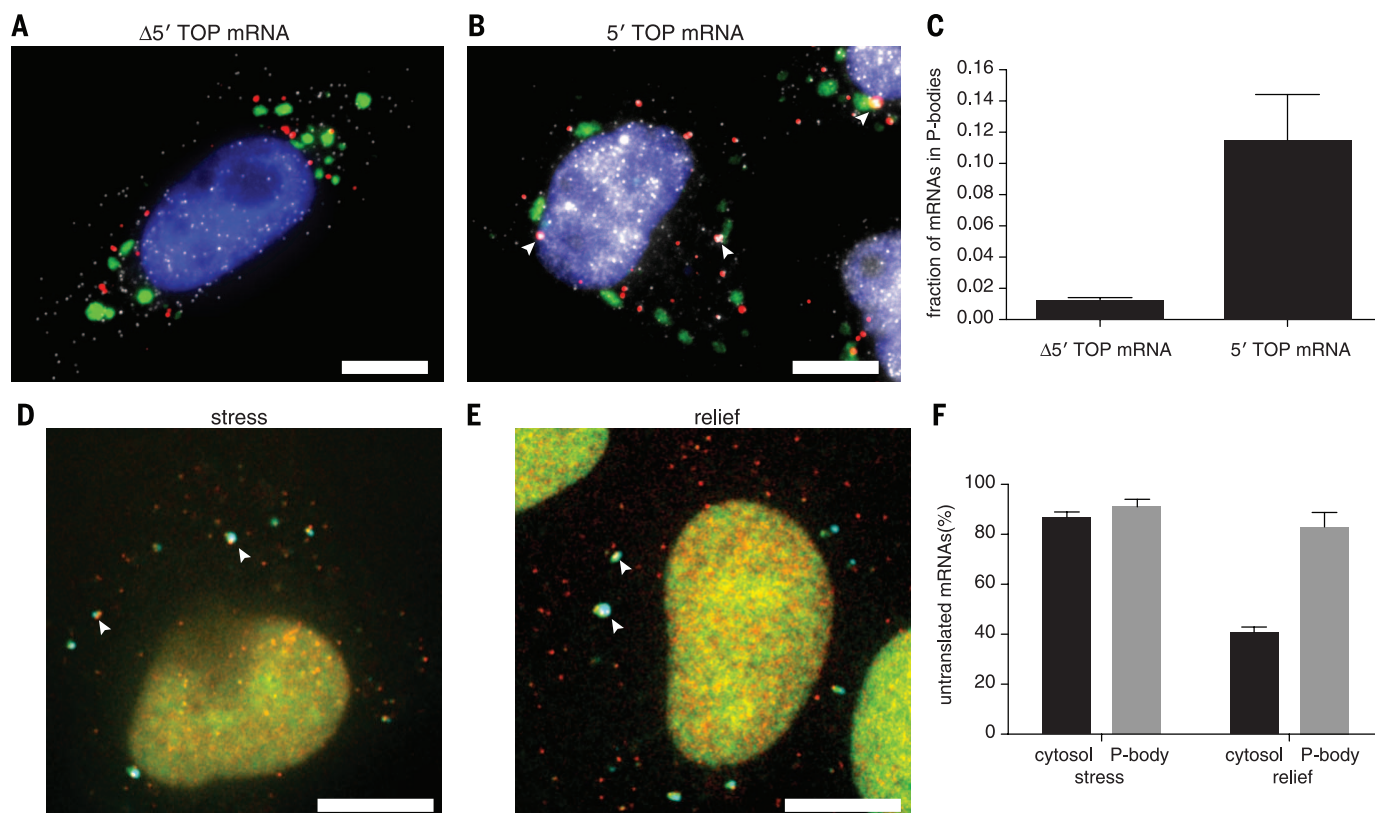


**Fig. 2. P-bodies are sites of translation regulation during stress in HeLa cells.** (A and B) IF-FISH of cells expressing  $\Delta 5'$  TOP TRICK reporter mRNA [(A), gray] or 5' TOP TRICK reporter mRNA [(B), gray] during arsenite stress (0.5 mM) contain stress granules (TIAR, green) and P-bodies (DDX6, red). Arrows: mRNA clusters in P-bodies. (C) Fraction of cytoplasmic  $\Delta 5'$  TOP ( $n = 19$  cells) and 5' TOP ( $n = 17$  cells) mRNAs located within P-bodies after 60 min of arsenite (0.5 mM) stress ( $P = 0.0009$ , unpaired  $t$  test). (D and E) Live-cell image of 5' TOP TRICK reporter mRNA during arsenite stress (D) and relief of

stress (E). In stressed cells, mRNAs (red, green) in cytosol and P-bodies (cyan) are untranslated. In relieved cells, many mRNAs (red, green) in cytosol have been translated whereas mRNAs retained in P-bodies (cyan) remain untranslated. Arrow: clustered mRNAs. Scale bar (A, B, D, E), 10  $\mu\text{m}$ . (F) Percentage of untranslated mRNAs (cytosol and P-bodies) during stress ( $n = 9$  cells) and relief of stress ( $n = 10$  cells). Upon relief of stress, 5' TOP mRNAs in P-bodies are not translated ( $P = 0.31$ , unpaired  $t$  test); mRNAs in the cytosol have undergone translation ( $P < 0.0001$ , unpaired  $t$  test).

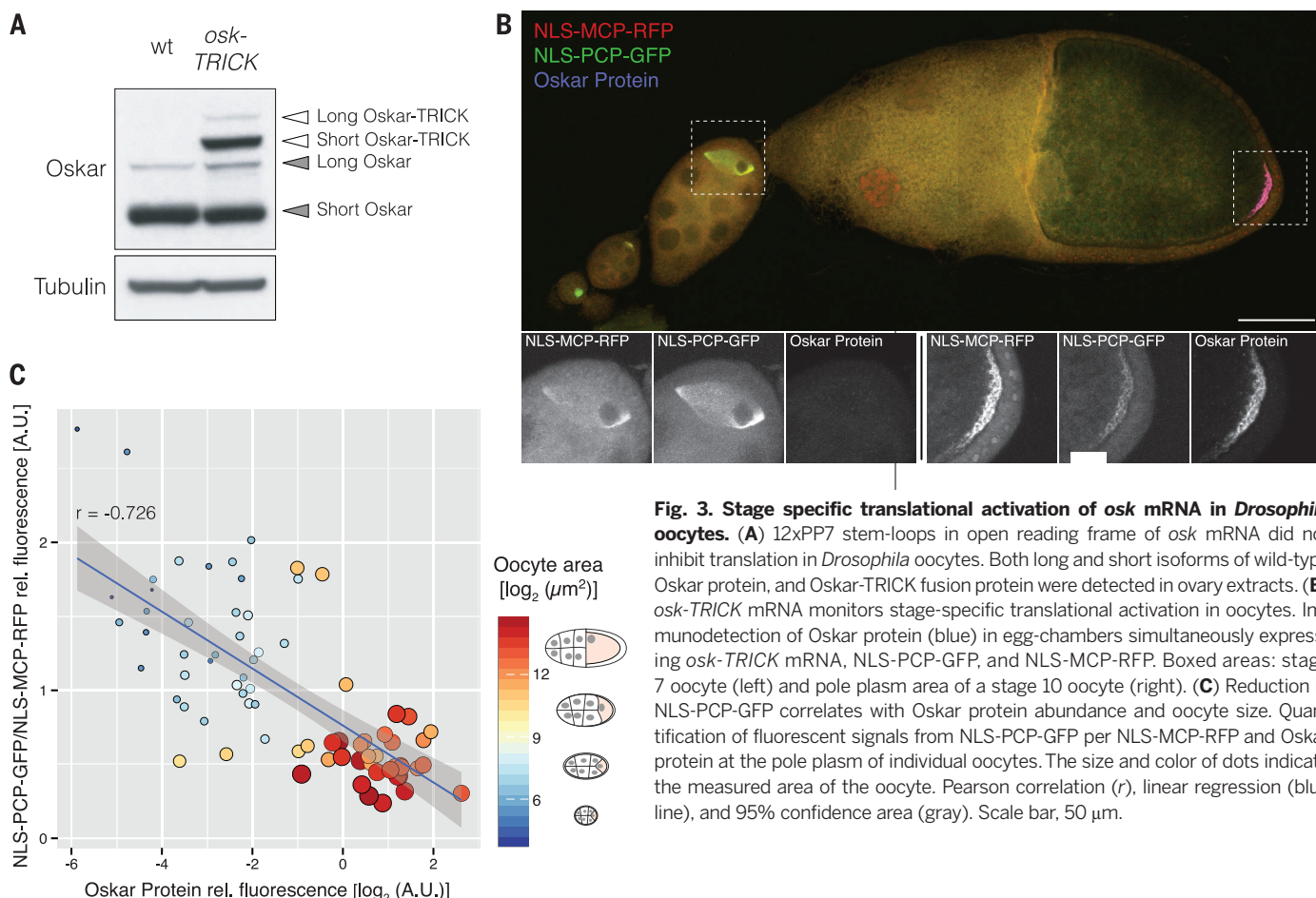


**Fig. 3. Stage specific translational activation of *osk* mRNA in *Drosophila* oocytes.** (A) 12xPP7 stem-loops in open reading frame of *osk* mRNA did not inhibit translation in *Drosophila* oocytes. Both long and short isoforms of wild-type Oskar protein, and Oskar-TRICK fusion protein were detected in ovary extracts. (B) *osk-TRICK* mRNA monitors stage-specific translational activation in oocytes. Immunodetection of Oskar protein (blue) in egg-chambers simultaneously expressing *osk-TRICK* mRNA, NLS-PCP-GFP, and NLS-MCP-RFP. Boxed areas: stage 7 oocyte (left) and pole plasm area of a stage 10 oocyte (right). (C) Reduction in NLS-PCP-GFP correlates with Oskar protein abundance and oocyte size. Quantification of fluorescent signals from NLS-PCP-GFP per NLS-MCP-RFP and Oskar protein at the pole plasm of individual oocytes. The size and color of dots indicate the measured area of the oocyte. Pearson correlation ( $r$ ), linear regression (blue line), and 95% confidence area (gray). Scale bar, 50 μm.

is transcribed, to the posterior pole of the oocyte, where Oskar protein first appears during mid-oogenesis (stage 9) (21, 22). Additional mechanisms ensure degradation of ectopically expressed Oskar protein; hence, absence of the protein does not indicate lack of translation of its mRNA (23).

To monitor translation, we generated an *osk-TRICK* reporter mRNA by placing 12xPP7 stem-loops within the coding region of a construct that contained 6xMS2 stem-loops in the 3' UTR (fig. S12) (24). Introducing 12xPP7 stem-loops into the open reading frame of *osk* mRNA did not inhibit translation of the reporter transcript, and the fusion protein was expressed at levels comparable to that of the wild-type protein (Fig. 3A). In early-stage oocytes of flies coexpressing *osk-TRICK* mRNA, NLS-MCP-RFP, and NLS-PCP-GFP, *osk-TRICK* mRNA was labeled by both NLS-PCP-GFP and NLS-MCP-RFP, indicating translational repression consistent with the absence of Oskar protein (Fig. 3B). In later stages, the NLS-PCP-GFP fluorescent signal was reduced at the posterior pole and Oskar protein was detected by immunofluorescence, consistent with translation of a portion of the transcripts (Fig. 3, B and C). This methodology provides a framework for analyzing the cascade of regulatory mechanisms required for local translation during *Drosophila* development. It will also be informative in neurons where regulation of the first round of translation has been

shown to be important for local protein synthesis in axons and dendrites (25, 26).

This methodology pinpoints the precise time and place of the first translation event of single mRNA molecules. It reveals the translation control of mRNAs sequestered within cytoplasmic organelles or when and where the translation of a key cell fate determinant occurs in an organism undergoing development. The kinetics of translational regulation can now be coupled with single-molecule imaging of proteins to provide insights into mechanisms of regulation that were previously unapproachable by ensemble biochemical or genetic approaches (27). Observing regulation of mRNA translation in single living cells will lead to a better understanding of disease mechanisms.

#### REFERENCES AND NOTES

1. N. T. Ingolia, S. Ghaemmaghami, J. R. Newman, J. S. Weissman, *Science* **324**, 218–223 (2009).
2. B. Schwahnhauser et al., *Nature* **473**, 337–342 (2011).
3. D. R. Larson, D. Zenklusen, B. Wu, J. A. Chao, R. H. Singer, *Nat. Methods* **332**, 475–478 (2011).
4. A. Raj, A. van Oudenaarden, *Annu. Rev. Biophys.* **38**, 255–270 (2009).
5. J. A. Chao, Y. J. Yoon, R. H. Singer, *Cold Spring Harb. Perspect. Biol.* **4**, a012310 (2012).
6. S. Hocine, P. Raymond, D. Zenklusen, J. A. Chao, R. H. Singer, *Nat. Methods* **10**, 119–121 (2013).
7. M. K. Doma, R. Parker, *Nature* **440**, 561–564 (2006).
8. D. No, T. P. Yao, R. M. Evans, *Proc. Natl. Acad. Sci. U.S.A.* **93**, 3346–3351 (1996).
9. K. Al-Jubran et al., *RNA* **19**, 1669–1683 (2013).

10. A. David et al., *J. Cell Biol.* **197**, 45–57 (2012).
11. Y. Shav-Tal et al., *Science* **304**, 1797–1800 (2004).
12. A. Mor et al., *Nat. Cell Biol.* **12**, 543–552 (2010).
13. C. P. Stanners, *Biochem. Biophys. Res. Commun.* **24**, 758–764 (1966).
14. T. Trcek, H. Sato, R. H. Singer, L. E. Maquat, *Genes Dev.* **27**, 541–551 (2013).
15. J. R. Buchan, R. Parker, *Mol. Cell* **36**, 932–941 (2009).
16. N. Kedersha, P. Ivanov, P. Anderson, *Trends Biochem. Sci.* **38**, 494–506 (2013).
17. N. Kedersha et al., *J. Cell Biol.* **169**, 871–884 (2005).
18. S. Mollet et al., *Mol. Biol. Cell* **19**, 4469–4479 (2008).
19. C. K. Damgaard, J. Lykke-Andersen, *Genes Dev.* **25**, 2057–2068 (2011).
20. A. Ephrussi, R. Lehmann, *Nature* **358**, 387–392 (1992).
21. J. Kim-Ha, K. Kerr, P. M. Macdonald, *Cell* **81**, 403–412 (1995).
22. F. H. Markussen, A. M. Michon, W. Breitwieser, A. Ephrussi, *Development* **121**, 3723–3732 (1995).
23. E. Morais-de-Sá, A. Vega-Rioja, V. Trovisco, D. St Johnston, *Dev. Cell* **26**, 303–314 (2013).
24. M. D. Lin et al., *Dev. Biol.* **322**, 276–288 (2008).
25. D. Colak, S. J. Ji, B. T. Porse, S. R. Jaffrey, *Cell* **153**, 1252–1265 (2013).
26. C. Giorgi et al., *Cell* **130**, 179–191 (2007).
27. M. E. Tanenbaum, L. A. Gilbert, L. S. Qi, J. S. Weissman, R. D. Vale, *Cell* **159**, 635–646 (2014).

#### ACKNOWLEDGMENTS

This work was supported by the Novartis Research Foundation (J.A.C.); NIH grants NS83085, EB013571, and GM57071 (R.H.S.); Howard Hughes Medical Institute (R.H.S. and T.L.); European Molecular Biology Laboratory (EMBL) (A.E.); and a postdoctoral fellowship from the EMBL Interdisciplinary Postdoc Program (EIPD) under Marie Curie COFUND actions (F.W.). We thank C. Damgaard (University of Aarhus) for providing the rpl32-



$\beta$ -globin plasmid; S. Shenoy (Albert Einstein College of Medicine), L. Gelman and S. Bourke (Friedrich Miescher Institute), and EMBL Advanced Light Microscopy Facility for microscopy support; D. Ciepielewski (Nikon) for providing access to NIS tracking software; C. Eliscovich (Albert Einstein College of Medicine) for advice on IF-FISH; L. Lavis (Janelia Farm) for providing JF<sub>549</sub> dye; M. Beal (Biosearch Technologies) for Stellaris FISH probes;

A. Arnold (FMI) for assistance with polysome analysis; I. Gáspár (EMBL) for pHsp83 vector; and S. Chao, U. Meier, and J. Warner for helpful discussions.

#### SUPPLEMENTARY MATERIALS

www.sciencemag.org/content/347/6228/1367/suppl/DC1  
Materials and Methods

Figs. S1 to S12  
Movies S1 to S7  
References (28–37)

20 November 2014; accepted 6 February 2015  
10.1126/science.aaa3380

## RNA BIOCHEMISTRY

# Determination of in vivo target search kinetics of regulatory noncoding RNA

Jingyi Fei,<sup>1</sup> Digvijay Singh,<sup>2</sup> Qiucen Zhang,<sup>1</sup> Seongjin Park,<sup>1</sup> Divya Balasubramanian,<sup>3</sup> Ido Golding,<sup>1,4</sup> Carin K. Vanderpool,<sup>3\*</sup> Taekjip Ha<sup>1,2,5,6\*</sup>

Base-pairing interactions between nucleic acids mediate target recognition in many biological processes. We developed a super-resolution imaging and modeling platform that enabled the in vivo determination of base pairing–mediated target recognition kinetics. We examined a stress-induced bacterial small RNA, SgrS, which induces the degradation of target messenger RNAs (mRNAs). SgrS binds to a primary target mRNA in a reversible and dynamic fashion, and formation of SgrS-mRNA complexes is rate-limiting, dictating the overall regulation efficiency in vivo. Examination of a secondary target indicated that differences in the target search kinetics contribute to setting the regulation priority among different target mRNAs. This super-resolution imaging and analysis approach provides a conceptual framework that can be generalized to other small RNA systems and other target search processes.

Base-pairing interactions between nucleic acids constitute a large category of target recognition processes such as noncoding RNA-based gene regulation [e.g., microRNAs (1) and long noncoding RNAs (2) in eukaryotes and small RNAs (sRNAs) in bacteria (3)], bacterial adaptive immunity [e.g., the clustered regularly interspaced short palindromic repeat (CRISPR) system (4)], and homologous recombination (5). Although target search kinetics by transcription factors has been studied in vivo (6), the rate constants for target identification via base-pairing interactions in vivo are not known for any system. Here, we developed a super-resolution imaging and analysis platform to assess the kinetics of base-pairing interaction-mediated target recognition for a bacterial sRNA, SgrS. SgrS is produced upon sugar-phosphate stress, and its function is dependent on an RNA chaperone protein Hfq. SgrS regulates several target mRNAs posttranscriptionally through base-pairing interactions that affect mRNA translation and stability (7). We combined single-molecule fluorescence in situ hybridization (smFISH) (8) with single-molecule localization-based super-resolution microscopy (9) to count RNAs and obtain infor-

mation on subcellular localization. High spatial resolution is required for accurate quantification of the high-copy-number RNAs and sRNA-mRNA complexes. Here, simultaneous measurements of sRNA, mRNA, and sRNA-mRNA complexes together with mathematical modeling allow determination of key parameters describing sRNA target search and downstream codegradation of sRNA-mRNA complexes.

We first studied the kinetic properties of SgrS regulation of *ptsG* mRNA, encoding a primary glucose transporter. SgrS binds within the 5' untranslated region (UTR) of *ptsG* mRNA, blocks its translation, and induces its degradation (10). We induced stress and SgrS production in *Escherichia coli* strains derived from wild-type MG1655 (table S1) using a nonmetabolizable sugar analog,  $\alpha$ -methyl glucoside ( $\alpha$ MG) (10, 11). Fractions of cell culture were taken at different time points after induction and fixed (12). Oligonucleotide probes (table S2) labeled with photo-switchable dyes, Alexa 647 and Alexa 568, were used to detect SgrS (9 probes) and *ptsG* mRNA (28 probes), respectively, using smFISH (8). We then imaged the cells using two-color three-dimensional (3D) super-resolution microscopy (9, 12) (Fig. 1A; compare to diffraction limited images in Fig. 1B).

In the wild-type strain (table S1), we observed production of SgrS and corresponding reduction of *ptsG* mRNA over a few minutes (Fig. 1A), consistent with SgrS-mediated degradation of *ptsG* mRNA (10). In a strain producing an SgrS that does not base pair with *ptsG* mRNA due to mutations in the seed region (13, 14) and in an Hfq deletion ( $\Delta$ hfq) strain (table S1), *ptsG* mRNA re-

duction was not observed (figs. S1 and S2). To quantify the copy number of RNAs in each cell, we employed a density-based clustering algorithm to map single-molecule localization signal to individual clusters corresponding to individual RNAs (12, 15, 16) (Fig. 1C and movies S1 and S2). The absolute copy number quantification was validated by quantitative polymerase chain reaction (qPCR) (12) (Fig. 1D).

We next built a kinetic model containing the following kinetic steps: transcription of SgrS (with rate constant  $\alpha_s$ ) and *ptsG* ( $\alpha_p$ ), endogenous degradation of *ptsG* mRNA (with rate constant  $\beta_p$ ), degradation of SgrS in the absence of codegradation with *ptsG* mRNA ( $\beta_{s,p}$ ), binding of SgrS to *ptsG* mRNA (with rate constant  $k_{on}$ ), dissociation of SgrS from *ptsG* mRNA ( $k_{off}$ ), and ribonuclease E (RNase E)–mediated codegradation of SgrS-*ptsG* mRNA complex ( $k_{cat}$ ) (Fig. 1E). We independently measured  $\beta_p$  and the total SgrS degradation rate, including endogenous and mRNA-coupled degradation [table S4, fig. S3, and supplementary materials section 1.9 (SM 1.9)]. Because *ptsG* mRNA levels remained constant in the absence of SgrS-mediated degradation, as observed in the base-pairing mutant strain (fig. S1), we determined  $\alpha_p$  as the product of  $\beta_p$  and *ptsG* mRNA concentration before SgrS induction (table S4 and SM 1.10).

To determine  $k_{on}$  and  $k_{off}$ , it is necessary to count the SgrS-*ptsG* mRNA complexes. Colocalization of *ptsG* mRNA and SgrS at the 40-nm resolution was rarely observed in the wild-type strain (up to ~5%, similar to ~3% colocalization by chance, estimated using the base-pairing mutant as a negative control) (Fig. 2). This is possibly because SgrS regulates several other target mRNAs (7) and/or the SgrS-*ptsG* mRNA complex may be unstable due to rapid codegradation or disassembly. In an RNase E mutant strain, in which codegradation is blocked (17, 18) (table S1), *ptsG* mRNA levels stayed the same as SgrS levels increased (fig. S4) (17, 18), and a fraction of *ptsG* mRNA colocalized with SgrS, increasing over time to reach ~15% (Fig. 2 and fig. S5). A positive control using *ptsG* mRNA simultaneously labeled with two colors (Fig. 2 and SM 1.8) showed a high degree of colocalization (~70%), similar to the reported detection efficiency of colocalization by super-resolution imaging (19).

We then applied these measured parameters ( $\alpha_p$  and  $\beta_p$ ), used total SgrS degradation rate as a constraint for  $\beta_{s,p}$ , determined the remaining parameters ( $\alpha_s$ ,  $\beta_{s,p}$ ,  $k_{on}$ ,  $k_{off}$ , and  $k_{cat}$ ) by fitting equations (Fig. 1E) to the six time-course changes of SgrS, *ptsG* mRNA, and SgrS-*ptsG* mRNA complex in both the wild-type and the RNase E mutant strains (Fig. 3A, table S4, and SM 1.10). We further validated the model by changing

<sup>1</sup>Center for the Physics of Living Cells, Department of Physics, University of Illinois, Urbana, IL, USA. <sup>2</sup>Center for Biophysics and Computational Biology, University of Illinois, Urbana, IL, USA.

<sup>3</sup>Department of Microbiology, University of Illinois, Urbana, IL, USA. <sup>4</sup>Verna and Marrs McLean Department of Biochemistry and Molecular Biology, Baylor College of Medicine, Houston, TX, USA. <sup>5</sup>Carl R. Woese Institute for Genomic Biology, Howard Hughes Medical Institute, Urbana, IL, USA. <sup>6</sup>Howard Hughes Medical Institute, Urbana, IL, USA.

\*Corresponding author. E-mail: tjha@illinois.edu (T.H.); cvanderp@life.uiuc.edu (C.K.V.)

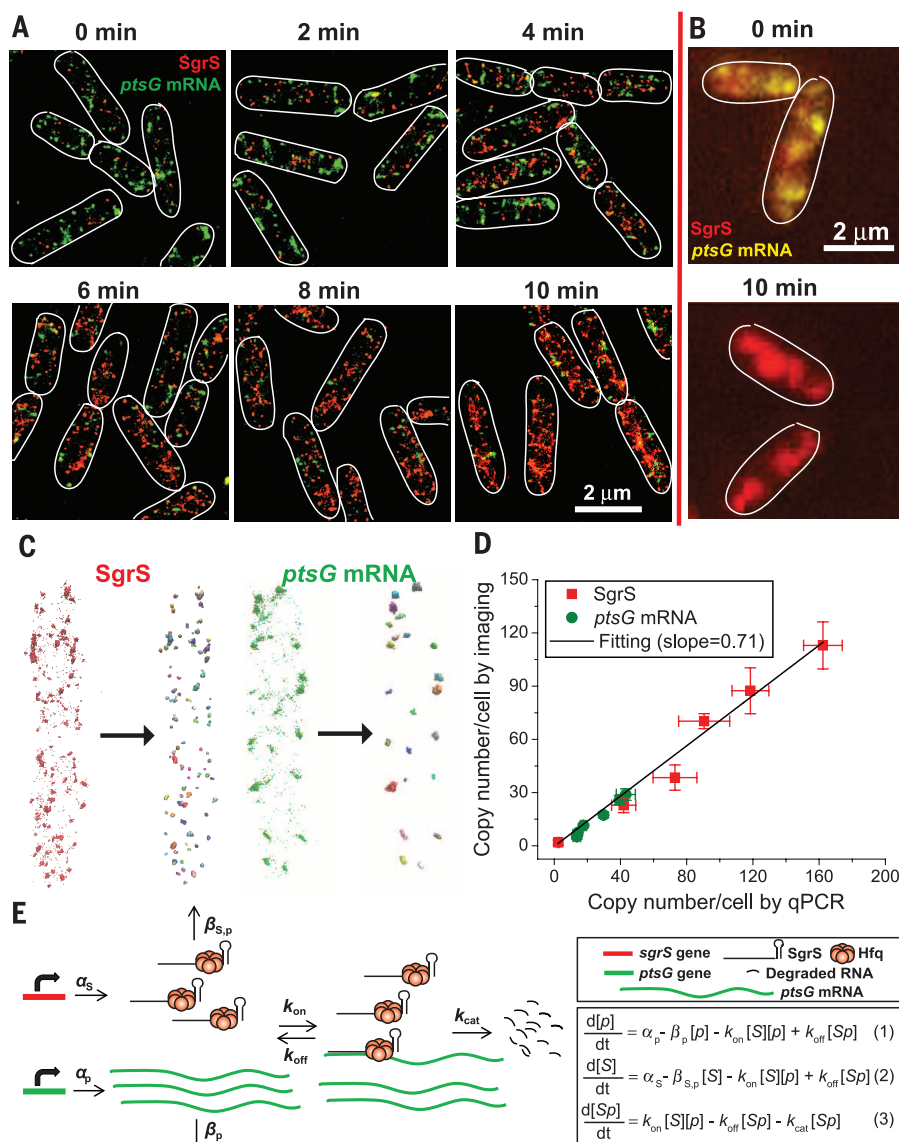


**Fig. 1. Super-resolution imaging and analysis.** (A) 3D Super-resolution images of SgrS and *ptsG* mRNA labeled by smFISH projected in 2D planes. (B) Diffraction-limited fluorescent images of SgrS and *ptsG* mRNA. Cell boundaries imaged by differential interference contrast in (A) and (B) are depicted by white solid lines. (C) Examples of clustering analysis with comparison of raw data (left) and clustered data (right). (D) Comparison of average RNA copy number per cell measured by super-resolution imaging and qPCR. (E) Kinetic scheme of SgrS-induced *ptsG* mRNA degradation. Kinetic steps are described in the main text.  $[p]$ ,  $[S]$ , and  $[Sp]$  are the concentrations of *ptsG* mRNA, SgrS, and their complex, respectively, in the mass-action equations.

experimental conditions to vary only the transcription rates of SgrS (with lower  $\alpha_{MG}$  concentration) and/or *ptsG* mRNA (in the absence of glucose in the growth media), and the model could account for the data with the same set of  $k_{on}$ ,  $k_{off}$ , and  $k_{cat}$  values (table S4, figs. S6 to S8, and SM 2.2).

We can now quantitatively examine the effect of Hfq, which functions by stabilizing the sRNA or promoting its annealing with the target mRNA (20). In the  $\Delta hfq$  strain, the degradation rate of SgrS increased by a factor of 20, whereas the SgrS-*ptsG* mRNA association rate decreased slightly (table S4, figs. S1 and S8, and SM 2.2). Therefore, for the SgrS-*ptsG* mRNA pair, the primary effect of Hfq in regulation kinetics is in SgrS stabilization.

This in vivo determination of base pairing-mediated target search kinetics revealed two important characteristics of SgrS-mediated *ptsG* mRNA degradation. First, the target search process is characterized by slow association [ $k_{on} = (2.0 \pm 0.2) \times 10^5 \text{ M}^{-1} \text{ s}^{-1}$ ] and fast dissociation ( $k_{off} = 0.20 \pm 0.04 \text{ s}^{-1}$ ), resulting in a dissociation constant ( $K_D = k_{off}/k_{on}$ ) of  $1.0 \pm 0.2 \text{ } \mu\text{M}$  (Fig. 3B and SM 1.11). To get a comparable apparent association rate,  $k_{a,app}$  ( $k_{on} \times [S]$ ), and  $k_{off}$  about one thousand SgrS molecules per cell need to be produced. The large  $K_D$  explains the need for excessive production of sRNA molecules to enable rapid regulation when cells experience high levels of stress. Despite the crowded cellular environment and large excess of non-target RNA molecules, the  $k_{on}$  is

within the wide range of Hfq-mediated sRNA and target mRNA association rates reported by in vitro measurements. In contrast,  $k_{off}$  is 1 to 2 orders of magnitude larger than in vitro estimates (21–23). The large  $K_D$  for target search in vivo is likely due to the limited availability of key players in the cell. For example, Hfq was suggested to be limited in the cell due to the dynamic competition for Hfq among different sRNAs (24, 25). Second,  $k_{cat}$  and  $k_{off}$  are comparable such that both codegradation and dissociation can occur with similar probabilities upon target binding. Disallowing dissociation by setting  $k_{off}$  to zero cannot explain our experimental data (fig. S9 and SM 2.1). The observed fast  $k_{cat}$  ( $0.4 \pm 0.1 \text{ s}^{-1}$ ) may be due to the formation of a ribonucleoprotein complex comprised of SgrS, Hfq, and RNase E, as suggested by biochemical studies (18); if so, once SgrS-Hfq-RNase E binds the *ptsG* mRNA, RNase E would be readily available for codegradation.

The kinetic model suggests that the overall rate of *ptsG* mRNA degradation is limited by its association with SgrS: At early time points after SgrS induction, when the copy number of SgrS is on the order of tens per cell,  $k_{a,app}$  is about two orders of magnitude smaller than the codegradation rate  $k_{cat}$ . The nonhomogenous spatial distribution of the sRNA and its target mRNA may also contribute to the slow target search. We observed membrane localization of *ptsG* mRNA, whereas SgrS is primarily localized in the cytoplasm (fig. S10). Further modeling incorporating the spatial information and stochastic gene expression may improve the kinetic analysis.

Regulation prioritization among multiple targets by one sRNA was suggested by computational modeling (26, 27) and experimental observation (28). However, how the kinetic prioritization is achieved remains to be elucidated. We propose that the combination of  $k_{on}$ ,  $k_{off}$ , and  $k_{cat}$  is characteristic of a specific sRNA-mRNA pair and determines the regulatory outcome.  $k_{cat}$  may reflect the regulatory mode (codegradation versus translation repression) and target search kinetics ( $k_{on}$  and  $k_{off}$ ) could contribute to the regulatory specificity and priority among many targets. To investigate this possibility, we examined *manXYZ* mRNA, which encodes a general sugar transporter for mannose and glucose and is also negatively regulated by SgrS. Compared with *ptsG*, *manXYZ* mRNA showed slower degradation kinetics (28) (figs. S11 to S13). The prioritization of *ptsG* over *manXYZ* by SgrS is consistent with the observation that SgrS regulation of *ptsG* (but not *manXYZ*) is absolutely essential for continued cell growth under most stress conditions (29). Using the RNase E mutant strain, we found that formation of SgrS-*manXYZ* mRNA complexes is slower than SgrS-*ptsG* mRNA complex formation (fig. S13C). The  $K_D$  for SgrS binding to *manXYZ* mRNA,  $2.3 \pm 0.2 \text{ } \mu\text{M}$ , was also higher than  $1.0 \pm 0.2 \text{ } \mu\text{M}$  for SgrS binding to *ptsG* mRNA (Fig. 3B and SM 1.11). This result indicates that the slower regulation kinetics observed for *manXYZ* may, at least partially, originate from the differences in target search kinetics.





**Fig. 2. Colocalization analysis of SgrS-ptsG complex.** (A) Example of colocalization under various conditions. (B) Quantification of colocalized fraction of *ptsG* mRNA in cases (ii), (iii) (at 10 min after SgrS induction), and (iv) (at 10 min after SgrS induction). Error bars are standard deviations from three to eight images. (C) Time-course changes in the fraction of colocalized *ptsG* mRNA with SgrS. Error bars are standard errors from 200 to 600 cells from two independent measurements.

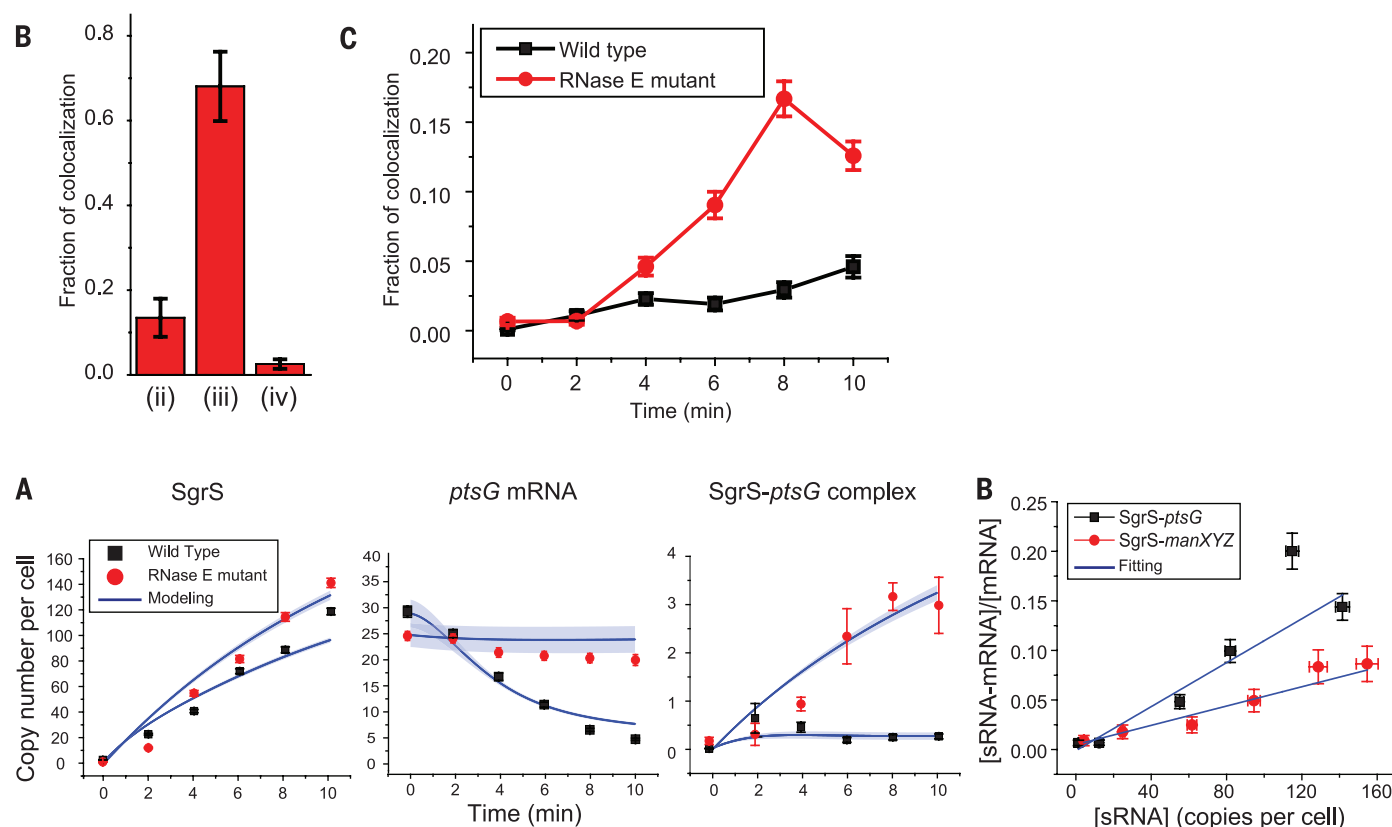


**Fig. 3. Estimation of kinetic parameters.** (A) Modeling of time-course changes of SgrS, *ptsG* mRNA, and SgrS-ptsG complexes. Average copy numbers per cell are plotted as a function of time. Rate constants and weighted  $R^2$  for modeling are reported in tables S4 and S5. (B) Extraction of  $K_D$  for SgrS-mRNA complex formation. The ratio of mRNA in complex with SgrS to free mRNA is plotted against average SgrS copy number and the slope of the linear fitting reports  $1/K_D$ . Error bars in (A) and (B) report standard errors from 200 to 600 cells from two independent measurements.

Overall, our results indicate that the formation of sRNA-mRNA complexes is reversible and highly dynamic in the cell, providing additional layers for regulating individual targets. Our kinetic model highlights the importance of target search kinetics on regulation prioritization. This super-resolution imaging and analysis platform provides a conceptual framework that can be generalized to other sRNA systems and potentially to other target search processes.

#### REFERENCES AND NOTES

- A. M. Gurtan, P. A. Sharp, *J. Mol. Biol.* **425**, 3582–3600 (2013).
- S. Geisler, J. Collier, *Nat. Rev. Mol. Cell Biol.* **14**, 699–712 (2013).
- G. Storz, J. Vogel, K. M. Wassarman, *Mol. Cell* **43**, 880–891 (2011).
- B. Wiedenheft, S. H. Sternberg, J. A. Doudna, *Nature* **482**, 331–338 (2012).
- A. Malkova, G. Ira, *Curr. Opin. Genet. Dev.* **23**, 271–279 (2013).
- J. Elf, G. W. Li, X. S. Xie, *Science* **316**, 1191–1194 (2007).
- M. Bobrovskyy, C. K. Vanderpool, *Annu. Rev. Genet.* **47**, 209–232 (2013).
- A. Raj, P. van den Bogaard, S. A. Rifkin, A. van Oudenaarden, S. Tyagi, *Nat. Methods* **5**, 877–879 (2008).
- B. Huang, S. A. Jones, B. Brandenburg, X. Zhuang, *Nat. Methods* **5**, 1047–1052 (2008).
- C. K. Vanderpool, S. Gottesman, *Mol. Microbiol.* **54**, 1076–1089 (2004).
- K. Kimata, Y. Tanaka, T. Inada, H. Aiba, *EMBO J.* **20**, 3587–3595 (2001).
- Materials and methods are available as supplementary materials on Science Online.
- H. Kawamoto, Y. Koide, T. Morita, H. Aiba, *Mol. Microbiol.* **61**, 1013–1022 (2006).
- C. S. Wadler, C. K. Vanderpool, *Nucleic Acids Res.* **37**, 5477–5485 (2009).
- M. Ester, H. Kriegl, J. Sander, X. Xu, in *Proceedings of the Second International Conference on Knowledge Discovery and Data Mining*, Portland, Oregon (Association for the Advancement of Artificial Intelligence, Palo Alto, CA, 1996), pp. 226–231.
- M. Daszykowski, B. Walczak, D. L. Massart, *Chemom. Intell. Lab. Syst.* **56**, 83–92 (2001).
- T. Morita, H. Kawamoto, T. Mizota, T. Inada, H. Aiba, *Mol. Microbiol.* **54**, 1063–1075 (2004).
- T. Morita, K. Maki, H. Aiba, *Genes Dev.* **19**, 2176–2186 (2005).
- E. Lubeck, L. Cai, *Nat. Methods* **9**, 743–748 (2012).
- J. Vogel, B. F. Luisi, *Nat. Rev. Microbiol.* **9**, 578–589 (2011).
- V. Arluison et al., *Nucleic Acids Res.* **35**, 999–1006 (2007).
- W. Hwang, V. Arluison, S. Hohng, *Nucleic Acids Res.* **39**, 5131–5139 (2011).
- T. J. Soper, S. A. Woodson, *RNA* **14**, 1907–1917 (2008).
- A. Fender, J. Elf, K. Hampel, B. Zimmermann, E. G. Wagner, *Genes Dev.* **24**, 2621–2626 (2010).
- R. Hussein, H. N. Lim, *Proc. Natl. Acad. Sci. U.S.A.* **108**, 1110–1115 (2011).
- E. Levine, Z. Zhang, T. Kuhlman, T. Hwa, *PLOS Biol.* **5**, e229 (2007).
- D. Jost, A. Nowojewski, E. Levine, *Biophys. J.* **104**, 1773–1782 (2013).
- J. B. Rice, C. K. Vanderpool, *Nucleic Acids Res.* **39**, 3806–3819 (2011).
- Y. Sun, C. K. Vanderpool, *J. Bacteriol.* **195**, 4804–4815 (2013).

## ACKNOWLEDGMENTS

We thank L. A. Sepulveda, L. H. So, M. Bates, X. Zhuang, Y. Liu, J. E. Stone, K. Schulten, H. Aiba, Z. Luthy-Schulten, T. E. Kuhlman, Y. Wang, and T. Lu for discussion, reagents, and software (12). This work was supported by grants from the National Science Foundation (PHY 082265 and PHY 1147498), the National Institutes of Health (GM 112659, GM065367, GM082837, and

GM092830), the Welch Foundation (Q-1759), and the Jane Coffin Childs Memorial Fund for Medical Research.

## SUPPLEMENTARY MATERIALS

www.sciencemag.org/content/347/6228/1371/suppl/DC1  
Materials and Methods  
Supplementary Text

Figs. S1 to S18  
Tables S1 to S5  
Movies S1 to S3  
References (30–54)

16 July 2014; accepted 16 January 2015  
10.1126/science.1258849

## STEM CELL AGING

# A mitochondrial UPR-mediated metabolic checkpoint regulates hematopoietic stem cell aging

Mary Mohrin,<sup>1\*</sup> Jiyung Shin,<sup>1\*</sup> Yufei Liu,<sup>2\*</sup> Katharine Brown,<sup>1\*</sup> Hanzhi Luo,<sup>1</sup> Yannan Xi,<sup>1</sup> Cole M. Haynes,<sup>3,4</sup> Danica Chen<sup>1†</sup>

Deterioration of adult stem cells accounts for much of aging-associated compromised tissue maintenance. How stem cells maintain metabolic homeostasis remains elusive. Here, we identified a regulatory branch of the mitochondrial unfolded protein response (UPR<sup>mt</sup>), which is mediated by the interplay of SIRT7 and NRF1 and is coupled to cellular energy metabolism and proliferation. SIRT7 inactivation caused reduced quiescence, increased mitochondrial protein folding stress (PFS<sup>mt</sup>), and compromised regenerative capacity of hematopoietic stem cells (HSCs). SIRT7 expression was reduced in aged HSCs, and SIRT7 up-regulation improved the regenerative capacity of aged HSCs. These findings define the deregulation of a UPR<sup>mt</sup>-mediated metabolic checkpoint as a reversible contributing factor for HSC aging.

**A**ging is characterized by physiological decline and increased susceptibility to pathologies and mortality. The rate of aging is controlled by evolutionarily conserved genetic pathways (1, 2). The general cause of aging is the chronic accumulation of cellular damage (2, 3). This conceptual framework raises fundamental questions about aging. What are the origins of aging-causing damage? What is the cell or tissue specificity for sensing or responding to such damage? Are the effects of cellular damage on physiological aging reversible?

Adult stem cells mostly reside in a metabolically inactive quiescent state to preserve their integrity but convert to a metabolically active proliferative state to replenish the tissue (4–6). The signals that trigger stem cells to exit the cell cycle and enter quiescence, and the signal transduction leading to the transition, remain elusive.

SIRT7 is a histone deacetylase that is recruited to its target promoters by interactions with transcription factors for transcriptional repression (7). We took a proteomic approach to identify SIRT7-interacting transcription factors. We transfected

human embryonic kidney–293T (HEK-293T) cells with Flag-tagged SIRT7, affinity-purified the Flag-tagged SIRT7 interactome, and identified SIRT7-interacting proteins by mass spectrometry. Among the potential SIRT7-interacting proteins was nuclear respiratory factor 1 (NRF1), a master regulator of mitochondria (8). Transfected Flag-SIRT7 and endogenous SIRT7 interacted with NRF1 in HEK-293T cells (Fig. 1, A and B).

SIRT7 bound the proximal promoters of mitochondrial ribosomal proteins (mRPs) and mitochondrial translation factors (mTFs) but not other NRF1 targets (Fig. 1C and fig. S1A) (7). NRF1 bound the same regions as SIRT7 at the proximal promoters of mRPs and mTFs but not RPS20 (Fig. 1D and fig. S1B), where SIRT7 binding is mediated through Myc (9). SIRT7 binding sites were found adjacent to NRF1 consensus binding motifs at the promoters of mRPs and mTFs (fig. S1C). NRF1 knockdown (KD) using small interfering RNA (siRNA) reduced SIRT7 occupancy at the promoters of mRPs and mTFs but not RPS20 (Fig. 1C and fig. S2). SIRT7 KD using short hairpin RNAs led to increased expression of mRPs and mTFs, which was abrogated by NRF1 siRNA (Fig. 2, A and B, and fig. S3). Thus, NRF1 targets SIRT7 specifically to the promoters of mRPs and mTFs for transcriptional repression.

Transcriptional repression of mitochondrial and cytosolic (7, 9) translation machinery by SIRT7 suggests that SIRT7 might suppress mitochondrial activity and proliferation. SIRT7 KD cells had increased mitochondrial mass, citrate synthase activity, adenosine triphosphate levels,

respiration, and proliferation, whereas cells overexpressing wild type (WT) but not a catalytically inactive SIRT7 mutant (H187Y) showed reduced mitochondrial mass, respiration, and proliferation (Fig. 2, C to E, and fig. S4, A to G) (10, 11). NRF1 siRNA abrogated the increased mitochondrial activity and proliferation of SIRT7 KD cells (fig. S4, H to J). Thus, SIRT7 represses NRF1 activity to suppress mitochondrial activity and proliferation.

Sirtuins are increasingly recognized as stress resistance genes (12–14). Nutrient deprivation induced SIRT7 expression (fig. S5A). Upon nutrient deprivation stress, cells reduce mitochondrial activity, growth, and proliferation to prevent cell death (15, 16). When cultured in nutrient-deprived medium, cells overexpressing SIRT7 showed increased survival, whereas SIRT7 KD cells showed reduced survival, which was improved by NRF1 siRNA (fig. S5). Thus, SIRT7 suppresses NRF1 activity to promote nutritional stress resistance.

Perturbation of mitochondrial proteostasis, a form of mitochondrial stress, activates the mitochondrial unfolded protein response (UPR<sup>mt</sup>), a retrograde signaling pathway leading to transcriptional up-regulation of mitochondrial chaperones and stress relief (17, 18). Mitochondrial dysfunction results in attenuated translation, which helps restore mitochondrial homeostasis (19). SIRT7-mediated transcriptional repression of the translation machinery suggests that SIRT7 may alleviate mitochondrial protein folding stress (PFS<sup>mt</sup>). PFS<sup>mt</sup> induced SIRT7 expression (Fig. 2F). Induction of PFS<sup>mt</sup> by overexpression of an aggregation-prone mutant mitochondrial protein, ornithine transcarbamylase ( $\Delta$ OTC), results in UPR<sup>mt</sup> activation and efficient clearance of misfolded  $\Delta$ OTC (18). In SIRT7 KD cells, misfolded  $\Delta$ OTC accumulated to a higher level (Fig. 2G). SIRT7 KD cells displayed increased apoptosis upon PFS<sup>mt</sup> (Fig. 2H) but are not prone to general apoptosis (9). Thus, SIRT7 alleviates PFS<sup>mt</sup> and promotes PFS<sup>mt</sup> resistance. Consistently, mitochondrial dysfunction is manifested in the metabolic tissues of SIRT7-deficient mice (20).

PFS<sup>mt</sup> induced the expression of canonical UPR<sup>mt</sup> genes in SIRT7-deficient cells (fig. S6, A and B), indicating that induction of SIRT7 and canonical UPR<sup>mt</sup> genes is in separate branches of the UPR<sup>mt</sup>. Untreated SIRT7 KD cells displayed increased expression of canonical UPR<sup>mt</sup> genes (fig. S6, A and B), but SIRT7 did not bind to their promoters (fig. S1A) (7), suggesting that SIRT7 deficiency results in constitutive PFS<sup>mt</sup> and compensatory induction of canonical UPR<sup>mt</sup> genes. NRF1 siRNA abrogated increased PFS<sup>mt</sup>, but not endoplasmic reticulum stress, in SIRT7 KD cells

<sup>1</sup>Program in Metabolic Biology, Nutritional Sciences and Toxicology, University of California, Berkeley, CA 94720, USA. <sup>2</sup>Department of Molecular and Cell Biology, University of California, Berkeley, CA 94720, USA. <sup>3</sup>Cell Biology Program, Memorial Sloan Kettering Cancer Center, New York, NY 10065, USA. <sup>4</sup>Biochemistry, Cell and Molecular Biology Allied Program, Weill Cornell Medical College, 1300 York Avenue, New York, NY, USA.

\*These authors contributed equally to this work. †Corresponding author. E-mail: danicac@berkeley.edu



(Fig. 2I and fig. S6C). Thus, the interplay between SIRT7 and NRF1 constitutes a regulatory branch of UPR<sup>mt</sup>, functioning as the nexus of reduced

mitochondrial translation for homeostasis reestablishment and repressed energy metabolism and proliferation (Fig. 2J).

What is the physiological relevance of the SIRT7-mediated UPR<sup>mt</sup>? In *Caenorhabditis elegans*, the UPR<sup>mt</sup> is activated during a developmental

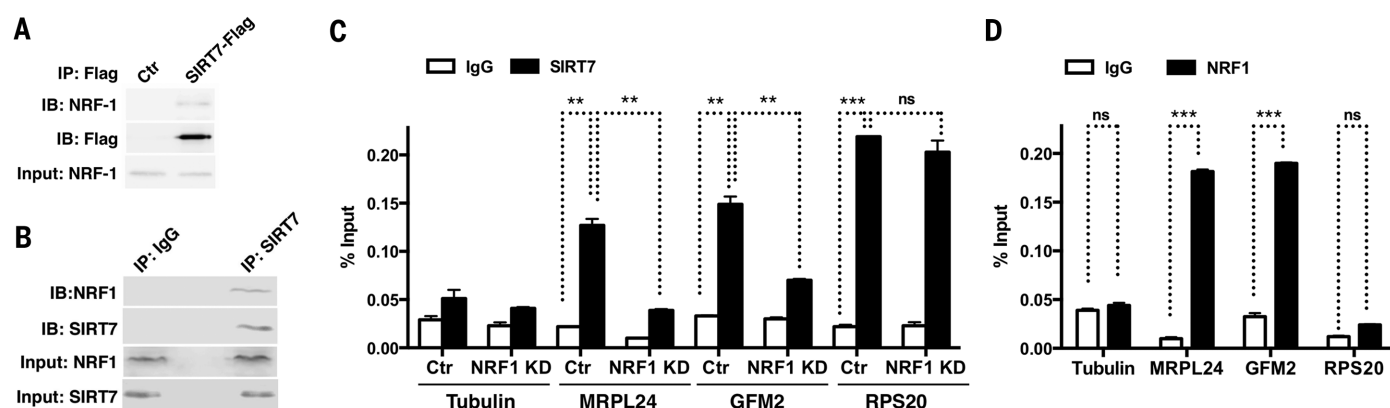


**Fig. 1. NRF1 stabilizes SIRT7 at the promoters of mitochondrial translational machinery components.** (A and B) Coimmunoprecipitation of transfected Flag-tagged or endogenous SIRT7 with endogenous NRF1 from HEK-293T cells. (C and D) ChIP followed by quantitative real-time polymerase chain reaction (ChIP-qPCR) showing SIRT7 (C) and NRF1 (D) occupancy at gene promoters. Error bars, mean  $\pm$  SE. \*\* $P < 0.01$ ; \*\*\* $P < 0.001$ ; ns,  $P > 0.05$ . Student's  $t$  test.

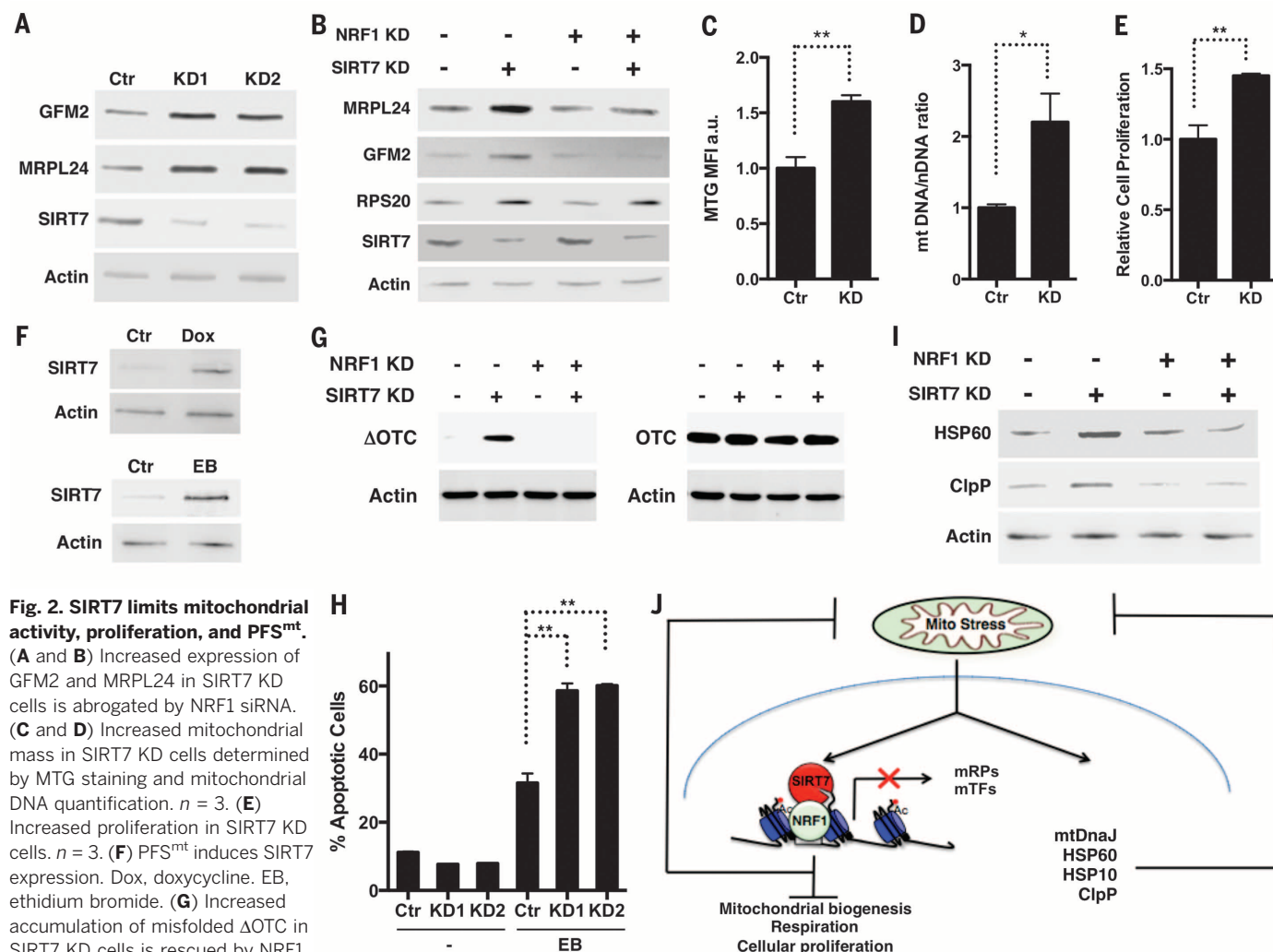


**Fig. 2. SIRT7 limits mitochondrial activity, proliferation, and PFS<sup>mt</sup>.** (A and B) Increased expression of GFM2 and MRPL24 in SIRT7 KD cells is abrogated by NRF1 siRNA. (C and D) Increased mitochondrial mass in SIRT7 KD cells determined by MTG staining and mitochondrial DNA quantification.  $n = 3$ . (E) Increased proliferation in SIRT7 KD cells.  $n = 3$ . (F) PFS<sup>mt</sup> induces SIRT7 expression. Dox, doxycycline. EB, ethidium bromide. (G) Increased accumulation of misfolded  $\Delta$ OTC in SIRT7 KD cells is rescued by NRF1 siRNA. OTC is used as a control. (H) Increased apoptosis in SIRT7 KD cells treated with EB.  $n = 3$ . (I) NRF1 siRNA abrogates increased PFS<sup>mt</sup> in SIRT7 KD cells. (J) A proposed model. Error bars, mean  $\pm$  SE. \* $P < 0.05$ . \*\* $P < 0.01$ . Student's  $t$  test.

stage when a burst of mitochondrial biogenesis takes place and is attenuated when mitochondrial biogenesis subsides (17). Thus, the SIRT7-mediated UPR<sup>mt</sup> may be important for cells that experience bursts of mitochondrial biogenesis and convert between growth states with markedly different bioenergetic demands and proliferative potentials, such as stem cells. Quiescent adult stem cells have low mitochondrial content, but mitochondrial biogenesis increases during proliferation and differentiation (4).

Because SIRT7 is highly expressed in the hematopoietic system, we focused on hematopoietic

stem cells (HSCs) isolated from SIRT7<sup>+/+</sup> and SIRT7<sup>-/-</sup> mice (fig. S7). SIRT7<sup>-/-</sup> HSCs had increased expression of UPR<sup>mt</sup> genes, indicative of increased PFS<sup>mt</sup> (Fig. 3A). Mitotracker green (MTG) staining, mitochondrial DNA quantification, and electron microscopy revealed increased mitochondrial numbers in SIRT7<sup>-/-</sup> HSCs (Fig. 3, B and C, and fig. S8). In vivo bromodeoxyuridine (BrdU) incorporation showed increased proliferation of SIRT7<sup>-/-</sup> HSCs (Fig. 3D). SIRT7<sup>-/-</sup> HSCs also exhibited an increased propensity to enter the cell cycle upon ex vivo culture with cytokines (Fig. 3E). However, there was no difference in mito-

chondrial number or proliferation in the differentiated subpopulations of these two genotypes (Fig. 3, B, D, and E). Animals with loss of HSC quiescence are sensitive to the myeloablative drug 5-fluorouracil (21). SIRT7<sup>-/-</sup> BMCs or purified HSCs displayed a 40% reduction in long-term reconstitution of the recipients' hematopoietic

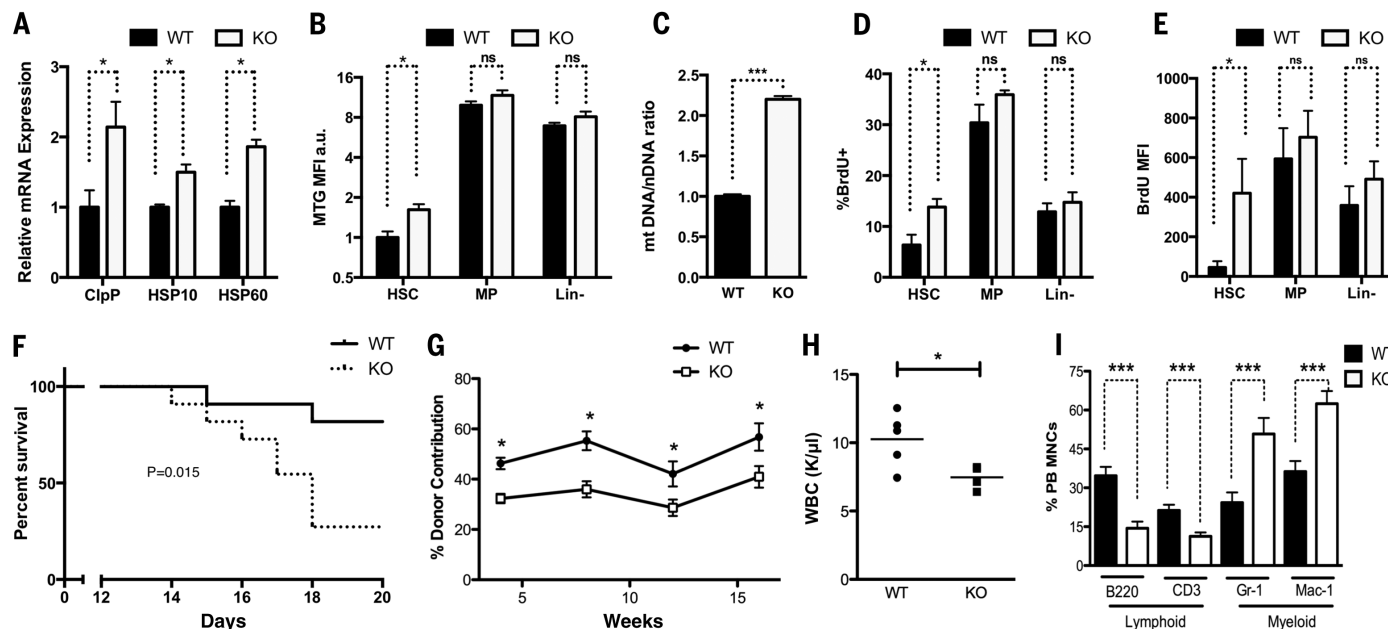


**Fig. 3. SIRT7 ensures HSC maintenance.** (A) qPCR showing increased PFS<sup>mt</sup> in SIRT7<sup>-/-</sup> HSCs. *n* = 4. (B and C) MTG staining and mitochondrial DNA quantification showing increased mitochondrial mass in SIRT7<sup>-/-</sup> HSCs. *n* = 4. MP, myeloid progenitor cells. Lin<sup>-</sup>, lineage-negative cells. (D) In vivo BrdU incorporation showing increased proliferation of SIRT7<sup>-/-</sup> HSCs. *n* = 4. (E) Increased propensity of SIRT7<sup>-/-</sup> HSCs to cycle upon ex vivo culture with cytokines, indicated by BrdU pulse. *n* = 4. (F) Mice reconstituted with SIRT7<sup>-/-</sup>

BMCs have increased sensitivity to 5-fluorouracil. *n* = 12. Log-rank test. (G) Competitive transplantation using SIRT7<sup>+/+</sup> and SIRT7<sup>-/-</sup> BMCs as donors showing reduced reconstitution capacity of SIRT7<sup>-/-</sup> HSCs. *n* = 15. Representative of five transplants. (H) Reduced white blood cell count in SIRT7<sup>-/-</sup> mice. (I) Myeloid-biased differentiation in the peripheral blood (PB) of SIRT7<sup>-/-</sup> mice. MNCs, mononuclear cells. *n* = 7. Error bars, mean ± SE. \**P* < 0.05. \*\*\**P* < 0.001. ns, *P* > 0.05. Student's *t* test.

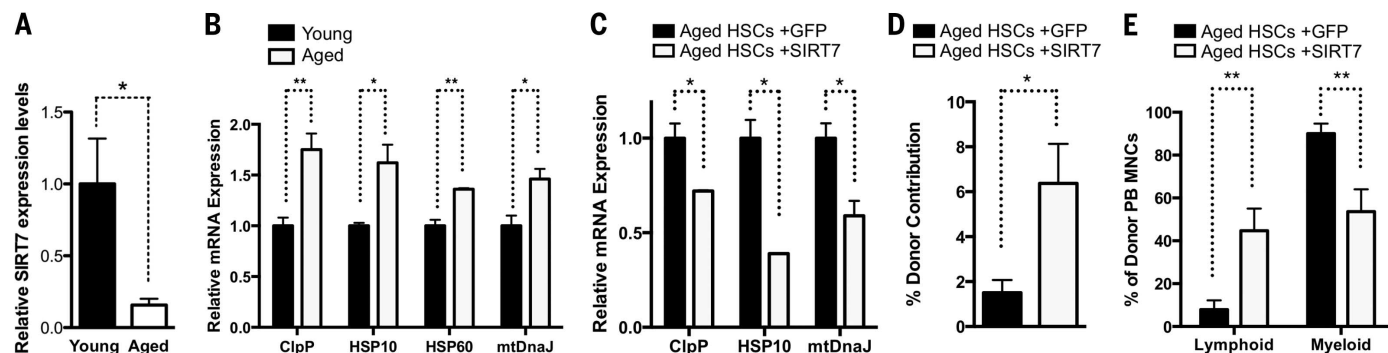


**Fig. 4. HSC aging is regulated by SIRT7.** (A) qPCR showing reduced SIRT7 expression in aged HSCs. *n* = 3. (B and C) qPCR showing that increased PFS<sup>mt</sup> in aged HSCs is rescued by SIRT7 overexpression. *n* = 3. (D and E) Competitive transplantation using aged HSCs transduced with SIRT7 or control lentivirus as donors. SIRT7 overexpression increases reconstitution capacity and reverses myeloid-biased differentiation of aged HSCs. *n* = 7. Error bars, mean ± SE. \**P* < 0.05. \*\**P* < 0.01. Student's *t* test.



system compared with their SIRT7<sup>+/+</sup> counterparts (Fig. 3G and fig. S9A). SIRT7<sup>-/-</sup> mice also had reduced numbers of white blood cells (Fig. 3H). Although SIRT7<sup>+/+</sup> and SIRT7<sup>-/-</sup> mice had comparable HSC frequency in the bone marrow under steady-state conditions, there was a 50% reduction in the frequency of SIRT7<sup>-/-</sup> HSCs upon transplantation (fig. S9, B and C). SIRT7<sup>-/-</sup> HSCs showed increased apoptosis upon transplantation (fig. S9D), which may account for compromised HSC engraftment. HSCs differentiate into lymphoid and myeloid lineages. Myeloid-biased differentiation was apparent in SIRT7<sup>-/-</sup> mice or in mice reconstituted with SIRT7<sup>-/-</sup> HSCs (Fig. 3I and fig. S9E). Thus, SIRT7 promotes HSC maintenance and prevents myeloid-biased differentiation.

Reintroduction of SIRT7 in SIRT7<sup>-/-</sup> HSCs improved reconstitution capacity and rescued myeloid-biased differentiation (fig. S9, F and G), indicating that SIRT7 regulates HSC maintenance cell-autonomously. NRF1 inactivation in SIRT7<sup>-/-</sup> HSCs reduced PFS<sup>mt</sup>; improved HSC quiescence, engraftment, and reconstitution; and rescued myeloid-biased differentiation (figs. S9C and S10). Thus, SIRT7 represses NRF1 activity to alleviate PFS<sup>mt</sup> and ensure HSC maintenance.

SIRT7 expression was reduced in aged HSCs (Fig. 4A) (22). Notably, defects manifested in SIRT7<sup>-/-</sup> HSCs (increased PFS<sup>mt</sup> and apoptosis, loss of quiescence, decreased reconstitution capacity, and myeloid-biased differentiation) resemble aspects of aged HSCs (23–25) (Fig. 4B). SIRT7 overexpression or NRF1 inactivation in aged HSCs reduced PFS<sup>mt</sup>, improved reconstitution capacity, and rescued myeloid-biased differentiation (Fig. 4, C to E, and fig. S11). Thus, SIRT7 down-regulation results in increased PFS<sup>mt</sup> in aged HSCs, contributing to their functional decline.

Collectively, our results highlight PFS<sup>mt</sup> as a trigger of a metabolic checkpoint that regulates HSC quiescence and establish the deregulation of UPR<sup>mt</sup> as a contributing factor for HSC aging. Using a stress signal as a messenger to return to quiescence may ensure the integrity of HSCs, which persist throughout the entire life span for tissue maintenance. The interplay between SIRT7,

which is induced upon PFS<sup>mt</sup>, and NRF1, a master regulator of mitochondria, is uniquely positioned to integrate PFS<sup>mt</sup> to metabolic checkpoint regulation.

SIRT7 represses NRF1 activity to reduce the expression of the mitochondrial translation machinery and to alleviate PFS<sup>mt</sup> (Figs. 1 and 2). In vivo gene expression studies cannot distinguish direct versus indirect effects. In this regard, chromatin immunoprecipitation (ChIP) sequencing studies are informative in identifying direct SIRT7 targets (7). Although gene expression changes in the metabolic tissues of SIRT7<sup>-/-</sup> mice are likely reflective of severe mitochondrial and metabolic defects (20), transiently knocking down SIRT7 in cultured cells can capture the direct effect of SIRT7 on its targets (7, 9) (Fig. 2) and may account for different gene expression changes. In contrast to the severe defects in metabolic tissues of SIRT7<sup>-/-</sup> mice, SIRT7<sup>-/-</sup> HSCs have increased mitochondria number and proliferation under homeostatic conditions but do not fare well upon transplantation stress (Fig. 3). These observations are consistent with the notion that while metabolic tissues have a large number of mitochondria, HSCs have very few mitochondria under homeostatic conditions and increase mitochondrial biogenesis upon transplantation. The combined power of biochemistry, cell culture, and mouse genetics is necessary to tease out direct and indirect effects of SIRT7 under various physiological conditions. Our proposed model (Fig. 2J) is consistent with the functions of SIRT7 in chromatin remodeling and gene repression (7), stress responses (9) (Fig. 2), and mitochondrial maintenance (20) (Fig. 2).

Reintroduction of SIRT7 in aged HSCs reduces PFS<sup>mt</sup> and improves their regenerative capacity. Thus, PFS<sup>mt</sup>-induced HSC aging is reversible. It appears that HSC aging is not due to the passive chronic accumulation of cellular damage over the lifetime but to the regulated repression of cellular protective programs, giving hope for targeting the dysregulated cellular protective programs to reverse HSC aging and rejuvenate tissue homeostasis.

## REFERENCES AND NOTES

1. C. J. Kenyon, *Nature* **464**, 504–512 (2010).
2. C. López-Otin, M. A. Blasco, L. Partridge, M. Serrano, G. Kroemer, *Cell* **153**, 1194–1217 (2013).
3. J. Vijg, J. Campisi, *Nature* **454**, 1065–1071 (2008).
4. C. D. Folmes, P. P. Dzeja, T. J. Nelson, A. Terzic, *Cell Stem Cell* **11**, 596–606 (2012).
5. L. Liu et al., *Cell Rep.* **4**, 189–204 (2013).
6. A. E. Webb et al., *Cell Rep.* **4**, 477–491 (2013).
7. M. F. Barber et al., *Nature* **487**, 114–118 (2012).
8. R. C. Scarpulla, *Physiol. Rev.* **88**, 611–638 (2008).
9. J. Shin et al., *Cell Rep.* **5**, 654–665 (2013).
10. J. Y. Lu, Y. Zhang, Y. F. Shen, *Acta Academiae Medicinae Sinicae* **31**, 724–727 (2009).
11. O. Vakhrusheva, D. Braeuer, Z. Liu, T. Braun, E. Bober, *J. Physiol. Pharmacol.* **59** (suppl. 9), 201–212 (2008).
12. K. Brown et al., *Cell Rep.* **3**, 319–327 (2013).
13. W. Giblin, M. E. Skinner, D. B. Lombard, *Trends Genet.* **30**, 271–286 (2014).
14. X. Qiu, K. Brown, M. D. Hirschey, E. Verdin, D. Chen, *Cell Metab.* **12**, 662–667 (2010).
15. K. Inoki, T. Zhu, K. L. Guan, *Cell* **115**, 577–590 (2003).
16. M. Laplante, D. M. Sabatini, *Cell* **149**, 274–293 (2012).
17. C. M. Haynes, D. Ron, *J. Cell Sci.* **123**, 3849–3855 (2010).
18. Q. Zhao et al., *EMBO J.* **21**, 4411–4419 (2002).
19. C. M. Haynes, C. J. Fiorese, Y. F. Lin, *Trends Cell Biol.* **23**, 311–318 (2013).
20. D. Ryu et al., *Cell Metab.* **20**, 856–869 (2014).
21. K. Miyamoto et al., *Cell Stem Cell* **1**, 101–112 (2007).
22. S. M. Chambers et al., *PLoS Biol.* **5**, e201 (2007).
23. V. Janzen et al., *Nature* **443**, 421–426 (2006).
24. J. Oh, Y. D. Lee, A. J. Wagers, *Nat. Med.* **20**, 870–880 (2014).
25. R. A. Signer, S. J. Morrison, *Cell Stem Cell* **12**, 152–165 (2013).

## ACKNOWLEDGMENTS

We thank H. Nolla, A. Valeros, and K. Heydari for cell sorting; R. Zalpuri for electron microscopy; U. Andersen for mass spectrometry; J. Kim for technical assistance; the Chua laboratory for SIRT7 antibody and constructs; and the Hoogenraad laboratory for OTC constructs. This work was supported by NIH R01 AG040990 (D.C.), R01AG040061 (C.M.H.), T32 AG000266 (M.M.), Ellison Medical Foundation (D.C.), Glenn Foundation (D.C.), NSF Graduate Research Fellowship Program (J.S.), and Siebel Stem Cell Institute (D.C. and M.M.). The supplementary materials contain additional data.

## SUPPLEMENTARY MATERIALS

www.sciencemag.org/content/347/6228/1374/suppl/DC1  
Materials and Methods  
Figs. S1 to S11  
Tables S1 to S3  
References (26–29)

5 November 2014; accepted 5 February 2015  
10.1126/science.aaa2361

# Power your next big breakthrough.

Sequencing power for every scale.



## **NEW** HiSeq X™ Series

### **Population power**

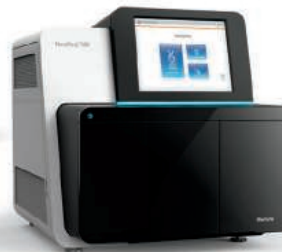
Maximum throughput and low cost population- and production-scale human whole-genome sequencing. Series includes the HiSeq X Ten and the new HiSeq X Five Systems.



## **NEW** HiSeq® Series

### **Production power**

Maximum throughput and lowest cost for production-scale genomics. Series includes the new HiSeq 3000 and HiSeq 4000 Systems.



## **NEW** NextSeq® Series

### **Flexible power**

Desktop speed and simplicity for everyday genomics. Series includes the NextSeq 500 and the new NextSeq 550 with cytogenomic array scanning.



## **MiSeq® Series**

### **Focused power**

Speed and simplicity for targeted and small-genome sequencing. Series includes the MiSeq and MiSeqDx™ Systems.\*

Compare our new systems with our product selector at [www.illumina.com/power](http://www.illumina.com/power).

FOR RESEARCH USE ONLY

\*MiSeqDx™ is a 510(k) cleared, CE-marked instrument. See instructions for use.

©2015 Illumina, Inc. All rights reserved.

**illumina**®



# DID YOU HEAR?

Thanks to them,  
she does.

Photo courtesy of MED<sup>EL</sup>

## 2015 Russ Prize recipients Developers of the cochlear implant **Creators of good:**

- Graeme M. Clark
- Erwin Hochmair
- Ingeborg J. Hochmair
- Michael M. Merzenich
- Blake S. Wilson



**OHIO**  
UNIVERSITY

Russ College of Engineering  
and Technology



### The 2015 National Academy of Engineering Fritz J. and Dolores H. Russ Prize

Promoting engineering, encouraging engineering education, recognizing achievements that improve our lives.

Ohio University thanks late alumnus Fritz Russ and his wife, Dolores, for creating the \$500,000 Russ Prize with an endowment to the University. We're proud to steward their vision in collaboration with the National Academy of Engineering.

[www.ohio.edu/engineering/russ-prize](http://www.ohio.edu/engineering/russ-prize)

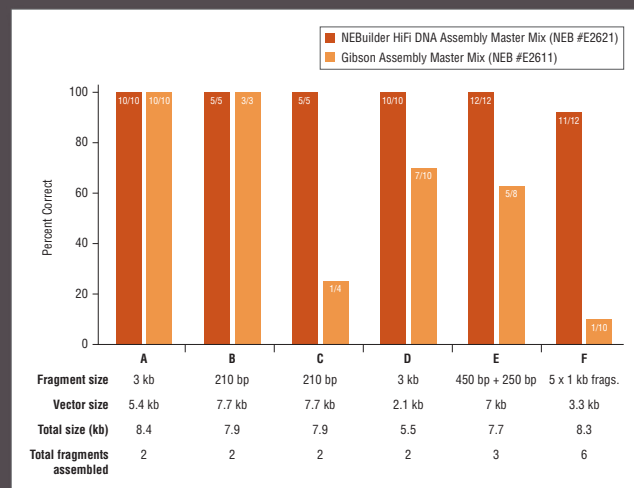
# The Next Generation of DNA Assembly and Cloning

## NEBuilder<sup>®</sup> HiFi DNA Assembly

The next generation of DNA assembly and cloning has arrived. With NEBuilder HiFi DNA Assembly, you'll enjoy virtually error-free joining of DNA fragments. More efficient assembly is now possible, even with larger fragments, low inputs, or 5'- and 3'-end mismatches. Additionally, use NEBuilder HiFi to bridge two dsDNA fragments with a ssDNA oligo. Save time with less screening or re-sequencing, and benefit from no licensing fee requirements from NEB when choosing NEBuilder products.

**Request a free sample\***  
**at [www.NEBuilderHiFi.com](http://www.NEBuilderHiFi.com)**

NEBuilder HiFi DNA Master Mix offers improved fidelity over Gibson Assembly Master Mix



*Fidelity of assembled products was compared between NEBuilder HiFi DNA Assembly Master Mix (NEB #E2621) and Gibson Assembly Master Mix (NEB #E2611). Experiments were performed using the various fragment and vector sizes, following suggested protocols. Experiments B and C vary because sequences of fragments are different. Experiments D and F were performed with fragments containing 3'-end mismatches.*

\* While supplies last. Offer valid in the US only. Limit one sample per customer.

NEW ENGLAND BIOLABS<sup>®</sup>, NEB<sup>®</sup> and NEBUILDER<sup>®</sup> are registered trademarks of New England Biolabs, Inc.  
GIBSON ASSEMBLY<sup>®</sup> is a registered trademark of Synthetic Genomics, Inc.





2015 **MRS**<sup>®</sup> FALL MEETING & EXHIBIT  
November 29 – December 4, 2015 | Boston, Massachusetts

# CALL FOR PAPERS

Abstract Submission Opens May 18, 2015 | Abstract Submission Deadline June 18, 2015

- A Engaged Learning of Materials Science and Engineering in the 21<sup>st</sup> Century

## BIOMATERIALS AND SOFT MATERIALS

- B Stretchable and Active Polymers and Composites for Electronics and Medicine  
C Tough, Smart and Printable Hydrogel Materials  
D Biological and Bioinspired Materials in Photonics and Electronics—Biology, Chemistry and Physics  
E Engineering and Application of Bioinspired Materials  
F Biomaterials for Regenerative Engineering  
G Plasma Processing and Diagnostics for Life Sciences  
H Multifunctionality in Polymer-Based Materials, Gels and Interfaces  
I Nanocellulose Materials and Beyond—Nanoscience, Structures, Devices and Nanomanufacturing  
J Wetting and Soft Electrokinetics  
K Materials Science, Technology and Devices for Cancer Modeling, Diagnosis and Treatment  
L Nanofunctional Materials, Nanostructures and Nanodevices for Biomedical Applications

## NANOMATERIALS AND SYNTHESIS

- M Micro- and Nanoscale Processing of Materials for Biomedical Devices  
N Magnetic Nanomaterials for Biomedical and Energy Applications  
O Plasmonic Nanomaterials for Energy Conversion  
P Synthesis and Applications of Nanowires and Hybrid 1D-0D/2D/3D Semiconductor Nanostructures  
Q Nano Carbon Materials—1D to 3D  
R Harsh Environment Sensing—Functional Nanomaterials and Nanocomposites, Materials for Associated Packaging and Electrical Components and Applications

## MECHANICAL BEHAVIOR AND FAILURE OF MATERIALS

- S Mechanical Behavior at the Nanoscale  
T Strength and Failure at the Micro- and Nanoscale—From Fundamentals to Applications  
U Microstructure Evolution and Mechanical Properties in Interface-Dominated Metallic Materials  
V Gradient and Laminate Materials  
W Materials under Extreme Environments (MuEE)  
Y Shape Programmable Materials

## ELECTRONICS AND PHOTONICS

- Z Molecularly Ordered Organic and Polymer Semiconductors—Fundamentals and Devices  
AA Organic Semiconductors—Surface, Interface and Bulk Doping  
BB Innovative Fabrication and Processing Methods for Organic and Hybrid Electronics  
CC Organic Bioelectronics—From Biosensing Platforms to Implantable Nanodevices  
DD Diamond Electronics, Sensors and Biotechnology—Fundamentals to Applications  
EE Beyond Graphene—2D Materials and Their Applications  
FF Integration of Functional Oxides with Semiconductors  
GG Emerging Materials and Platforms for Optoelectronics  
HH Optical Metamaterials—From New Plasmonic Materials to Metasurface Devices  
II Phonon Transport, Interactions and Manipulations in Nanoscale Materials and Devices—Fundamentals and Applications  
JJ Multiferroics and Magnetoelectrics  
KK Materials and Technology for Non-Volatile Memories

## ENERGY AND SUSTAINABILITY

- LL Materials and Architectures for Safe and Low-Cost Electrochemical Energy Storage Technologies  
MM Advances in Flexible Devices for Energy Conversion and Storage  
NN Thin-Film and Nanostructure Solar Cell Materials and Devices for Next-Generation Photovoltaics  
OO Nanomaterials-Based Solar Energy Conversion  
PP Materials, Interfaces and Solid Electrolytes for High Energy Density Rechargeable Batteries  
QQ Catalytic Materials for Energy  
RR Wide-Bandgap Materials for Energy Efficiency—Power Electronics and Solid-State Lighting  
SS Progress in Thermal Energy Conversion—Thermoelectric and Thermal Energy Storage Materials and Devices

## THEORY, CHARACTERIZATION AND MODELING

- TT Topology in Materials Science—Biological and Functional Nanomaterials, Metrology and Modeling  
UU Frontiers in Scanning Probe Microscopy  
VV *In Situ* Study of Synthesis and Transformation of Materials  
WW Modeling and Theory-Driven Design of Soft Materials  
XX Architected Materials—Synthesis, Characterization, Modeling and Optimal Design  
YY Advanced Atomistic Algorithms in Materials Science  
ZZ Material Design and Discovery via Multiscale Computational Material Science  
AAA Big Data and Data Analytics for Materials Science  
BBB Liquids and Glassy Soft Matter—Theoretical and Neutron Scattering Studies  
CCC Integrating Experiments, Simulations and Machine Learning to Accelerate Materials Innovation  
DDD Lighting the Path towards Non-Equilibrium Structure-Property Relationships in Complex Materials

- X *Frontiers of Material Research*

[www.mrs.org/fall2015](http://www.mrs.org/fall2015)

The MRS/E-MRS Bilateral Conference on Energy will be comprised of the energy-related symposia at the 2015 MRS Fall Meeting.

## Meeting Chairs

**T. John Balk** University of Kentucky  
**Ram Devanathan** Pacific Northwest National Laboratory  
**George G. Malliaras** Ecole des Mines de St. Etienne  
**Larry A. Nagahara** National Cancer Institute  
**Luisa Torsi** University of Bari "A. Moro"

## Don't Miss These Future MRS Meetings!

### 2016 MRS Spring Meeting & Exhibit

March 28 - April 1, 2016  
Phoenix, Arizona

### 2016 MRS Fall Meeting & Exhibit

November 27 - December 2, 2016  
Boston, Massachusetts



**MATERIALS RESEARCH SOCIETY<sup>®</sup>**  
*Advancing materials. Improving the quality of life.*

506 Keystone Drive • Warrendale, PA 15086-7573  
Tel 724.779.3003 • Fax 724.779.8313  
info@mrs.org • [www.mrs.org](http://www.mrs.org)

### Ultracentrifuge

A new ultracentrifuge combines speed with safety and ergonomics, allowing researchers to easily protect samples while achieving reliable and consistent results. The Sorvall WX+ ultracentrifuge features an intuitive color LCD touchscreen to keep programming simple and easy to navigate. Designed to accommodate a multiple-user environment, the Sorvall WX+ ultracentrifuge monitors run data with optional Log Manager software that recalls past operating parameters with up to 5,120 cases of recorded histories to assist with GMP/GLP compliance. In addition, the Sorvall WX+ ultracentrifuge offers: up to 100,000 rpm performance in a small footprint to maximize space in the lab; lightweight and fatigue-resistant Fiberlite carbon fiber rotors; automatic tube balancing compensation, which accelerates sample preparation by allowing visual sample balancing up to 5 mm; and a self-locking rotor system that provides confidence that the rotor is automatically and securely locked.

#### Thermo Fisher Scientific

For info: 800-556-2323  
www.thermoscientific.com

### UV Spectrophotometer

Improved optical characterization systems are now available for spectral measurements from the vacuum ultraviolet to the near infrared. The vacuum ultraviolet universal spectrophotometer is an optical test system optimized for emitting samples like phosphors or photo- and electroluminescent crystals. It can measure reflectance, transmission, and fluorescence emission over its complete working range, 120 nm to 2.2  $\mu\text{m}$ . Options are available to extend the range even more. The user-friendly sample chamber includes high-efficiency toroidal optics for focused excitation and sensitive detection. It can operate purged or under vacuum and can interface to commercial cryogenic and heated sample mounts. Auxiliary ports are in the sample area for addition of HV leads for electrical excitation, auxiliary sample by X-ray sources or conventional lasers, and output to diverse and even fiber-connected spectrometers. The vacuum ultraviolet universal spectrophotometer feature easily interchangeable five-position sample holders. Samples index while the system is under vacuum.

#### McPherson

For info: 978-256-4512  
www.mcphersoninc.com



### 50 $\mu\text{L}$ Electronic Pipettes

The popular VIAFLO II electronic pipette range has been expanded to include the new 50  $\mu\text{L}$  models, which perfectly fill the gap between the 0.5–12.5  $\mu\text{L}$  and 5–125  $\mu\text{L}$  ranges. Now available for single-, 8-, 12-, and 16-channel VIAFLO II pipettes, the new models deliver optimized precision pipetting in the volume range of 2–50  $\mu\text{L}$ . The VIAFLO II multichannel electronic pipette range combines ultralightweight design and unsurpassed operational comfort enabling users to improve efficiency in their working environment. VIAFLO II electronic pipettes together with INTEGRA's wide range of GripTip pipette tips form the perfect pipetting system. GripTips snap into place with minimal tip loading effort, providing a secure connection. GripTips never fall off and are always perfectly aligned, resulting in superior accuracy and high precision.

#### INTEGRA Biosciences

For info: 603-578-5800  
www.integra-biosciences.com

### Clean Air Protection System

The Clean Air Protection (CAP) system is Hamilton's first intelligent HEPA-Filtered clean air hood. The system's small design and price eliminates the need to buy bulky and expensive laminar fume hoods for their MicroLab NIMBUS liquid handler. The system installs and is up and running in less than one hour. It uses Hamilton's latest monitoring and detecting technology, enabling labs to meet ISO 14644-1, Federal Standard 209E. Using a 99.99% 0.3  $\mu\text{L}$  HEPA filter with a high-density pre-filter, the CAP system delivers clean air to the working environment. The monitoring system maintains flows in the NIMBUS enclosure via an integrated flow sensor creating a constant positive pressure regardless of the door being open or closed. The monitoring system also features real-time temperature and humidity display with built-in customer set alarm settings and a HEPA filter diagnostic sensor that alerts the user when the filter needs to be changed.

#### Hamilton Robotics

For info: 800-648-5950  
www.hamiltoncompany.com

### Automated Sample Thawing System

The ThawSTAR automated sample thawing system is a breakthrough technology that addresses the "last mile" in the cryopreservation process. Utilizing STAR sensing technology, ThawSTAR system tailors the thaw cycle to the specific characteristics of each frozen sample. ThawSTAR technology integrates multiple detection algorithms to ensure uniform thermal

profiles and reproducible recovery of the frozen contents, eliminating the subjectivity found in conventional thaw methods that rely on human interpretation, such as swirling frozen vials in water baths and rolling vials between hands. Users simply insert a frozen vial and retrieve it when the vial is raised at the end of the thaw cycle. The automatic release of the vial coupled with built-in audio and visual alarms allow users to quickly retrieve thawed vials for downstream processing. ThawSTAR thawing system was engineered to deliver results similar to those achieved when thawing in a 37°C water bath, but with reproducibility and standardization built in.

#### BioCision

For info: 415-785-8516  
www.biocision.com

Electronically submit your new product description or product literature information! Go to [www.sciencemag.org/products/newproducts.dtl](http://www.sciencemag.org/products/newproducts.dtl) for more information.

Newly offered instrumentation, apparatus, and laboratory materials of interest to researchers in all disciplines in academic, industrial, and governmental organizations are featured in this space. Emphasis is given to purpose, chief characteristics, and availability of products and materials. Endorsement by *Science* or AAAS of any products or materials mentioned is not implied. Additional information may be obtained from the manufacturer or supplier.



# Will you be in Stockholm this December?

(If you have a recent PhD you could be.)

Stockholm in the second week of December is a special place. The city is alive with excitement as it welcomes and celebrates the new Nobel Laureates at the annual Nobel Prize ceremony.

If you are a recent PhD graduate you could be here too, and receive a rather special prize yourself.

The journal *Science* & SciLifeLab have established The *Science* & SciLifeLab Prize for Young Scientists, to recognize and reward excellence in PhD research and support young scientists at the start of their careers. It's about bright minds, bright ideas and bright futures.

Four winners will be selected for this international award. They will have their essays published in the journal *Science* and share a new total of 60,000 USD in prize money. The winners will be awarded in Stockholm, in December, and take part in a unique week of events including meeting leading scientists in their fields.

*"The last couple of days have been exhilarating. It has been an experience of a lifetime. Stockholm is a wonderful city and the Award winning ceremony exceeds my wildest dreams."*

—Dr. Dan Dominissini, 2014 Prize Winner

Who knows, The *Science* & SciLifeLab Prize for Young Scientists could be a major stepping stone in your career and hopefully one day, during Nobel week, you could be visiting Stockholm in December once again.

**The 2015 Prize is now open. The deadline for submissions is August 1, 2015.**

Enter today: [www.sciencemag.org/scilifelabprize](http://www.sciencemag.org/scilifelabprize)

**The 2015 Prize categories are:**

- Cell and Molecular Biology
- Ecology and Environment
- Genomics and Proteomics
- Translational Medicine



*For over 130 years the journal Science has been the world's leading journal of original scientific research, global news and commentary.*

*SciLifeLab is a collaboration among four universities in Stockholm and Uppsala, Sweden, and is a national center for molecular biosciences with focus on health and environmental research.*

*This prize is made possible with the kind support of the Knut and Alice Wallenberg Foundation.*

*Knut och Alice  
Wallenbergs  
Stiftelse*

**Science**  
AAAS

**SciLifeLab**



WE DO ALL THIS, SO  
YOU DON'T HAVE TO.

52

Book No.

From Page No.

Reviewer #1  
How do we know  
the Ab is Specific?

Test in positive/negative celllines,  
try siRNA, etc.

Single band @  
correct MW

NO

Multiple bands?  
No signal?  
Incorrect signal?  
(Positive stain in  
negative cells)

YES

NEED  
A NEW  
ANTIBODY!

YES

Correct subcellular  
localization?  
Translocation in  
response to  
agonist?

NO

NO

YES

Reproducible  
across multiple  
experiments?

YES

ANTIBODY  
IS  
SPECIFIC!

BOUGHT ANTIBODY  
FROM CST

TITLE

From Page No.

To Page No.

Date

Invented by:

Recorded by:

Witnessed & Understood by me,

Date

Learn more. [www.cellsignal.com/labexpectations](http://www.cellsignal.com/labexpectations)

For Research Use Only. Not For Use In Diagnostic Procedures.

© 2015 Cell Signaling Technology, Inc. Cell Signaling Technology, CST, and XP are trademarks of Cell Signaling Technology, Inc.



Cell Signaling  
TECHNOLOGY®





There's only one **Science**

## Science Careers Advertising

For full advertising details, go to [ScienceCareers.org](http://ScienceCareers.org) and click For Employers, or call one of our representatives.

### Tracy Holmes

Worldwide Associate Director  
Science Careers  
Phone: +44 (0) 1223 326525

### THE AMERICAS

E-mail: [advertise@sciencecareers.org](mailto:advertise@sciencecareers.org)  
Fax: 202 289 6742

### Tina Burks

Phone: 202 326 6577

### Nancy Toema

Phone: 202 326 6578

### Marci Gallun

Sales Administrator  
Phone: 202 326 6582

### Online Job Posting Questions

Phone: 202 312 6375

### EUROPE / INDIA / AUSTRALIA / NEW ZEALAND / REST OF WORLD

E-mail: [ads@science-int.co.uk](mailto:ads@science-int.co.uk)  
Fax: +44 (0) 1223 326532

### Axel Gesatzki

Phone: +44 (0) 1223 326529

### Sarah Lelarge

Phone: +44 (0) 1223 326527

### Kelly Grace

Phone: +44 (0) 1223 326528

### JAPAN

Katsuyoshi Fukamizu (Tokyo)

E-mail: [kfukamizu@aaaas.org](mailto:kfukamizu@aaaas.org)  
Phone: +81 3 3219 5777

Hiroyuki Mashiki (Kyoto)

E-mail: [hmashiki@aaaas.org](mailto:hmashiki@aaaas.org)  
Phone: +81 75 823 1109

### CHINA / KOREA / SINGAPORE / TAIWAN / THAILAND

### Ruolei Wu

Phone: +86 186 0082 9345  
E-mail: [rwu@aaaas.org](mailto:rwu@aaaas.org)

All ads submitted for publication must comply with applicable U.S. and non-U.S. laws. *Science* reserves the right to refuse any advertisement at its sole discretion for any reason, including without limitation for offensive language or inappropriate content, and all advertising is subject to publisher approval. *Science* encourages our readers to alert us to any ads that they feel may be discriminatory or offensive.

**Science Careers**

FROM THE JOURNAL SCIENCE ■ AAAS

[ScienceCareers.org](http://ScienceCareers.org)

# Cernet

# Science Careers

“《科学》职业”

已经与Cernet/

赛尔互联开展合

作。中国大陆的

高校可以直接联

系Cernet/赛尔互

联进行国际人才

招聘。



请访问

[Sciencecareers.org/CER](http://Sciencecareers.org/CER)

点得联系信息。

中国大陆高校以外的 招聘广告，或  
者高校 的其它业务，请与国 际合  
作、出版副总监吴若蕾联系：

+86-186 0082 9345  
[rwu@aaaas.org](mailto:rwu@aaaas.org)

# Science

POSITIONS OPEN



## EDUCATION MANAGEMENT POSITION Medical School

The Saint James School of Medicine, an international medical school is seeking a qualified academic medical professional to fill the position of **Associate Clinical Dean** in its Chicago office. Qualified applicants must be M.D. or M.D.-Ph.D. with a minimum of 12 years of medical school teaching and administrative experience.

A competitive compensation package is offered. Interested individuals should electronically send their curriculum vitae with cover letter to e-mail: [jobs@mail.sjsm.org](mailto:jobs@mail.sjsm.org).

## ASSISTANT PROFESSORSHIP Tenure Track Position Department of Biology

California State University, Northridge invites applications for tenure-track Assistant Professor positions in Cellular or Molecular Biology in the Department of Biology to begin August 19, 2015. Applicants must hold a Ph.D. and have postdoctoral experience. The successful candidate, whose eukaryotic cell biology research uses proteomics/systems/computational, or molecular approaches, shall involve undergraduate and Master's students in their research, seek extramural research funding, demonstrate teaching excellence, and must demonstrate ability to effectively work with a diverse student population.

For more information and application procedure visit: **website:** <http://www.csun.edu/science-mathematics/biology/jobs>

Screening application will begin on March 31, 2015.

California State University, Northridge is an Equal Opportunity Employer committed to excellence through diversity.

## OPEN RANK FACULTY POSITION

As part of the Second Century Initiative (**website:** <http://www.gsu.edu/secondcentury/>) at Georgia State University, the Department of Mathematics and Statistics (**website:** <http://mathstat.gsu.edu/>) invites applications for an anticipated Open Rank, Associate, or Full Professor level senior faculty position in mathematical disease modeling, beginning 2015 pending budgetary approval.

Candidates should have a strong background in mathematical modeling and analysis related to diseases and big data. A Ph.D. in Mathematics, Bioinformatics, Physics, Chemical Engineering, Biomedical Engineering, or related area is required. Preference will be given to those candidates who have a strong record of research and external funding support.


Please submit curriculum vitae and a cover letter indicating research interests to **website:** <http://www.academicjobs.org> and choose Disease Modeling option. Inquiries could be sent to e-mail: [BDMModeling@gsu.edu](mailto:BDMModeling@gsu.edu).

Post your jobs Fast and Easy



**Science Careers**

[employers.sciencecareers.org](http://employers.sciencecareers.org)



**There's only one Science**

## Science Careers Advertising

For full advertising details, go to [ScienceCareers.org](http://ScienceCareers.org) and click For Employers, or call one of our representatives.

**Tracy Holmes**  
Worldwide Associate Director  
Science Careers  
Phone: +44 (0) 1223 326525

**THE AMERICAS**  
E-mail: [advertise@sciencecareers.org](mailto:advertise@sciencecareers.org)  
Fax: 202 289 6742

**Tina Burks**  
Phone: 202 326 6577

**Nancy Toema**  
Phone: 202 326 6578

**Marci Gallun**  
Sales Administrator  
Phone: 202 326 6582

**Online Job Posting Questions**  
Phone: 202 312 6375

**EUROPE / INDIA / AUSTRALIA / NEW ZEALAND / REST OF WORLD**  
E-mail: [ads@science-int.co.uk](mailto:ads@science-int.co.uk)  
Fax: +44 (0) 1223 326532

**Axel Gesatzki**  
Phone: +44 (0) 1223 326529

**Sarah Lelarge**  
Phone: +44 (0) 1223 326537

**Kelly Grace**  
Phone: +44 (0) 1223 326528

**JAPAN**  
**Katsuyoshi Fukamizu** (Tokyo)  
E-mail: [kfukamizu@aaas.org](mailto:kfukamizu@aaas.org)  
Phone: +81 3 3219 5777

**Hiroyuki Mashiki** (Kyoto)  
E-mail: [hymashiki@aaas.org](mailto:hymashiki@aaas.org)  
Phone: +81 75 823 1109

**CHINA / KOREA / SINGAPORE / TAIWAN / THAILAND**  
**Ruolei Wu**  
Phone: +86 186 0082 9345  
E-mail: [rwu@aaas.org](mailto:rwu@aaas.org)

All ads submitted for publication must comply with applicable U.S. and non-U.S. laws. Science reserves the right to refuse any advertisement at its sole discretion for any reason, including without limitation for offensive language or inappropriate content, and all advertising is subject to publisher approval. Science encourages our readers to alert us to any ads that they feel may be discriminatory or offensive.

**Science Careers**  
FROM THE JOURNAL SCIENCE AAAS

[ScienceCareers.org](http://ScienceCareers.org)

## POSITIONS OPEN



### EDUCATION MANAGEMENT POSITION Medical School

The Saint James School of Medicine, an international medical school is seeking a qualified academic medical professional to fill the position of **Associate Clinical Dean** in its Chicago office. Qualified applicants must be M.D. or M.D.-Ph.D. with a minimum of 12 years of medical school teaching and administrative experience.

A competitive compensation package is offered. Interested individuals should electronically send their curriculum vitae with cover letter to e-mail: [jobs@mail.sjmsm.org](mailto:jobs@mail.sjmsm.org).

### ASSISTANT PROFESSORSHIP Tenure Track Position Department of Biology

California State University, Northridge invites applications for tenure-track Assistant Professor positions in Cellular or Molecular Biology in the Department of Biology to begin August 19, 2015. Applicants must hold a Ph.D. and have postdoctoral experience. The successful candidate, whose eukaryotic cell biology research uses proteomics/systems/computational, or molecular approaches, shall involve undergraduate and Master's students in their research, seek extramural research funding, demonstrate teaching excellence, and must demonstrate ability to effectively work with a diverse student population.

For more information and application procedure visit: **website:** <http://www.csun.edu/science-mathematics/biology/jobs>

Screening application will begin on March 31, 2015.

*California State University, Northridge is an Equal Opportunity Employer committed to excellence through diversity.*

### OPEN RANK FACULTY POSITION

As part of the Second Century Initiative (**website:** <http://www.gsu.edu/secondcentury/>) at Georgia State University, the Department of Mathematics and Statistics (**website:** <http://mathstat.gsu.edu/>) invites applications for an anticipated Open Rank, Associate, or Full Professor level senior faculty position in mathematical disease modeling, beginning 2015 pending budgetary approval.

Candidates should have a strong background in mathematical modeling and analysis related to diseases and big data. A Ph.D. in Mathematics, Bioinformatics, Physics, Chemical Engineering, Biomedical Engineering, or related area is required. Preference will be given to those candidates who have a strong record of research and external funding support.

Please submit curriculum vitae and a cover letter indicating research interests to **website:** <http://www.academicjobs.org> and choose Disease Modeling option. Inquiries could be sent to e-mail: [BDModeling@gsu.edu](mailto:BDModeling@gsu.edu).

**Post your jobs Fast and Easy**



**Science Careers**  
[employers.sciencecareers.org](http://employers.sciencecareers.org)

# Cernet

# Science Careers

“《科学》职业”  
已经与Cernet/  
赛尔互联开展合作。中国大陆的高校可以直接联系Cernet/赛尔互联进行国际人才招聘。



请访问  
[Sciencecareers.org/CER](http://Sciencecareers.org/CER)  
点得联系信息。

中国大陆高校以外的 招聘广告，或者高校 的其它业务，请与国际合  
作、出版副总监吴若蕾联系：  
+86-186 0082 9345  
[rwu@aaas.org](mailto:rwu@aaas.org)

**Science**





## Faculty Positions Department of Biomedical Sciences

The Department of Biomedical Sciences at Virginia Tech Carilion School of Medicine (VTC-SOM - <http://medicine.vtc.vt.edu/>) and Research Institute (VTCRI - <http://research.vtc.vt.edu/>) in Roanoke, Virginia (<http://www.vtc.vt.edu/about/>) is recruiting to fill several new faculty positions at the assistant, associate or full professor levels. Faculty with teaching expertise in either medical school biochemistry, developmental biology/embryology, epidemiology, histology/pathology, neuroscience or systems' physiology and with research interests in either neuroscience, cardiovascular sciences, regenerative medicine, cancer, infectious disease or immunology are especially encouraged to apply.

The successful candidates will have a primary responsibility for teaching first and second year medical students in a dynamic fully accredited, research intensive allopathic medical school. Some participation in teaching graduate students in Virginia Tech's Translational Biology, Medicine and Health (TBMH - <http://www.tbmh.vt.edu/>) PhD program is also possible. Faculty will have 25% time available for research in the VTCRI, working as part of a laboratory team with an established investigator. Twelve month faculty salaries and fringe benefits will be fully supported through three year renewable appointments with no obligation for salary coverage or PI status on grants. The VTC-SOM and VTCRI opened in 2010.

The medical school graduated its first class in 2014 and maintains a small class size (42) with a focus on patient centered learning and student research/discovery throughout the curriculum that incorporates four value domains – basic science, clinical science, research and interprofessionalism. Teaching and research facilities are state of the art with a research grant portfolio of \$45M between 23 lab PIs among which faculty may carry out research. We are especially interested in colleagues who are passionate about teaching, value scholarship and enjoy a highly collaborative environment, interacting with teachers and researchers from their own as well as other disciplines. The successful candidates will have a Ph.D. (or M.D./Ph.D. or D.V.M./Ph.D.), experience in teaching medical students and postdoctoral training. The medical school and research institute are located in the picturesque Roanoke Valley midway between Washington DC and Charlotte, NC.

To apply, please visit [www.jobs.vt.edu](http://www.jobs.vt.edu), posting #TR0150019. Please send cover letter, CV, statement of teaching philosophy/experience, statement of research interests/experience and have at least three reference letters of support. Candidate review will begin April 15, 2015. Please indicate Biomedical Science Positions on all correspondence.

*Virginia Tech has a strong commitment to the principle of diversity, and in that spirit seeks a broad spectrum of candidates including women, minorities, veterans, and people with disabilities.*



## TEXAS TECH UNIVERSITY HEALTH SCIENCES CENTER

School of Medicine

### Department of Immunology and Molecular Microbiology Tenure-Track Faculty Position

The Department of Immunology and Molecular Microbiology at Texas Tech University Health Sciences Center (<http://www.ttuhsu.edu/>) invites applications for a tenure track faculty position at the rank of Assistant Professor. The Department is particularly interested in candidates with cross-disciplinary approaches to problems related to host-microbe interactions, microbiome informatics and microbial pathogenesis. Excellent opportunities exist for collaborations with faculty members in basic science and clinical departments. A 12-month, institution-supported salary as well as generous start-up funding and laboratory space will be provided. In addition, the institution provides ongoing support with our state-of-the-art imaging/flow cytometry and molecular biology core facilities. Appointees will be expected to conduct an active research program, procure and maintain extramural funding and participate in medical and graduate student teaching. Special consideration will be given to candidates with current extramural funding.

Texas Tech University Health Sciences Center (TTUHSC) together with Texas Tech University and Angelo State University comprise the Texas Tech University System. TTUHSC offers programs in Allied Health Sciences, Biomedical Sciences, Medicine, Nursing, Pharmacy, and Public Health. The Graduate School of Biomedical Sciences at TTUHSC offers the M.S. and Ph.D. degrees in six concentrations of study including cell and molecular biology; biochemistry and molecular genetics; immunology and infectious diseases; pharmaceutical sciences; pharmacology and neuroscience; and physiology. The TTUHSC campus is located across the street from Texas Tech University whose current enrollment exceeds 40,000 undergraduate and graduate students. In addition to ongoing research programs at TTUHSC, the successful candidate will also have unlimited opportunities to interact with numerous well-funded faculty on the TTU campus with research programs in biology, microbiology, chemistry, biochemistry, physics and engineering.

Review of applications will begin on **April 1, 2015** and continue until the position is filled. Applicants should submit an application, cover letter explaining their interest in the Department, a curriculum vitae that includes honors and publications, and a succinct research plan to <http://jobs.brspring.com/TGWebHost/jobdetails.aspx?partnerid=25898&siteid=5281&areq=3327BR>. To expedite the review process, applicants should invite three individuals who are familiar with their work and potential for success to upload recommendation letters at the same web address.

*The TTUHSC is an Equal Opportunity/Affirmative Action/Veterans/Disability Employer.*



Knowledge that will change your world

The University of Alabama at Birmingham

## Department of Pathology DIRECTOR, DIVISION OF INFORMATICS

The University of Alabama at Birmingham (UAB) Department of Pathology is seeking an outstanding candidate at the **tenure/tenure-earning Associate Professor or Full Professor** level with experience in the field of biomedical informatics to lead its Division of Informatics. Extensive experience in biomedical informatics, or bioinformatics/computational biology and a **M.D.** or a **Ph.D.** in a related professional field is required. Candidates must have a demonstrated expertise in one of the areas of biomedical informatics and the ability to attract extramural funding. He/she will work across departments, centers and schools to enhance medical informatics, public health informatics and bioinformatics at UAB.

Four years ago, the UAB School of Medicine committed significant resources to the establishment of a Division of Informatics in the Department of Pathology and the implementation of a campus-wide clinical informatics infrastructure. During that time the division grew to five faculty, hosting multiple informatics resources in sequence and image analysis, and offering a suite of well attended immersive courses in Biomedical Informatics and Computational Pathology for both medical and graduate trainees. The new Director will be expected to continue the expansion of the Division through additional recruitment and new investments that further advance its research, education and service portfolio. The Director will participate in the development of two new Institutes at UAB, Informatics and Personalized Medicine.

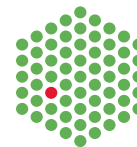
The UAB-School of Medicine is located in Birmingham, AL and is ranked 26<sup>th</sup> in NIH funding. The UAB Health System is a >\$2 billion/year enterprise, consisting of University Hospital (981 beds with installed Cerner enterprise software), The Kirklin Clinic (1,100 physician group practice), VIVA Health (a regional HMO), UAB Highlands Hospital (specialty hospital), Prime Care (primary care network), and affiliated hospitals in Montgomery and Bessemer. UAB has established high performance computing and high speed connectivity to the Lambda Rail, as well as supports the Alabama Supercomputer Facility in Huntsville, AL. The UAB Comprehensive Cancer Center, together with its partner HudsonAlpha Genomics Research Institute in Huntsville, is a key participant in The Cancer Genome Atlas.

The position offers an excellent and comprehensive compensation and benefits package. All inquiries should be directed to: **Kevin A. Roth, M.D., Ph.D., Robert and Ruth Anderson Professor and Chair, Department of Pathology, UAB, 619 South 19<sup>th</sup> Street, WP 210, Birmingham, AL 35233-7331 email: [path-informdir@mail.ad.uab.edu](mailto:path-informdir@mail.ad.uab.edu)**. Interested applicants should submit: 1) a cover letter; 2) curriculum vitae with the names of three references; and 3) a statement of research interests.

Evaluation of applications will occur as they are received and will continue until the position is filled. A Pre-employment background investigation is performed on candidates selected for employment. In addition, physicians and other clinical faculty candidates who will be employed by the University of Alabama Health Services Foundation (UAHSF) or other UAB Medicine entities must successfully complete a pre-employment drug and nicotine screen to be hired.

*UAB is an Equal Opportunity/Affirmative Action Employer committed to fostering a diverse, equitable and family-friendly environment in which all faculty and staff can excel and achieve work/life balance irrespective of race, national origin, age, genetic or family medical history, gender, faith, gender identity and expression as well as sexual orientation. UAB also encourages applications from individuals with disabilities and veterans.*

EMBL



*The European Molecular Biology Laboratory is searching for Group and Team Leaders. EMBL offers a highly collaborative, uniquely international culture. It fosters top quality, interdisciplinary research by promoting a vibrant environment consisting of young, independent researchers with access to outstanding graduate students and postdoctoral fellows.*

## Group Leader / Team Leader Cell Biology and Biophysics at EMBL Heidelberg, Germany (2 Positions)

The Cell Biology and Biophysics Unit is an interdisciplinary department where biologists, physicists and chemists work closely together. This highly collaborative mix of groups employs technologies ranging from advanced electron and light microscopy, chemical biology and biochemistry, genetics and functional genomics to modelling and computer simulations. The research focuses on comprehensive understanding of the molecular mechanism of essential cellular functions, currently including transport, signalling, migration, differentiation and division.

We are seeking to recruit outstanding group/team leaders in the general area of cutting-edge molecular cell biology. We also welcome applications to establish technology development oriented groups/teams, especially in the areas of imaging technologies, image analysis methods, as well as modelling of complex dynamic biological processes. In addition to biologists, applicants with a strong background in optical engineering, bioinformatics, chemistry or physics and a keen interest in cell biological applications are especially encouraged to apply.

The successful candidate should have a strong motivation to work in the multidisciplinary and collaborative environment of EMBL, grasping the opportunity to interact with many other research groups. In general, EMBL appoints group/team leaders early in their career and provides them with a very supportive environment for their first independent position to achieve highly ambitious and original research goals.

EMBL is an inclusive, equal opportunity employer offering attractive conditions and benefits appropriate to an international research organisation with a very collegial and family friendly atmosphere. The remuneration package comprises from a competitive salary, a comprehensive pension scheme, medical, educational and other social benefits, as well as financial support for relocation and installation, including family, and the availability of an excellent child care facility on campus.

Please apply online through [www.embl.org/jobs](http://www.embl.org/jobs) and include a cover letter, CV and a concise description of research interests and future research plans. Please also arrange for 3 letters of recommendation to be emailed to [references@embl.de](mailto:references@embl.de) at the latest by 10 April 2015.

**Interviews** are planned for 28, 29 and 30 April 2015.

Further information about the position can be obtained from the Head of Unit Jan Ellenberg ([jan.ellenberg@embl.de](mailto:jan.ellenberg@embl.de)).

An initial contract of 5 years will be offered to the successful candidate. This is foreseen to be extended to a maximum of 9 years, subject to an external review.

Further details on Group Leader appointments can be found under [www.embl.org/gl\\_faq](http://www.embl.org/gl_faq).

[www.embl.org](http://www.embl.org)



# UAB MEDICINE

## PEDIATRICS

The University of Alabama at Birmingham



Children's  
of Alabama

### Department of Pediatrics POSTDOCTORAL FELLOW

A postdoctoral fellow position is open to study airway remodeling in pediatric cystic fibrosis (CF). Of particular interest is the modulation link between CFTR dysfunction and TGF-beta associated pathobiology. Primary projects available include (1) investigating the direct effect that CFTR has on TGF-beta transcription, activation and signaling; (2) the mechanisms that contribute to increased TGF-beta activation and signaling in the diseased CF lung, including assessment of mechanical stimulation, pH, and inflammatory stimuli; and (3) utilization of CF animal models to assess the response to the potential therapeutic benefit of TGF-beta inhibition to ameliorate disease progression. The successful applicant will have the opportunity to develop multiple projects using cell culture and animal models in a well-equipped, multi-disciplinary laboratory with multiple collaborative opportunities. The post-doctoral fellow will design, interpret, and perform experiments that address important molecular pathways applicable to pediatric lung disease with significant opportunity for manuscript preparation and oral presentation at national/international meetings.

Prior experience in cell and molecular biology is highly valued, but most importantly, the position requires a high level of self-motivation with a strong interest in the health implications of biomedical research. The successful candidate must be innovative and interested in pursuing an independent research effort upon successful completion of the fellowship. Ph.D. and/or M.D. degree required.

Applicants should submit their CV and the names and contact information of three references to:

UAB Department of Pediatrics  
Attn: Tom Harris, MD  
1600 7<sup>th</sup> Ave S, Lowder 620  
Birmingham, Alabama 35233  
E-mail: [tharris@peds.uab.edu](mailto:tharris@peds.uab.edu)  
Tel: 205-638-9583, Fax: 205-975-5983

*UAB is an Equal Opportunity/Affirmative Action Employer committed to fostering a diverse, equitable and family-friendly environment in which all faculty and staff can excel and achieve work/life balance irrespective of race, national origin, age, genetic or family medical history, gender, faith, gender identity and expression as well as sexual orientation. UAB also encourages applications from individuals with disabilities and veterans.*

A pre-employment background investigation is performed on candidates selected for employment.



### AAAS is here – helping scientists achieve career success.

Every month, over 400,000 students and scientists visit ScienceCareers.org in search of the information, advice, and opportunities they need to take the next step in their careers.

A complete career resource, free to the public, Science Careers offers hundreds of career development articles, webinars and downloadable booklets filled with practical advice, a community forum providing answers to career questions, and thousands of job listings in academia, government, and industry. As a AAAS member, your dues help AAAS make this service available to the scientific community. If you're not a member, join us. Together we can make a difference.

To learn more, visit  
[aaas.org/plusyou/sciencecareers](http://aaas.org/plusyou/sciencecareers)



### Director for the Nebraska Center for Virology

The University of Nebraska - Lincoln (UNL) is seeking an extraordinary research scholar to serve as Director of the Nebraska Center for Virology (NCV). NCV was founded in 2000 and has been funded continuously by an NIH Center for Biomedical Research Excellence Grant. NCV is a Regents' designated Center of Excellence and includes about 35 virologists from UNL, University of Nebraska Medical Center and Creighton University Medical Center. NCV faculty conduct research on human, animal, and plant viral diseases.

Candidates must have: (1) a PhD, MD, DVM or equivalent in a related area of science; (2) a nationally recognized, federally funded research program in virology; (3) administrative experience including leadership of scientists and research teams through the ability to envision, facilitate, develop, and coordinate innovative, interdisciplinary and collaborative research; and (4) a record of scholarly achievements and qualifications for appointment as a tenured, full professor in an appropriate department at UNL. Preferred qualifications include: (1) experience building new research partnerships to capitalize on emerging research opportunities; (2) experience working with university administrators to enhance research capacity; and (3) leading submission of competitive applications for large, center grants to support research or training efforts. The specific area of research is open to all disciplines of virology. In addition to competitive start-up support and a state-funded salary line as NCV Director, several new junior tenure track faculty positions will be available for recruitment by the successful candidate.

To learn more about the University of Nebraska and the Nebraska Center for Virology visit <http://unl.edu/virologycenter>. To be considered for this position go to <http://employment.unl.edu> and search for requisition #F\_150060. Click on "Apply to this job." Attach CV, cover letter, statement of management and research philosophy and up to 3 reprints (other). Review of applications will begin **May 8, 2015** and will continue until a suitable candidate is selected.

*The University of Nebraska-Lincoln is committed to a pluralistic campus community through affirmative action, equal opportunity, work-life balance, and dual careers. UNL is the flagship land-grant University in Nebraska with a total enrollment of more than 25,000 students.*

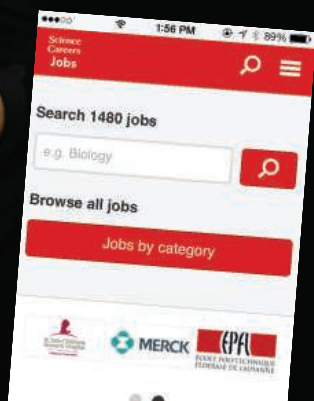
### Download the Science Careers jobs app from Science



Jobs are updated 24/7

Search thousands of jobs  
on your schedule

Receive push notifications  
per your job search criteria



### Get a job on the go.

Search worldwide for thousands of scientific jobs in academia, industry, and government. The application process is seamless, linking you directly to job postings from your customized push notifications.



Scan this code to  
download app or visit  
[apps.sciencemag.org](http://apps.sciencemag.org)  
for information.

ScienceCareers | AAAS  
FROM THE JOURNAL SCIENCE

ScienceCareers.org

# CALL FOR NOMINATIONS:

Sanofi and the Institut Pasteur are pleased to announce the Sanofi - Institut Pasteur 2015 Awards.

**These Awards will honor four scientists, whose outstanding research in the life sciences is contributing to progress in global public health, specifically in the following fields:**

**TROPICAL AND NEGLECTED DISEASES**

**IMMUNOLOGY**

**DRUG RESISTANCE**

**NEURODEGENERATIVE DISEASES AND AGEING**

There will be three categories of awards:

- **One International Senior award** (€ 125 000)
- **One International Mid-career award<sup>1</sup>** (€ 75 000)
- **Two National Junior awards<sup>2</sup>** (€ 50 000 each)

More information and the nomination form are available on the website

[www.sanofi-institutpasteur-awards.com](http://www.sanofi-institutpasteur-awards.com)

Deadline to submit nominations:  
**Tuesday, 28th April, 2015**

Awards Ceremony:  
**Wednesday, 4th November, 2015 in Paris**



**INSPIRED BY PASTEUR  
SUPPORTED BY SANOFI**

**A distinguished international Jury will choose the Awardees:**

Prof. Peter C Agre, Prof. Elizabeth H. Blackburn, Prof. Pascale Cossart, Prof. Catherine Dulac, Prof. Alain Fischer, Prof. Jörg H. Hacker, Prof. Jules A. Hoffmann, Dr Gary J. Nabel, Prof. Staffan Normark, Prof. Jeffrey V. Ravetch and Prof. Philippe Sansonetti.

**Contact:** 2015awards@pasteur.fr

<sup>1</sup>The candidates should not be more than 52 years old on 1-7-2015 - <sup>2</sup>The candidates should not be more than 45 years old on 1-7-2015 and should work in France



[www.sanofi-institutpasteur-awards.com](http://www.sanofi-institutpasteur-awards.com)



## POSITIONS OPEN



**Opportunities for POSTDOCTORAL RESEARCHERS in Biomedical Research at the Spanish National Centre for Cardiovascular Research CNIC, Madrid - Spain**

The CNIC is dedicated to excellence in cardiovascular research and to translating new knowledge into real improvements in clinical practice.

The scientific project of the centre has been structured in three research areas:

- Vascular Pathophysiology
- Myocardial Pathophysiology
- Cell & Developmental Biology

To be eligible, candidates must:

- Hold a PhD degree that must have been awarded no more than five years ago (exceptions will be made for documented career breaks and candidates with children)
- Have, at least, one publication as first author in an international peer reviewed journal
- Candidates must not have resided or carried out their main activity in Spain for more than twelve months in the last three years

The CNIC offers TEN (10) fellowships in this call:

- A 3-year contract
- An internationally competitive salary
- State of the art infrastructure and latest generation of technological equipment
- Scientific-technical support and complementary training

**Deadline for submission of proposals: 5 May 2015**

CNIC is an inclusive, equal opportunity employer, irrespective of nationality, ethnic origin, gender, marital or parental status, sexual orientation, creed, disability, age or political belief. Confidentiality is guaranteed throughout the selection process and all current regulations relating to the protection of personal data will be strictly adhered to.

For further information and applications, please visit [www.cnic.es](http://www.cnic.es)



**John P. Long Chair in Pharmacology - Neuroscience**

The University of Iowa Department of Pharmacology seeks exceptional applicants at the senior Associate or full Professor level to hold the John P. Long Chair in Pharmacology (Neuroscience). Applicants should have an outstanding record of innovative research and academic excellence and demonstrated expertise in any area of neuroscience including systems, molecular/cellular, behavioral, neurodegenerative disorders, and pain, employing cutting edge methodologies. The candidate will join a strong and growing community of neuroscientists. The Carver College of Medicine has designated neuroscience as a strategic priority for growth and investment. Newly remodeled research space with state-of-the-art shared instrumentation is available. This position includes a 12-month salary (funded partially by the endowment), benefits and a highly competitive start-up package. All applicants must have a relevant doctoral degree and a record of accomplishment consistent with appointment as Associate Professor with Tenure or Professor with Tenure. The successful candidate will maintain a vigorous, independent, extramurally funded research program, have a desire to train students and postdoctoral fellows, and participate in departmental teaching.

To apply for this position, visit The University of Iowa website at <http://jobs.uiowa.edu>, requisition #65982.

*The University of Iowa is an Equal Opportunity/Affirmative Action Employer. All qualified applicants are encouraged to apply and will receive consideration for employment free from discrimination on the basis of race, creed, color, national origin, age, sex, pregnancy, sexual orientation, gender identity, genetic information, religion, associational preference, status as a qualified individual with a disability, or status as a protected veteran.*





For recruitment in science, there's only one **Science**

### What makes *Science* the best choice?

- Read and respected by 570,400 readers around the globe
- 78% of readers read *Science* more often than any other journal
- Your ad sits on specially labeled pages to draw attention to the ad
- Your ad dollars support AAAS and its programs, which strengthens the global scientific community.

### Why choose this cancer section for your advertisement?

- Relevant ads lead off the career section with special Cancer Research banner
- Bonus distribution to:
  - American Association for Cancer Research  
April 18–22, 2015, Philadelphia, PA
  - American Association for Cancer Research Career Fair  
April 18, 2015, Philadelphia, PA
- Special distribution to 42,000 scientists beyond our regular circulation.

### Expand your exposure. Post your print ad online to benefit from:

- Link on the job board homepage directly to cancer research jobs
- Dedicated landing page for jobs in cancer research
- Additional marketing driving relevant job seekers to the job board.



\* Ads accepted until March 30 on a first-come, first-served basis.

SCIENCECAREERS.ORG

**ScienceCareers**

FROM THE JOURNAL SCIENCE AAAS

To book your ad: [advertise@sciencecareers.org](mailto:advertise@sciencecareers.org)

The Americas  
202-326-6582

Europe/RoW  
+44(0) 1223-326500

Japan

+81-3-3219-5777

China/Korea/Singapore/Taiwan  
+86-186-0082-9345

## Deputy Director - Science Programs

Department of Energy's Joint Genome Institute (JGI) is a large-scale genome science user facility focused on studies related to Energy and the Environment. It is seeking a worldclass scientist and dynamic leader to inspire and lead the Institute's Scientific Programs. The Deputy Director reports directly to the JGI Director and will provide leadership and oversight for key scientific departments at the JGI including the Plant, Fungal, Metagenome, Microbial and DNA Synthesis science programs as well as manage the JGI user programs. Will also be responsible for the strategic direction and planning for new and existing programs and will act as a liaison/ spokesperson and represent the JGI to external agencies. The Deputy will have the opportunity and support to lead an independent research initiative relevant to the activities at the Institute.

The JGI is part of the Lawrence Berkeley National Laboratory, providing high-throughput sequencing and computational analysis capabilities. The DOE JGI serves a diverse scientific community as a user facility, enabling the application of large-scale genomics and analysis of plants, microbes and communities of microbes to address the DOE mission goals in bioenergy and environment. <http://jgi.doe.gov>

### How to Apply:

Please go to <http://50.73.55.13/counter.php?id=30815> Then follow the application instructions. Please include a CV, summary of research interests, and references. For informal inquiries, contact [wrcannan@lbl.gov](mailto:wrcannan@lbl.gov)

Berkeley Lab is an affirmative action/equal opportunity employer committed to the development of a diverse workforce.



## The CAS-MPG Partner Institute for Computational Biology is searching for "Group Leader" in Shanghai, China

The CAS-MPG Partner Institute for Computational Biology (PICB) is an internationally recognized research institute based in Shanghai, China and jointly operated by the Chinese Academy of Sciences (CAS) and the German Max Planck Society (MPG). Work at this institute is driven by the accelerating importance of statistical and computational methods in modern biology, and we seek to do innovative research in the interdisciplinary field of biology, mathematics, physics and computer science.

PICB is eager to receive applications for Group Leader positions from talented scientists working in the broad area of quantitative biology, including but not limited to:

- Genome biology;
- Epigenomics and RNA processing;
- Computational biology;
- Biostatistics;
- Biomathematics.

PICB will offer a competitive salary package to successful applicants, including a basic salary, position allowance, housing allowance and other benefits.

Interested applicants should send a covering letter, a curriculum vitae, a brief summary of past research achievements and future plans, 3 letters of recommendation to:

**Prof. Jing-Dong Jackie Han**  
**CAS-MPG Partner Institute for Computational Biology**  
**320 Yueyang Road, Shanghai 200031**  
**Tel: 86-21-54920458**  
**Fax: 86-21-54920451**  
**E-mail: [jdhan\(at\)picb.ac.cn](mailto:jdhan(at)picb.ac.cn)**

THE UNIVERSITY OF HONG KONG

香港大學



Founded in 1911, the University of Hong Kong is committed to the highest international standards of excellence in teaching and research, and has been at the international forefront of academic scholarship for many years. The University has a comprehensive range of study programmes and research disciplines spread across 10 faculties and over 140 academic departments and institutes/centres. There are over 27,700 undergraduate and postgraduate students who are recruited globally, and more than 2,000 members of academic and academic-related staff coming from multi-cultural backgrounds, many of whom are internationally renowned.

## Post-doctoral Fellowships

Applications are invited for a number of positions as Post-doctoral Fellow (PDF) at the University of Hong Kong. Appointments will be made for a period of 2 to 3 years and the appointees must be in post on or before February 29, 2016.

PDF posts are created specifically to bring new impetus and vigour to the University's research enterprise. Positions are available from time to time to meet the strategic research needs identified by the University. Positions are available in the following Faculties/Departments/Schools/Centres/Units:

- |  |   |
|--|---|
| • Faculty of Dentistry                                       | • Pharmacology and Pharmacy                       |
| • Faculty of Education                                       | • School of Public Health                         |
| • Civil Engineering  | • Public Health Research Centre                   |
| • Computer Science   | • Centre for Reproduction, Development and Growth |
| • Electrical and Electronic Engineering                      | • Stem Cell and Regenerative Medicine Consortium  |
| • Mechanical Engineering                                     | • Surgery   |
| • Biochemistry   | • School of Biological Sciences                   |
| • Centre for Cancer Research                                 | • Chemistry                                       |
| • Research Centre of Heart, Brain, Hormone and Healthy Aging | • Physics   |
| • Centre for Genomic Sciences                                | • The Swire Institute of Marine Science           |
| • Research Centre of Infection and Immunology                | • HKJC Centre for Suicide Research and Prevention |
| • Pathology  | • The State Key Laboratory for Liver Research     |

### Post-doctoral Fellows

PDFs are expected to devote full-time to research. Applicants should be doctoral degree holders having undertaken original research that has contributed to the body of knowledge. A highly competitive salary commensurate with qualifications and experience will be offered. Annual leave and medical benefits will also be available.

### Procedures

Prospective applicants are invited to visit our webpage at <http://jobs.hku.hk/> to view the list of the Faculties/Departments/Schools/Centres/Units and their research areas for which PDF positions are currently available. Before preparing an application, they should contact the Head of the appropriate academic unit, or the contact person as specified, to ascertain that their research expertise matches the research area for which a vacant PDF post is available.

Applicants must submit a completed University application form, which should clearly state **which position they are applying for**; and in which academic discipline. They should also provide further information such as details of their research experience, publications, research proposals, etc.

Application forms (341/1111) can be downloaded at <http://www.hku.hk/apptunit/form-ext.doc> and further particulars can be obtained at <http://jobs.hku.hk/>. **Closes April 17, 2015.** The University thanks applicants for their interest, but advises that only shortlisted applicants will be notified of the application result.

The University is an equal opportunities employer and is committed to a No-Smoking Policy



By Andrew Gaudet

# A grad school survival guide

Since becoming a postdoc, I've mentored several incoming graduate students. In doing so, I've reflected on my own scientific experiences studying spinal cord injury repair. I've compiled a short tutorial aimed at making the road to a Ph.D. less bumpy, with a focus on the day-to-day tasks that fill a graduate student's life, common hazards to avoid, and useful shortcuts you can take. These tips will help you build and maintain momentum and keep your projects moving forward. Think of it as a practical survival guide for graduate students.

**Craft good questions.** Don't just show up and do the work in front of you. Read about it, think about it, talk about it with other scientists, and plan it out. Hard questions and deep thinking lead to new and better ideas. Revisit and revise your questions as new results come in.

**Ask for help.** Ask that grizzled old postdoc for advice on experimental design, or ask the lab technician for assistance with PCR. To troubleshoot my cell migration assays, I sought the advice of a postdoc in a different lab. Along the way I learned a lot about cell culture techniques, published a paper in a respectable journal, and finished my Ph.D. You don't get extra points for doing it on your own.

**Respect and appreciate your lab mates.** If you often work with undergraduates or technicians, take them to lunch to show your appreciation. If someone helps you even a little, acknowledge them generously in your presentations.

**Have at least two projects.** If you have downtime on one, you can focus on another and keep your momentum. During my postdoc at Ohio State University, a certain protein expressed after spinal cord injury looked promising at first but didn't lead anywhere. Fortunately, a second molecule turned out to be important not only in spinal cord injury but also in obesity and depression. By spreading energy among multiple projects, you increase the chances of discovering something novel and exciting.

**Sleep on it.** If a lab mate or mentor irritates you, write down your thoughts (discreetly and securely), but don't respond right away. Sleeping on it will clear your head and allow you to compose a balanced, respectful response the next day—if you decide to reply at all.

**If you need guidance from your mentor, set up a meeting.** Unless she prefers to keep things informal, schedule a time to seek direction.



*“Along the route to a Ph.D., rough seas can be navigated or avoided entirely.”*

before you check your e-mail. You'll find the rest of your day goes better with that out of the way. For more daunting, longer term tasks, plan them out and take the first steps as soon as you can.

**Balance bouts of focused work with short breaks.** Intermittent breaks are invigorating and help you maintain focus for the entire day.

**Get organized.** Online calendars can ensure that you never miss an important meeting, experiment, or workshop. Cloud-based aggregators (e.g., Evernote) allow you to access practical information such as details for ordering supplies, locations of samples in the lab, and ideas for future experiments.

Along the route to a Ph.D., rough seas can be navigated or avoided entirely. It takes many small successes, achieved day by day, to reach your long-term goals. So stay focused. ■

Andrew Gaudet is a postdoc at the University of Colorado, Boulder. Send your story to [SciCareerEditor@aaas.org](mailto:SciCareerEditor@aaas.org). For more on life and careers, visit [sciencecareers.org](http://sciencecareers.org).